PRINCIPE FELIPE
CENTRO DE INVESTIGACION

Department: **Biochemistry and Molecular Biology**

Doctoral Program: **Biomedicine and Biotechnology**

Doctoral Thesis

DEVELOPMENT OF POLYPEPTIDE-BASED THERAPEUTICS FOR THE TREATMENT OF CASTRATION RESISTANT PROSTATE CANCER

Sonia Vicente-Ruiz Salvador

University of Valencia, December 2019

Thesis Director: **Dr. María J. Vicent Docón**

Thesis Co-director: **Dr. Ana Armiñán de Benito**

Dr. María J. Vicent Docón, Ph.D. in Chemistry and Head of the Polymer Therapeutics Laboratory at the Centro de Investigación Príncipe Felipe, Valencia, Spain, and Dr. Ana Armiñán de Benito, Ph.D. in Biology and senior researcher of the same laboratory CERTIFY, that the work

"DEVELOPMENT OF POLYPEPTIDE-BASED THERAPEUTICS FOR THE TREATMENT OF CASTRATION RESISTANT PROSTATE CANCER"

has been developed by Sonia Vicente-Ruiz Salvador under their supervision in the Centro de Investigación Príncipe Felipe in Valencia, as a thesis project to obtain a Ph.D. degree in Biomedicine and Biotechnology from the University of Valencia, Faculty of Biological Sciences, Biochemistry and Molecular Biology Department.

Dr. María J. Vicent Docón

Dr. Ana Armiñán de Benito

Index

Acknowledgments **13**

Abbreviations **19**

Abstract **29**

Objectives **41**

CHAPTER I: GENERAL INTRODUCTION **45**

I.1. Prostate Cancer **47**

I.1.1. Prostate Cancer Prevalence 47

I.1.2. Stages and Cellular Classification in Prostate Cancer Progression 48

I.2. Prostate Cancer Biomarkers and Sub-molecular Classification **52**

I.3. Role of Insulin-Like Growth Factor System in Prostate Cancer **56**

I.3.1. IGF-1R Signaling Pathways and Internalization 58

I.3.2. Feedback regulation between Phosphoinositide 3-kinase and Androgen Receptor Signaling Pathways 61

I.3.3. The Role of Insulin Growth Factor-1 Receptor in Prostate Cancer Development 62

I.4. Castration-resistant Prostate Cancer **64**

I.4.1. Molecular Mechanisms Involved in Castration-Resistant Prostate Cancer 65

I.4.1.1. Androgen Receptor-dependent Mechanisms *65*

I.4.1.2. Androgen Receptor-independent Mechanisms *67*

I.4.1.3. Androgen Receptor-bypassing Signaling *69*

I.4.2. Castration-Resistant Prostate Cancer Therapies: Current Therapeutic Approaches 71

I.4.3. Castration-Resistant Prostate Cancer Therapies: Potential Therapeutic Approaches 74
I.4.3.1. PARP Inhibitors 74
I.4.3.2. Angiogenesis Inhibitors 75
I.4.3.3. Growth Factor Receptor Inhibitors 76
I.5. Nanomedicine for PCa treatment: Principal Aspects and Classification 78
I.5.1. Biological Barriers to Nanomedicine 81
I.5.2. Current Studies in Nanomedicine for Prostate Cancer 83
I.6. Polymers Therapeutics 87
I.6.1. Classification of Polymer Therapeutics 88
I.6.2. Enhanced Permeability and Retention Effect 91
I.6.3. Intracellular Trafficking of Polymer Therapeutics 92
I.6.4. Polymer-based Combination Therapy 94
I.7. Polymer Conjugates as Therapeutics 96
I.7.1. Polymer-protein Conjugates 96
I.7.2. Polymer-drug Conjugates 99
I.8. Polypeptide-Based Conjugates as Therapeutics 109
I.9. Bibliography 110

CHAPTER II: MATERIALS & METHODS 137

II.1 Materials 139

II.1.1. Chemical and Biological Reagents 139
II.1.2. Cell Lines and Culture Conditions 141
II.1.2.1. Cell Line Growth Medium 141
II.1.3. Antibodies 142
II.1.3.1. Primary Antibodies 142
II.1.3.2. Secondary Antibodies 143
II.1.4. Animals 144

II.2. Methods 144

II.2.1. AVE1642 and PGA-AVE1642 Synthesis 144

II.2.1.1. Synthesis of Pyridyl Disulfide-modified PGA 144

II.2.1.2. Modification of AVE1642 with N-succinimidyl-S-acetylthiopropionate 146

II.2.1.3. Conjugation of SATP-modified AVE1642 to PGA-PD 146

II.2.2. Labeling of AVE1642 and PGA-AVE1642 with Cyanine Dyes 147

II.2.3. Characterization of AVE1642 and PGA-AVE1642 148

II.2.3.1. Amino-acid Analysis 148

II.2.3.2. Ultraviolet-Visible Spectroscopy 148

II.2.3.3. Size-exclusion Chromatography 149

II.2.3.4. SDS-PAGE Electrophoresis 149

II.2.3.5. Dynamic Light Scattering and Zeta Potential Measurements 149

II.2.3.6. Circular Dichroism Spectroscopy 150

II.2.3.7. ELISA assays 151

II.2.3.8. Hemolysis Assays 152

II.2.4. Lentiviral Infection Protocol 153

II.2.5. In vitro Toxicity Studies 154

II.2.6. ERG Gene Silencing by siRNA 155

II.2.7. AVE1642 and PGA-AVE1642 Internalization Studies 156

II.2.7.1. Flow Cytometry 156

II.2.7.2. Confocal Microscopy 158

II.2.7.3. Stochastic Optical Reconstruction Microscopy 159

II.2.8. IGF-1R Internalization Analysis 161

II.2.9. Protein Analysis in Cell and Tumor Samples 162

II.2.9.1. Cellular Pellet Processing 162

II.2.9.2. Tumoral Sample Processing 163

II.2.9.3. Cellular and Tumoral Extraction and Quantification 163

II.2.9.4. Protein Detection 164

II.2.10. In Vivo Analyses 166

II.2.10.1. Ethical Considerations 166

II.2.10.2. Development of Orthotopic Prostate Cancer Mouse Model 166

II.2.10.3. Enhanced Permeability and Retention Effect Analysis 167
II.2.10.4. Biodistribution Experiment and Fluorescent Quantification 168
II.2.10.5. Antitumoral Activity Analysis..... 169
II.2.10.6. Tumor Immunohistochemistry..... 170

II.3. Statistical Analysis 171

II.4. Bibliography 172

CHAPTER III: PGA CONJUGATION ALTERS AVE1642 BIOACTIVITY IN PROSTATE CANCER MODELS_____175

III.1. Antecedents and Background.....177

III.2. Synthesis of PGA-conjugated AVE1642 179

III.2.1. Synthesis of Pyridyl Dithiol-modified PGA..... 179

III.2.2. Synthesis of N-Succinimidyl-S-acetylthiopropionate-modified AVE1642 180

III.2.3. Design and Synthesis of PGA-AVE1642 Conjugates 181

III.3. Cytotoxicity Analysis Suggests that High Levels of PGA Conjugation do not Negatively Influence AVE1642 Activity in the Adequate Prostate Cancer (PCa) Cell Line. 182

III.3.1. Selection of Adequate PCa Cell model 182

III.3.2. Cytotoxicity of AVE1642 derivatives..... 184

III.4. Characterization of 2:1 PGA-AVE1642 conjugate.....185

III.4.1. SDS-PAGE Gel Electrophoresis Analysis..... 185

III.4.2. Size Analysis by Size Exclusion Chromatography..... 186

III.4.3. Size and Charge Analysis by Dynamic Light Scattering and Z-Potential Analyses..... 187

III.4.4. Structural Analysis by Circular Dichroism..... 188

III.5. PGA-conjugation Enhances Stability, Improves Affinity for IGF-1R, and Maintains Hemocompatibility of AVE1642 191

III.5.1. PGA-conjugation Protects AVE1642 from Degradation 191

III.5.2. PGA Conjugation Enhances the Affinity of AVE1642 for IGF-1R 192

III.5.3. PGA Conjugation of AVE1642 does not Promote Hemolysis 194

III.6. AVE1642 and PGA-AVE1642 Displays Cell Line Specific Cytotoxic Activity 195

III.6.1. Cytotoxicity of AVE1642 and PGA-AVE1642 in VCaP Cells 195

III.6.2. Lack of Cytotoxicity of AVE1642 and PGA-AVE1642 in Alternative PCa Cell Lines 196

III.6.3. AVE1642 and PGA-AVE1642 Mediated Cytotoxicity depends on ERG Expression 198

III.7. PGA-conjugation Leads to Altered Molecular Responses and Cellular Trafficking in vitro 200

III.7.1. PGA-conjugation Prevents IGF-1R Internalization after AVE1642 Binding 200

III.7.2. PGA-conjugation of AVE1642 Prevents Energy-dependent Internalization 202

III.7.3. PGA-conjugation Modifies AVE1642 Cell Trafficking 203

III.7.3.1. Super-resolution Microscopy Confirms that PGA-conjugation Alters AVE1642 Internalization 208

III.7.3.2. PGA-conjugation Prevents the Activation of PI3K and MAPK Pathways by AVE1642 211

III.8. Development of an Orthotopic PCa Mouse model 214

III.8.1. Development of Stable Luciferase Expressing VCaP Cells 214

III.8.2. Optimization of the Orthotopic PCa Mouse Model 217

III.8.3. Analysis of Luciferase Stability in vivo 220

III.8.4. Analysis of the Enhanced Permeability and Retention Effect 221

IV.8.5. PGA-conjugation Maintains AVE1642 Tumor Accumulation 222

III.9. In vivo Antitumoral Activity of AVE1642 and PGA-AVE1642 223

III.9.1. PGA-conjugation Improves AVE1642 Antitumor Activity 224

III. 9.2. PGA Conjugation of AVE1642 Improves IGF-1R Inhibition 230

III.10. Modulation of the Tumor Microenvironment by AVE1642 and PGA-AVE1642 232

III.10.1. Evaluation of Tumor Vasculature in the Orthotopic PCa Mouse Model 232

III.10.2. Cell Proliferation and Angiogenic Studies in the Orthotopic PCa Mice Tumors *236*

III.10.2.1. PGA-conjugation Significantly Improves Inhibition of Prostate Tumor Proliferation by AVE1642 236

III.10.2.2. PGA-conjugation Significantly Improves Inhibition of Tumor Angiogenesis by AVE1642 237

III.11. Conclusions 239

III.12. Bibliography 240

CHAPTER IV: EVALUATION OF A NOVEL COMBINATION THERAPY FOR CASTRATION-RESISTANT PROSTATE CANCER 245

IV.1. Antecedents and Background 247

IV.2. PGA-AVE1642 Synergizes with Abiraterone in VCaP cells 250

IV.3. Combination Therapy Exhibits T2E-dependent Synergistic Effects in Prostate Cancer Cells 253

IV.4. The Synergistic Effect of the Combination Therapy Requires T2E Expression 258

IV.5. Antitumoral Activity of Prostate Cancer Combination Therapy In vivo 260

IV.5.1. Optimization of the Orthotopic Mouse PCa Model to Evaluate Responses to Combination Therapy 260

IV.5.2. DHEA Supplementation Does Not Interfere with the Anti-tumoral Activity of AVE1642 and PGA-AVE1642 266

IV.5.3. Evaluation of Combination Therapy in an Orthotopic Prostate Cancer Mouse Model 270

IV.6. Combination Therapy Improves IGF-1R Inhibition 274

IV.7. Conclusions.....280

IV.8. Bibliography.....281

General Discussion.....285

Final Conclusions.....311

Memoria de la Tesis.....315

1. Introducción.....317
2. Objetivos.....322
3. Material y Métodos.....324
4. Resultados.....331
5. Conclusiones.....339
6. Bibliografía.....341

Acknowledgments

Acknowledgments

A lo largo de todos estos años como estudiante predoctoral, la tesis ha sido para mí tanto un reto profesional como personal. En este mismo instante miro atrás y a pesar de haber pasado buenos y no tan buenos momentos me doy cuenta donde estoy y todo aquello que he aprendido y superado. Este camino científico no es fácil, necesita constancia, mucha dedicación y sacrificio, pero todo esto al final tiene una gran recompensa que merece muchísimo la pena. Para alcanzar esta meta me han acompañado muchas personas a las que quiero agradecer inmensamente su presencia en esta etapa de mi vida.

En primer lugar, me gustaría agradecer a mi directora de tesis, la Dra. María Jesús Vicent Docón por darme la oportunidad de realizar mi tesis doctoral en su laboratorio y por aportarme grandes conocimientos científicos. Durante estos cinco años podría decir que has sido mi "*madre científica*", me has guiado y me has educado para llegar a ser una buena investigadora, y lo más importante, me has enseñado a creer y confiar en mí misma. Moltes gràcies MJ.

En segundo lugar, agradecer a mi codirectora de tesis, la Dra. Ana Armiñán de Benito por todos sus consejos y por haber sido la primera persona que apostó por mí para pedir la beca predoctoral. Muchísimas gracias Ana, gracias por tu tiempo y tu dedicación para enseñarme "*ciencia*" y "*vida*". Gracias por enseñarme a ser crítica con los resultados y a saber relacionar los conceptos. Ahora siempre que veo algún resultado, automáticamente mi cerebro piensa….¿y el control?. Aunque parezca mentira echaré de menos estar en el quirófano contigo haciendo ortotópicos de próstata como churros.

También me gustaría agradecer al profesor Twan Lammers por haberme acogido en su laboratorio durante mi estancia en Alemania. Allí aprendí nuevas técnicas y conocimientos que me han servido para evolucionar y completar mis

trabajos científicos. He de agradecer a cada persona del laboratorio su simpatía y su ayuda durante todo el tiempo que estuve allí y por hacerme sentir como una más del grupo. Esta estancia fue muy gratificante para mí, aparte de los resultados científicos puedo decir que me llevo a grandes amigos como Tarun, Vertika, Gurbet, Okan, Fedi, Ilaria y Elena. Nunca olvidaré todo el apoyo que me habéis dado y lo bien que me habéis cuidado, gracias por ser mi familia durante esa época y por poder contar con cada uno de vosotros en la actualidad.

Una mención muy especial para mí después de todo lo vivido durante estos años es para mis compañeros del laboratorio I-36. Tantas horas juntos y tantos momentos vividos han convertido la ciencia en una convivencia. En estos últimos años aquellas personas que formaban parte del laboratorio cuando yo empecé han terminado, pero han llegados nuevas incorporaciones. Nunca olvidaré a mi primera estudiante, Marieke Remue, gracias a ti aprendí a enseñar todo lo que yo había aprendido. Me gustaría agradecer a Vicent, Aroa, Amaya, Elena, Luz y Dani vuestra dedicación cuando lo he necesitado. Juanjo, muchas gracias por ser mi compañero durante la gran parte de mi tesis y en esos momentos en los que se hacían las mil en el laboratorio. A mis "*Superpredocs*", Irene y Fernanda por poder contar con vuestro apoyo. Paula, gracias por escucharme y por tu compañía. A nuestro técnico David, nada hubiera sido lo mismo sin esos bailoteos de reggaetón luego de un largo día, sabes que tenemos un concierto pendiente. A nuestra técnico María Helena, gracias por todos tus consejos y tu paciencia cuando he necesitado cualquier cosa, siempre has estado ahí. Stuart, "*you are my friend*", gracias infinitas por tu paciencia y por enseñarme y ayudarme a redactar mis trabajos científicos en inglés, echaré de menos ver tu cara millones de veces en una hoja llena de comentarios, jeje. Inma, Esther, Zoraida, gracias por vuestros ánimos. Alex, Tetiana, Alessio y María, agradeceros vuestra ayuda cuando la he necesitado. Katia, mi postdoc polimérica, muchas gracias por ayudarme en todo momento y estar siempre disponible cuando lo he necesitado. También quiero agradecer a mis "*babys*

científicos" Snetzana, Paz y Toni por todo vuestro cariño. A todos vosotros gracias por vuestro tiempo y amistad.

Como no dar las gracias a mis amigos de toda la vida, Katia, Yerai, Jessica y Amanda. Puedo decir que sois unos grandes amigos, gracias por entender todas mis ausencias durante estos años y darme esos abrazos milagrosos que me recomponían cuando más lo necesitaba. Con vosotros la risoterapia funciona a la perfección, gracias por estar siempre presentes, tanto en las buenas como en las malas en todas las etapas de mi vida.

No podía faltar las gracias a mi Rosi, Alberto y Albertito. Como ya os he dicho muchísimas veces y os lo seguiré diciendo, ¡qué haría yo sin vosotros!. Gracias por estar disponibles las 24 horas los 365 días del año, para mí sois mi segunda familia. Especialmente a ti Rosi, gracias por ser mi confidente y estar a mi lado en todo momento.

Por otro lado, quiero dar las gracias a mi Lucía. Ens vam conéixer en la carrera de Bioquímica i fins ara no t'has separat mai de mi, sent el meu suport moral en tot moment. Les nostres converses telefòniques per a solucionar problemes científics i no tan científics han significat molt per a mi.

Ara arriba el vostre moment, el moment d'agrair a les meues "Biosalpoder" María, Sandra, Cristina i Gemma absolutament tota la vostra amistat. Ens coneixem des de primer de carrera i fins ara heu sigut, sou i sereu un pilar fonamental en la meua vida. Gràcies per estar sempre ahí.

Papá, mamá, no hay ninguna duda que gracias a vuestro esfuerzo durante muchos años ha hecho que llegue donde he llegado y a ser quien soy. No existen palabras en el mundo para agradeceros todo vuestro amor y apoyo incondicional. Sabéis que no solo sois mis padres, también os habéis convertido en mis mejores amigos. Desde que empecé a estudiar en Valencia, siempre he necesitado vuestra

llamada telefónica diaria y veros semanalmente porque me dais la energía que necesito para afrontar la semana. Durante toda mi vida y especialmente desde que empecé el doctorado me habéis dados sabios consejos que nunca olvidaré. En las buenas y en las malas somos un equipo y ahora más que nunca. Esta tesis también es vuestra. Gracias por TODO, os quiero.

Para finalizar tengo que agradecer a una persona muy especial para mí, Lolo, el haber llegado a mi vida durante esta etapa y formar parte de ella. Situaciones de la vida nos pusieron en contacto y a día de hoy eres una de las mejores cosas que me han pasado. Gracias por quererme tal y como soy, por entenderme, estar siempre a mi lado y cuidarme, esta tesis no hubiera sido lo mismo sin ti. Darte las gracias por acompañarme y vivir juntos esta aventura, espero que vivamos muchas más.

Abbreviations

Abbreviations

%	Percentage
ºC	Degrees Celsius
µg	Microgram
µl	Microliter
µm	Micrometer
3βHSD1/2	3-Beta-Hydroxysteroid Dehydrogenase Type-1/2
AA	Abiraterone Acetate
AABA	α-aminobutyric acid
Abi	Abiraterone
ADA	Adenosine Deaminase
ADT	Androgen-Deprivation Therapy
AF	Area Fraction
Akt	Protein Kinase B
APS	Ammonium Persulfate
AQC	6-Aminoquinolyl-N-Hydroxysuccinimidyl Carbamate
AR	Androgen Receptor
ARE	Androgen Response Element
AR-V	Androgen Receptor Splice Variant
AUC	Area Under Curve
B-ALP	Serum Bone Alkaline Phosphatase
bFGF	basic Fibroblast Growth Factor
B_{max}	Maximum Binding
BSA	Bovine Serum Albumin
CD	Circular Dichroism
CDDP	Cis-dichlorodiamminiplatinum
CDR	Complementary Determining Region
CI	Combination Index

cm	Centimeter
CRPC	Castration-Resistant Prostate Cancer
CTC	Circulating Tumor Cell
Cy3	Cyanine 3
Cy5	Cyanine 5
Cy5.5	Cyanine 5.5
CYP17A1	Cytochrome P450 Family 17 Subfamily A Member 1
D_2O	Deuterium Oxide
DAPI	4´,6-diamidin-2-phenylindole
DBD	DNA-Binding Domain
DDS	Drug Delivery System
DHEA	Dehydroepiandrosterone 3-Acetate
DHEA-S	Dehydroepiandrosterone sulfate
DHT	Dihydrotestosterone
DIEA	N,N-Diisopropylethylamine
DLS	Dynamic Light Scattering
DMF	N,N-Dimethylformamide
DMSO	Dimethyl Sulfoxide
DMTMM.BF4	4-(4,6-dimethoxy-1,3,5-triazin-2-yl)-4-methylmorpholinium tetrafluoroborate
DTT	Dithiothreitol
DTX	Docetaxel
EB	Evans Blue
ECM	Extracellular Matrix
EDTA	Ethylenediaminetetraacetic Acid
EGF	Epidermal Growth Factor
EGFR	Epidermal Growth Factor Receptor
ELK-1	ETS like-1
EPHB2	Ephrin type-B Receptor 2

EPR	Enhanced Permeability and Retention
Equiv.	Equivalents
ER	Estrogen Receptor
ERG	ETS-Related Gene
ETS	Erythroblast Transformation-Specific
EZH2	Enhancer of Zeste Homolog 2
Fa	Fraction Affected
Fab	Antibody Antigen-binding Fragment
FACS	Fluorescence Activate Cell Sorting
FBS	Fetal Bovine Serum
Fc	Antibody Fragment Crystallizable Region
FDA	Food and Drug Administration
FGFR	Fibroblast Growth Receptor Factor
FI	Fluorescence Intensity
FITC	Fluorescein isothiocyanate
FKBP5	FK506 Binding Protein 5
FPLC	Fast Protein Liquid Chromatography
FR	Folate Receptor
Fv	Antibody Variable Fragment
GAU	Glutamic Acid Units
G-CSF	Granulocyte Colony-Stimulating Factor
GPCR	G-Protein-Coupled Receptor
GR	Glucocorticoid Receptor
h	Hours
HA	Hyaluronic Acid
HER2/3	Human Epidermal Growth Factor Receptor 2/3
HGF	Human Growth Hormone
HGFR	Hepatocyte Growth Receptor Factor
HPLC	High-Performance Liquid Chromatography

HPMA	N-(2-Hydroxypropyl)methacrylamide
HPN	Serine Peptidase Hepsin
HSP	Heat Shock Protein
i.v.	Intravenous
IC50	Half Maximal Inhibitory Concentration
IF	Immunofluorescence
IFP	Interstitial Fluid Pressure
IGF	Insulin Growth Factor
IGF-1	Ligand Insulin-like Growth Factor-1
IGF-1R	Insulin-like Growth Factor 1 Receptor
IGFBP	Insulin-like Growth factor Binding Protein
IH	Immunohistochemistry
IL-6R	Interleukin 6 Receptor
IL-8	Interleukin 8
INSR	Insulin Receptor
IRS1	Insulin Receptor Substrate 1
K	Kelvin
K_d	Dissociation Constant
KDa	Kilodalton
Kg	Kilogram
KLK3	kallikrein 3
L	Liter
LBD	Ligand-Binding Domain
LHRH	Hormone-Releasing Hormone
lncRNA	long non-coding RNA
Luc	Luciferase
M	Molar
mA	Milliampere
mAb	monoclonal Antibody

MAPK	Mitogen-Activated Protein Kinase
mAU	Milli-Absorbance Unit
mCRPC	Metastatic Castration-Resistant Prostate Cancer
mg	Milligrams
mHNPC	Metastatic Hormone-Sensitive Prostate Cancer
MHz	Megahertz
mins	Minutes
ml	Milliliter
mM	Millimolar
mmol	Millimole
MMP-9	Metallopeptidase 9
MPS	Mononuclear Phagocyte System
MRW	Mean residue weight
mTOR	Mechanistic Target of Rapamycin
mTORC1/2	Mechanistic Target of Rapamycin Complex 1/2
MTS	3-(4,5-dimethylthiazol-2-yl)-5-(3-carboxymethoxyphenyl)-2-(4-sulfophenyl)-2H-tetrazolium
mV	Millivolt
Mw	Molecular Weight
NA	Numerical Aperture
NCE	New Chemical Entity
NDGA	Nordihydroguaiaretic Acid
NFKB	Nuclear Factor κB
NHS	N-Hydroxysuccinimide
nm	Nanometer
nM	Nanomolar
NMR	Nuclear Magnetic Resonance
NP	Nanoparticle
NSCLC	Non-Small-Cell Lung Cancer

NT	Non-transfected
NTD	Amino-Terminal Domain
OD	Optical Density
P/S	Penicillin/Streptomycin
P1NP	Procollagen Type 1 N-Terminal Propeptide
PAA	Polyamino Acid
PAP	Prostatic Acid Phosphatase
PARP	Poly ADP-Ribose Polymerase
PBS	Phosphate Buffered Saline
PCa	Prostate Cancer
PCA3	Prostate Cancer Antigen 3
PDC	Polymer-Drug Conjugate
PDI	Polydispersity Index
PDEPT	Polymer-Directed Enzyme Prodrug Therapy
PDGFRβ	Platelet Derived Growth Factor Receptor Beta
PECAM-1	Platelet Endothelial Cell Adhesion Molecule-1
PEG	Polyethylene Glycol
PELT	Polymer-Enzyme Liposome Therapy
PFA	Paraformaldehyde
pfu	Particles Forming Unit
PGA	Poly-L-Glutamic Acid
PGR	Progesterone Receptor
PHLPP	PH domain and Leucine-rich repeat Protein Phosphatase
PI3K	Phosphoinositide 3-Kinase
PIN	Prostate Intraepithelial Neoplasia
PIP3	Phosphatidylinositol-3,4,5-triphosphate
PK	Pharmacokinetics
PMS	Phenazine Methosulfate
PPC	Polymer-Protein Conjugate

ppm	Part Per Million
PSA	Prostate-Specific Antigen
PSMA	Prostate-Specific Membrane Antigen
PT	Polymer Therapeutics
PTEN	Phosphatase and Tensin Homolog
PVDF	Polyvinylidene Difluoride
Ra-223	Radium-223
RanBP2	Ran Binding Protein 2
RBCs	Red Blood Cells
rcf	Relative Centrifugal Force
RES	Reticuloendothelial System
RIPA	Radio-Immunoprecipitation Assay (Buffer)
RLU	Relative Luminescence Units
rpm	Revolutions Per Minute
RT	Room Temperature
s	Second
s.c.	Subcutaneous
SATP	N-Succinimidyl-S-acetylthiopropionate
SCHLAP1	Second Chromosome Locus Associated with Prostate 1
SCID	Severe Combined Immunodeficiency
SCR	Scrambled Control siRNA
SDS	Sodium Dodecyl Sulfate
SEC	Size Exclusion Chromatography
SEM	Standard Error of the Mean
Shc	SHC-transforming protein 1
siRNA	Small interfering RNA
SMA	Smooth Muscle Actin
SPOP	Speckle-type Poz Protein
STAT3	Signal Transducer and Activator of Transcription 3

STORM	Stochastic Optical Reconstruction Microscopy
T2E	TMPRSS2: ERG Fusion Gene
TEMED	N,N,N',N'-Tetramethylethylenediamine
tGFP	Turbo Green Fluorescent Protein
TGN	Trans-Golgi Network
TIRF	Total Internal Reflection Fluorescence
TKI	Tyrosine Kinase Inhibitor
TKR	Tyrosine Kinase Receptor
T_m	Melting Temperature
TMB	3,3´,5,5´-Tetramethylbenzine
TME	Tumor Microenvironment
TMPRSS2	Transmembrane Serine Protease 2
UV	Ultraviolet
V	Voltage
v/v	Volume/Volume
VEGF	Vascular Endothelial Growth Factor
VEGFR2	Vascular Endothelial Growth Factor Receptor 2
w/v	Weight/Volume
w/w	Weight/Weight
WB	Western Blot

Abstract

Abstract

Prostate Cancer (PCa) is currently the most prevalent non-cutaneous malignancy and the second most prevalent cancer in men. Advances in early diagnosis, identification of biomarkers for specific subtypes, and the application of effective treatments represent critical parameters in the clinical management of PCa patients. Effective treatment options for cancer in general now include combination-based therapies, given the general complexity of cancers and the rise of resistance to some single-drug approaches. Furthermore, the modification of existing drugs, including polymer conjugation, can allow for greater stability in plasma, enhanced tumor targeting, altered cell trafficking, and improved pharmacokinetics to foster improvements in patient outcomes.

Studies have established the TMPRSS2 (androgen-dependent serine protease) and ERG (ETS family transcription factor) fusion gene (T2E) as a potential biomarker of metastatic castration-resistant PCa, with overexpression observed in 50-70% of PCa cases. In these cases, the androgen receptor (AR) and insulin-like growth factor 1 receptor (IGF-1R) reciprocal signaling pathways potently drive tumor progression; therefore, the dual inhibition of these pathways may represent a promising means to inhibit PCa progression.

The inhibition of IGF-1R signaling with an anti-IGF-1R-specific monoclonal antibody (mAb - AVE1642) has shown potential in the treatment of T2E-positive PCa patients; however, patients treated with anti-IGF-1R inhibitors in several clinical trials only experienced a partial response to therapy and suffered from significant side toxicities. The application of nanomedicine to PCa has the potential to overcome many of the limitations of current therapies in both localized and metastatic disease, and we hypothesized that the polymer-modification of AVE1642 might improve therapeutic outcomes in the T2E-positive PCa subtype.

To this end, we conjugated AVE1642 with a biodegradable and biocompatible polypeptide (poly-L-glutamic acid (PGA)) to create PGA-AVE1642, which we then evaluated as an optimized treatment approach. While we aimed to generate an advanced therapeutic approach, we also sought to fully understand the effect of PGA conjugation to a mAb regarding pharmacological activity *in vitro* and *in vivo*.

Our initial *in vitro* analyses showed similar cell viability in the T2E-positive VCaP PCa cell line treated with both AVE1642 and PGA-AVE1642, confirming that PGA-conjugation does not impede AVE1642 function. PGA-AVE1642 maintained a general specificity for T2E-positive cells, but instead of binding to IGF-1R and becoming internalized rapidly as occurs for unmodified AVE1642, PGA-AVE1642 displayed enhanced stability in plasma and stronger binding to IGF-1R, which maintained PGA-AVE1642 at the cell membrane and prevented IGF-1R internalization.

We also discovered that PGA-conjugation of AVE1642 altered cellular trafficking; while confocal/STORM microscopy in VCaP cells established that AVE1642 mainly colocalized with endosomes and clathrin, PGA-AVE1642 mostly colocalized with caveolin-1 but not with endosomes, demonstrating PGA-conjugation modifies IGF-1R mediated endocytosis probably due to a modified interaction with the receptor. Furthermore, altered trafficking coincided with a differential signaling pathway inhibition pattern upon PGA conjugation. While unmodified AVE1642 inhibited the PI3K pathway downstream of IGF-1R inhibition, PGA-AVE1642 inhibited both the PI3K and MAPK pathways, thereby displaying increased anti-tumorigenic potential.

Subsequent *in vivo* analyses in a newly developed orthotopic PCa mouse model employing luciferase-expressing VCaP cells revealed higher anti-tumoral activity for PGA-AVE1642 compared with AVE1642 using an equivalent dose. Again,

we found that PGA-AVE1642 treatment inhibited both the PI3K and MAPK pathways; however, subsequent tumor microenvironmental studies revealed that PGA-AVE1642 treatment also potently inhibited tumor blood vessel functionality and maturity, cell proliferation, and angiogenesis when compared to treatment with unmodified AVE1642.

Overall, polymer conjugation improves AVE1642 antitumoral activity both *in vitro* and *in vivo* by stronger IGF-1R inhibition, which avoids the activation of MAPK and PI3K downstream signaling pathways preventing cancer cell progression. Furthermore, our results suggest that polymer conjugation of AVE1642 promotes alterations to the tumor microenvironment in PCa tumor models, thereby enhancing therapeutic efficacy.

As a means to further improve PCa treatment with PGA-AVE1642, we looked to evaluate a combination therapy-based approach through the additional inhibition of the AR signaling pathway via treatment with the anti-androgen drug abiraterone. Polymer-based combination therapies employing synergistic drugs aimed at different pharmacological targets represent an exciting means to target tumor cells effectively. As a first step towards the generation of a PGA-antibody conjugate, we evaluated the combination of AVE1642 or PGA-AVE1642 with free abiraterone *in vitro* and *in vivo*.

Our *in vitro* analyses provided evidence for a synergistic effect for both combination therapies in T2E-positive PCa cells; however, we only found synergy with regards to primary tumor growth for free AVE1642 in combination with abiraterone, and not for PGA-AVE1642. This is most probably due to the differential molecular mechanism achieved upon conjugation that it is already providing the role that abiraterone plays in T2E-positive PCa tumors. Both combination therapies (AVE1642 or PGA-AVE1642 with abiraterone) provided for dual PI3K and MAPK pathway inhibition *in vivo*. Exploration on the effect on tumor microenvironment is

still ongoing as even if not synergistic, significant differences have been encountered when abiraterone is present not only for free but also for conjugated AVE1642.

Overall, our studies have demonstrated that polymer-conjugation of a monoclonal antibody alters the function and improves anti-tumorigenic capacity. Furthermore, we have also provided evidence for the anti-tumor efficacy of a new combination therapy for advanced PCa based on the inhibition of both IGF-1R and AR pathways.

Resumen

Resumen

El cáncer de próstata (CaP) es actualmente el tumor maligno no cutáneo más común y el segundo cáncer más frecuente en los hombres. Los avances en el diagnóstico precoz, la identificación de biomarcadores para subtipos específicos y la aplicación de tratamientos efectivos representan parámetros fundamentales en el manejo clínico de los pacientes con CaP. Las opciones para tratamientos eficaces contra el cáncer ahora incluyen terapias de combinación dada la complejidad general de los cánceres y la mayor resistencia a los métodos de un solo fármaco. Además, la modificación de los fármacos existentes, como la conjugación de polímeros, puede permitir una mayor estabilidad en plasma, una mejor selectividad tumoral, la alteración del tráfico celular y una mejora en la farmacocinética para favorecer los resultados del paciente.

Los estudios han establecido el gen de fusión (T2E) compuesto por TMPRSS2 (serina proteasa dependiente de andrógenos) y ERG (factor de transcripción de la familia ETS) como un biomarcador potencial de CaP metastásico resistente a la castración, con una sobreexpresión observada en un 50-70% de los casos de CaP. En estos casos, las vías de señalización recíproca entre el receptor de andrógenos (AR) y el receptor del factor de crecimiento de insulina 1 (IGF-1R) potencialmente impulsan la progresión del tumor; por lo tanto, la doble inhibición de estas vías puede representar un método prometedor para inhibir la progresión del CaP.

La inhibición de la señalización de IGF-1R con un anticuerpo monoclonal específico anti-IGF-1R (mAb – AVE1642) ha demostrado un gran potencial en el tratamiento de los pacientes con CaP T2E positivos, aunque pacientes tratados con inhibidores anti-IGF-1R en varios ensayos clínicos solo experimentaron una respuesta parcial al tratamiento y sufrieron toxicidades importantes. La aplicación de la nanomedicina en el CaP tiene un excelente potencial como un enfoque

novedoso para combatir las limitaciones de las terapias actuales tanto en afecciones localizadas como metastásicas, y planteamos la hipótesis de que la modificación del AVE1642 con el polímero podría mejorar los resultados terapéuticos en el subtipo de pacientes de CaP T2E positivos.

Para ello, conjugamos AVE1642 con un polipéptido biodegradable y biocompatible (ácido poli-L-glutámico (PGA)) para crear PGA-AVE1642, que luego evaluamos como un enfoque de tratamiento mejorado. Si bien nuestro objetivo era generar una opción terapéutica avanzada, también tratamos de comprender el efecto de la conjugación del PGA a un mAb con respecto a la actividad farmacológica *in vitro* e *in vivo*.

Nuestros análisis *in vitro* iniciales mostraron una viabilidad celular similar en la línea celular VCaP T2E positiva tratada con AVE1642 y PGA-AVE1642, confirmando que la conjugación del PGA no interfiere con la función del AVE1642. PGA-AVE1642 mantuvo una especificidad general para las células T2E positivas, pero en lugar de unirse al IGF-1R e internalizarse rápidamente como ocurre con el AVE1642 no modificado, el PGA-AVE1642 mostró una mayor estabilidad plasmática y una unión más fuerte con IGF-1R, que mantuvo al PGA-AVE1642 en la membrana celular y evitó la internalización de IGF-1R.

También descubrimos que la conjugación del PGA al AVE1642 alteró el tráfico celular; mientras que la microscopía confocal/STORM en la línea celular VCaP determinó que el AVE1642 colocalizaba principalmente con endosomas y clatrina, el PGA-AVE1642 colocalizaba en su mayoría con caveolina-1 pero no con endosomas, demostrando que la conjugación del PGA modifica la endocitosis mediada por IGF-1R, probablemente debido a una interacción diferente con el receptor. Además, la alteración del tráfico celular coincidió con un patrón de inhibición diferencial en las vías de señalización cuando se conjuga el PGA. Mientras que el AVE1642 no modificado inhibió la vía PI3K aguas abajo del IGF-1R, el

PGA-AVE1642 inhibió tanto la vía PI3K como la vía MAPK, mostrando así un mayor efecto antitumoral.

Los análisis posteriores *in vivo* en un modelo ortotópico de ratón de CaP recientemente desarrollado utilizando la línea celular VCaP con expresión de luciferasa revelaron una mayor actividad antitumoral para el PGA-AVE1642 en comparación con AVE1642 utilizando una dosis equivalente. Una vez más, encontramos que el tratamiento con PGA-AVE1642 inhibió las dos vías de señalización PI3K y MAPK; sin embargo, estudios posteriores basados en el microambiente tumoral mostraron que el tratamiento con PGA-AVE1642 también presentaba una alta inhibición de la funcionalidad y madurez de los vasos sanguíneos tumorales, de la proliferación celular y de la angiogénesis en comparación con el tratamiento con el AVE1642 no modificado.

En general, la conjugación del polímero mejora la actividad antitumoral de AVE1642 tanto *in vitro* como *in vivo* al aumentar la inhibición de IGF-1R, que impide la activación de las vías de señalización de PI3K y MAPK aguas abajo evitando la progresión de las células cancerosas. Además, nuestros resultados sugieren que la conjugación del polímero con el AVE1642 induce alteraciones en el microambiente tumoral en modelos tumorales de CaP, mejorando así la eficacia terapéutica.

Para mejorar aún más el tratamiento de CaP usando PGA-AVE1642, buscamos evaluar un enfoque basado en la terapia de combinación a través de una mayor inhibición de la vía de señalización de AR utilizando abiraterona, un fármaco antiandrogénico. Las terapias de combinación basadas en polímeros empleando fármacos sinérgicos dirigidos a diferentes dianas farmacológicas proporcionan una mayor eficacia para atacar las células tumorales. Como primer paso hacia la generación de un anticuerpo conjugado con PGA, se evaluó la combinación de AVE1642 y PGA-AVE1642 con abiraterona libre *in vitro* e *in vivo*.

Nuestros análisis *in vitro* proporcionaron evidencia de un efecto sinérgico para ambas terapias de combinación en las células de CaP T2E positivas; sin embargo, con respecto al crecimiento del tumor primario solo encontramos sinergia para el AVE1642 en combinación con abiraterona *in vivo,* pero no para el PGA-AVE1642. Esto se debe muy probablemente al mecanismo molecular diferencial logrado en la conjugación que ya está proporcionando el papel que desempeña la abiraterona en los tumores de CaP positivos para T2E. Ambas terapias de combinación (AVE1642 o PGA-AVE1642 con abiraterona) proporcionaron una doble inhibición de las vías de señalización PI3K y MAPK *in vivo*. La exploración sobre el efecto en el microambiente tumoral está aún en curso, ya que, aunque no sean sinérgicas, se han encontrado diferencias significativas cuando la abiraterona está presente no sólo de forma libre sino también en combinación con el conjugado AVE1642.

En general, nuestros estudios han demostrado que la conjugación del polímero a un anticuerpo monoclonal altera su funcionalidad y mejora su capacidad antitumoral. Además, también proporcionamos evidencia de la eficacia antitumoral de una nueva terapia de combinación potencialmente interesante para el CaP avanzado basada en la inhibición de las vías de señalización IGF-1R y AR.

Objectives

Objectives

The long-term objective of this Ph.D. thesis is the development of advanced therapeutics for the treatment of advanced-stage prostate cancer (PCa) in a personalized manner, which currently represents an unmet clinical need. In particular, we focused on the design and development of a biocompatible and biodegradable polypeptide-based-antibody conjugate (PGA-AVE1642) to block IGF-1R to improve therapeutic outcomes in the T2E-positive PCa subtype. Furthermore, based on the reciprocal negative feedback between androgen receptor (AR) and PI3K/Akt signaling pathways, we also aimed to study a combination therapy comprising the combination of AVE1642 or PGA-AVE1642 with abiraterone to promote a stronger inhibition of both pathways - a strategy that could represent a promising means to treat advanced PCa.

These main objectives will be achieved through the following specific objectives:

1. The development, synthesis, and chemical characterization of a new polymer-based conjugate using a biodegradable and multivalent polymeric carrier (poly-L-glutamic acid or PGA) conjugated to a human monoclonal antibody anti-IGF-1R (AVE1642) for the treatment of metastatic castration-resistant prostate cancer (mCRPC). The full characterization of PGA-AVE1642 will employ a range of techniques (e.g., SEC, DLS, and FUV-CD) to determine parameters such as size, charge, and structure.

2. The study of the influence of PGA conjugation on AVE1642 stability by assessing affinity for IGF-1R and overall safety through hemocompatibility assays.

3. The determination of AVE1642/PGA-AVE1642 cytotoxicity and any dependence of cytotoxic activity on the ERG overexpression associated with the presence of the T2E fusion gene in various PCa cell lines and normal prostate cells.

4. The study of how PGA conjugation influences cellular trafficking and the cellular fate of AVE1642 *in vitro* by confocal/STORM microscopy in the VCaP cell line by labeling of AVE1642 and PGA-AVE1642 with different fluorophores.

5. The investigation of the molecular response of AVE1642 and PGA-AVE1642 *in vitro* in the VCaP cell line by protein analysis.

6. The design and optimization of a suitable *in vivo* orthotopic mouse model of advanced PCa using the VCaP cell line transfected with luciferase, which will be used to prove the anti-tumoral activity of AVE1642 and PGA-AVE1642, via monitor tumor progression by optical imaging (IVIS Spectrum®). Tumors will also be assessed at the protein level to explore the potential different molecular responses to AVE1642 and PGA-AVE1642 treatments.

7. The evaluation of tumor microenvironment alterations, such as blood vessel functionality and maturity, tumor proliferation, and angiogenesis, following AVE1642 and PGA-AVE1642 treatment by immunohistochemistry.

8. The study of the synergy between AVE1642/PGA-AVE1642 with abiraterone *in vitro* and *in vivo*, while evaluating the dependence of both combination therapies on the presence of the T2E fusion gene.

Chapter I

General Introduction

I.1. Prostate Cancer

I.1.1. Prostate Cancer Prevalence

Cancer relates to a set of related diseases in which cells proliferate without control and suffer from cell cycle deregulation. Given the involvement of distinct tumor-specific oncogenes, each cancer type may require a distinct treatment approach.

Cancer incidence has recently increased drastically due to several factors, including increased life expectancy, improvements in diagnosis, and increased exposure to several risk factors. According to the estimate of cancer incidence and mortality produced by the International Agency for Research on Cancer using the GLOBOCAN 2018 platform (male and female sexes combined), lung cancer represents the most commonly diagnosed cancer and the leading cause of death. This is followed by breast, colorectal, and prostate cancer (PCa) with regards to incidence, and colorectal, stomach, and liver cancer regarding the leading cause of death [1].

PCa is the second most frequent cancer in men and the fifth cause of cancer deaths around the world [2, 3] (**Figures 1.A** and **B**) and the most commonly diagnosed cancer in Europe (**Figures 1.C** and **D**). 2018 alone saw 1.3 million new cases of PCa [3], mostly in men over the age of 65, with a higher prevalence among white men and men of African origin [4]. Fortunately, an early diagnosis can provide a better prognosis; however, the metastatic form of PCa, mainly affecting the lymph nodes and bones, remains challenging to treat and presents with high levels of mortality [5].

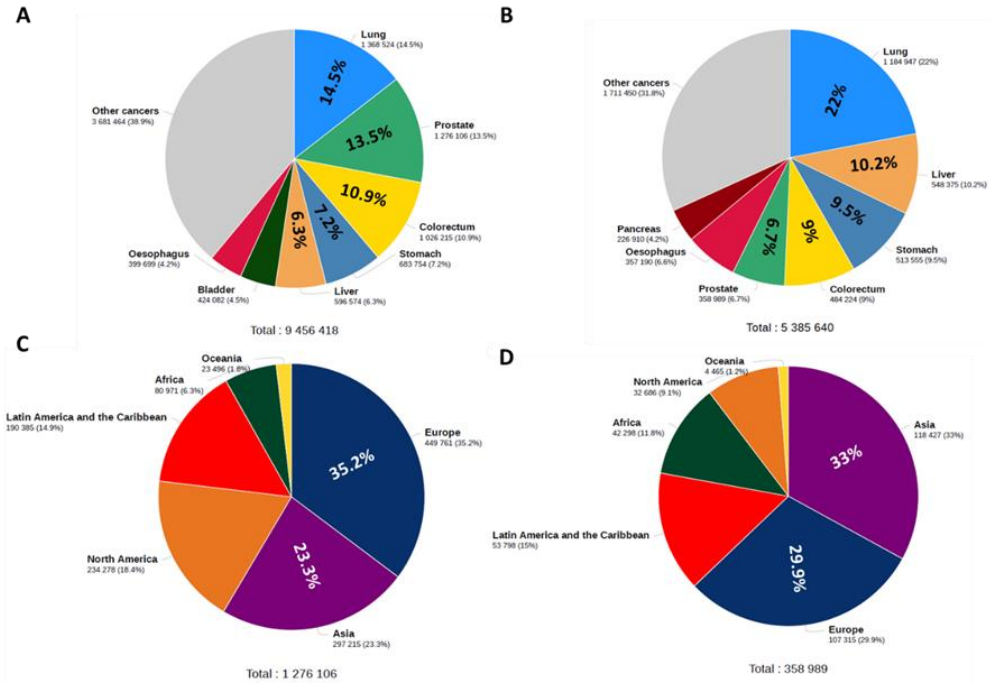

Figure 1: Estimated Prostate Cancer Incidence and Mortality Worldwide (2018). A) Estimated number of new cases of different cancers in males. **B)** Estimated number of deaths in different cancers in males. **C)** Estimated number of new cases of PCa. **D)** Estimated number of deaths from PCa. *Adapted from* GLOBOCAN 2018.

I.1.2. Stages and Cellular Classification in Prostate Cancer Progression

Normal prostate cells are composed of two generic cell types - stromal and epithelial cells. Stromal cells include fibroblasts and smooth muscle cells, while epithelial cells comprise luminal, basal, and neuroendocrine cells [6]. PCa originates from epithelial cells located in the peripheral area of the prostate gland, which subsequently spread to the prostate capsule and seminal vesicles before eventually metastasizing to the bones and lymph nodes [7].

The known stages of PCa progression include prostate intraepithelial neoplasia (PIN), followed by invasive adenocarcinoma, and metastases with distinct

biological processes and molecular changes characterizing each phase. PIN, a precursor to carcinoma, is characterized by telomere shortening, as well as the loss of Homeobox protein NKX3-1 expression, the presence of a Transmembrane Serine Protease 2: ETS-related gene (TMPRSS2:ERG) fusion gene, mutations to the Speckle-type Poz Protein (SPOP) gene, and deregulation of the erythroblast transformation-specific (ETS) family of transcription factors. Additionally, PIN differs from invasive adenocarcinoma by a lack of stromal invasion and the possession of an intact basal membrane [8-11]. Invasive adenocarcinoma occurs due to luminal cell hyperproliferation, the loss of the basal epithelium and breakdown of the basal membrane, and immune cell infiltration. During this stage, the telomerase holoenzyme becomes active, while the cell loses phosphatase and tensin homolog (PTEN) and retinoblastoma protein (pRb) function [8-11]. Finally, the transition to metastasis involves the loss of epithelial-mesenchymal transition (EMT) and the passage of cells into the vascular or lymphatic system that allows for tumorigenic seeding in the bones as primary metastases or lung, liver, or pleura as secondary metastases [8-11]. At the genetic levels, metastatic PCa cells present with the amplification of the proto-oncogene c-Myc, the serine peptidase Hepsin (HPN), the proto-oncogene serine/threonine Kinase Pim1, and the epigenetic modifying enzyme Enhancer of Zeste Homolog 2 (EZH2) and the loss of microRNA-101 and Ephrin type-B receptor 2 (EPHB2) expression (**Figure 2**) [8-11].

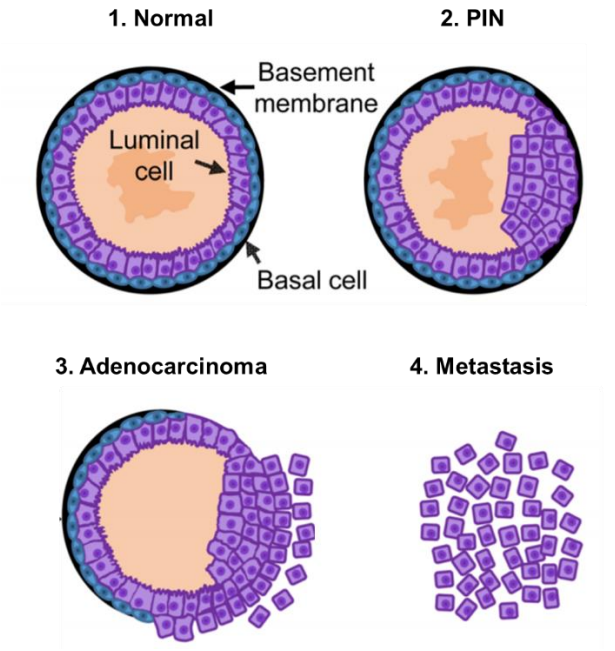

Figure 2: Prostate Cancer Progression. PCa progression arises from luminal cells located in a normal human prostatic duct (1) to PIN (precursor lesions) (2), invasive adenocarcinoma (3), and finally metastasis to bone or lymph nodes (4). *Adapted from* [8-11].

Another means to evaluate PCa progression employs the Gleason score - a histological assessment of the appearance and distribution of tumor glands. Glands are classified into five distinct categories ranging from well-differentiated glands with non-invasive cells to aggressive neoplasms with no glandular differentiation. Prostate tumors usually present with an appearance and distribution indicative of different stages; for this reason, the total score is calculated based on the assignation of two categories to each patient being the first number assigned, the most common grade in the tumor (Gleason score 1-5), and the second number assigned, the following highest grade (Gleason score 1-5). These two numbers are then combined to produce a total score for the cancer, which currently is classified in five different grades; grade 1 (Gleason score 3+3=6), grade 2 (Gleason score 3+4=7), grade 3 (Gleason score 4+3=7), grade 4 (Gleason score 4+4=8) and grade 5

(Gleason score 9-10)). Patients with Gleason scores of 2-4 have a good prognosis as this represents the initial stages of PCa, while a score of 6 marks less aggressive tumors, and a score of 7 marks intermediate tumors. Gleason scores of 8-10 indicate the presence of aggressive tumors, and patients in this bracket suffer from the worst prognosis (**Figure 3**) [12].

As mentioned with regards to Gleason scores, heterogeneity characterizes PCa at the level of individual tumors, and also between patients. Therefore, genetic profiling forms an integral part of treatment.

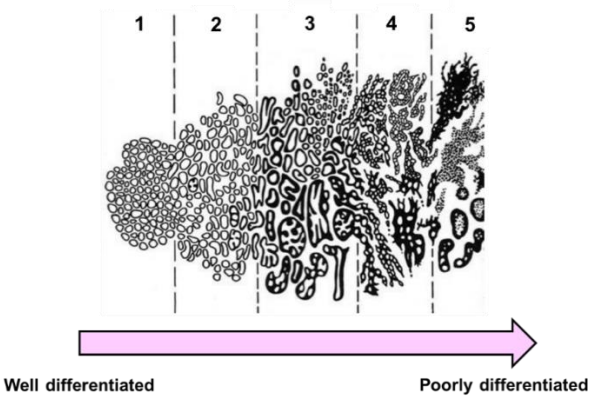

Figure 3: Gleason Score Grading and Prostate Cancer Progression. Glands that are small, close together, uniform, and with minimal signs of cancer are graded with a Gleason score of 1. A score of 2 is related to larger glands, still separated by stroma. Notable changes in glandular size, which are even further apart, correspond with Gleason score 3, while a score of 4 is used when cells have lost their ability to form glands. In Gleason score 5, cells are completely undifferentiated. *Modified from* [13].

I.2. Prostate Cancer Biomarkers and Sub-molecular Classification

Despite recent advances made in the early detection and treatment of localized PCa, the number of deaths caused by this cancer type remains alarmingly high. Two main factors are responsible for this fact; the absence of validated and predictive biomarkers with a clinical utility in early diagnosis and molecular sub-classification of PCa, and the lack of precise and personalized therapies [14].

The rapid evolution of PCa disease and the absence of effective therapies is associated with tumor heterogeneity. Heterogeneity arises from the continual variations in the cancer cell genome, leading to the appearance of new tumor clones and sub-clones under pressures of external factors [15]. For these reasons, the prevalent and heterogeneous nature of PCa requires more precise diagnostics, the characterization of malignant potential, and treatment monitoring. The identification of PCa at the earliest stage and the optimal choice of a treatment modality will provide the best therapeutic outcomes.

The blood-based biomarker prostate-specific antigen (PSA) detection, a glycoprotein enzyme produced exclusively by the prostate gland and encoded by the kallikrein 3 gene (KLK3), digital rectal examination, and prostate tissue biopsy represent the current clinical tools generally employed to diagnose PCa [16].

While PSA-based tests, which first met US FDA approval in 1986, revolutionized PCa management and reduced mortality due to early disease detection [16], PSA represents a prostate biomarker rather than a PCa biomarker. The normal prostate expresses low levels of PSA; however, PSA levels rise due to the architectural disruption caused by PCa, but also by benign prostate diseases such as prostatitis or benign prostatic hyperplasia [17, 18]. Moreover, two randomized trials of PSA-based screening for PCa (the European Randomized Study

for Prostate Cancer [ERSPC] and the Prostate, Lung, Colorectal and Ovarian Cancer Screening Trial [PLCO]) recommended against PSA-based screening for PCa due to its propensity to provide false-positives and false-negatives [19]. Therefore, PSA-based diagnoses do not permit the accurate formulation of treatment strategies, a situation that can lead to both under- and over-treatment of patients. Overall, the choice of treatment cannot be made using PSA levels alone, highlighting the need for the identification of additional biomarkers.

In recent years, common genetic alterations have been detected in PCa samples, such as mutations in AR, alterations in the genes responsible for repairing damaged DNA, and fusion genes involving the ETS family transcription factors. In addition, constantly evolving technologies have advanced the detection of biomarkers from blood and urine samples of PCa patients, which have led to the development of new treatment approaches [20].

An ideal PCa biomarker should integrate information regarding molecular subtyping, the biology of disease, and prognosis to guide treatment approaches in a quick, easy, and economical manner. Herein, we provide a summary of recently identified biomarkers for PCa.

Integrating genomic, transcriptomic, epigenetic, and metabolomic data has led to the description of a rising number of next-generation PCa biomarkers, supposing a significant leap forward in PCa clinical management. Furthermore, these advances have applications in tumor sub-molecular classification, which represents the next crucial step with relevant clinical implications, by increasing the accuracy of clinical decision-making and fostering the development of precision therapies via patient stratification.

Next-generation PCa biomarkers include the Prostate Cancer Antigen 3 (PCA3) [21], SCHLAP1 [22], Androgen Receptor Splice-variant 7 (AR-V7) [23];

mutations and loss of function in PTEN [24]; and chromosomal rearrangement such as TMPRSS2:ERG [25].

PCA3, a highly PCa-specific long non-coding RNA (lncRNA) highly expressed in prostate tumors (>95%) [26], was established as a biomarker for PCa by Bussemarker *et al*. [27]. PCA3 controls the transcriptional regulation of AR target genes, and, therefore, controls PCa cell growth and survival [28, 29]. In 2012, the FDA authorized the use of a commercial kit (PROGENSA™, San Diego, USA) for the detection of PCA3 [30] in urine and prostatic fluid.

The SCHLAP1 lncRNA, highly expressed in aggressive prostate tumors and also associates with prostate tumor recurrence and metastasis, suppresses the function of tumor suppressor genes [22, 31, 32]. SCHLAP1 can be detected in the urine, thereby providing for non-invasive detection.

The AR-V7 possesses a deletion in exon 7, and its detection in circulating tumor cells (CTCs) can be used as a measure of treatment responses in CRPC patients [23, 33].

Specific and recurrent genomic variations also suppose a potential strategy for PCa molecular sub-classification. Mutations and loss of function in the PTEN tumor suppressor gene occur in a high percentage of prostate tumors [34]; this leads to PI3K signaling pathway activation, Akt phosphorylation, and increased tumor cell proliferation and survival. Loss of *PTEN* function occurs in 50% of prostate tumors, with patients suffering from poor prognosis in PCa patients due to increased resistance to anti-androgenic treatment [34, 35]. PI3K/Akt activation demonstrates the importance of this signaling pathway in PCa and is now considered a promising therapeutic target for PCa [36].

Moreover, insertional chromosomal rearrangements and intrachromosomal deletions are common aberrations in PCa that lead to the

formation of fusion genes. The formation of TMPRSS2-ETS fusion genes derive from chromosomal rearrangements common to PCa [37]. While rearrangements have been detected between *TMPRSS2* (21q22) and ETS family members such as *ERG* (21q21), *ETV1* (7p21), *ETV3,* and *ETV4* (17q21) [38], the rearrangement between TMPRSS2 (exon 1) and ERG (exon 4) to form the T2E fusion gene is the most common. TMPRSS2 encodes a serine protease expressed in PCa cells, whereas ERG encodes an oncogenic protein involved in the development of PIN into carcinoma and functions in the regulation of the cell cycle and DNA replication [16]. TMPRSS2 and ERG are located in the same chromosome 21 [39, 40] (**Figure 4**), and T2E formation occurs due to the deletion of those genes lying between them or from a chromosomal translocation. The T2E fusion gene comprises the 5´ regulatory regions of the TMPRSS2 gene, which contains numerous consensus AR binding sites, controlling the expression of the ERG gene [39]. In the presence of the T2E fusion gene, androgens drive the expression of ERG, leading to ERG overexpression in androgen-dependent tumors [41]. T2E expression is observed in approximately 50-70% of PCa patients, defining a particular T2E PCa subtype that is indicative of poor prognosis [42]. Those PCa patients positive for T2E expression can be treated specifically with therapies focused on ERG gene overexpression [43]; however, recent scientific studies have also demonstrated a relationship between T2E presence and high levels of IGF-1R in PCa progression [44].

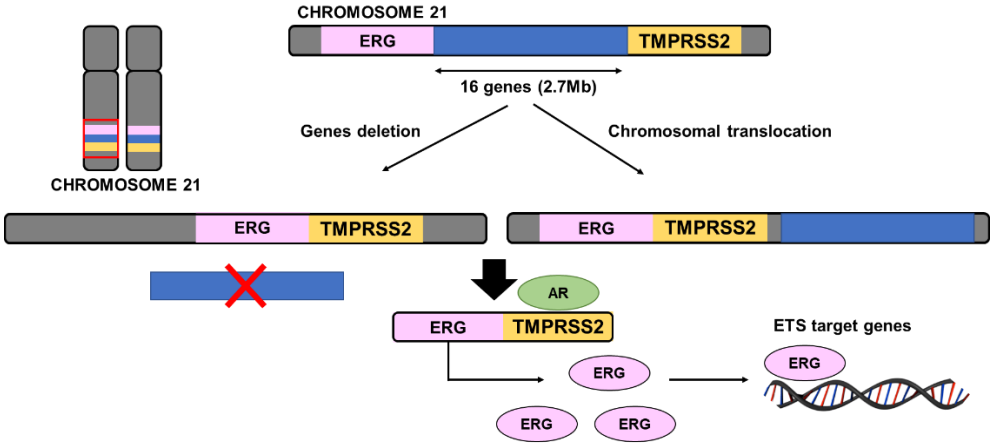

Figure 4: TMPRSS2-ERG Rearrangement and ERG Overexpression. The T2E fusion gene occurs via the deletion of those genes lying between the ERG and TMPRSS2 or by a chromosomal translocation. The androgen-regulated promotor of TMPRSS2 then drives ERG overexpression and the subsequent expression of ETS target genes.

This doctoral thesis focuses on of the generation of personalized nanomedicines for the TMPRSS2-ERG fusion gene expressing PCa subtype.

I.3. Role of Insulin-Like Growth Factor System in Prostate Cancer

Various growth factors, such as insulin growth factor (IGF) and epidermal growth factor (EGF), are important mitogens for PCa. Growth factors bind to the tyrosine kinase receptors (TKRs) located in the cellular membrane to activate downstream signaling pathways, including mitogen-activated protein kinases (Ras/Raf/MAPK) and Phosphoinositide 3-kinase, protein Kinase B, and mechanistic target of rapamycin (PI3K/Akt/mTOR) to promote PCa cell growth and proliferation. IGF-1R plays a vital role in both normal prostate gland growth and cancer development and progression. Studies of IGF signaling in human PCa suggests that IGF-1R overexpression represents a critical trigger of CRPC [45].

The IGF signaling pathway comprises various TKR, such as IGF-1R and INSR (INSR-A and INSR-B), and non-TKR such as IGF-2R. The primary ligands for these receptors include IGF-1, IGF-2, and insulin [46, 47]. Moreover, Insulin-like Growth factor Binding Proteins (IGFBPs) bind to IGFs to aid their transport and protection [48, 49].

IGF-1R, a transmembrane TKR, comprises two extracellular α-chains (130 kDa) and two transmembrane-intracellular β-subunits (95 kDa) formed into a disulfide-linked α_2-β_2 heterodimeric glycoprotein complex. The α-chains form the growth factor binding site while the β-subunits possess intrinsic tyrosine kinase activity. IGF-1R displays a 60% sequence homology to the insulin receptor (INSR) and possesses a higher affinity for IGF-1 and significantly lower affinity for IGF-2 and insulin [46, 48]. IGF-2R is a monomeric transmembrane protein consisting of a large extracellular domain and short cytoplasmic tail. IGF-2R displays multiple similarities to the mannose-6-phosphate-receptor acts in the transport of lysosomal enzymes and possesses high affinity for IGF-2. Additionally, IGF-2R lacks tyrosine kinase activity and does not transduce mitogenic IGF-2 signals [46].

Both IGF-1 and insulin can bind to hybrid receptors (IGF-1R/INSR-A or IGF-1R/INSR-B), but with significantly lower affinity when compared to IGF-1R and INSR homodimers. While, for example, IGF-1 binding to IGF-1R promotes receptor homodimerization, binding of IGF-1 to hybrid receptors promotes heterodimerization [46] (**Figure 5**).

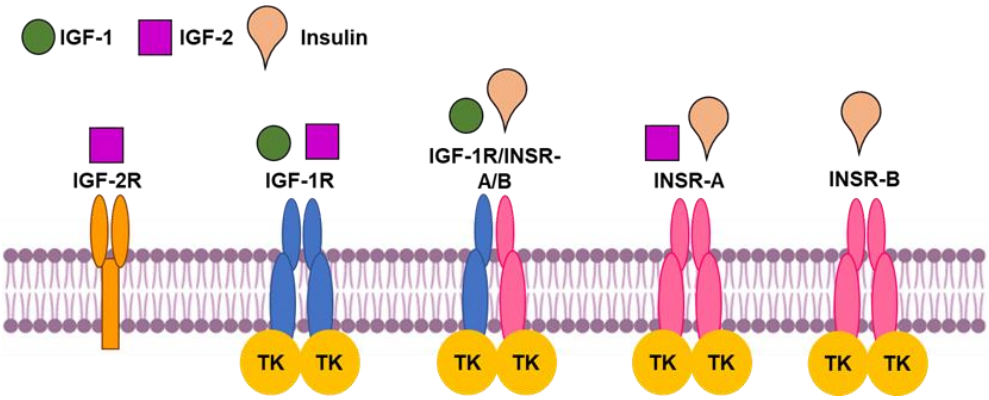

Figure 5: Insulin Growth Factor Family. The IGF system is composed of TKRs such as IGF-1R, INSR-A, INSR-B, and hybrid receptors IGF-1R/INSR-A/B and non-TKRs such as IGF-2R. IGF-1 ligands bind to IGF-1R and hybrid receptors, IGF-2 ligands bind to IGF-2R, IGF-1R, and INSR-A, and insulin ligands bind to hybrid receptors, INSR-A, and INSR-B.

I.3.1. IGF-1R Signaling Pathways and Internalization

IGF-1/IGF-2 binding to IGF-1R prompts autophosphorylation of the tyrosine kinase domain due to conformational changes to the receptor that activates the β subunits kinase domain. Subsequent PI3K/Akt/mTOR and Ras/Raf/MAPK signaling pathway activation occurs through binding to intracellular adaptor proteins, including insulin receptor substrate 1 (IRS1) and Shc [48].

IRS-1 is activated by IGF-1R, and then binds to the p85 subunit of PI3K to promote the synthesis of phosphatidylinositol-3,4,5-triphosphate (PIP3). PIP3 then activates protein kinase B (Akt), which activates mTOR to regulate cell growth, survival, and cell cycle regulation and avoid pro-apoptotic signaling [50]. The phosphatase PTEN regulates this pathway through the dephosphorylation of PIP3; therefore, the loss of PTEN activity increases PIP3 levels and activates mTOR signaling. However, Shc activation promotes the movement of small G protein Ras and protein serine kinase Raf to the inner cell surface through the son-of-sevenless (Sos) protein complex. This activates Ras and Raf, which, in turn, activates the MAPK

signaling pathway, resulting in the transcription of genes related to cell proliferation (such as cyclins type D) in addition to promoting cell differentiation via transduction of mitogenic signals by ETS like-1 (ELK-1) transcription activator [46, 50]. The existence of crosstalk between the PI3K/Akt/mTOR and Ras/Raf/MAPK signaling pathways leads to compensatory activatory/inhibitory mechanisms [51] (**Figure 6**).

Following internalization after ligand binding, IGF-1R becomes directed to the endosomal system where are processed for return to the plasma membrane (recycling), or undergo to the lysosomes, or can translocate to the nucleus after IGF-1R SUMOylation to promote IGF-1R target gene activation [52-54] (**Figure 6**).

Of note, activation of the IRS-1 signaling pathway does not require IGF-1R internalization; however, activation of the Shc signaling pathway does require internalization [55].

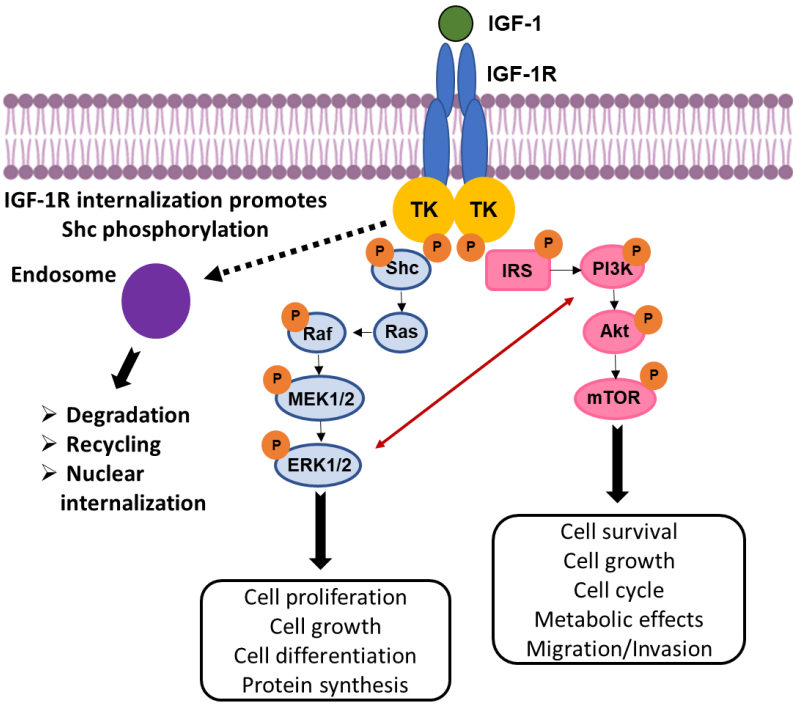

Figure 6: Insulin Growth Factor-1 Receptor Signaling Pathway. IGF-1R activation due to IGF-1 binding promotes the phosphorylation and activation of the PI3K/Akt/mTOR and Ras/Raf/MAPK signaling pathways, which elicit differing biological effects. These signaling pathways regulate each other via compensatory mechanisms (red line). IGF-1R internalization promotes Shc phosphorylation and MAPK pathway activation followed by IGF-1R degradation, recycling to the cellular membrane, or translocation to the nucleus after transport through the endosomal pathway.

IGF-1R internalization is mediated by both clathrin-dependent and caveolin-1-dependent endocytic pathways. Inhibition of both internalization routes in Ewing's sarcoma and HaCaT cells blocks IGF-1R internalization [56, 57]. Interestingly, clathrin-mediated endocytosis regulates both Ras/Raf/MAPK and the PI3K/Akt/mTOR signaling pathways, whereas caveolin-1-mediated endocytosis regulates only the PI3K/Akt/mTOR signaling pathway. In the case of caveolin-1-mediated endocytosis, IGF-1R recruitment to the caveolae prompts caveolin-1

phosphorylation, which then promotes IRS-1 phosphorylation and PI3K/Akt/mTOR pathway activation [58]. In contrast, clathrin-mediated endocytosis promotes Shc and IRS-1 phosphorylation, thereby activating the Ras/Raf/MAPK and PI3K/Akt/mTOR signaling pathways, respectively [56] (**Figure 7**).

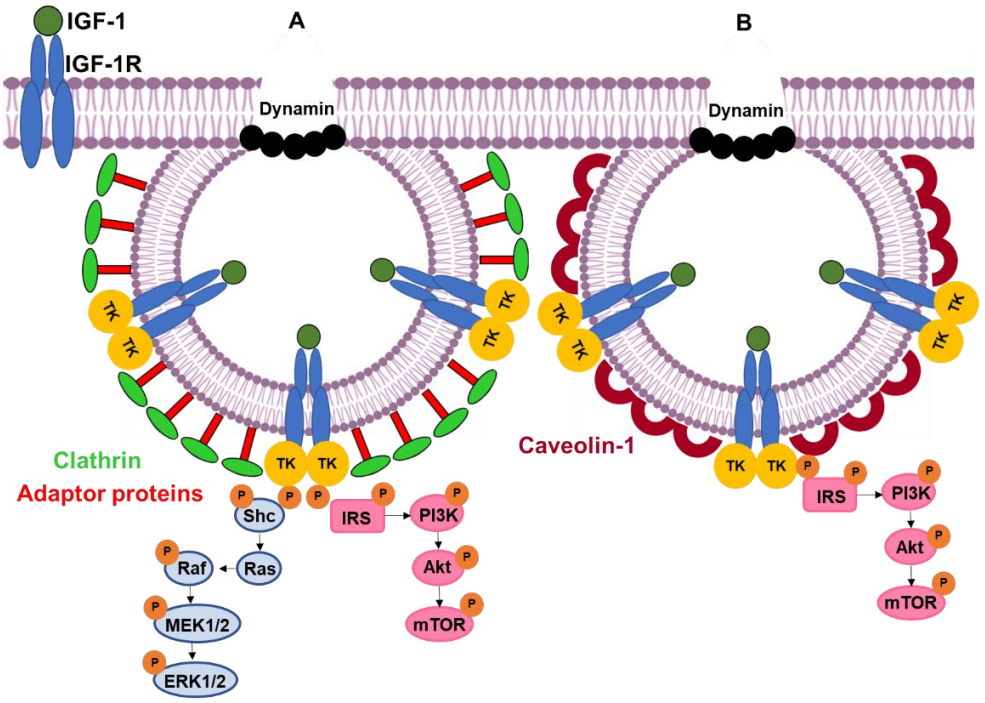

Figure 7: Model of IGF-1R pathway Regulating Endocytosis. A) Schematic representation of clathrin-internalization-dependent IGF-1R signaling. **B)** Schematic representation of caveolin-internalization-dependent IGF-1R signaling.

I.3.2. Feedback Regulation between Phosphoinositide 3-kinase and Androgen Receptor Signaling Pathways

PCa is characterized by its dependence on AR and the activation of the PI3K signaling pathway, and these two oncogenic pathways regulate each other by reciprocal negative feedback to control tumor growth; when one pathway is inhibited, the other becomes activated and vice versa. PI3K pathway inhibition

promotes the activation of human epidermal growth factor receptor 2/3 (HER2/3) by reducing the inhibitory effect of mechanistic target of rapamycin complex 1/2 (mTORC1/2) on HER2/3. This effect allows AR pathway activation in the absence of androgens through the AR phosphorylation by Akt downstream HER2/3 signaling pathway and subsequent AR binding to ARE target sequences [59, 60].

In contrast, AR inhibition leads to a decrease in FK506 binding protein 5 (FKBP5) protein levels, which then inactivates the PH domain and Leucine-rich repeat Protein Phosphatases (PHLPP), thereby causing phosphorylation of the Akt Ser-473 and the activation of Akt signaling (**Figure 8**).

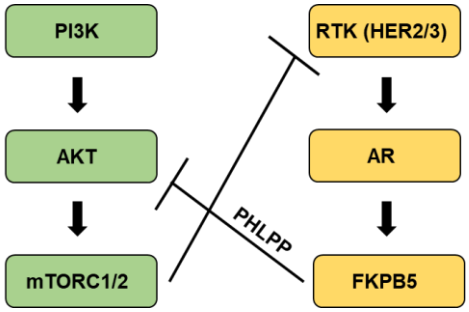

Figure 8: Crosstalk Between the Androgen Receptor and Phosphoinositide 3-kinase Signaling Pathways. Inhibition of the PI3K signaling pathway stimulates HER2/3 receptor promoting AR phosphorylation and activation, while AR inhibition decrease FKBP5 levels leading to Akt phosphorylation and activation. *Adapted from* [61].

I.3.3. The Role of Insulin Growth Factor-1 Receptor in Prostate Cancer Development

While IGF-1R participates in the growth and development of normal prostate glands, it also plays a role in tumorigenic initiation. High IGF-1 levels and low IGFBP-3 levels associate either a greater predisposition for PCa development [62]. Furthermore, the relation between the T2E fusion gene and IGF-1R was further investigated. It is known that the T2E gene is regulated and driven by the

presence of androgens via an androgen-responsive promoter located in TMPRSS2, leading to increased ERG levels. In addition, the overexpressed ERG binds directly to the IGF-1R promoter region, and thus increases the IGF-1R expression.

Additionally, T2E expression correlates with higher IGF-1R expression at the mRNA and protein level (**Figure 9**) [63].

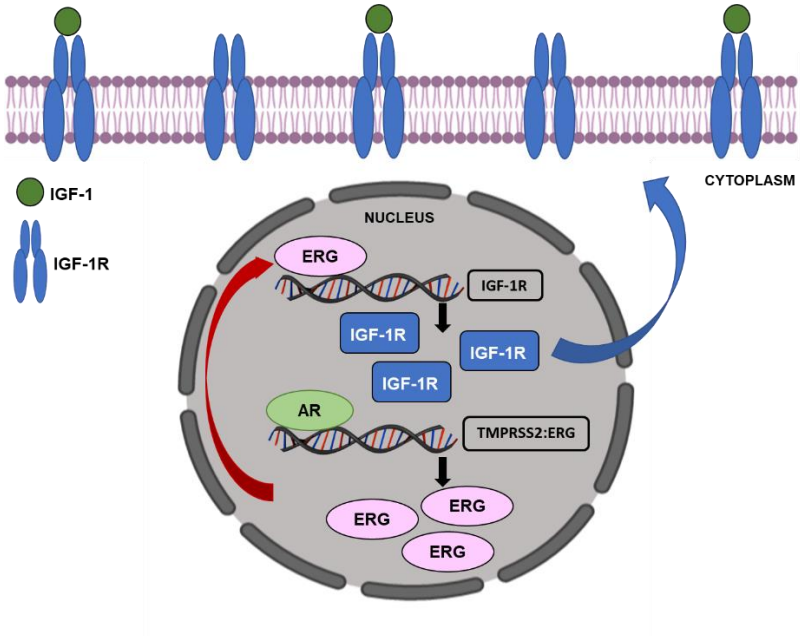

Figure 9: ERG Overexpression is Related to Insulin Growth Factor-1 Receptor Transcription. AR binds to the TMPRSS2 promoter region, which induces ERG overexpression via the T2E fusion gene. In turn, ERG transcriptionally activated IGF-1R mRNA transcription. IGF-1R protein subsequently locates to the cellular membrane.

These findings provide the rationale followed in this doctoral thesis and our studies on the mechanism of action and cellular trafficking in order to determine the signaling pathway with an anti-IGF-1R-targeted monoclonal antibody. Furthermore, due to AR and PI3K oncogenic pathways cross-regulation by reciprocal feedback, we aimed to evaluate a combinatorial therapy based on the administration of an anti-androgen drug and an anti-IGF-1R therapy in an orthotopic PCa mouse model, in the hope of a synergistic anti-cancer effect.

I.4. Castration-resistant Prostate Cancer

Almost all PCa cases are adenocarcinomas; malignant tumors formed from glandular structures in epithelial tissue. Primary or localized PCa present a wide range of treatment options that vary according to patient age, clinical tumor stage, PCa biomarker levels, or Gleason score. Radical prostatectomy and radiotherapy (external beam therapy or brachytherapy) represent standard local treatments for localized PCa. Regardless of the initial positive results of these therapies, the recurrence of the disease occurs in one-third of patients. At this stage of recurrent and advanced PCa, androgen deprivation therapy (ADT) represents the current gold-standard treatment [64]. ADT is based on surgical or chemical castration through the administration of different drugs such as luteinizing hormone-releasing hormone (LHRH) agonist/antagonist, AR antagonists, or androgen synthesis inhibitors, which will be described in more detail below.

PCa is considered a hormone-dependent tumor in which the AR is needed to promote tumor progression; however, patients can develop treatment resistance and display tumor relapse after 18-24 months. The resulting CRPC, previously known as hormone-refractory PCa [65-67], still displays a response to hormone therapy through AR to activate growth [68].

I.4.1. Molecular Mechanisms Involved in Castration-Resistant Prostate Cancer

The understanding of the molecular mechanisms involved in CRPC development includes AR-dependent mechanisms, AR-independent mechanisms and AR-bypassing signaling, as described below, will aid in the development of novel therapeutics [69].

I.4.1.1. Androgen Receptor-dependent Mechanisms

Androgens, such as the hormones testosterone and dihydrotestosterone (DHT), bind to the AR and help to mediate PCa progression. AR, which becomes overexpressed in CRPC patients, exhibits four different functional domains; the ligand-binding domain (LBD), DNA-binding domain (DBD), hinge area, and the variable region (amino-terminal domain, NTD), with the latter domain presenting phosphorylation sites that promote AR activation [70]. In the absence of androgens, the inactive AR localizes mainly to the cytoplasm and interacts with heat shock proteins (HSPs) to avoid nuclear transport. DHT, which is converted from testosterone by the 5α-reductase enzyme, binds to the AR through the LBD, promoting changes to the AR conformation. These changes allow the release of HSPs and the subsequent phosphorylation of AR, causing AR dimerization and successive translocation into the nucleus. The AR then binds to androgen response elements (AREs) located in the promoter/enhancer regions of genes that promote cell proliferation, activate anti-apoptotic pathways, and regulate several androgenic genes such as prostate-specific antigen (PSA) or TMPRSS2:ERG fusion gene (**Figure 10.A**) [71].

Several aspects of the AR-dependent response can explain CRPC evolution, including the amplification of the AR gene, overexpression of the AR protein, AR mutations, expression of AR splice variants (AR-Vs), altered expression and function

of AR co-regulators, and synthesis of adrenal androgens and intratumoral androgens [72].

High AR protein expression via AR gene amplification represents a common occurrence in CRPC patients [73, 74]. AR overexpression leads to receptor hypersensitivity, thereby allowing low levels of androgens to prompt heightened tumor cell proliferation [75].

AR mutations are more common in advanced PCa stages than in early-stage disease, and while more than 100 mutations have been documented, the most prevalent mutations occur in the NTD and LBD regions. Most of NTD mutations occur following ADT and increase AR response to DHT; furthermore, mutations in the LBD region increase AR activity and decrease ligand specificity [76, 77]. Other mutations in the LBD region can alter AR antagonist properties changing the effectiveness of treatments; in this way, AR antagonists can act as agonists and thus promote tumor growth [77]. The most frequent AR mutation (T878A) increases the binding sensitivity of AR for steroid hormones, such as progesterone and estrogen [78].

AR-Vs present in the cytoplasm and the nucleus include truncated AR forms lacking the LBD regions prompting the activation of the NTD and DBD regions in a stimuli-insensitive manner [79]. Therefore, said AR-Vs (AR-V 1-7) promote AR target gene activation and transcription independently of the presence of androgens [80]. Of note, the nuclear-localized AR-V7 is the most abundant truncated form of AR in CRPC patients and associates with a worse prognosis [81].

The altered expression of AR co-regulators can modify the transcriptional activity of AR, indicating that these co-regulators may regulate CRPC progression. Most co-regulators are enzymes that regulate other proteins by phosphorylation, methylation, acetylation, or ubiquitination [82]. Co-regulators can be divided into co-activators and co-repressors; co-activators enhance the transcriptional activity

of the AR [83], while the loss of co-repressor expression or function can lead to an increase in AR-mediated gene transcription [84].

As 90% of testosterone is produced in the testicles (with the remaining 10% generated in the adrenal glands), medical and surgical castration can reduce testosterone levels in the blood; however, CRPC still develops in this situation, suggesting the existence of an alternative androgen production pathway [85, 86]. Indeed, studies have found that prostate tumor cells convert adrenal androgenic precursors such as dehydroepiandrosterone (DHEA) and sulfated-dehydroepiandrosterone (DHEA-S) into DHT to support their own growth; this represents one of the so-called "*back-door*" pathways of androgen synthesis. ADT does not affect DHEA/DHEA-S levels, and 3β-hydroxysteroid dehydrogenase (3βHSD1) and 3-beta-hydroxysteroid dehydrogenase type-2 (3βHSD2) enzymes converts them into androstenedione (AD) in the suprarenal glands and prostate, respectively [87]. Next, the primary and the secondary "*back-door*" pathways prevalent in CRPC uses androstanediol and 5α-androstenedione (5α-dione) respectively to convert AD into DHT, bypassing testosterone synthesis. Additionally, tumor cells can also produce androgens by de novo synthesis from cholesterol [85, 88, 89].

I.4.1.2. Androgen Receptor-independent Mechanisms

CRPC evolution results from the failure of ADT, which inhibits AR-driven proliferation and survival pathways by targeting the AR signaling axis. Reactivation of AR through the androgen-dependent mechanisms describe above has been identified as the primary driver of CRPC. Androgen-independent signaling pathways can provide additional mechanisms supporting CRPC development [90]. Androgen receptor-independent mechanisms involved in CRPC development (**Figure 10.B**) can be divided into three different pathways; the PI3K/Akt/mTOR, Src, and Growth factor signaling pathways [72].

Activation of PI3K/Akt/mTOR pathway through G-protein-coupled receptors (GPCRs) or TKRs promotes proliferation, cell, survival, and angiogenesis in CRPC [91, 92]. The loss of expression of PTEN tumor suppressor, via mutations, promoter methylation, microRNA interference, phosphorylation, or delocalization from the plasma membrane [93-95] activate the PI3K/Akt/mTOR pathway [96, 97].

The activation of the Src proto-oncogene tyrosine-protein kinase signaling pathway during CRPC development promotes cell growth, inhibition of anti-apoptotic pathways, and tumor progression regardless of androgen levels [98]. Furthermore, this pathway promotes angiogenesis via the regulation of vascular endothelial growth factor (VEGF) and interleukin 8 (IL-8) expression by the induction of metallopeptidase 9 (MMP-9) [99-101]. Additionally, Src signaling can activate nuclear factor KB (NFkB) to promote bone metastasis of PCa [102].

In the absence of androgens or in the presence of extremely low levels of androgens, AR can still be activated and translocated into the nucleus to promote cell survival, tumor growth, and CRPC evolution. AR activation occurs through the actions of various growth factor receptors, such as IGF-1R, epidermal growth factor receptor (EGFR), and interleukin 6 receptor (IL-6R), which can all activates PI3K, MAPK, and signal transducer and activator of transcription 3 (STAT3) pathways [103, 104]. Activation of AR via phosphorylation occurs thanks to various mechanisms depending on the pathway involved. Activated IGF-1R, via IGF-1 binding, interacts with AR through integrin beta (β_{1A}) [105]. In the case of IL-6R, a physical interaction between STAT3 and AR promotes AR phosphorylation [106]. EGFR activation induced by EGF ligand binding promotes MAPK signaling pathway activation, which functionally interacts with AR [107].

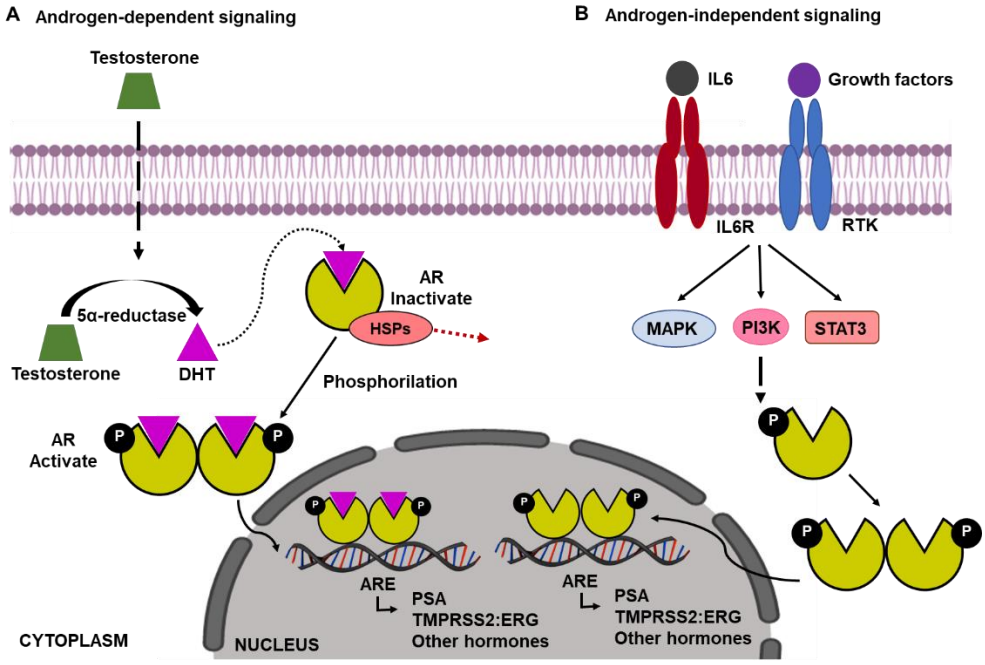

Figure 10: Schematic of Androgen-dependent and -independent Signaling. A) Androgen-dependent Signaling. Testosterone is transformed into DHT by the 5α-reductase enzyme; DHT then binds and activates AR so prompting the release of HSPs. AR then dimerizes and translocates to the nucleus to bind ARE sequences to promote the expression of PCa-associated genes. **B) Androgen-independent Signaling.** Protein kinase signaling pathways promote androgen-responsive gene transcription by activating the PI3K, MAPK, and STAT3 signaling pathways.

I.4.1.3. Androgen Receptor-bypassing Signaling

AR-bypassing signaling is based on the activation of AR transcription genes which promote tumor proliferation through others steroids hormone nuclear receptors different from AR. Steroid hormone nuclear receptors such as the AR, estrogen receptor (ER), progesterone receptor (PGR), glucocorticoid receptor (GR), and mineralocorticoid receptor act as transcription factors. All present a common structure of four domains: the NTD, DBD, hinge region, and LBD [108]. AR and GR recognize the same DNA binding sites and, therefore, can activate the same target

genes involved in the development of CRPC [109]. Moreover, mutations to the LBD region of the AR (L701H and T877A) allow the AR to respond to glucocorticoids and promote tumor cell proliferation [77]. Furthermore, progesterone, apart from acting as a precursor for androgen synthesis *de novo* in PCa, the PGR is structurally related to the AR and also activates AR target genes crucial to PCa progression [110, 111]. The therapeutic blockade of AR promotes the increased expression of GR, so suggesting GR and PGR as therapeutic targets for PCa treatment as both steroid receptors play an essential role in the development of CRPC (**Figure 11**) [112].

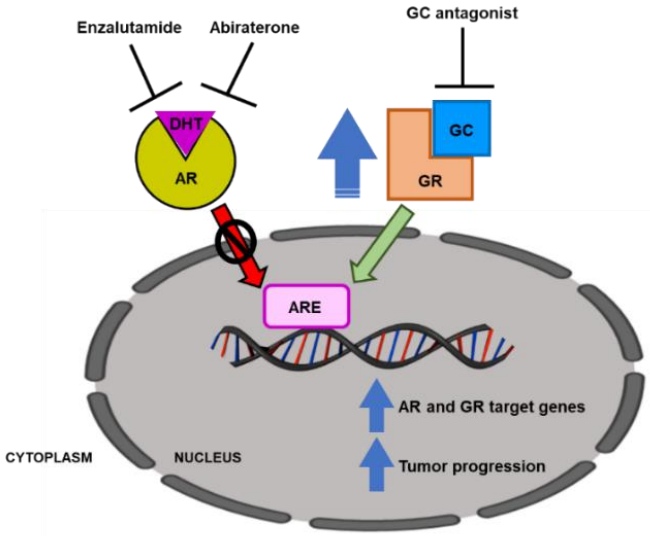

Figure 11: Schematic of Glucocorticoid Receptor Activation through Androgen Receptor Suppression. AR inhibition by enzalutamide or abiraterone leads to increased levels of the GR due to the relief of AR-mediated feedback repression of GR expression, which binds to the same DNA region as the AR and results in the tumor progression and the transcription of AR and GR target genes. *Modified from* [109].

I.4.2. Castration-Resistant Prostate Cancer Therapies: Current Therapeutic Approaches

Despite recent advances in PCa molecular biology that have allowed the improvement of current treatment strategies and the development of novel clinical approaches, mortality rates in CRPC patients remain high. Traditional therapies employed to treat CRPC include hormonal therapy, chemotherapy, immunotherapy, and radiotherapy.

New hormonal therapies have been developed based on the critical role that AR plays in PCa. The evolution of PCa to CRPC relies on the capacity of cancer cells to grow with extremely low levels of androgens and is due to aberrations in AR that maintain transcriptional activity in the absence of the binding-ligand domain. Abiraterone acetate was approved by the FDA in 2011 as a treatment for patients with CRPC previously treated with docetaxel, based on the critical role that AR plays in PCa [113, 114]. Abiraterone acetate is an irreversible, highly selective inhibitor of Cytochrome P450 Family 17 Subfamily A Member 1 (CYP17) enzyme that offers clinical benefit to patients with hormone-refractory prostate cancer by inhibiting androgen, estrogen, and glucocorticoid synthesis in testis, adrenal glands, and prostate tumors. In addition, the second generation of DHT antagonist ligands has been designed that aim to prevent AR activation and nuclear translocation, thus blocking AR target genes synthesis in CRPC patients. Antagonists have a greater affinity for the AR, competitively binds to the ligand-domain, thereby prompting higher levels of inhibition. These include Enzalutamide, approved by FDA in 2012 for mCRPC following docetaxel [115], and Apalutamide, which possesses a chemical structure similar to enzalutamide and was approved by FDA in 2018 for non-metastatic castration-sensitive PCa [116]. Interestingly, hormonal therapies can synergize with classical chemotherapeutic agents.

The current recommendation for mCRPC treatment is based on the use of chemotherapeutic treatments include docetaxel and cabazitaxel, which were approved by the FDA in 2004 and 2010, respectively [117, 118]. Both drugs are taxanes and inhibit cell division and cause cell death by binding to microtubules to prevent cellular mitosis. Furthermore, taxanes also inhibit the nuclear translocation of AR [119, 120]. However, these strategies only provide for a median overall survival of 18 months due to the development of different mechanisms of resistance [121].

Novel therapeutic approaches include Sipuleucel-T and Radium-223 (Ra-223). Sipuleucel-T, the first immunotherapy for CRPC approved in 2010 by the FDA [122], is an autologous cellular immunotherapy (cancer vaccine) in which patient-derived peripheral blood mononuclear cells are cultured in the presence of recombinant prostatic acid phosphatase (PAP) coupled to granulocyte-macrophage-colony-stimulating factor to prompt the maturation of antigen-presenting cells [123]. Ra-223, an alpha therapy that specifically targets bone metastases, was approved by the FDA in Japan in 2013 for the treatment of CRPC patients [124, 125]. Ra-223 mimics calcium and binds to the bone mineral hydroxyapatite present in bone metastases and damages DNA, leading to an anti-tumor effect.

Advanced PCa is divided into three different stages - (i) metastatic hormone-sensitive PCa (mHNPC), (ii) non-metastatic CRPC, and (iii) metastatic CRPC (mCRPC) – which require different treatment approaches (**Figure 12**).

mHNPC patients are treated with ADT and chemotherapies such as abiraterone acetate and docetaxel, non-metastatic CRPC patients are treated with ADT with enzalutamide or apalutamide, and mCRPC patients are treated with different drugs combinations depending on the first, second, or third line therapy. The first line for symptomatic patients uses hormonal therapy

(Abiraterone/Enzalutamide) or chemotherapy (Docetaxel/Cabazitaxel), and for asymptomatic patient therapy is based on the use and immunotherapy (Sipuleucel-T). The second line for symptomatic patients is based on the use of chemotherapy (Docetaxel/Cabazitaxel) or radiopharmaceuticals (Ra-223), and for asymptomatic patient therapy is based on ADT (Abiraterone/Enzalutamide). The third line for symptomatic patients is based on the use of chemotherapy (Cabazitaxel) or radioisotope (Ra-223), and for asymptomatic patient therapy is based on the use of chemotherapy (Docetaxel/Cabazitaxel).

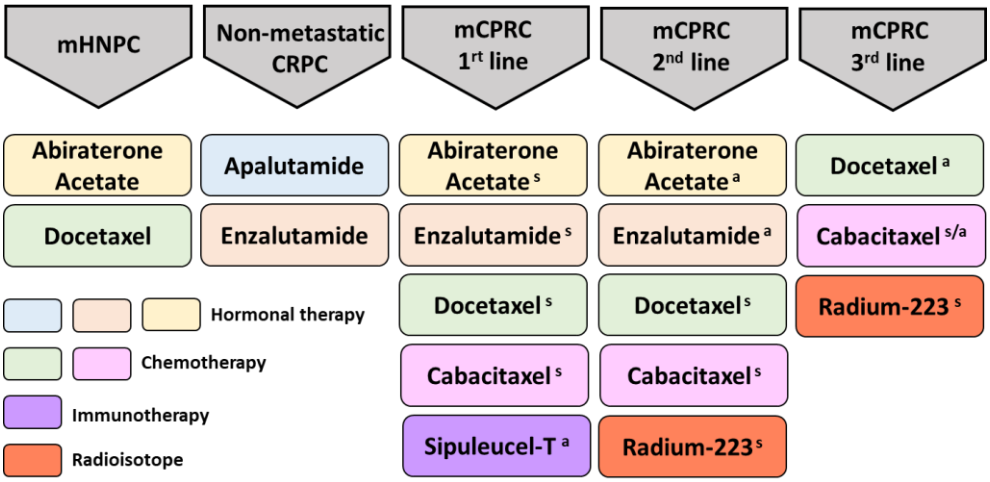

Figure 12: Treatment Sequencing Strategy for Advanced Prostate Cancer. mHNPC therapies employ hormonal therapy and chemotherapy and non-metastatic CRPC therapies use hormonal therapy alone. Meanwhile mCRPC first line therapy uses a combination of hormonal therapy, chemotherapy and immunotherapy, while second line uses hormonal therapy, chemotherapy and radiotherapy, and while the third line focuses on chemotherapy and radiotherapy. [s] treatment for symptomatic patients, [a] treatment for asymptomatic patients. *Adapted from* [310].

I.4.3. Castration-Resistant Prostate Cancer Therapies: Potential Therapeutic Approaches

Unfortunately, in spite of the increased arsenal of drugs employed to treat advanced PCa, a lack of targeting and efficiency has failed to improve survival rates and reduce side effects. However, recent advances in PCa treatment and drug discovery offer different treatment options and novel therapies which are being evaluated in clinical trials in the hope of improving therapeutic outcomes.

Clinical trial studies have explored different targeted therapies, including poly ADP-ribose polymerase (PARP) inhibitors, angiogenesis inhibitors, and growth factor receptor inhibitors.

I.4.3.1. PARP Inhibitors

Damage to DNA due to exposure to ultraviolet (UV) light, ionizing radiation, chemicals, and cellular metabolism or derived from replication errors must be recognized and repaired for proper cell function. The BRCA (Breast cancer susceptibility protein) and PARP proteins repair DNA through homologous recombination repair (HRR) and nucleotide excision repair (NER), respectively; however, the altered expression or function of proteins involved in DNA damage repair can mute the DNA damage response, heighten mutation load, and promote the development of tumorigenesis [126]. Mutations to the BRCA1 and 2 genes lead to the reduced repair of DNA double-strand breaks (DSBs); however, cancer cells lacking functional BRCA1 or 2 can continue to grow due to the presence of PARP proteins that repair single-strand breaks (SSBs) [71, 72].

CRPC is characterized by BRCA2 mutations [127] and suffers problems related to a dysfunctional DNA damage repair [128], thereby highlighting PARP inhibition as a potentially effective treatment for PCa patients. Said inhibitors

prevent the repair of SSBs, leading to the accumulation of mutations, and eventual cell death [129, 130].

The PARP inhibitor Olaparib has provided promising results in selected mCRPC patients in phase III clinical trials [131], while Veliparib [132], Niraparib [133], and Rucaparib [134] have also been studied in clinical trials alone and in combination with other drugs [123].

I.4.3.2. Angiogenesis Inhibitors

Angiogenesis, the formation of new blood vessels from other existing vessels, occurs in various steps [135, 136] and is regulated by a balance between pro-angiogenic and anti-angiogenic factors. However, an increase in pro-angiogenic factors, including endothelial growth factor (VEGF)-A and basic fibroblast growth factor (bFGF) [137-139], leads to dysregulated angiogenesis in cancer patients.

VEGF signaling promotes the generation of new vessels by binding to VEGFR, and advanced stage PCa patients present with elevated levels of VEGF-A, indicative of a worse prognosis for PCa patients [140]. For this reason, VEGFR targeting can inhibit angiogenesis in cancer patients [139, 141]. Such inhibitors can either prevent VEGF ligand binding to VEGFR or block the VEGFR itself to prevent pro-angiogenic signaling, inhibit the formation of new blood vessels, and decrease tumor growth and the development of metastasis.

Examples used in clinical trials include Bevacizumab, a humanized monoclonal antibody that inhibits VEGF-A binding to VEGFR2 on endothelial cells [142], Aflibercept, a protein that binds to VEGF-A to prevent receptor binding [143], Sunitinib, a multi-targeted TKR inhibitor targeting VEGFR2 and Platelet-derived growth factor receptor-beta (PDGFRβ) [144], and Lenalidomide, a VEGF inhibitor [145].

Unfortunately, anti-angiogenic therapies have not proved successful due to an increased rate of toxicity and adverse effects such as lymphopenia, neutropenia, and anemia [146]. Furthermore, treatment can also fail due to PCa heterogeneity; currently, we lack biomarkers that can select those patients who may benefit from antiangiogenic therapies. For this reason, the study of the angiogenic signaling pathway may provide information that allows the design of effective PCa therapeutics.

I.4.3.3. Growth Factor Receptor Inhibitors

Aberrantly increased levels of growth factors, such as EGFR, fibroblast growth receptor factor (FGFR), hepatocyte growth receptor factor (HGFR) and IGF-1R [147], bind to cell membrane receptors to promote proliferation, survival, and migration of PCa cells [148]. Therefore, they represent therapeutic targets for the inhibition of PCa tumor growth and metastasis.

With a focus on IGF-1R, current strategies in clinical trials have been developed to avoid its activation, including tyrosine kinase inhibitors (TKIs), IGF neutralizing antibodies, and anti-IGF-1R monoclonal antibodies (mAbs).

a) Insulin Growth Factor-1 Receptor Tyrosine Kinase Activity Inhibitors

IGF-1R TKIs are small molecules that nullify the effect of IGF binding to its receptor (IGF-1R). As the INSR-A and INSR-B receptors share some similarities with the IGF-1R, inhibitors may interact with all three receptor types [149]. However, INSR-B inhibition can modify glucose metabolism by producing hyperglycemia [150], and because of this, clinical studies have not yielded promising results. Furthermore, IGF-1R TKIs suffer from short half-lives, so they do not completely block tyrosine kinase activity [151]. IGF-1R TKIs in clinical trials for PCa include Linsitinib in patients with asymptomatic or mildly symptomatic mCRPC [152] and

nordihydroguaiaretic Acid (NDGA) in patients with non-metastatic recurrent PCa and non-metastatic relapsed PCa [311].

b) Insulin Growth Factor-neutralizing Antibodies

Humanized IGF-neutralizing monoclonal antibodies bind to and block the interaction of IGF1 and IGF2 with IGF-1R, INSR-A, and the hybrids receptors IGF-1R/INSR-A or IGF-1R/INSR-B. This approach suffers from fewer side effects (such as hyperglycemia) as the homodimer INSR-B receptor is unaffected [153]. One mAb (Xentuzumab) that neutralizes the IGF1 and IGF2 ligands is currently under evaluation in clinical trials for PCa in combination with enzalutamide [154, 311].

c) Anti-Insulin Growth Factor-1 Receptor Monoclonal Antibodies

Anti-IGF-1R mAbs bind to the alpha subunit of IGF-1R to prevent IGF from binding to the receptor and avoid signaling pathway activation and inhibit cancer cell growth and proliferation [155]. mAbs also promote receptor internalization and degradation [155]. Of note, anti-IGF-1R mAbs possess a high specificity for IGF-1R with respect to the insulin receptor (INSR), although some can bind hybrid receptors composed of IGF-1R and INSR isoforms which forms a heterodimer receptor (IGF-1R/INSR-A or IGF-1R/INSR-B), thereby promoting a decrease in insulin receptor activity that can produce side effects such as hyperglycemia [156]. Unfortunately, some reports have noted that anti-IGF-1R mAbs can actually act as agonists, thereby promoting pathway signaling activation [157].

Anti-IGF-1R mAbs for PCa evaluated in clinical trials include Ganitumab in mCRPC [158-160], Figitumumab combined with pegvisomant for prostatic neoplasm [158, 161], and Cixutumumab in mCRPC [158, 311].

IGF-1R inhibitors as single agents or in combination with other therapeutic strategies have been evaluated in clinical trial in CRPC patients; however, patients only experienced a partial response to therapy due to resistance mechanisms, incomplete blockage of the signaling pathways, or inadequate treatment, while also suffering from significant side toxicities (neutropenia, diarrhea, hyperglycemia, etc.). For these reasons, some clinical trials of mAbs were discontinued [162, 163]. **Of these mAbs, we sought to evaluate a modified AVE1642 in this doctoral thesis, as a single or combinatorial therapeutic approach, to inhibit the IGF-1R signaling pathway.**

I.5. Nanomedicine for PCa treatment: Principal Aspects and Classification

Conventional treatments for PCa consist of surgical tumor resection, radiotherapy, or chemotherapy. Radiotherapy and chemotherapy treatments can cause damage to healthy tissues close to the tumor due to their non-specificity, low efficacy, and low bioavailability. Furthermore, it remains challenging to control pharmacokinetics due to several factors, such as the different transient states of the drug in adhesion, metabolism, excretion, and distribution. Chemotherapy can lead to the development of drug resistance; therefore, encountering new, efficient, personalized, and targeted treatment approaches represents a pressing concern. Furthermore, faster cancer progression promotes hypoxic and necrotic regions, which represent challenging targets for systemic treatments [164]. For this reason, the development of advanced therapeutics such as nanomedicines may represent a promising means to improve the specificity and efficacy of anti-cancer therapeutic agents while decreasing side effects [165, 166].

The development of nanomedicine for anti-cancer therapies can provide the following advantages: nanomedicines can (i) increase both the solubility and

the chemical stability of treatments, (ii) modify pharmacokinetics and pharmacodynamics, thereby enhancing accumulation in the pathological site (by the EPR passive effect [167-169] or active targeting, **See Section I.6** for further detail) and protecting compounds from non-specific organ accumulation, biodegradation or excretion, (iii) improve the distribution and penetration of treatments by specifically targeting tumor cells allowing a controlled release of the drug and reduced toxicity and adverse effects on healthy cells, (iv) improve therapeutic efficacy and effectiveness, and (v) inhibit drug-resistance due to different cell internalization mechanisms [170, 171].

There are already more than 50 nanomedicines in routine clinical use and 75 nanosystems in clinical trials [172]. Nanomedicine can be classified in different product families, which include lipid-based nanocarriers, polymer therapeutics, polymeric nanoparticles, crosslinked (nano) gels, bioactive synthetic polymers/vesicles, and nano-sized drug crystals (**Figure 13**) [170].

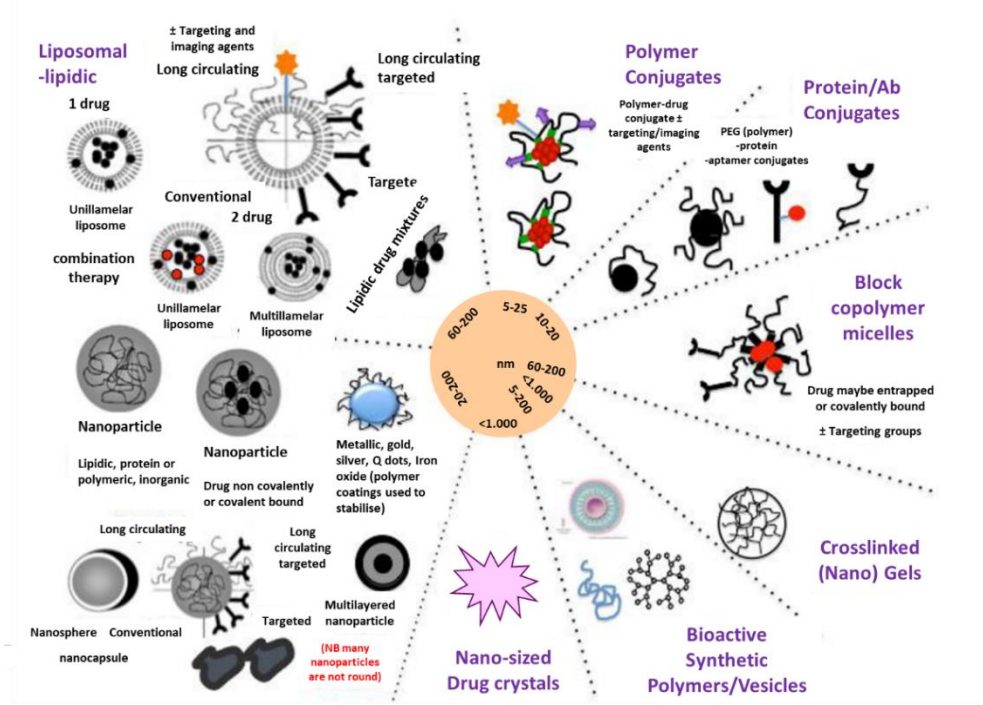

Figure 13: Established Nanotherapeutic Platforms. *Modified from* [170].

Perhaps the most promising nanomedicinal approaches involve multivalent carriers that can allow the simultaneous delivery of two or more anticancer drugs in a synergistic ratio, thus allowing an efficient combination therapy. Relevant clinical milestones for combination nanomedicines include Combiplex®, a liposome including a combination of two chemotherapeutic agents recently approved by the FDA [173].

After adequate rational design, nanomedicines can cross biological barriers and transport drugs specifically to target sites thus reducing any adverse effects on healthy tissues**.** As biological barriers represent the bodies primary defense mechanism and block the penetration of foreign substances, the development of efficient nanopharmaceuticals requires an understanding of said barriers [174].

I.5.1. Biological Barriers to Nanomedicine

First Level: Absorption

One of the first limitations to treatments with nanomedicine is the distribution throughout the body via the bloodstream. Initial design strategies must allow nanomedicines to reach their destination and maintain their characteristics and integrity in response to different physiological conditions, including the presence of proteases, redox potential, different pH, etc. While intravenous injection is commonly employed and allows for adequate drug distribution, other administration routes, including topical administration, oral, different mucosal barriers, are also employed [175].

Second Level: Circulatory Barriers

The reticuloendothelial system (RES), the immune system, and the hepatic system also represent barriers to the desired output of an administered nanomedicine as they function to recognize and eliminate foreign objects. Loading, form, and size of nanomedicines are related to glomerular filtration [189]. The addition of polyethylene glycol moieties to nanomedicines (PEGylation) can avoid recognition by the RES; Doxil®, a PEGylated liposomal formulation of doxorubicin employed for anti-cancer treatments [177, 178], represents the first example of this strategy. Nevertheless, some nanoparticles present long retention times, which can lead to systemic toxicity causing an inflammatory reaction and decreasing therapeutic efficacy [176, 190]. For this reason, nanomedicines must be designed with suitable properties to obtain better renal filtration and thus avoid toxicity [191, 192]. As recognition by phagocytes, another immune system component, can lead to nanomedicine clearance, the surface modification of nanomedicines with cellular components can decrease phagocytosis and improve treatment outcomes [175, 179].

Third Level: Tissue-specific Barriers and Tumor Stroma

Some organs exhibit specific barriers, including blood-brain, ocular, retinal, testis barriers, and blood-thymus barriers [175]. A detailed description of these barriers lies out with the scope in this doctoral thesis; however, more information can be found in the following references [180-184].

The tumor microenvironment (TME) represents the cellular environment in which the tumor exists and is formed by non-cancerous cells and stromal components, such as the extracellular matrix (ECM), blood vessels, infiltrating inflammatory cells, and a variety of associated tissue-specific cells [185, 186].

The advanced design of nanomedicine to allow highly effective delivery of nanomedicine to tumors, has further enhanced its therapeutic benefits. However, these advances have not yet been able to overcome the delivery barriers of a TME due to a heterogeneous blood flow, dense ECM, abundant stroma cells, and high interstitial fluid pressure (IFP), which severely impede the vascular transport of nanomedicines, hinder its effective extravasation, and prevent its interstitial transport to achieve an equal distribution within tumors [185, 186]. Therefore, modulation of tumor microenvironment, including different strategies such as improving tumor perfusion, facilitating tumor extravasation, or enhancing interstitial transport, has now emerged as an important strategy to improve nanomedicine delivery to tumors [309].

Fourth Level: Cellular Barriers

Nanomedicines can internalize into the cell using routes that depend on molecular weight (Mw). Passive diffusion occurs when the Mw of the nanomedicine is less than 1KDa, while nanomedicines with a Mw higher than this internalize through different endocytic pathways, including endocytosis, phagocytosis, and micropinocytosis [175].

Fifth Level: Subcellular Barriers

While the nucleus and the mitochondria represent challenging organelles to target, nanomedicines display certain advantages that can make therapeutic targeting possible [175]. Endocytic processes define the cellular trafficking of nanomedicines to different nanomedicines follow an endocytic pathway by clathrin-mediated endocytosis for transport to the lysosome, which can allow for nanomedicine degradation and drug release in the case of polymer/peptide-based nanomedicines (described below) [175]. In clathrin-mediated endocytosis, only endosomal escape ensures access of the nanomedicine to the proper target organelle. Moreover, nanomedicines can also be targeted to the peroxisomes or reticulum endoplasmic; in these cases, the incorporation of specific targeting sequences are required [187, 188].

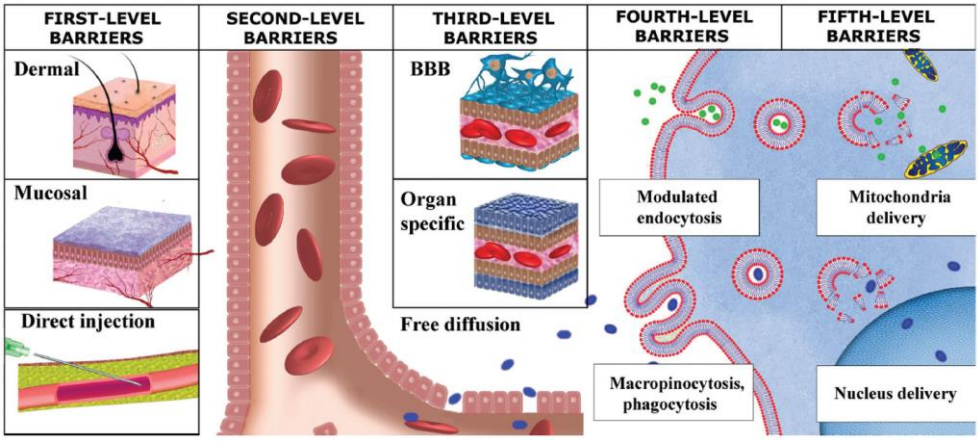

Figure 14: Biological barriers represented at five various levels. The blood-brain barrier (BBB). *Adapted from* [175].

I.5.2. Current Studies in Nanomedicine for Prostate Cancer

Apart from the general biological barriers described above, the design of nanomedicines in PCa must take into account prostate-specific barriers, including:

(i) anatomical barriers; the prostate is divided into different regions, which are regulated by androgens, (ii) physiological barriers; disease progression variations occur in the lymphatic system affecting the transport of the drug, and (iii) cellular and molecular barriers; PCa physiopathology affects the distribution of drugs [193].

Ongoing research regarding these physiological barriers and a greater understanding of the disease have prompted the design of nanomedicinal and strategies for PCa treatment (**See Table 1**). Nanoparticle formulations displayed decreased toxicity in patients, while the nanoencapsulation of chemotherapeutic agents improved their bioactivity leading to an increase in the specificity and efficacy of the drug [194].

Area of prostate nanomedicine	Delivery system
Nanomedicine delivery	Magnetic nanocomplex-doxorubicin
	cis Dichlorodiamminoplatinum (II) glyconanoparticles
	Carbon nanotubes catechin
	Succinoyl-tocopheryl polyethylene glycol succinate nanomicelles doxorubicin
	Gum arabic-coated radioactive gold nanoparticles (GA-198AuNPs)
	Liposomal-dexamethasone
	Mesoporous silica nanoparticles–mannose-6-phosphate receptor
	Histone deacetylase inhibitors
	N-(2-hydroxypropyl) methacrylamide
	Poly(styrene)-b-poly(DL-lactide) copolymer-based (NPs)-delivery of docetaxel NPs
	Iron oxide magnetic nanoparticles-prostate-specific membrane antigen
	Quantum dot-prostate-specific antigen
	Raloxifene nanomicelles
	Goserelin-conjugated gold nanorods
	Docetaxel and curcumin coencapsulated

Table 1: Examples of nanomedicines for the treatment of PCa. *Adapted from* [194].

Nanomedicinal approaches to PCa treatment often take advantage of specific proteins overexpressed on the cancer cell surface, a strategy that aims to boost therapeutic outcomes and eliminate the often-adverse effects caused by the administration of the free drug on non-target cells and tissues. Relevant proteins include prostate-specific membrane antigen (PSMA), folate receptor (FR), CD44, and CD24.

PSMA is a transmembrane protein located in prostate tissues whose overexpression relates to the progression and evolution of PCa [196]. Nanomedicinal approaches employing PSMA-specific aptamers, single-stranded oligonucleotides (ssDNA and RNA) that recognize different target molecules and are more resistant to heat and pH variations compared to antibodies [197], have been employed to target docetaxel-loaded nanoparticles to prostate cancer cells to improve drug effectiveness [198]. Furthermore, nanomedicinal approaches also include BIND-014, a docetaxel within a matrix of polylactic acid nanoparticle covered with a coating of polyethylene glycol in which are ligands targeted to PSMA. This nanoparticle was the first PMSA-targeted nanomedicine evaluated in clinical trials for mCRPC. Preclinical studies in xenograft mice PCa models showed an increase in antitumoral activity [199] and a subsequent Phase I clinical trial provided evidence for BIND-014 safety and determined the appropriate dose (60mg/m^2 every 3 weeks) to proceed with the experiments in further phase II clinical trial [200]. Phase II clinical trials confirmed the safety and tolerability of BIND-014 in patients with mCRPC, although the trial failed to provide evidence of significantly enhanced tumor accumulation and was discontinued [172, 201].

FR receptors are overexpressed in several types of cancer and has been used in combination with gene therapy to treat PCa [202]. As an example, on study employed surface modified gold nanoparticles with polyethyleneimine that had been covalently functionalized with folic acid (FR ligand) for the complexation of a small interfering RNA (siRNA) via electrostatic interactions. These nanoparticles were designed as non-viral vectors for gene therapy and resulted in significant endogenous gene silencing following by endolysosomal escape in comparison with non-targeted formulations [203].

CD44, a hyaluronic acid (HA) receptor, is overexpressed on prostate cancer cells surface and HA can be used as a carrier to transport the drugs to CD44 positive

PCa cells [204]. As an example, the attachment of HA to the anticarcinogenic drug cis-dichlorodiamminiplatinum (II) (CDDP), was used to treat those CD44-positive PCa, with an observed increase in antitumorigenic activity compared with those cells with lower CD44 cellular expression [205].

CD24 expression associates with the early development and subsequent progression of PCa and one study demonstrated that a docetaxel-loaded nanoparticle conjugated with an anti-CD24 antibody promoted higher drug accumulation in cancer cells [206].

OsteoDex, a poly-bisphosphonate containing the polysaccharide dextran, alendronate, and guanidine, currently represents the only nanomedicine for mCRPC (skeletal metastasis) being evaluated in clinical trials. Alendronate binds to hydroxyapatite to inhibit osteoclast-mediated bone resorption [207], dextran is a polysaccharide formed by different glucose molecules and guanidine is used to modify the poly-bisphosphonate molecule in order to promote higher Alendronate effectivity. OsteoDex binds to hydroxyapatite, where it promotes a cytotoxic effect on the osteoclasts, and promotes a cytotoxic effect in tumoral cells, with preclinical *in vivo* and *in vitro* studies demonstrating a potent anti-tumoral efficacy in PCa cells [208-210]. Phase I clinical studies found OsteoDex to be well-tolerated with mild side effects, and phase II are currently under way. The main objective of the phase II clinical trial is to evaluate the relative change of response in different bone metabolism markers to bone metabolism such as human serum bone alkaline phosphatase (B-ALP) and N-terminal propeptide of type 1 collagen (P1NP) using different OsteoDex doses (3.0, 6.0 and 9.0 mg/kg) [311].

Finally, different routes of nanomedicine administration for the treatment of PCa are being explored both in preclinical studies and in clinical trials, including systemic, intra-prostatic (locoregional), trans-vasal (vas-deferens) and trans-rectal

routes. Each administration route presents advantages and disadvantages for the release of nanomedicines, which are described in **Figure 15** [211].

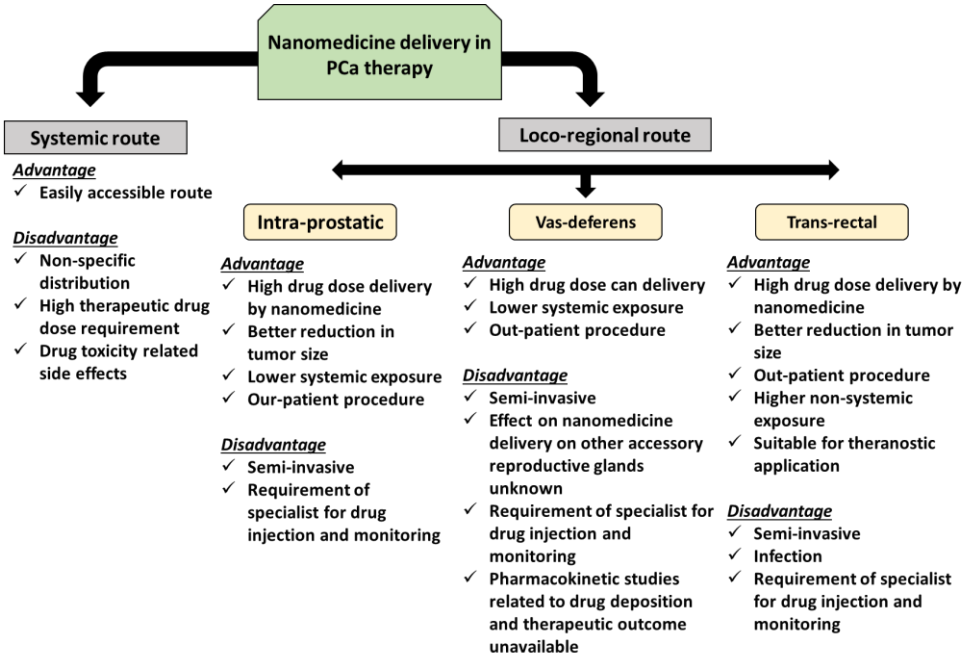

Figure 15: Drug Delivery Strategies for Prostate Cancer Therapy. *Modified from* [211].

I.6. Polymers Therapeutics

Polymer Therapeutics are considered the first generation of polymeric nanomedicines (5-100 nm in diameter) and have already demonstrated clinical benefits [212-214]. They are considered as "new chemical entities" (NCEs) and not as simple conventional systems for the transport of drugs, that simply captures, solubilizes, or releases the drug in a controlled manner without using the chemical conjugation. In contrast, polymer therapeutics are divided into five hybrids nano-constructions, which use water-soluble polymers that can be bio-active and/or as an inert carrier that for the chemical conjugation of bioactive molecules [213, 215]. The next generation of nanomedicines have taken advantage of a

decade of research findings, and they hope to offer benefits to patients and open new markets in the pharmaceutical industry [216, 217].

The potential of polymer therapeutic can be illustrated by the appearance of two polymer therapeutics among the 10 top-selling drugs in the USA in 2013. Copaxone® (Teva Pharmaceutical Industries, Petah Tikva, Israel) a polymeric drug (glatiramer acetate) has been used in the treatment of relapsing-remitting multiple sclerosis, while Neulasta® (Amgen, California, USA), a polyethylene glycol (PEG)-filgrastim conjugate has been used for the treatment of neutropenia in patients with malign tumors [218].

I.6.1. Classification of Polymer Therapeutics

Polymer therapeutics are composed of different macromolecular families, including polymer-drug conjugates (PDCs) [214, 219, 220], polymer-peptide or polymer-protein conjugates [221, 222], polymeric drugs [223], polymeric micelles [224, 225], characterized by a covalent bond between the drug and the polymer, and multicomponent polyplexes which are develop as non-viral vectors [225, 226] (**Figure 16**).

In this doctoral thesis, we focused on the development of a polymer-protein conjugate (polymer-antibody conjugate).

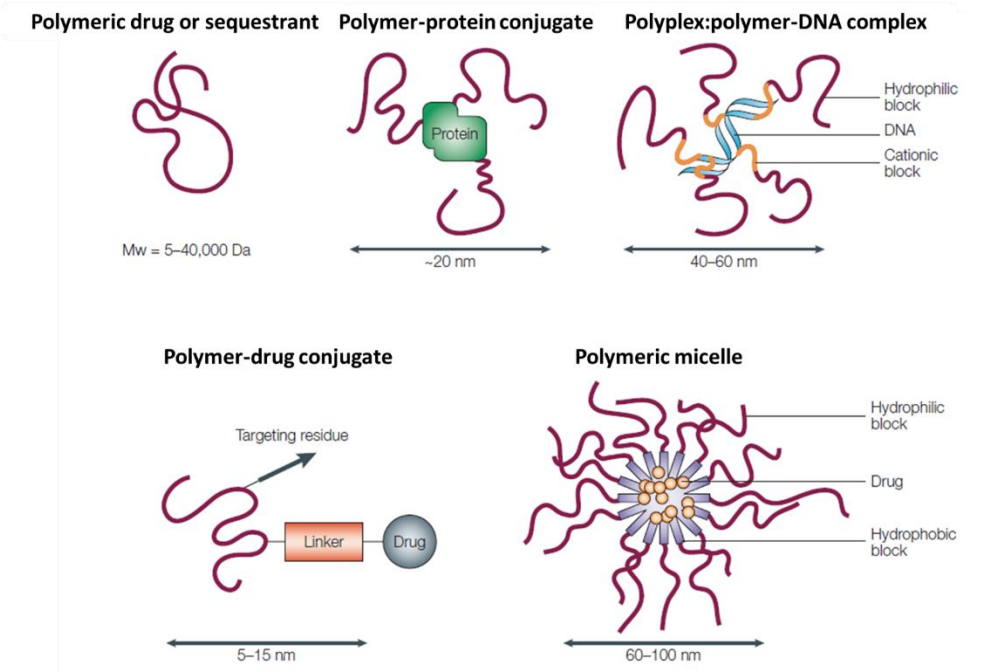

Figure 16: Overview of the Polymer Therapeutics Family. *Adapted from* [213].

All of the polymer therapeutics described employ specific water-soluble polymers, thus achieving a better administration of drugs in patients to improve drug, protein, or gene delivery. In addition, they allow greater diversity in their chemical synthesis, weight, and control of molecular loading. Furthermore, polymer therapeutics allow the combination of several drugs, and biological characteristics can be used to promote drug release under specific conditions (pH-sensitive or peptidase-sensitive linkers are widely used) [212]. Since the first polymer-protein conjugate (PEG-adenosine deaminase [ADAGEN ™]) appeared on the market in 1990, the polymer therapeutics field has come to be considered a routine clinical therapy that is steadily increasing [227].

Besides linear polymers, polymeric structures include graft, star, multivalent, dendrimer, and dendronized polymers. Potential advantages of these architectures include enhanced chemical composition, multivalency, and the establishment of a defined three-dimensional cross-linked system with potentially longer blood circulation time (**Figure 17**) [213, 228].

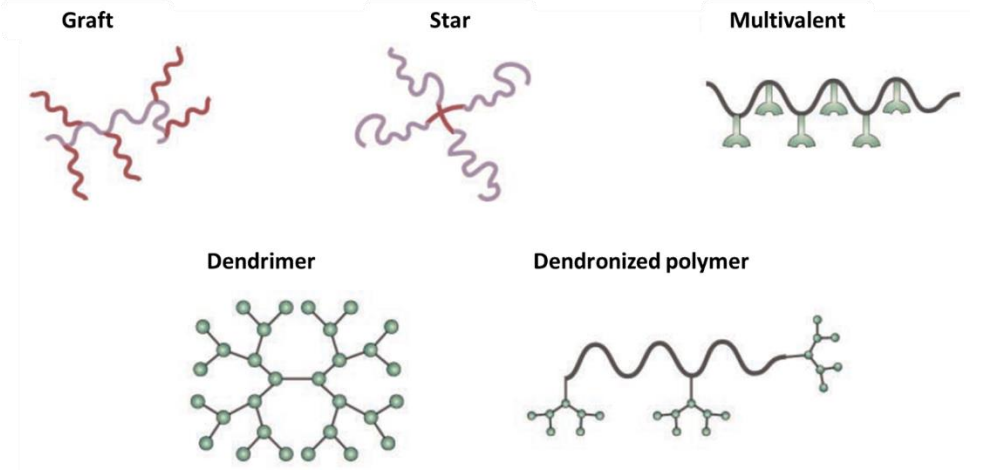

Figure 17: Overview of Novel Polymeric Structures. *Adapted from* [213].

Due to their intrinsic characteristics at the nanoscale (conjugate size < 25 nm), polymer therapeutics offer advantages compared to other nanomedicines such as (i) greater ability to cross different biological barriers using different types of cellular trafficking, thus reaching places that other nanocarriers cannot reach and (ii) improve drug pharmacokinetics due to the presence of bio-sensitive chemicals, (iii) greater water solubility, (iv) increase plasma half-life by means of a higher hydrodynamic volume decreasing kidney clearance, (v) protection against proteolytic enzymes, or non-specific cellular uptake, and (vi) prevention or reduction of antigenicity, immunogenicity, and aggregation.

I.6.2. Enhanced Permeability and Retention Effect

The advantages of polymer therapeutics relate to their controllable size and the related macromolecular properties. After intravenous administration, polymer therapeutics can extravasate more selectively at tumor tissues by passive targeting due to increased permeability of blood vessels and lack of lymphatic drainage (due to high IFP caused by increased density in the components of the ECM). Most nanomedicines in the clinics rely on passive targeting effect provided by this so-called enhanced permeability and retention (EPR) effect [229], first described by Matsumura and Maeda in 1986 [232]. This effect allows more considerable passive accumulation in the tumor and retains macromolecules in the tumor tissues compared to free drugs, thus improving therapeutic efficacy [231, 233]. Nanomedicines with a Mw between 40-800 KDa and 20-200nm show a predisposition to accumulate in the tumor via the EPR effect [230], while the associated longer blood half-lives also promote tumor uptake (**Figure 18**) [231]. Furthermore, for the development nanomedicines, various physicochemical properties such as surface loading, size, and size distribution need to be considered because these properties can affect the EPR effect [234].

However, there exist limitations to the EPR effect [235], including the significant heterogeneity in patients with the same disease or between different cancer types, which them promotes different nanomedicine distribution profiles [236, 237].

However, strategies also exist to potentiate the EPR effect to boost the therapeutic outcomes of nanomedicine; these include pharmacological strategies to modulate vessel permeabilization, vessel normalization, vessel disruption or vessel promotion, and physical strategies, including hyperthermia, radiotherapy, sonoporation, and phototherapy [235].

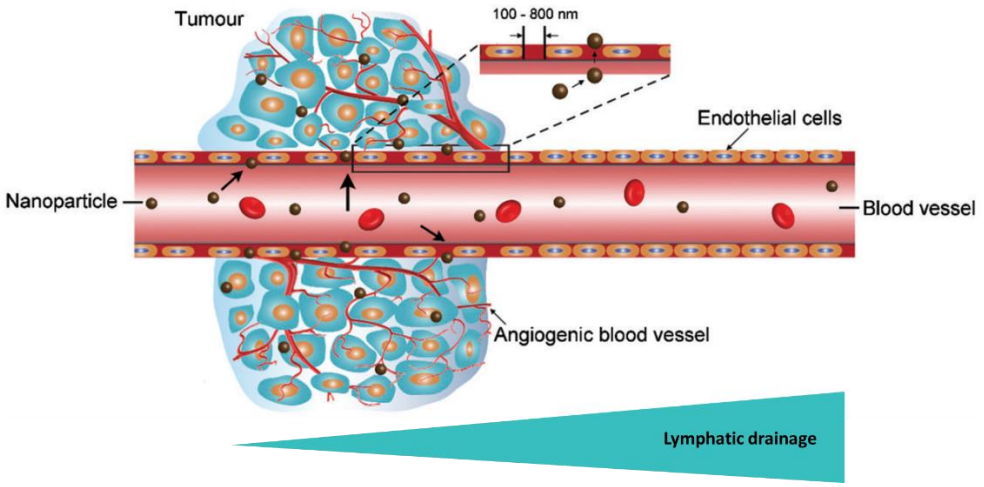

Figure 18: Passive Targeting via the Enhanced Permeability and Retention Effect. Due to deficient lymphatic drainage and the space between endothelial cells present in the tumor vasculature, nanomedicines can preferentially accumulate in the tumor. Nanoparticles must be >5 nm in size to avoid rapid renal filtration by increasing blood circulation time and <200nm to be able to extravasate the vasculature. *Modified from* [230].

I.6.3. Intracellular Trafficking of Polymer Therapeutics

After tumor accumulation, endocytotic mechanisms control the intracellular journey of polymer therapeutics into the tumor cell. The endocytosis of polymer therapeutics can occur via clathrin/caveolin-dependent and/or -independent vesicular pathways or by macropinocytosis. Of note, the endocytic pathways employed by a given polymer therapeutic will be differ based in individual characteristics, with the lysosomotropic route and the endosomotropic route having particularly relevance (**Figure 19**) [238].

The design of *polymer-protein conjugates* for clinical use aims for increased protein blood circulation time by improving serum stability and protection against immune clearance or proteolytic degradation, without the need for intracellular release. However, the design of the polymer-protein conjugate should aim for

endosomotropic transport given a requirement for intracellular trafficking of proteins or peptides [215], including the use of biodegradable linkers. In this case, the endocytosed vesicle containing the polymer therapeutic will be transferred to the early endosomes, from where the nanoparticles can be directed to different organelles such as the reticulum endoplasmic, the trans-Golgi network, late endosomes (resulting from early endosome maturation), or the can be recycled by exocytosis. In this endosomotropic transport, the nanoparticles are directed to the late endosomes and will subsequently be released via membrane destabilization produced by the interaction between the nanoparticles with the endosomal membrane, osmotic rupture due to the presence of amines in the nanoparticles, or particle expansion causing a rupture of the endosomal membrane [239], thereby preventing protein degradation in the lysosome.

In contrast, *polymer-drug conjugates* mostly require lysosomotropic intracellular transport, in which the bioactive agent must be protected from proteolytic degradation. In this case, polymer therapeutics are internalized via endocytosis and become directed to the early and late endosomes, and finally to the lysosome, where the presence of proteolytic enzymes (such as cathepsin B) or acidic pH permit drug release from the polymer, by the degradation of the polymer itself or a cleavable linking moiety [240][213]. The lysosomes present ion channels and transmembrane proteins to transport the drug to the cytosol to access the therapeutic target [239].

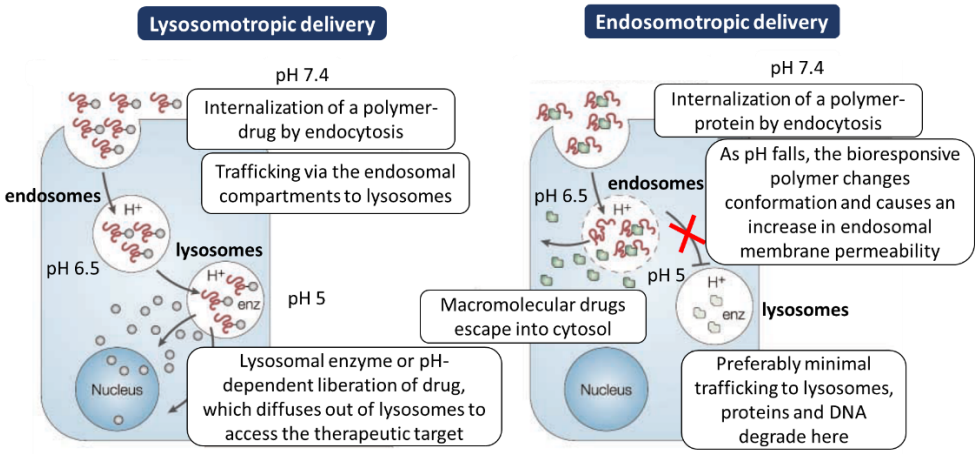

Figure 19: Overview of Lysosomotropic and Endosomotropic Routes Employed for the Delivery of Nanomedicines. Lysosomotropic transport (release through the lysosome) is suitable for bioactive agents protected from proteolytic degradation, while endosomotropic transport (release through the endosome) is preferred for the trafficking of proteins or peptides. *Modified from* [213].

I.6.4. Polymer-based Combination Therapies

The multivalency of polymeric carriers allows the binding of one or more active agents (e.g. a drug) to provide synergistic effects following their site-specific release at a desired ratio. However, there exist four main types of polymer-based combination therapies (**Figure 20**) [241].

I. Type I: polymer-drug conjugate + free drug(s) or a different type of therapy (i.e., radiotherapy), with examples already in the clinic [241]
II. Type II: polymer-drug conjugate + polymer-drug conjugate
III. Type III: Single polymeric carrier carrying a combination of drugs, ensuring the delivery of both drugs to the same cell at the same time, thereby potentiating synergism and therapeutic efficacy
IV. 4. Type IV: Polymer-directed enzyme prodrug therapy (PDEPT) + polymer-enzyme liposome therapy (PELT)

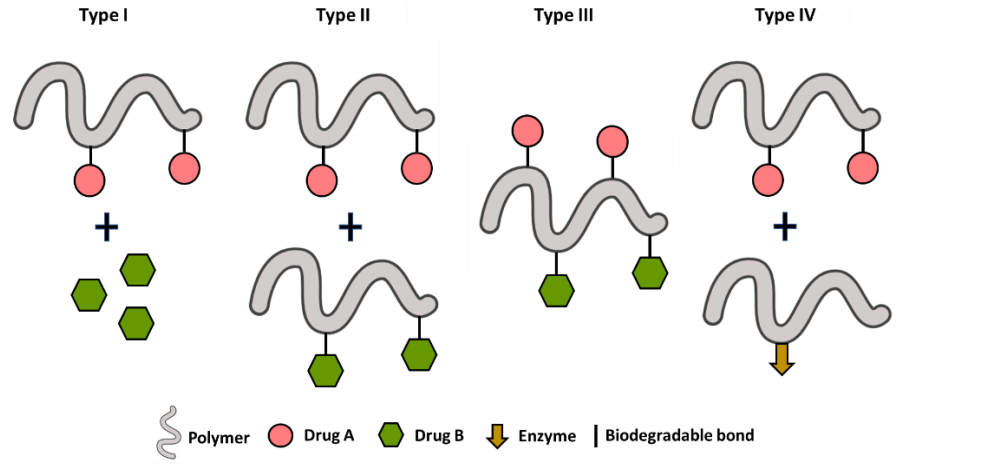

Figure 20: Polymer-based Combination Therapies. *Modified from* [241].

In this thesis, we evaluated a novel treatment strategy based on a polymer-monoclonal antibody polymer conjugate in combination with the free form of a small anti-androgen drug to generate a novel combination therapy. Specifically, we assessed the anti-tumor activity of a PGA-conjugated antibody in combination with abiraterone for the treatment of CRPC (Type I).

However, the overall complexity of the development of combination therapies leads to certain challenges [241], which include:

(i) The identification of optimal drug combinations and ratios for synergistic effects
(ii) The requirement for strict control of drug release kinetics
(iii) The possibility of reduced loading capacity due to steric impediments
(iv) The overall enhanced complexity of the nanosystem due to the incorporation of two different active agents

I.7. Polymer Conjugates as Therapeutics

The translation of polymer conjugation into clinical practice has demonstrated their huge potential in the improvement of patient outcomes. Recent advances in this area, which include biodegradable polymeric backbones and new conjugation chemistries, have driven their application in the treatment of a wide range of conditions.

In this section, we discuss two main polymer conjugate families: polymer-protein and polymer-drug conjugates.

I.7.1. Polymer-protein Conjugates

Abuchowski *et al*. reported the first polymer-protein conjugate (PPC) in 1977, observing altered immunological properties and circulation half-life of bovine serum albumin (BSA) following the covalent attachment of PEG [242, 243]. PEG is a biocompatible polymer that presents singular characteristics, such as higher water solubility, flexible, and neutral charges, suitable for use in the pharmaceutical industry. Through steric repulsions, PEG decreases protein immunogenicity by covering antigenic epitopes [244]. Moreover, steric repulsion avoids protein degradation, improves proteolytic resistance, and inhibits opsonization by the mononuclear phagocyte system. Furthermore, PEG-conjugation increases blood circulation time by reducing renal filtration produced by an increase in hydrodynamic volume and molecular weight. Additionally, PEG-conjugation improves protein solubility, bioavailability, stability, and reduces toxicity [245, 246].

PEGylation of proteins as a strategy has also reached the clinic, with various therapies have approved for the treatment of a range of diseases (**Table 2**) [247]. Adagen®, a PEG-adenosine deaminase conjugate, was approved by the FDA in 1990 for the treatment of patients with severe combined immunodeficiency disease

(SCID), related to a deficiency of the enzyme adenosine deaminase [227]. Other examples include Oncaspar® (PEG-L-asparaginase) for the treatment of lymphoblastic leukemia [248], Mircera® (PEG-epoetin beta) for the treatment of renal anemia in patients with chronic kidney disease, and two new polymer therapeutic proteins marketed in 2018 including Palynziq® (PEG-phenylalanine ammonia lyase) for lower blood levels of phenylalanine and Jivi® (PEG-factor VIII) for the treatment of hemophilia A (**Table 2**) [249].

These promising results prompted the clinical evaluation of various other PEGylated proteins, including nucleic acids, cytokines, enzymes, growth factors, and antibodies (**Table 2**,**3** and **4**). In particular, antibodies and antibody fragments are widely used therapeutic agents, **and in this thesis, we focused on the study of a polymer-antibody conjugate.**

Antibodies, immune proteins known as immunoglobulins, consists of four polypeptides chains comprising two identical heavy chains and two identical light chains, which form a flexible "Y" structure. Each chain possesses a variable region (V) and a constant region (C). The V regions, located at the amino-terminal group of the light and heavy chains, are involved in antigen-binding and vary greatly between different antibodies. In addition, these regions are subdivided into complementary determining regions (CDRs) that directly contact the antigen surface. The C region determines the isotype; in particular, the isotype of the heavy chain determines the functional properties of the antibody. Antibodies are divided into five different classes based on the C region structure - IgM, IgG, IgA, IgD, and IgE. The light chains are bound to heavy chains by covalent interactions through disulfide bonds.

Antibody fragmentation by proteolytic digestion produces antigen-binding fragment (Fab) generated from variable and constant regions, variable fragments (Fv) generated from variable regions, and fragment crystallizable (Fc) generated

from the constant region in the heavy chain. While the Fab and Fv fractions recognize the antigen, the Fc fragments are responsible for complement fixation (**Figure 21**) [250].

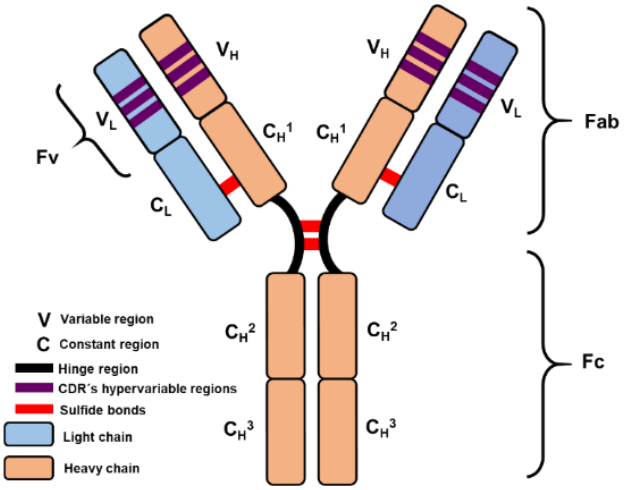

Figure 21: Antibody Structure. Antibodies are composed of two light chains and two heavy chains. Variable regions containing complementary determining regions recognize the antigen, and the constant regions determine the antibody functional properties. Antibody fragmentation generates different fragment regions such as variable fraction, antigen-binding fragment, and crystallizable fragment.

Antibodies are currently used for different applications in which cancer treatment being one of the most explored fields. Regarding polymer-antibody conjugates, the production of antibodies that have been genetically engineered to lack immunogenicity has led to a low number of studies evaluating the PEGylation of antibodies [251, 252]. In addition, the prohibitive cost of antibody production in mammalian cell culture has been replaced by a more economical system based on antibody fragments production such as Fab´s and Fv in microbial systems.

Both the PEGylation of antibodies/antibody fragments have been studied as potential treatments for cancer, with higher tumor accumulation observed; however, the advantages observed, including increased blood circulation time, are greater for antibody fragments [253-256]. Furthermore, their small size, rapid penetration into the tumors, and the lack of Fc region have made PEGylated antibody fragments a focus for basic research and therapeutic applications [246].

Of significant note, the non-biodegradable nature of PEG represents a significant limitation to clinical application. The increase in the molecular weight of PEGylated proteins has a negative effect due to avoid glomerular filtration, moreover, can activate the immune system responses and promote lysosomal storage disease related with the polymer accumulation [257].

New biodegradable alternatives to PEG include polyoxazolidines or polypept(o)ides such as polysarcosines, which can improve pharmacokinetics, and offer new opportunities to develop novel polymer-protein conjugates [258-260].

I.7.2. Polymer-drug Conjugates

Polymer-drug conjugates (PDCs) are macromolecular structures in which one or more therapeutic agents are attached to a polymeric carrier by covalent bonds. Advantages of PDCs include higher solubility, a longer half-life, and a drug release depending on tumor vascularization. The first PDC aiming to improve therapeutic drug efficacy by conjugation to macromolecules was described in 1955 by Von Horst Jatzkewitz [261]; the conjugation of poly(vinylpyrrolidone) to mescaline led to a longer retention time and control of intracellular release [262].

The main components of PDCs are the bioactive agent, a polymer-drug linker, and a water-soluble polymeric carrier [270]. However, multivalent polymers offer the opportunity to conjugate more than one component to the polymeric

backbone allowing, for example, the introduction of targeting residues [271] or more than one drug for combination therapies (**See Section I.6.4**) [227].

Their general success has led to clinical trials of several PDCs, including:

I. Poly(N-hydroxypropyl methacrylamide)-Doxorrubicin (polyHPMA)-Dox, with (PK2) and without (PK1) galactosamine as active residue [271-274]
II. PGA conjugates of paclitaxel (Xyotax™ or Opaxio™) or camptothecin (CT-2106) [275-277]
III. PEG-cyclodextrin-camptothecin nanoparticulated conjugate (CRLX101 or IT-101) [278, 279]
IV. PEG-polypeptide block copolymer conjugated with SN-38 (NK-012), Doxorubicin (NK-911), or Cisplatin (NC-6004) [280-282]

PK1, the first clinically investigated water-soluble PDC, comprises Doxorubicin bound to an HPMA copolymer by a lysosomal cleavable peptidyl linker [213]. In preclinical mice models studies, PK1 showed elevated antitumoral efficacy, with higher tumor accumulation, a better safety profile, and prolonged plasma circulation time compared to unconjugated doxorubicin [283]. After a successful Phase I clinical trial [284] and promising data arising from Phase II, PK1 was discontinued due to economic decisions on behalf of the parent company [285].

Higher molecular weight and the lack of biodegradability in the first generation of PEG and HMPA conjugates produced several limitations related to side product accumulation. To solve this problem, water-soluble, biocompatible, and biodegradable alternatives such as polycarbonates or polypeptides are being explored for further drug conjugation [286, 287]. Additionally, alterations to polymer architecture, molecular weight, and linking chemistry can optimize drug release profiles and enhanced therapeutic efficacy.

PDC marketed include Movantik®, approved by the FDA in 2014 for the treatment of opioid-induced constipation in adult patients with chronic non-oncologic pain (**Table 2**); furthermore, Copaxone® and Neulasta®, which previously reached the top ten best-selling drugs in the USA [288, 289].

Name (company)	Polymer carrier	Drug	Indication(s)	Year approved[a]
Adagen (Enzon Pharmaceuticals)	PEG	ADA	ADA-SCID	1990
SMANCS (Astellas Pharma)	Poly(styrene-co-maleic acid)	Neocarzinostatin	Liver and renal cancer	1993 (Japan)
Oncaspar (Enzon Pharmaceuticals)	PEG	L-asparaginase	Acute lymphoblastic leukemia	1994
PegIntron (Merck & Co.)	PEG	Interferon α2b	Hepatitis C	2001
Pegasys (Genentech)	PEG	Interferon α2a	Hepatitis B and C	2002
Neulasta (Amgen)	PEG	G-CSF	Chemotherapy-induced neutropenia	2002
Somavert (Pfizer)	PEG	HGF receptor antagonist	Acromegaly	2003
Macugen (Baush& Lomb)	PEG	Anti-VEGF aptamer	Neovascular age-related macular degeneration	2004
Mircera (Roche)	PEG	Epoetin beta	Anemia associated with chronic kidney disease	2007

Table 2: Marketed polymer conjugates. *Adapted from* [247].

Name (company)	Polymer carrier	Drug	Indication(s)	Year approved[a]
Cimzia (UCB Pharma)	PEG	Anti-TNF Fab´	Crohn´s disease, rheumatoid arthritis, psoriatic arthritis and ankylosing spondylitis	2008
Krystexxa (Horizon Pharma)	PEG	Uricase	Chronic gout	2010
Plegridy (Biogen)	PEG	Interferon β1a	Relapsing multiple sclerosis	2014
Movantik (AstraZeneca)	PEG	Naloxone	Opioid-induced constipation	2014
Adynovate (Baxalta)	PEG	Factor VIII	Haemophilia A	2015
Palynziq (BioMarin)	PEG	Phenylalanine ammonia lyase	Phenylketonuria	2018
Jivi (Bayer)	PEG	Factor VIII	Haemophilia A	2018

Table 2: Marketed polymer conjugates (continuation). *Adapted from* [247].

Name (company)	Polymer carrier	Drug	Indication(s)	Stage (ClinicalTrials.gov identifier)
Turoctocog alfa pegol (Novo Nordisk)	PEG	Factor VIII	Haemophilia A	Pre-registration (NCT01480180)
Calaspargase pegol (Shire)	PEG	Asparaginase	Acute lymphoblastic leukaemia and lymphoblastic lymphoma	Pre-registration (NCT01574274)
Elapegademase (Leadiant Biosciences)	PEG	ADA	ADA-SCID	Pre-registration (NCT01420627)
Pegvorhyaluronidase alfa (Halozyme Therapeutics)	PEG	Hyaluronidase	Pancreatic cancer	Phase III (NCT02715804)
TransCon Growth Hormone (Ascendis Pharma)	PEG	Human growth hormone	Growth hormone deficiency	Phase III (NCT03444458)
Pegilodecakin (ARMO BioSciences)	PEG	IL-10	Pancreatic cancer	Phase III (NCT02923921)
Pegargiminase (Polaris Pharmaceuticals)	PEG	Arginine deiminase	Mesothelioma	Phase II/III (NCT02709512)
BCT-100(Bio-Cancer Treatment International)	PEG	Arginase 1	Acute myeloid leukemia	Phase II (NCT02899286)
Pegsiticase (Selecta Biosciences)	PEG	Uricase	Chronic gout	Phase II (NCT02959918)
Sanguinate (Prolong Pharmaceuticals)	PEG	Carboxyhaemoglobin	Sickle cell disease	Phase II (NCT02411708)

Table 3: Polymer-protein conjugates in clinical development. *Adapted from* [247].

Name (company)	Polymer carrier	Drug	Indication(s)	Stage (ClinicalTrials.gov identifier)
Pegzilarginase (Aeglea Bio Therapeutics)	PEG	Arginase 1	Arginase 1 deficiency	Phase II (NCT03378531)
BMS-986036 (Bristol-Myers Squibb)	PEG	FGF21	Nonalcoholic steatohepatitis	Phase II (NCT03486899)
Dapirolizumab pegol (UCB Pharma)	PEG	Anti-CD40LFab´	Systemic lupus erythematosus	Phase II (NCT02804763)
Zimura (Ophthothech Corporation)	PEG	Aptamer complement C5 inhibitor	Neovascular age-related macular degeneration	Phase II (NCT03362190)
NKTR-214 (Nektar Therapeutics)	PEG	IL-2	Solid tumors	Phase I/II (NCT02869295)
BIVV001 (Bioverativ Therapeutics)	XTEN	Recombinant factor VIII Fc-von Willebrand factor	Haemophilia A	Phase I/II (NCT03205163)
Olaptesed pegol (NOXXON Pharma)	PEG	Anti-CXCL12 aptamer	Colorectal cancer and pancreatic cancer	Phase I/II (NCT03168139)
Fovista (Ophtotech Corporation)	PEG	Anti-PDGFB aptamer	Ocular von Hippel-Lindau syndrome	Phase I/II (NCT02859441)
BMS-986171 (Bristol-Myers Squibb)	PEG	FGF21	Nonalcoholic steatohepatitis	Phase I (NCT02538874)
NKTR-358 (Nektar Therapeutics)	PEG	IL-2	Systemic lupus erythematous	Phase I (NCT03556007)

Table 3: Polymer-protein conjugates in clinical development (continuation). *Adapted from* [247].

Name (company)	Polymer carrier	Drug	Indication(s)	Stage (ClinicalTrials.gov identifier)
Onzeald (Nektar Therapeutics)	PEG	Irinotecan	Breast cancer	Pre-registration (NCT02915744)
NKTR-181 (Nektar Therapeutics)	PEG	μ-Opioid receptor agonist	Chronic low back pain and chronic non-cancer pain	Pre-registration (NCT03486899)
PEX168 (Jiangsu-Hansoh Pharmaceutical)	PEG	Loxenatide	Type 2 diabetes	Phase II (NCT02367820)
NC-6004 (NanoCarrier)	PEG-b-poly(glutamic acid) micelle	Cisplatin	Pancreatic cancer	Phase III (NCT02477969)
Opaxio (CTI BioPharma)	Polyglutamic acid	Paclitaxel	Ovarian cancer, peritoneal cancer and fallopian tube cancer	Phase III (NCT02043288)
APL-2 (Apellis Pharmaceuticals)	PEG	Cyclic peptide complement C3 inhibitor	Paroxysmal nocturnal haemoglobinuria	Phase III (NCT00108745)
CRLX101(BlueLink Pharmaceuticals)	Cyclodextrin-PEG that self-assembles into nanoparticle	Camptothecin	Ovarian cancer, peritoneal cancer and fallopian tube cancer	Phase II (NCT01652079)
NK012 (Nippon Kayaku)	PEG-b-poly(glutamic acid) micelle	SN-38	Breast cancer	Phase II (NCT00951574)
OsteoDex (Dextech Medical)	Dextran	Alendronate	Prostate cancer	Phase II (NCT02825628)
Somadex (DexTech Medical)	Dextran	Somastostatin	Neuroendocrine tumorus and acromegaly	Phase II (NA)
BP-C1 (Meabco A/S)	Benzo-polycarbonic acid polymer	Pt(II)	Breast cancer	Phase II (NCT02783794)

Table 4: Polymer-drug conjugate. *Adapted from* [247].

Name (company)	Polymer carrier	Drug	Indication(s)	Stage (ClinicalTrials.gov identifier)
Pegcantratinib (Sienna Biopharmaceuticals)	PEG	TrkA inhibitor	Pruritus	Phase II (NCT03322137)
DEP docetaxel (Starpharma)	PEG-polylysine dendrimer	Docetaxel	Solid tumors	Phase II (NA)
NC-6300 (NanoCarrier)	PEG-b-poly(aspartic acid) micelle	Epiribicin	Solid tumors and soft tissue sarcoma	Phase I/II (NCT03168061)
CRLX301 (BlueLink Pharmaceuticals)	Cyclodextrin-PEG that self-assembles into nanoparticles	Docetaxel	Solid tumors	Phase I/II (NCT02380677)
DEP cabazitaxel (Starpharma)	PEG-polylysine dendrimer	Cabacitaxel	Solid tumors	Phase I/II (NA)
NKTR-262 (Nektar Therapuetics)	PEG	TLR7/TLR8 agonist	Solid tumors	Phase I/II (NCT03435640)
CriPec docetaxel (Cristal Therapeutics)	Core-crosslinked PEG-polymer micelle	Docetaxel	Solid tumors	Phase I (NCT02442531)
NC-4016 (NanoCarrier)	PEG-b-poly(glutamic acid) micelle	Oxaliplatin	Solid tumors and lymphoma	Phase I (NCT03168035)
RadProtect (Original BioMedicals)	PEG-b-poly(glutamic acid) chelating complex micelle	Amifostine	Acute radiation syndrome	Phase I (NCT02587442)
SER-214 (Serina Therapeutics)	Poly(2-ethyl-2-oxazoline)	Rotigotine	Parkinson disease	Phase I (NCT02579473)
DFP-13318 (ProLynx)	PEG	SN-38	Solid tumors	Phase I (NCT02646852)

Table 4: Polymer-drug conjugate (continuation). *Adapted from* [247].

Another separate field of research is based on using targeted polymers -antibodies- with small molecules conjugates as a therapeutic agent in order to direct the drug to a specific target. In 1958, *Mathé et al* conjugated for the first time drugs to immunoglobulins, known as antibody-drug conjugates (ADCs), establishing the first platform for PDCs. Specifically, there are four ADCs approved by the FDA highlighting Gemtuzumab ozogamicin (Mylotarg™) to treat acute myeloid leukemia [263], trastuzumab emtansine (Kadcyla™) to treat breast cancer [264], brentuximab vedotin (Adcetris®) for adult patients with Hodgkin´s lymphoma (HL) [265] and Inotuzumab ozogamicin (Besponsa™) for acute lymphoblastic leukemia [266], additionally approximately 50 are in clinical trials [267]. Ringsdorf, in 1975, conceptualized the development of biocompatible polymers as efficient drug carriers, causing a switch in the field of PDCs [268, 269].

Combining advantages of both PDCs and ADCs strategies the therapeutic potential can be increased [290-293]. Antibody-targeted polymer-drug conjugates provide better pharmacokinetics and bioavailability, improving therapeutic effectiveness compared to ADCs [294, 295]. In this way, the dosage of the drug administered is reduced, decreasing side effects and improving therapeutic specificity in the target cell [294, 295].

Doxorubicin is one of the most commonly used chemotherapeutic agents in antibody-targeted PDCs [291]. Several studies have demonstrated benefits both *in vivo* and *in vitro*, providing higher specificity, reduced drug toxicity, increased survival, and inhibition of tumor growth compared to non-targeted PDCs [292].

I.8. Polypeptide-Based Conjugates as Therapeutics

Polyamino acids (PAA or polypeptide) present notable biocompatibility and biodegradability mimicking natural proteins, which has promoted their exploration as a therapeutic strategy [296-298]. The increase in the number of polypeptide-based conjugates evaluated in preclinical and clinical trials demonstrate the applicability of polypeptide-based materials for drug delivery [297].

Polypeptide-based conjugates have been applied in numerous areas of medicine, including the elaboration of anti-microbial [299, 300], anti-cancer [301, 302], anti-virus [303], anti-apoptotic [301], anti-diabetic [304], and anti-tuberculosis drugs [304], as well as magnetic resonance imaging agents [305], and theragnostic agents [306]. Furthermore, polypeptides also present advantages due to their structural versatility, which allows the formation of multiple architectures with different physicochemical features (loading, polarity, and hydrophilicity).

Several features should be considered for the design of a polypeptide-based drug conjugate including (i) the structural elements (matrix, linker, drug nature, ligand pattern, and surface modification), (ii) the physico-chemical properties (size, charge, conformation, geometry, and topology), and (iii) the biological barriers previously explained (**See Section I.5.1**).

Moreover, the selection of the adequate administration route, the cellular target, the tumor environment, and the dosing schedule are required to obtain a successful translation of a drug delivery system and achieve an optimal therapeutic response [307, 308].

I.9. Bibliography

1. Bray, F., et al., *Global Cancer Statistics 2018: GLOBOCAN Estimates of Incidence and Mortality Worldwide for 36 Cancers in 185 Countries: Global Cancer Statistics 2018.* CA: A Cancer Journal for Clinicians, 2018. **68**(6): p. 394-424.
2. Siegel, R.L., K.D. Miller, and A. Jemal, *Cancer statistics, 2018.* CA: A Cancer Journal for Clinicians, 2018. **68**(1): p. 7-30.
3. Bray, F., et al., *Global Cancer Statistics 2018: GLOBOCAN Estimates of Incidence and Mortality Worldwide for 36 Cancers in 185 Countries: Global Cancer Statistics 2018.* CA: A Cancer Journal for Clinicians, 2018. **68**(6): p. 394-424.
4. DeSantis, C.E., et al., *Cancer statistics for African Americans, 2016: Progress and opportunities in reducing racial disparities.* CA: A Cancer Journal for Clinicians, 2016. **66**(4): p. 290-308.
5. Asmane, I., et al., *New Strategies for Medical Management of Castration-Resistant Prostate Cancer.* Oncology, 2011. **80**(1-2): p. 1-11.
6. Zhang, D., et al., *Stem cell and neurogenic gene-expression profiles link prostate basal cells to aggressive prostate cancer.* Nature Communications, 2016. **7**: p. 10798-10798.
7. Mora, L.B., et al., *Prostate Adenocarcinoma: Cellular and Molecular Abnormalities.* Cancer Control, 2001. **8**(6): p. 551-561.
8. Packer, J.R. and N.J. Maitland, *The molecular and cellular origin of human prostate cancer.* Biochimica et Biophysica Acta (BBA) - Molecular Cell Research, 2016. **1863**(6, Part A): p. 1238-1260.
9. Sfanos, K.S., et al., *The inflammatory microenvironment and microbiome in prostate cancer development.* Nature Reviews Urology, 2017. **15**: p. 11.
10. Rybak, A.P., R.G. Bristow, and A. Kapoor, *Prostate cancer stem cells: deciphering the origins and pathways involved in prostate tumorigenesis and aggression.* Oncotarget, 2015. **6**(4): p. 1900-1919.
11. Knudsen, B.S. and V. Vasioukhin, *Chapter 1 - Mechanisms of Prostate Cancer Initiation and Progression*, in *Advances in Cancer Research*, G.F. Vande Woude and G. Klein, Editors. 2010, Academic Press. p. 1-50.
12. Shah, R.B. and M. Zhou, *Recent advances in prostate cancer pathology: Gleason grading and beyond.* Pathology International, 2016. **66**(5): p. 260-272.

13. Gleason, D.F., *Histologic grading of prostate cancer: A perspective.* Human Pathology, 1992. **23**(3): p. 273-279.
14. Miyahira, A., et al., *Tumor cell heterogeneity and resistance; report from the 2018 Coffey-Holden Prostate Cancer Academy Meeting.* The Prostate, 2018. **79**(3): p. 244-258.
15. Abida, W., et al., *Genomic correlates of clinical outcome in advanced prostate cancer.* Proceedings of the National Academy of Sciences, 2019. **116** (23): p. 11428-11436.
16. Koo, K., et al., *Merging new-age biomarkers and nanodiagnostics for precision prostate cancer management.* Nature Reviews Urology, 2019. **16** (5): p. 302-317.
17. Gjertson, C. and P. Albertsen, *Use and Assessment of PSA in Prostate Cancer.* The Medical Clinics of North America, 2011. **95** (1): p. 191-200.
18. Tabayoyong, W. and R. Abouassaly, *Prostate Cancer Screening and the Associated Controversy.* Surgical Clinics of North America, 2015. **95** (5): p. 1023-39.
19. Pinsky, P., P. Prorok, and B. Kramer, *Prostate Cancer Screening - A Perspective on the Current State of the Evidence.* New England Journal of Medicine, 2017. **376** (13): p. 1285-1289.
20. Wedge, D., et al., *Sequencing of prostate cancers identifies new cancer genes, routes of progression and drug targets.* Nature Genetics, 2018. **50** (5): p. 682-692.
21. Lemos, A.E.G., et al., *The long non-coding RNA PCA3: an update of its functions and clinical applications as a biomarker in prostate cancer.* Oncotarget, 2019. **10**(61): p. 6589-6603.
22. Chua, M.L.K., et al., *A Prostate Cancer "Nimbosus": Genomic Instability and SChLAP1 Dysregulation Underpin Aggression of Intraductal and Cribriform Subpathologies.* European Urology, 2017. **72**(5): p. 665-674.
23. Scher, H.I., et al., *Assessment of the Validity of Nuclear-Localized Androgen Receptor Splice Variant 7 in Circulating Tumor Cells as a Predictive Biomarker for Castration-Resistant Prostate Cancer.* JAMA Oncology, 2018. **4**(9): p. 1179-1186.
24. Lotan, T.L., et al., *PTEN loss detection in prostate cancer: comparison of PTEN immunohistochemistry and PTEN FISH in a large retrospective prostatectomy cohort.* Oncotarget, 2017. **8**(39): p. 65566-65576.

25. Song, C. and H. Chen, *Predictive significance of TMRPSS2-ERG fusion in prostate cancer: A meta-analysis.* Cancer Cell International, 2018. **18**: p. 177.
26. Day, J.R., et al., *PCA3: From basic molecular science to the clinical lab.* Cancer Letters, 2011. **301**(1): p. 1-6.
27. Bussemakers, M.J.G., et al., *DD3:A New Prostate-specific Gene, Highly Overexpressed in Prostate Cancer.* Cancer Research, 1999. **59**(23): p. 5975.
28. Yang, Z., L. Yu, and Z. Wang, *PCA3 and TMPRSS2-ERG gene fusions as diagnostic biomarkers for prostate cancer.* Chinese Journal of Cancer Research, 2016. **28**(1): p. 65-71.
29. Ferreira, L.B., et al., *PCA3 noncoding RNA is involved in the control of prostate-cancer cell survival and modulates androgen receptor signaling.* BMC Cancer, 2012. **12**: p. 507-507.
30. Prensner, J.R., et al., *Beyond PSA: the next generation of prostate cancer biomarkers.* Science Translational Medicine, 2012. **4**(127): p. 127-127.
31. Mehra, R., et al., *Overexpression of the Long Non-coding RNA SChLAP1 Independently Predicts Lethal Prostate Cancer.* European Urology, 2016. **70**(4): p. 549-552.
32. Yin, C., et al., *Molecular Profiling of Pooled Circulating Tumor Cells from Prostate Cancer Patients Using a Dual-Antibody-Functionalized Microfluidic Device.* Analytical Chemistry, 2018. **90**(6): p. 3744-3751.
33. Ware, K.E., et al., *Biologic and clinical significance of androgen receptor variants in castration resistant prostate cancer.* Endocrine-Related Cancer, 2014. **21**(4): p. 87-103.
34. Wise, Helen M., Miguel A. Hermida, and Nicholas R. Leslie, *Prostate cancer, PI3K, PTEN and prognosis.* Clinical Science, 2017. **131**(3): p. 197.
35. Barbieri, C.E., et al., *The mutational landscape of prostate cancer.* European Urology, 2013. **64**(4): p. 567-576.
36. Yoshimoto, M., et al., *Absence of TMPRSS2:ERG fusions and PTEN losses in prostate cancer is associated with a favorable outcome.* Modern Pathology, 2008. **21**(12): p. 1451-1460.
37. Edwards, P., *Fusion genes and chromosome translocations in the common epithelial cancers.* The Journal of Pathology, 2009. **220** (2): p. 244-54.
38. Flajollet, S., et al., *Abnormal Expression of the ERG Transcription Factor in Prostate Cancer Cells Activates Osteopontin.* Molecular Cancer Research, 2011. **9**(7): p. 914-24.

39. Linn, D., et al., *Deletion of Interstitial Genes between TMPRSS2 and ERG Promotes Prostate Cancer Progression.* Cancer Research, 2016. **76**(7): p. 1869-1881.
40. Mani, R., et al., *Inflammation-Induced Oxidative Stress Mediates Gene Fusion Formation in Prostate Cancer.* Cell Reports, 2016. **17**(10): p. 2620-2631.
41. Adamo, P. and M. Ladomery, *The oncogene ERG: A key factor in prostate cancer.* Oncogene, 2015. **35**(4): p. 403-414.
42. Fernández-Serra, A., et al., *Molecular characterization and clinical impact of TMPRSS2-ERG rearrangement on prostate cancer: Comparison between FISH and RT-PCR.* BioMed Research International, 2013. **2013**: p. 465179.
43. Lucas, J., et al., *The Androgen-Regulated Protease TMPRSS2 Activates a Proteolytic Cascade Involving Components of the Tumor Microenvironment and Promotes Prostate Cancer Metastasis.* Cancer Discovery, 2014. **4**(11): p. 1310-1325.
44. Ryan, C., et al., *Inhibitory effects of nordihydroguaiaretic acid (NDGA) on the IGF-1 receptor and androgen dependent growth of LAPC-4 prostate cancer cells.* The Prostate, 2008. **68**(11): p. 1232-40.
45. Wu, J. and E. Yu, *Insulin-like growth factor receptor-1 (IGF-IR) as a target for prostate cancer therapy.* Cancer Metastasis Reviews, 2014. **33**(2-3): p. 607-617.
46. Iams, W.T. and C.M. Lovly, *Molecular Pathways: Clinical Applications and Future Direction of Insulin-like Growth Factor-1 Receptor Pathway Blockade.* Clinical Cancer Research, 2015. **21**(19): p. 4270-4277.
47. Pollak, M., *Insulin and insulin-like growth factor signalling in neoplasia.* Nature Reviews Cancer, 2008. **8**(12): p. 915-928.
48. Favelyukis, S., et al., *Structure and autoregulation of the insulin-like growth factor 1 receptor kinase.* Nature Structural Biology, 2001. **8**(12): p. 1058-1063.
49. Khandwala, H.M., et al., *The Effects of Insulin-Like Growth Factors on Tumorigenesis and Neoplastic Growth.* Endocrine Reviews, 2000. **21**(3): p. 215-244.
50. Haisa, M., *The type 1 insulin-like growth factor receptor signalling system and targeted tyrosine kinase inhibition in cancer.* Journal of International Medical Research, 2013. **41**(2): p. 253-264.

51. Mendoza, M.C., E.E. Er, and J. Blenis, *The Ras-ERK and PI3K-mTOR pathways: cross-talk and compensation.* Trends in Biochemical Sciences, 2011. **36**(6): p. 320-328.
52. Crudden, C., et al., *Below the Surface: IGF-1R Therapeutic Targeting and Its Endocytic Journey.* Cells, 2019. **8**(10): p. 1223.
53. Packham, S., et al., *Nuclear translocation of IGF-1R via p150Glued and an importin-β/RanBP2-dependent pathway in cancer cells.* Oncogene, 2015. **34**(17): p. 2227-2238.
54. Sehat, B., et al., *SUMOylation Mediates the Nuclear Translocation and Signaling of the IGF-1 Receptor.* Science Signaling, 2010. **3**(108): p. 10.
55. Kenneth, S., *Signalling by insulin and IGF receptors: supporting acts and new players.* Journal of Molecular Endocrinology, 2011. **47**(1): p. 1-10.
56. Martins, A.S., et al., *IGF1R signaling in Ewing sarcoma is shaped by clathrin-/caveolin-dependent endocytosis.* PLoS One, 2011. **6**(5): p. 19846.
57. Salani, B., et al., *IGF-IR internalizes with Caveolin-1 and PTRF/Cavin in HaCat cells.* PLoS One, 2010. **5**(11): p. 14157.
58. Chen, J., et al., *Regulation of insulin receptor substrate-1 expression levels by caveolin-1.* Journal of Cellular Physiology, 2008. **217**(1): p. 281-289.
59. Mellinghoff, I., et al., *Mellinghoff IK, Vivanco I, Kwon A, Tran C, Wongvipat J, CLHER2/neu kinase-dependent modulation of androgen receptor function through effects on DNA binding and stability.* Cancer Cell, 2004. **6**(5): p. 517-27.
60. Wang, Y., J. Kreisberg, and P. Ghosh, *Cross-talk between the androgen receptor and the phosphatidylinositol 3-kinase/Akt pathway in prostate cancer.* Current Cancer Drug Targets, 2007. **7**(6): p. 591-604.
61. Carver, B., et al., *Reciprocal Feedback Regulation of PI3K and Androgen Receptor Signaling in PTEN-Deficient Prostate Cancer.* Cancer Cell, 2011. **19**(5): p. 575-86.
62. Liao, Y., et al., *Up-regulation of insulin-like growth factor axis components in human primary prostate cancer correlates with tumor grade.* Human Pathology, 2005. **36**(11): p. 1186-1196.
63. Mancarella, C., et al., *ERG deregulation induces IGF-1R expression in prostate cancer cells and affects sensitivity to anti-IGF-1R agents.* Oncotarget, 2015. **6**(18): p. 16611-16622.
64. Beltran, H., et al., *New Therapies for Castration-Resistant Prostate Cancer: Efficacy and Safety.* European Urology, 2011. **60**(2): p. 279-290.

65. Pagliarulo, V., et al., *Contemporary Role of Androgen Deprivation Therapy for Prostate Cancer.* European Urology, 2012. **61**(1): p. 11-25.
66. Quigley, D.A., et al., *Genomic Hallmarks and Structural Variation in Metastatic Prostate Cancer.* Cell, 2018. **174**(3): p. 758-769.
67. Robinson, D., et al., *Integrative clinical genomics of advanced prostate cancer.* Cell, 2015. **161**(5): p. 1215-1228.
68. Taylor, B., et al., *Integrative Genomic Profiling of Human Prostate Cancer.* Cancer Cell, 2010. **18**(1): p. 11-22.
69. Chandrasekar, T., et al., *Mechanisms of resistance in castration-resistant prostate cancer (CRPC).* Translational Andrology and Urology, 2015. **4**(3): p. 365-380.
70. Maughan, B.L. and E.S. Antonarakis, *Androgen pathway resistance in prostate cancer and therapeutic implications.* Expert Opinion on Pharmacotherapy, 2015. **16**(10): p. 1521-1537.
71. Davey, R.A. and M. Grossmann, *Androgen Receptor Structure, Function and Biology: From Bench to Bedside.* The Clinical Biochemist. Reviews, 2016. **37**(1): p. 3-15.
72. Hoang, D.T., et al., *Androgen receptor-dependent and -independent mechanisms driving prostate cancer progression: Opportunities for therapeutic targeting from multiple angles.* Oncotarget, 2017. **8**(2): p. 3724-3745.
73. Olson, B.M., et al., *Prostate Cancer Cells Express More Androgen Receptor (AR) Following Androgen Deprivation, Improving Recognition by AR-Specific T Cells.* Cancer Immunology Research, 2017. **5**(12): p. 1074-1085.
74. Bubendorf, L., et al., *Survey of Gene Amplifications during Prostate Cancer Progression by High-Throughput Fluorescence in Situ Hybridization on Tissue Microarrays.* Cancer Research, 1999. **59**(4): p. 803.
75. Carlsson, A., et al., *Paired High-Content Analysis of Prostate Cancer Cells in Bone Marrow and Blood Characterizes Increased Androgen Receptor Expression in Tumor Cell Clusters.* Clinical Cancer Research, 2017. **23**(7): p. 1722-1732.
76. Rathkopf, D.E., et al., *Androgen receptor mutations in patients with castration-resistant prostate cancer treated with apalutamide.* Annals of Oncology, 2017. **28**(9): p. 2264-2271.
77. Tan, M.H.E., et al., *Androgen receptor: structure, role in prostate cancer and drug discovery.* Acta Pharmacologica Sinica, 2015. **36**(1): p. 3-23.

78. Prekovic, S., et al., *The Effect of F877L and T878A Mutations on Androgen Receptor Response to Enzalutamide.* Molecular Cancer Therapeutics, 2016. **15**(7): p. 1702.
79. He, Y., et al., *Androgen receptor splice variants bind to constitutively open chromatin and promote abiraterone-resistant growth of prostate cancer.* Nucleic Acids Research, 2018. **46**(4): p. 1895-1911.
80. Uo, T., et al., *Systematic and functional characterization of novel androgen receptor variants arising from alternative splicing in the ligand-binding domain.* Oncogene, 2017. **36**(10): p. 1440-1450.
81. Li, H., et al., *Androgen-receptor splice variant-7-positive prostate cancer: a novel molecular subtype with markedly worse androgen-deprivation therapy outcomes in newly diagnosed patients.* Modern Pathology, 2018. **31**(1): p. 198-208.
82. Linja, M.J., et al., *Expression of Androgen Receptor Coregulators in Prostate Cancer.* Clinical Cancer Research, 2004. **10**(3): p. 1032.
83. Groner, A.C., M. Brown, and J.-P. Theurillat, *Targeting transcriptional co-activators in advanced prostate cancer.* Cell Cycle, 2016. **15**(24): p. 3333-3334.
84. Burd, C., L. Morey, and K. Knudsen, *Androgen receptor corepressors and prostate cancer.* Endocrine-Related Cancer, 2007. **13**: p. 979-94.
85. Kumagai, J., et al., *Intratumoral conversion of adrenal androgen precursors drives androgen receptor-activated cell growth in prostate cancer more potently than de novo steroidogenesis.* The Prostate, 2013. **73**(15): p. 1636-1650.
86. Knuuttila, M., et al., *Castration Induces Up-Regulation of Intratumoral Androgen Biosynthesis and Androgen Receptor Expression in an Orthotopic VCaP Human Prostate Cancer Xenograft Model.* The American Journal of Pathology, 2014. **184**(8): p. 2163-2173.
87. Wu, Y., et al., *Adrenal androgens rescue prostatic dihydrotestosterone production and growth of prostate cancer cells after castration.* Molecular and Cellular Endocrinology, 2019. **486**: p. 79-88.
88. Chang, K.-H., et al., *Dihydrotestosterone synthesis bypasses testosterone to drive castration-resistant prostate cancer.* PNAS, 2011. **108**(33): p. 13728-13733.

89. Fiandalo, M.V., et al., *Inhibition of dihydrotestosterone synthesis in prostate cancer by combined frontdoor and backdoor pathway blockade.* Oncotarget, 2018. **9**(13): p. 11227-11242.
90. Hoang, D.T., et al., *Androgen receptor-dependent and -independent mechanisms driving prostate cancer progression: Opportunities for therapeutic targeting from multiple angles.* Oncotarget, 2016. **8**(2): p.3724-3745.
91. Chang, L., et al., *Targeting PI3K/Akt/mTOR signaling pathway in the treatment of prostate cancer radioresistance.* Critical Reviews in Oncology/Hematology, 2015. **96**(3): p. 507-517.
92. Statz, C.M., S.E. Patterson, and S.M. Mockus, *mTOR Inhibitors in Castration-Resistant Prostate Cancer: A Systematic Review.* Targeted Oncology, 2017. **12**(1): p. 47-59.
93. Wiencke, J.K., et al., *Methylation of the PTEN promoter defines low-grade gliomas and secondary glioblastoma.* Neuro-Oncology, 2007. **9**(3): p. 271-279.
94. Silva, A., et al., *PTEN posttranslational inactivation and hyperactivation of the PI3K/Akt pathway sustain primary T cell leukemia viability.* The Journal of Clinical Investigation, 2008. **118**(11): p. 3762-3774.
95. Molina, J.R., et al., *Loss of PTEN binding adapter protein NHERF1 from plasma membrane in glioblastoma contributes to PTEN inactivation.* Cancer Research, 2010. **70**(17): p. 6697-6703.
96. Chalhoub, N. and S.J. Baker, *PTEN and the PI3-kinase pathway in cancer.* Annual Review of Pathology, 2009. **4**: p. 127-150.
97. Yue, S., et al., *Cholesteryl Ester Accumulation Induced by PTEN Loss and PI3K/AKT Activation Underlies Human Prostate Cancer Aggressiveness.* Cell Metabolism, 2014. **19**(3): p. 393-406.
98. Varkaris, A., et al., *Src signaling pathways in prostate cancer.* Cancer Metastasis Reviews, 2014. **33**(2-3): p. 595-606.
99. Hu, Z., et al., *Acute Mechanical Stretch Promotes eNOS Activation in Venous Endothelial Cells Mainly via PKA and Akt Pathways.* PLoS One, 2013. **8**(8): p. 71359.
100. Huang, Y.-H., et al., *Interleukin-6 Induces Vascular Endothelial Growth Factor-C Expression via Src-FAK-STAT3 Signaling in Lymphatic Endothelial Cells.* PLoS One, 2016. **11**(7): p. 0158839.

101. Inoue, K., et al., *Interleukin 8 Expression Regulates Tumorigenicity and Metastases in Androgen-independent Prostate Cancer.* Clinical Cancer Research, 2000. **6**(5): p. 2104.
102. Jin, R., et al., *Activation of NF-kappa B signaling promotes growth of prostate cancer cells in bone.* PLoS One, 2013. **8**(4): p. 60983.
103. Thomas, C., et al., *Synergistic Targeting of PI3K/AKT Pathway and Androgen Receptor Axis Significantly Delays Castration-Resistant Prostate Cancer Progression In Vivo.* Molecular Cancer Therapeutics, 2013. **12**(11): p. 2342.
104. Bluemn, E.G., et al., *Androgen Receptor Pathway-Independent Prostate Cancer Is Sustained through FGF Signaling.* Cancer Cell, 2017. **32**(4): p. 474-489.
105. Sayeed, A., et al., *Insulin-like growth factor 1 stimulation of androgen receptor activity requires β(1A) integrins.* Journal of Cellular Physiology, 2012. **227**(2): p. 751-758.
106. Handle, F., et al., *The STAT3 Inhibitor Galiellalactone Reduces IL6-Mediated AR Activity in Benign and Malignant Prostate Models.* Molecular Cancer Therapeutics, 2018. **17**(12): p. 2722.
107. Zhu, M.-L. and N. Kyprianou, *Androgen receptor and growth factor signaling cross-talk in prostate cancer cells.* Endocrine-Related Cancer, 2008. **15**(4): p. 841-849.
108. Coons, L.A., et al., *DNA Sequence Constraints Define Functionally Active Steroid Nuclear Receptor Binding Sites in Chromatin.* Endocrinology, 2017. **158**(10): p. 3212-3234.
109. Hirayama, Y. and M.D. Sadar, *Does increased expression of glucocorticoid receptor support application of antagonists to this receptor for the treatment of castration resistant prostate cancer?.* AME Medical Journal, 2018. **3**: p. 66.
110. Grindstad, T., et al., *Progesterone Receptors in Prostate Cancer: Progesterone receptor B is the isoform associated with disease progression.* Scientific Reports, 2018. **8**: p. 11358.
111. Chen, R., Y. Yu, and X. Dong, *Progesterone receptor in the prostate: A potential suppressor for benign prostatic hyperplasia and prostate cancer.* The Journal of Steroid Biochemistry and Molecular Biology, 2017. **166**: p. 91-96.

112. Puhr, M., et al., *The Glucocorticoid Receptor Is a Key Player for Prostate Cancer Cell Survival and a Target for Improved Antiandrogen Therapy.* Clinical Cancer Research, 2018. **24**(4): p. 927.
113. Attard, G. and J. de Bono, *Translating Scientific Advancement into Clinical Benefit for Castration-Resistant Prostate Cancer Patients.* Clinical Cancer Research, 2011. **17**(12): p. 3867-75.
114. Reid, A., et al., *CYP17 inhibition as a hormonal strategy for prostate cancer.* Nature Clinical Practice. Urology, 2008. **5**: p. 610-20.
115. Bianchini, D., et al., *Antitumour activity of enzalutamide (MDV3100) in patients with metastatic castration-resistant prostate cancer (CRPC) pre-treated with docetaxel and abiraterone.* European Journal of Cancer, 2014. **50**(1): p. 78-84.
116. Aschenbrenner, D., *FDA Approves First Treatment for Nonmetastatic, Castration-Resistant Prostate Cancer.* American Journal of Nursing, 2018. **118**(6): p. 26.
117. Calvo, O., et al., *Metastatic castration-resistant prostate cancer: Changing landscape with cabazitaxel.* Anti-Cancer Drugs, 2013. **25**(3): p.237-243.
118. Francini, E. and C. Sweeney, *Docetaxel Activity in the Era of Life-prolonging Hormonal Therapies for Metastatic Castration-resistant Prostate Cancer.* European Urology, 2016. **70**(3): p. 410-412.
119. Tsao, C.-K., et al., *The role of cabazitaxel in the treatment of metastatic castration-resistant prostate cancer.* Therapeutic Advances in Urology, 2014. **6**(3): p. 97-104.
120. Darshan, M.S., et al., *Taxane-induced blockade to nuclear accumulation of the androgen receptor predicts clinical responses in metastatic prostate cancer.* Cancer Research, 2011. **71**(18): p. 6019-6029.
121. Sumanasuriya, S. and J. de Bono, *Treatment of Advanced Prostate Cancer—A Review of Current Therapies and Future Promise.* Cold Spring Harbor Perspectives in Medicine, 2017. **8**(6): p. 030635.
122. Handy, C.E. and E.S. Antonarakis, *Sipuleucel-T for the treatment of prostate cancer: novel insights and future directions.* Future Oncology, 2018. **14**(10): p. 907-917.
123. Nevedomskaya, E., S.J. Baumgart, and B. Haendler, *Recent Advances in Prostate Cancer Treatment and Drug Discovery.* International Journal of Molecular Sciences, 2018. **19**(5): p. 1359.

124. Kluetz, P., et al., *Radium Ra 223 Dichloride Injection: US Food and Drug Administration Drug Approval Summary.* Clinical Cancer Research, 2013. **20**(1): p. 9-14.
125. Parker, C.C., et al., *A Randomized, Double-Blind, Dose-Finding, Multicenter, Phase 2 Study of Radium Chloride (Ra 223) in Patients with Bone Metastases and Castration-Resistant Prostate Cancer.* European Urology, 2013. **63**(2): p. 189-197.
126. Kim, I.E., Jr., et al., *Similar incidence of DNA damage response pathway alterations between clinically localized and metastatic prostate cancer.* BMC Urology, 2019. **19**(1): p. 33-33.
127. Oh, M., et al., *The association of BRCA1 and BRCA2 mutations with prostate cancer risk, frequency, and mortality: A meta-analysis.* The Prostate, 2019. **79**(8): p. 880-895.
128. Schweizer, M. and E. Antonarakis, *Prognostic and therapeutic implications of DNA repair gene mutations in advanced prostate cancer.* Clinical Advances in Hematology and Oncology, 2017. **15**(10): p. 785-795.
129. Virtanen, V., et al., *PARP Inhibitors in Prostate Cancer—The Preclinical Rationale and Current Clinical Development.* Genes, 2019. **10**(8): p. 565.
130. Przybycinski, J., et al., *Poly-ADP-ribose polymerases (PARPs) as a therapeutic target in the treatment of selected cancers.* Expert Opinion on Therapeutic Targets, 2019. **23**(9): p. 773-785.
131. Martin, G.A., A.H. Chen, and K. Parikh, *A Novel Use of Olaparib for the Treatment of Metastatic Castration-Recurrent Prostate Cancer.* Pharmacotherapy: The Journal of Human Pharmacology and Drug Therapy, 2017. **37**(11): p. 1406-1414.
132. Yin, L., et al., *PARP inhibitor veliparib and HDAC inhibitor SAHA synergistically co-target the UHRF1/BRCA1 DNA damage repair complex in prostate cancer cells.* Journal of Experimental & Clinical Cancer Research, 2018. **37**(1): p. 153-153.
133. Smith, M.R., et al., *Phase II study of niraparib in patients with metastatic castration-resistant prostate cancer (mCRPC) and biallelic DNA-repair gene defects (DRD): Preliminary results of GALAHAD.* Journal of Clinical Oncology, 2019. **37**(7_suppl): p. 202-202.
134. Kossatz, S., et al., *Direct Imaging of Drug Distribution and Target Engagement of the PARP Inhibitor Rucaparib.* Journal of Nuclear Medicine, 2018. **59**(8): p. 1316-1320.

135. Delongchamps, N., M. Peyromaure, and A.T. Dinh-Xuan, *Role of vascular endothelial growth factor in prostate cancer.* Urology, 2006. **68**(2): p. 244-8.
136. Ziyad, S. and L. Iruela-Arispe, *Molecular Mechanisms of Tumor Angiogenesis.* Genes & Cancer, 2011. **2**(12): p. 1085-1096.
137. Akl, M., et al., *Molecular and clinical significance of fibroblast growth factor 2 (FGF2 /bFGF) in malignancies of solid and hematological cancers for personalized therapies.* Oncotarget, 2016. **7**(28): p. 44735-44762.
138. Lee, C., et al., *Dual targeting c-met and VEGFR2 in osteoblasts suppresses growth and osteolysis of prostate cancer bone metastasis.* Cancer Letters, 2017. **414**: p. 205-213.
139. Kerbel, R.S., *Tumor angiogenesis.* NEJM, 2008. **358**(19): p. 2039-2049.
140. Green, M.M.L., et al., *Expression of vascular endothelial growth factor (VEGF) in locally invasive prostate cancer is prognostic for radiotherapy outcome.* International Journal of Radiation Oncology Biology Physics, 2007. **67**(1): p. 84-90.
141. Siveen, K., et al., *Vascular Endothelial Growth Factor (VEGF) Signaling in Tumour Vascularization: Potential and Challenges.* Current Vascular Pharmacology, 2017. **15**(4): p. 339-351.
142. Gille, H., et al., *Functional characterization of a VEGF-A-targeting Anticalin, prototype of a novel therapeutic human protein class.* Angiogenesis, 2015. **19**(1): p. 79-94.
143. Tannock, I., et al., *Aflibercept versus placebo in combination with docetaxel and prednisone for treatment of men with metastatic castration-resistant prostate cancer (VENICE): A phase 3, double-blind randomised trial.* The Lancet Oncology, 2013. **14**(8): p. 760-768.
144. Diaz, R., et al., *Sunitinib reduces tumor hypoxia and angiogenesis, and radiosensitizes prostate cancer stem-like cells: Sunitinib Reduces Tumor Hypoxia and Angiogenesis.* The Prostate, 2015. **75**(11): p. 1137-1149.
145. Vogelzang, N., et al., *Circulating Tumor Cells in a Phase 3 Study of Docetaxel and Prednisone with or without Lenalidomide in Metastatic Castration-resistant Prostate Cancer.* European Urology, 2016. **71**(2): p. 168-171.
146. Michaelson, M.D., et al., *Randomized, Placebo-Controlled, Phase III Trial of Sunitinib Plus Prednisone Versus Prednisone Alone in Progressive, Metastatic, Castration-Resistant Prostate Cancer.* Journal of Clinical Oncology, 2013. **32**(2): p. 76-82.

147. Joshi, G., et al., *Growth factors mediated cell signalling in prostate cancer progression: Implications in discovery of anti-prostate cancer agents.* Chemico-Biological Interactions, 2015. **240**: p. 120-133.
148. Nabhan, C., et al., *Novel approaches and future directions in castration-resistant prostate cancer.* Annals of Oncology, 2011. **22**(9): p. 1948-57.
149. Li, R., A. Pourpak, and S. Morris, *ChemInform Abstract: Inhibition of the Insulin-Like Growth Factor-1 Receptor (IGF1R) Tyrosine Kinase as a Novel Cancer Therapy Approach.* Journal of Medicinal Chemistry, 2009. **52**(16): p. 4981-5004.
150. Cao, H., et al., *Combinational Therapy Enhances the Effects of Anti-IGF-1R mAb Figitumumab to Target Small Cell Lung Cancer.* PLoS One, 2015. **10**(8): p. 0135844-0135844.
151. Oza, A., et al., *Phase 2 study evaluating intermittent and continuous linsitinib and weekly paclitaxel in patients with recurrent platinum resistant ovarian epithelial cancer.* Gynecologic Oncology, 2018. **149**(2): p. 275-282.
152. Barata, P., et al., *A phase 2 study of OSI-906 (linsitinib, an insulin-like growth factor receptor-1 inhibitor) in patients with asymptomatic or mildly symptomatic (non-opioid requiring) metastatic castrate resistant prostate cancer (CRPC).* Investigational New Drugs, 2018. **36**(3): p. 451-457.
153. Friedbichler, K., et al., *Pharmacodynamic and Antineoplastic Activity of BI 836845, a Fully Human IGF Ligand-Neutralizing Antibody, and Mechanistic Rationale for Combination with Rapamycin.* Molecular Cancer Therapeutics, 2013. **13**(2): p. 399-409.
154. Hussain, S., et al., *Targeting IGF-1/2 with xentuzumab (Xe) plus enzalutamide (En) in metastatic castration-resistant prostate cancer (mCRPC) after progression on docetaxel chemotherapy (DCt) and abiraterone (Abi): Randomized phase II trial results.* Journal of Clinical Oncology, 2019. **37**: p. 5030.
155. King, H., et al., *Can we unlock the potential of IGF-1R inhibition in cancer therapy?*. Cancer Treatment Reviews, 2014. **40**(9): p. 1096-1105.
156. Slaaby, R., *Specific insulin/IGF1 hybrid receptor activation assay reveals IGF1 as a more potent ligand than insulin.* Scientific Reports, 2015. **5**: p. 7911.
157. Crudden, C., A. Girnita, and L. Girnita, *Targeting the IGF-1R: The Tale of the Tortoise and the Hare.* Frontiers in Endocrinology, 2015. **6**: p. 64.

158. Qu, X., et al., *Update of IGF-1 receptor inhibitor (Ganitumab, Dalotuzumab, Cixutumumab, Teprotumumab and Figitumumab) effects on cancer therapy.* Oncotarget, 2015. **8**(17): p. 29501-29518.
159. Beltran, P., et al., *AMG 479, a fully human anti-insulin-like growth factor receptor type I monoclonal antibody, inhibits the growth and survival of pancreatic carcinoma cells.* Molecular Cancer Therapeutics, 2009. **8**(5): p. 1095-105.
160. Vlahovic, G., et al., *A Phase I Trial of the IGF-1R Antibody Ganitumab (AMG 479) in Combination with Everolimus (RAD001) and Panitumumab in Patients with Advanced Cancer.* The Oncologist, 2018. **23**(7): p. 2016-0377.
161. Zhang, T., et al., *Antitumor effects and molecular mechanisms of figitumumab, a humanized monoclonal antibody to IGF-1 receptor, in esophageal carcinoma.* Scientific Reports, 2014. **4**: p. 6855.
162. Chi, K.N., et al., *A Phase II Pharmacodynamic Study of Preoperative Figitumumab in Patients with Localized Prostate Cancer.* Clinical Cancer Research, 2012. **18**(12): p. 3407.
163. Dean, J.P., et al., *Response of the insulin-like growth factor (IGF) system to IGF-IR inhibition and androgen deprivation in a neoadjuvant prostate cancer trial: effects of obesity and androgen deprivation.* The Journal of Clinical Endocrinology and Metabolism, 2013. **98**(5): p. 820-828.
164. Kobayashi, H., R. Watanabe, and P.L. Choyke, *Improving conventional enhanced permeability and retention (EPR) effects; what is the appropriate target?* Theranostics, 2013. **4**(1): p. 81-89.
165. Arruebo, M., et al., *Assessment of the evolution of cancer treatment therapies.* Cancers, 2011. **3**(3): p. 3279-3330.
166. Kaliberov, S.A. and D.J. Buchsbaum, *Chapter seven--Cancer treatment with gene therapy and radiation therapy.* Advances in Cancer Research, 2012. **115**: p. 221-263.
167. Ram, P.D., et al., *Passive and Active Drug Targeting: Role of Nanocarriers in Rational Design of Anticancer Formulations.* Current Pharmaceutical Design, 2019. **25**(28): p. 1-23.
168. Maeda, H., *Polymer therapeutics and the EPR effect.* Journal of Drug Targeting, 2017. **25**(9-10): p. 781-785.
169. Danhier, F., *To exploit the tumor microenvironment: Since the EPR effect fails in the clinic, what is the future of nanomedicine?.* Journal of Controlled Release, 2016. **244**: p. 108-121.

170. Wicki, A., et al., *Nanomedicine in cancer therapy: Challenges, opportunities, and clinical applications.* Journal of Controlled Release, 2015. **200**: p. 138-157.
171. Duncan, R. and R. Gaspar, *Nanomedicine(s) under the Microscope.* Molecular Pharmaceutics, 2011. **8**(6): p. 2101-2141.
172. He, H., et al., *Survey of Clinical Translation of Cancer Nanomedicines—Lessons Learned from Successes and Failures.* Accounts of Chemical Research, 2019. **52**(9): p. 2445-2461.
173. Tolcher, A.W. and L.D. Mayer, *Improving combination cancer therapy: the CombiPlex® development platform.* Future Oncology, 2018. **14**(13): p. 1317-1332.
174. Lehr, C.-M., *Biological barriers and nanomedicine – Timely challenges in advanced drug delivery research.* European Journal of Pharmaceutics and Biopharmaceutics, 2009. **72**(2): p. 287-288.
175. Zagorodko, O., et al., *Polypeptide-Based Conjugates as Therapeutics: Opportunities and Challenges.* Macromolecular Bioscience, 2017. **17**(1): p. 1600316.
176. Markiewski, M.M., et al., *Modulation of the antitumor immune response by complement.* Nature Immunology, 2008. **9**(11): p. 1225-1235.
177. Ikeda, Y. and Y. Nagasaki, *PEGylation Technology in Nanomedicine*. Advances in Polymer Science, 2011. **247**(1): p.115-140.
178. Fang, L., et al., *Pharmacokinetics of pegylated liposomal doxorubicin in Chinese tumor patients.* Chinese Pharmaceutical Journal, 2012. **47**(3): p. 223-228.
179. Barclay, A. and T. van den Berg, *The Interaction Between Signal Regulatory Protein Alpha (SIRP α) and CD47: Structure, Function, and Therapeutic Target.* Annual Review of Immunology, 2013. **32**: p. 25-50.
180. Tamai, I. and A. Tsuji, *Transporter-Mediated Permeation of Drugs Across the Blood-Brain Barrier.* Journal of Pharmaceutical Sciences, 2000. **89**(11): p. 1371-1388.
181. Duro-Castano, A., et al., *Capturing "Extraordinary" Soft-Assembled Charge-Like Polypeptides as a Strategy for Nanocarrier Design.* Advanced Materials, 2017. **29**(39): p. 1702888.
182. Tsai, C.-H., et al., *Ocular Drug Delivery: Role of Degradable Polymeric Nanocarriers for Ophthalmic Application.* International Journal of Molecular Sciences, 2018. **19**(9): p. 2830.

183. Himawan, E., et al., *Drug delivery to retinal photoreceptors.* Drug Discovery Today, 2019. **24**(8): p. 1637-1643.
184. Chen, H., et al., *Effective Delivery of Male Contraceptives Behind the Blood-Testis Barrier (BTB)-Lesson from Adjudin.* Current Medicinal Chemistry, 2016. **23**(7): p. 701-713.
185. Valkenburg, K.C., A.E. de Groot, and K.J. Pienta, *Targeting the tumour stroma to improve cancer therapy.* Nature reviews. Clinical Oncology, 2018. **15**(6): p. 366-381.
186. Josson, S., et al., *Tumor–stroma co-evolution in prostate cancer progression and metastasis.* Seminars in Cell & Developmental Biology, 2010. **21**(1): p. 26-32.
187. Roncador, A., et al., *Use of polymer conjugates for the intraperoxisomal delivery of engineered human alanine:glyoxylate aminotransferase as a protein therapy for primary hyperoxaluria type I.* Nanomedicine: Nanotechnology, Biology and Medicine, 2017. **13**(3): p. 897-907.
188. Parodi, A., et al., *Enabling cytoplasmic delivery and organelle targeting by surface modification of nanocarriers.* Nanomedicine, 2015. **10**(12): p. 1923-1940.
189. Wang, J., et al., *More Effective Nanomedicines through Particle Design.* Small, 2011. **7**(14): p. 1919-1931.
190. Kobayashi, H., *Pharmacokinetics and clearance properties of nano-sized particles and molecules as multi-modality imaging agents: Considerations and caveats.* Technical Proceedings of the 2011 NSTI Nanotechnology Conference, 2011. **3**: p. 125-128.
191. Liu, J., et al., *Renal clearable inorganic nanoparticles: A new frontier of bionanotechnology.* Materials Today, 2013. **16**: p. 477–486.
192. Wu, W., et al., *Endogenous pH-Responsive Nanoparticles with programmable size change for Targeting Tumor Therapy and Imaging Applications.* Theranostics, 2018. **8**(11): p.3038-3058.
193. Aravindsiva, S. and K. Kamalasanan, *Nanomedicine for prostate cancer using nanoemulsion: A review.* Journal of Controlled Release, 2017. **260**: p. 111-123.
194. Lakshmanan, V.-K., *Therapeutic efficacy of nanomedicines for prostate cancer: An update.* Investigative and Clinical Urology, 2016. **57**(1): p. 21-29.

195. Ji, C., et al., *Activatable Photodynamic Therapy for Prostate Cancer by NIR Dye/Photosensitizer Loaded Albumin Nanoparticles.* Journal of Biomedical Nanotechnology, 2019. **15**(2): p. 311-318.
196. Wüstemann, T., et al., *Targeting prostate cancer: Prostate-specific membrane antigen based diagnosis and therapy.* Medicinal Research Reviews, 2017. **39**(1): p. 40-69.
197. Huang, C.-J., et al., *Integrated microfluidic system for rapid screening of CRP aptamers utilizing systematic evolution of ligands by exponential enrichment (SELEX).* Biosensors & Bioelectronics, 2010. **25**(7): p. 1761-1766.
198. Chen, Z., et al., *Aptamer-mediated Delivery of Docetaxel to Prostate Cancer through Polymeric Nanoparticles for Enhancement of Antitumor Efficacy.* European Journal of Pharmaceutics and Biopharmaceutics, 2016. **107**: p. 130-141.
199. Hrkach, J., et al., *Preclinical Development and Clinical Translation of a PSMA-Targeted Docetaxel Nanoparticle with a Differentiated Pharmacological Profile.* Science Translational Medicine, 2012. **4**(128): p. 128-139.
200. Von Hoff, D., et al., *Phase I Study of PSMA-Targeted Docetaxel-Containing Nanoparticle BIND-014 in Patients with Advanced Solid Tumors.* Clinical Cancer Research, 2016. **22**(13): p. 3157-3163.
201. Autio, K.A., et al., *Safety and Efficacy of BIND-014, a Docetaxel Nanoparticle Targeting Prostate-Specific Membrane Antigen for Patients with Metastatic Castration-Resistant Prostate Cancer: A Phase 2 Clinical Trial.* JAMA Oncology, 2018. **4**(10): p. 1344-1351.
202. Zagami, R., et al., *Folate-Decorated Amphiphilic Cyclodextrins as Cell-Targeted Nanophototherapeutics.* Biomacromolecules, 2019. **20**(7): p. 2530-2544.
203. Rahme, K., J. Guo, and J. Holmes, *Bioconjugated Gold Nanoparticles Enhance siRNA Delivery in Prostate Cancer Cells*. Methods Molecular Biology, 2019. **1974**: p. 291-301.
204. Miyake, H., et al., *Interaction between CD44 and hyaluronic acid regulates human prostate cancer development.* The Journal of Urology, 1998. **160**(4): p. 1562-6.
205. Spadea, A., et al., *Evaluating the Efficiency of Hyaluronic Acid for Tumor Targeting via CD44.* Molecular Pharmaceutics, 2019. **16**(6): p. 2481-2493.

206. Bharali, D., et al., *Anti-CD24 Nano-targeted Delivery of Docetaxel for the Treatment of Prostate Cancer.* Nanomedicine: Nanotechnology, Biology and Medicine, 2016. **13**.
207. Liu, J., et al., *Bisphosphonates in the Treatment of Patients with Metastatic Breast, Lung, and Prostate Cancer: A Meta-Analysis.* Medicine, 2015. **94**(46): p. 2014.
208. Holmberg, A., et al., *Development of a novel poly bisphosphonate conjugate for treatment of skeletal metastasis and osteoporosis.* International Journal of Oncology, 2010. **37**(3): p. 563-567.
209. Meurling, L., et al., *Polymer-conjugated guanidine is a potentially useful anti-tumor agent.* International Journal of Oncology, 2009. **35**(2): p. 281-285.
210. Farrell, K.B., et al., *Bisphosphonate conjugation for bone specific drug targeting.* Bone Reports, 2018. **9**: p. 47-60.
211. Gupta, S., et al., *Current prospects and challenges of nanomedicine delivery in prostate cancer therapy.* Nanomedicine, 2017. **12**(23): p. 2675-2692.
212. Duncan, R., *Polymer therapeutics as nanomedicines: New perspectives.* Current Opinion in Biotechnology, 2011. **22**(4): p. 492-501.
213. Duncan, R., *The dawning era of polymer.* Nature reviews. Drug discovery, 2003. **2**(5): p. 347-360.
214. Canal, F., J. Sanchis, and M. Vicent, *Polymer-drug conjugates as nano-sized medicines.* Current Opinion in Biotechnology, 2011. **22**(6): p. 894-900.
215. Vicent, M. and R. Duncan, *Polymer conjugates: Nanosized medicines for treating cancer.* Trends in Biotechnology, 2006. **24**(1): p. 39-47.
216. Duncan, R. and R. Gaspar, *Nanomedicine(s) under the Microscope.* Molecular Pharmaceutics, 2011. **8**(6): p. 2101-2141.
217. Petros, R. and J. DeSimone, *Strategies in the design of nanoparticles for therapeutic applications.* Nature Reviews Drug Discovery, 2010. **9**(8): p. 615-627.
218. Duncan, R., *Polymer therapeutics: Top 10 selling pharmaceuticals — What next?*. Journal of Controlled Release, 2014. **190**: p. 371-380.
219. Kopeček, J., *Polymer-drug conjugates: Origins, progress to date and future directions.* Advanced Drug Delivery Reviews, 2012. **65**(1): p. 49-59.
220. Feng, Q. and R. Tong, *Anticancer Nanoparticulate Polymer-Drug Conjugate.* Bioengineering & Translational Medicine, 2016. **1**(3): p.277-296.

221. Grover, G. and H. Maynard, *Protein-Polymer Conjugates: Synthetic Approaches by Controlled Radical Polymerizations & Interesting Applications.* Current Opinion in Chemical Biology, 2010. **14**(6): p. 818-827.
222. Qi, Y. and A. Chilkoti, *Protein-Polymer Conjugation—Moving Beyond PEGylation.* Current Opinion in Chemical Biology, 2015. **28**: p. 181-193.
223. Li, J., et al., *Polymeric drugs: Advances in the development of pharmacologically active polymers.* Journal of Controlled Release, 2015. **219**: p. 369-382.
224. Yang, Y., et al., *Biodegradable and Amphiphilic Block Copolymer–Doxorubicin Conjugate as Polymeric Nanoscale Drug Delivery Vehicle for Breast Cancer Therapy.* Biomaterials, 2013. **34**: p. 8430-8443.
225. Li, N., et al., *Amphiphilic peptide dendritic copolymer-doxorubicin nanoscale conjugate self-assembled to enzyme-responsive anti-cancer agent.* Biomaterials, 2014. **35**(35): p. 9529-9545.
226. Kulasingam, V. and E. Diamandis, *Strategies for discovering novel cancer biomarkers through utilization of emerging technologies.* Nature Clinical Practice. Oncology, 2008. **5**(10): p. 588-599.
227. Duncan, R. and M. Vicent, *Polymer Therapeutics-Prospects for 21st Century: The End of the Beginning.* Advanced Drug Delivery Reviews, 2012. **65**(1): p.60-70.
228. Duro Castaño, A., et al., *Well-Defined Star-Shaped Polyglutamates with Improved Pharmacokinetic Profiles as Excellent Candidates for Biomedical Applications.* Molecular Pharmaceutics, 2015. **12**(10): p. 3639-3649.
229. Maeda, H., *Polymer therapeutics and the EPR effect.* Journal of Drug Targeting, 2017. **25**(9-10): p. 781-785.
230. Dai, Y., et al., *Nanoparticle design strategies for enhanced anticancer therapy by exploiting the tumour microenvironment.* Chemical Society Reviews, 2017. **46**(12): p. 3830-3852.
231. Duncan, R., et al., *Polymer-drug conjugates: Towards a novel approach for the treatment of endrocine-related cancer.* Endocrine-Related Cancer, 2005. **12 Suppl 1**: p. 189-199.
232. Matsumura, Y. and H. Maeda, *A new concept for macromolecular therapeutics in cancer chemotherapy: Mechanism of tumoritropic accumulation of proteins and the antitumor agent SMANCS.* Cancer Research, 1986. **25**: p. 865-869.

233. Vicent, M., H. Ringsdorf, and R. Duncan, *Polymer therapeutics: Clinical applications and challenges for development.* Advanced Drug Delivery Reviews, 2009. **61**(13): p. 1117-1120.
234. Bor, G., I. Azmi, and A. Yaghmur, *Nanomedicines for cancer therapy: Current status, challenges and future prospects.* Therapeutic Delivery, 2018. **10**(2): p. 113-132.
235. Ojha, T., et al., *Pharmacological and Physical Vessel Modulation Strategies to Improve EPR-mediated Drug Targeting to Tumors.* Advanced Drug Delivery Reviews, 2017. **119**: p. 40-60.
236. Prabhakar, U., et al., *Challenges and Key Considerations of the Enhanced Permeability and Retention Effect for Nanomedicine Drug Delivery in Oncology.* Cancer Research, 2013. **73**(8): p. 2412-2417.
237. Lammers, T., et al., *Drug targeting to tumors: Principles, pitfalls and (pre-) clinical progress.* Journal of Controlled Release, 2011. **161**(2): p. 175-187.
238. Duncan, R., E. Ferguson, and S. Deacon, *Polymer therapeutics as anticancer nanomedicines.* Journal of Pharmacy and Pharmacology, 2009. **61**: p. 147.
239. Patel, S., et al., *Brief update on endocytosis of nanomedicines.* Advanced Drug Delivery Reviews, 2019. **144**: p. 90-111.
240. El-Sayed, M., A. Hoffman, and P. Stayton, *El-Sayed, ME, Hoffman, AS and Stayton, PS. Smart polymeric carriers for enhanced intracellular delivery of therapeutic macromolecules. Expert Opinion on Biological Therapy 5: 23-32.* Expert Opinion on Biological Therapy, 2005. **5**: p. 23-32.
241. Greco, F. and M. Vicent, *Combination therapy: Opportunities and challenges for polymer–drug conjugates as anticancer nanomedicines.* Advanced Drug Delivery Reviews, 2009. **61**(13): p. 1203-1213.
242. Abuchowski, A., et al., *Effect of covalent attachment of polyethylene glycol on immunogenicity and circulating life of bovine liver catalase.* The Journal of Biological Chemistry, 1977. **252**(11): p. 3582-3586.
243. Davis, F., et al., *Enzyme-Polyethylene Glycol Adducts: Modified Enzymes with Unique Properties*, 1978. p. 169-173.
244. Caliceti, P. and F. Veronese, *Pharmacokinetic and biodistribution properties of poly(ethylene glycol)-protein conjugates.* Advanced Drug Delivery Reviews, 2003. **55**: p. 1261-77.
245. Veronese, F.M. and G. Pasut, *PEGylation, successful approach to drug delivery.* Drug Discovery Today, 2005. **10**(21): p. 1451-1458.

246. Chapman, A., *Chapman, A.P. PEGylated antibodies and antibody fragments for improved therapy: a review.* Advanced Drug Delivery Reviews, 2002. **54**: p. 531-45.
247. Ekladious, I., Y. Colson, and M. Grinstaff, *Polymer–drug conjugate therapeutics: advances, insights and prospects.* Nature Reviews Drug Discovery, 2018. **18**(4): p. 273-294.
248. Dinndorf, P., et al., *FDA Drug Approval Summary: Pegaspargase (Oncaspar(R)) for the First-Line Treatment of Children with Acute Lymphoblastic Leukemia (ALL).* The Oncologist, 2007. **12**: p. 991-998.
249. Palmer, S., et al., *Erythropoiesis-stimulating agents for anaemia in adults with chronic kidney disease: a network meta-analysis.* The Cochrane Database of Systematic Reviews, 2014. **12**: p. CD010590.
250. Cymer, F., et al., *Therapeutic monoclonal antibody N-glycosylation – Structure, function and therapeutic potential.* Biologicals, 2018. **52**: p. 1-11.
251. Rathore, A., A. Sarker, and R. Gupta, *Recent Developments Toward Antibody Engineering and Affinity Maturation.* Protein & Peptide Letters, 2018. **25**(10): p. 886-896.
252. Waldmann, H., *Human Monoclonal Antibodies: The Benefits of Humanization. Methods and Protocols*, 2019. **1904**: p. 1-10.
253. Kitamura, K., et al., *Polyethylene glycol modification of the monoclonal antibody A7 enhances its tumor localization.* Biochemical and Biophysical Research Communications, 1990. **171**: p. 1387-1394.
254. Otsuji, E., et al., *Applicability of monoclonal antibody Fab fragments as a carrier of neocarzinostatin in targeting chemotherapy.* Journal of Surgical Oncology, 1996. **61**: p. 149-154.
255. Pedley, R.B., et al., *Comparative radioimmunotherapy using intact or F(ab')2 fragments of 131I anti-CEA antibody in a colonic xenograft model.* British Journal of Cancer, 1993. **68**(1): p. 69-73.
256. Humm, J., L. Chin, and R. Macklis, *F(ab')2 fragments versus intact antibody--an isodose comparison.* Journal of Nuclear Medicine, 1990. **31**: p. 1045-107.
257. Turecek, P., et al., *PEGylation of Biopharmaceuticals: A Review of Chemistry and Nonclinical Safety Information of Approved Drugs.* Journal of Pharmaceutical Sciences, 2016. **105**: p. 460-475.

258. Gao, W., et al., *In situ growth of a PEG-like polymer from the C terminus of an intein fusion protein improves pharmacokinetics and tumor accumulation.* PNAS, 2010. **107**: p. 16432-16437.
259. Gao, W., et al., *In situ growth of a stoichiometric PEG-like conjugate at a protein's N-terminus with significantly improved pharmacokinetics.* PNAS, 2009. **106**(36): p. 15231-15236.
260. Steinbach, T. and F. Wurm, *Degradable Polyphosphoester-Protein Conjugates: "PPEylation" of Proteins.* Biomacromolecules, 2016. **17** (10): p. 3338-3346.
261. Jatzkewitz, H., *Peptamin (glycyl-L-leucyl-mescaline) bound to blood plasma expander (polyvinylpyrrolidone) as a new depot form of a biologically active primary amine (mescaline).* Zeitschrift für Naturforschung, 1955. **10**: p. 27-31.
262. Kopecek, J., *Biomaterials and drug delivery: past, present, and future.* Molecular Pharmaceutics, 2010. **7**(4): p. 922-925.
263. Illangeswaran, R.S., et al., *A personalized approach to acute myeloid leukemia therapy: current options.* Pharmacogenomics and Personalized Medicine, 2019. **12**: p. 167-179.
264. Hurvitz, S., et al., *Neoadjuvant trastuzumab, pertuzumab, and chemotherapy versus trastuzumab emtansine plus pertuzumab in patients with HER2-positive breast cancer (KRISTINE): A randomised, open-label, multicentre, phase 3 trial.* The Lancet Oncology, 2017. **19**(1): p. 115-126.
265. Fukuhara, N., et al., *Retreatment with brentuximab vedotin in patients with relapsed/refractory classical Hodgkin lymphoma or systemic anaplastic large-cell lymphoma: a multicenter retrospective study.* Leukemia & Lymphoma, 2020. **61**(1): p. 176-180.
266. Hoelzer, D., *Targeted therapy with monoclonal antibodies in acute lymphoblastic leukemia.* Current Opinion in Oncology, 2013. **25**(6): p. 701-706.
267. Dan, N., et al., *Antibody Drug Conjugates for Cancer Therapy Chemistry to Clinical Implications.* Pharmaceuticals, 2018. **11**(2). p. E32.
268. Ringsdorf, H., *Structure and properties of pharmacologically active polymers.* Journal of Polymer Science: Polymer Symposia, 1975. **51**(1): p. 135-153.
269. Duncan, R., H. Ringsdorf, and R. Satchi-Fainaro, *Polymer therapeutics: Polymers as drugs, drug and protein conjugates and gene delivery systems:*

Past, present and future opportunities. Journal of Drug Targeting, 2006. **14**: p. 337-41.

270. Ringsdorf, H., *Ringsdorf, H.: Structure and properties of pharmacologically active polymers.* Journal of Polymer Science: Polymer Symposia, 2007. **51**: p. 135-153.
271. Seymour, L., et al., *Hepatic Drug Targeting: Phase I Evaluation of Polymer-Bound Doxorubicin.* Journal of Clinical Oncology, 2002. **20**: p. 1668-1676.
272. Duncan, R., *Biological effects of soluble synthetic polymers as drug carriers.* Critical Reviews in Therapeutic Drug Carrier Systems, 1985. **1**: p. 281-310.
273. Kopeček, J., et al., *HPMA copolymer-anticancer drug conjugates: Design, activity, and mechanism of action.* European Journal of Pharmaceutics and Biopharmaceutics, 2000. **50**: p. 61–81.
274. Seymour, L., et al., *Phase II studies of polymer-doxorubicin (PK1, FCE28068) in the treatment of breast, lung and colorectal cancer.* International Journal of Oncology, 2009. **34**: p. 1629-36.
275. Li, C., et al., *Complete Regression of Well-established Tumors Using a Novel Water-soluble Poly(L-Glutamic Acid)-Paclitaxel Conjugate.* Cancer Research, 1998. **58**(11): p. 2404.
276. Singer, J., *Paclitaxel poliglumex (XYOTAX™, CT-2103): a macromolecular taxane.* Journal of Controlled Release, 2006. **109**: p. 120-6.
277. Homsi, J., et al., *Phase I Trial of Poly-L-Glutamate Camptothecin (CT-2106) Administered Weekly in Patients with Advanced Solid Malignancies.* Clinical Cancer Research, 2007. **13**: p. 5855-61.
278. Davis, M., *Design and development of IT-101, a cyclodextrin-containing polymer conjugate of camptothecin.* Advanced Drug Delivery Reviews, 2009. **61**: p. 1189-92.
279. Pham, E., et al., *Translational Impact of Nanoparticle-Drug Conjugate CRLX101 with or without Bevacizumab in Advanced Ovarian Cancer.* Clinical Cancer Research, 2014. **21**(4): p. 808-18.
280. Cabral, H. and K. Kataoka, *Progress of drug-loaded polymeric micelles into clinical studies.* Journal of Controlled Release, 2014. **190**: p. 465-476.
281. Koizumi, F., et al., *Novel SN-38–Incorporating Polymeric Micelles, NK012, Eradicate Vascular Endothelial Growth Factor–Secreting Bulky Tumors.* Cancer Research, 2006. **66**(20): p. 10048.

282. Uchino, H., et al., *Cisplatin-incorporating polymeric micelles (NC-6004) can reduce nephrotoxicity and neurotoxicity of cisplatin in rats.* British Journal of Cancer, 2005. **93**: p. 678-87.
283. Stirland, D.L., et al., *Mind the gap: a survey of how cancer drug carriers are susceptible to the gap between research and practice.* Journal of Controlled Release, 2013. **172**(3): p. 1045-1064.
284. Vasey, P.A., et al., *Phase I Clinical and Pharmacokinetic Study of PK1 (N-(2-Hydroxypropyl) methacrylamide Copolymer Doxorubicin]: First Member of a New Class of Chemotherapeutic Agents—Drug-Polymer Conjugates.* Clinical Cancer Research, 1999. **5**(1): p. 83.
285. Duncan, R., *Polymer therapeutics at a crossroads? Finding the path for improved translation in the twenty-first century.* Journal of Drug Targeting, 2017. **25**(9-10): p. 759-780.
286. Cho, S., et al., *Functionalizable Hydrophilic Polycarbonate, Poly(5-methyl-5-(2-hydroxypropyl) aminocarbonyl-1,3-dioxan-2-one), Designed as a Degradable Alternative for PHPMA and PEG.* Macromolecules, 2015. **48**(24): p. 8797-8805.
287. Tsai, F.-T., Y. Wang, and D. Darensbourg, *Environmentally Benign CO2-Based Copolymers: Degradable Polycarbonates Derived from Dihydroxybutyric Acid and Their Platinum-Polymer Conjugates.* Journal of the American Chemical Society, 2016. **138**(13): p. 4626-33.
288. Lawson, R., et al., *Cost Effectiveness of Naloxegol for Opioid-Induced Constipation in the UK.* PharmacoEconomics, 2016. **35**(2): p. 225-235.
289. G. Pasut and S. Zalipsky, *PEGylation and polymer conjugation*. Elsevier, 2020. p. 471-472.
290. Pola, R., et al., *Polymer Cancerostatics Targeted by Recombinant Antibody Fragments to GD2-Positive Tumor Cells.* Biomacromolecules, 2018. **20** (1): p. 412-421.
291. Gada, K., et al., *Bispecific antibody complex pre-targeting and targeted delivery of polymer drug conjugates for imaging and therapy in dual human mammary cancer xenografts: Targeted polymer drug conjugates for cancer diagnosis and therapy.* European Journal of Nuclear Medicine and Molecular Imaging, 2014. **41**(8): p. 1603-16.
292. Lidický, O., et al., *Anti-Lymphoma Efficacy Comparison of Anti-CD20 Monoclonal Antibody-Targeted and Non-Targeted Star-Shaped Polymer-Prodrug Conjugates.* Molecules, 2015. **20**: p. 19849-19864.

293. Kopecek, J. and P. Kopecková, *HPMA copolymers: Origins, early developments, present, and future.* Advanced Drug Delivery Reviews, 2009. **62**: p. 122-49.
294. Lane, D., et al., *Well-defined single polymer nanoparticles for the antibody-targeted delivery of chemotherapeutic agents.* Polymer Chemistry, 2014. **6** (8): p. 1286-1299.
295. Ulbrich, K., et al., *Antibody-targeted Polymer–doxorubicin Conjugates with pH-controlled Activation.* Journal of Drug Targeting, 2004. **12**: p. 477-89.
296. Deming, T.J., *Synthetic polypeptides for biomedical applications.* Progress in Polymer Science, 2007. **32**(8): p. 858-875.
297. Conejos-Sanchez, I., A. Duro Castaño, and M. Vicent, *Peptide-Based Polymer Therapeutics.* Polymers, 2014. **6**: p. 515-551.
298. Hehir, S. and N. Cameron, *Recent Advances in Drug Delivery Systems based on Polypeptides Prepared from N-Carboxyanhydrides.* Polymer International, 2014. **63**(6): p.943-954.
299. Engler, A., et al., *Effects of Side Group Functionality and Molecular Weight on the Activity of Synthetic Antimicrobial Polypeptides.* Biomacromolecules, 2011. **12**: p. 1666-74.
300. Cohen, C.R., et al., *A phase I randomized placebo controlled trial of the safety of 3% SPL7013 Gel (VivaGel®) in healthy young women administered twice daily for 14 days.* PLoS One, 2011. **6**(1): p. 16258-16258.
301. Feng, Z., et al., *Poly (γ, L-glutamic acid)-cisplatin bioconjugate exhibits potent antitumor activity with low toxicity: A comparative study with clinically used platinum derivatives.* Cancer Science, 2010. **101**: p. 2476-82.
302. Paz-Ares, L., et al., *Phase III trial comparing paclitaxel poliglumex vs docetaxel in the second-line treatment of non-small-cell lung cancer.* British Journal of Cancer, 2008. **98**: p. 1608-13.
303. Karmaker, S., et al., *A novel drug delivery system for type 1 diabetes: Insulin-mimetic vanadyl-poly(γ-glutamic acid) complex.* Journal of Inorganic Biochemistry, 2006. **100**: p. 1535-46.
304. Vicent, M. and E. Pérez-Payá, *Poly- l -glutamic acid (PGA) Aided Inhibitors of Apoptotic Protease Activating Factor 1 (Apaf-1): An Antiapoptotic Polymeric Nanomedicine.* Journal of Medicinal Chemistry, 2006. **49**: p. 3763-5.

305. Islam, M., et al., *Mucoadhesive Alginate/Poly (L-Lysine)/Thiolated Alginate Microcapsules for Oral Delivery of Lactobacillus Salivarius 29.* Journal of Nanoscience and Nanotechnology, 2011. **11**: p. 7091-5.
306. Xing, T., et al., *Synthesis of polypeptide conjugated with near infrared fluorescence probe and doxorubicin for pH-responsive and image-guided drug delivery.* Journals of Material Chemistry, 2012. **22**: p. 22290-22300.
307. Duncan, R. and L. Izzo, *Dendrimer biocompatibility and toxicity.* Advanced Drug Delivery Reviews, 2006. **57**: p. 2215-37.
308. Dobrovolskaia, M., *Pre-clinical immunotoxicity studies of nanotechnology-formulated drugs: Challenges, considerations and strategy.* Journal of Controlled Release, 2015. **220**: p. 571-583.
309. Zhang, B., Hu, Y. and Pang, Z., *Modulating the tumor microenvironment to enhance tumor nanomedicine delivery*. Frontiers in Pharmacology, 2017. **8**: p. 952.
310. https://www.cancer.net/
311. https://clinicaltrials.gov/

Chapter II

Materials & Methods

II.1. Materials

II.1.1. Chemical and Biological Reagents

Poly-L-glutamic acid (PGA, acid form, 200 glutamic acid units) was purchased from Polypeptide Therapeutics Solutions (PTS, Spain). AVE1642 was provided by Sanofi-Aventis (Bridgewater, New Jersey, USA). N-succinimidyl-S-acetylthiopropionate (SATP), sterile 96-well plates, DharmaFECT® reagent, penicillin/streptomycin (P/S), Nunc™ Lab-Tek™ chamber slides, trypsin-EDTA, and Prostate Specific Antigen (PSA) (Free)/KLK3 Human ELISA Kit were purchased from Thermo Scientific (Waltham, Massachusetts, USA). Vivaspin centrifugal concentrator tubes, protein markers, ECL Prime Western Blotting Detection Reagent, and Hyperfilm™ MP were purchased from GE Healthcare (Chicago, Illinois, USA). Dithiothreitol (DTT), N-hydroxysuccinimide (NHS), fetal bovine serum (FBS), dextran, phenazine methosulfate (PMS), cathepsin B inhibitor CA-074, Insulin-like Growth Factor-I (IGF-1), 4´,6-diamidin-2-phenylindole (DAPI), Bradford reagent, bovine serum albumin (BSA), Evans Blue dye (EB), formamide, sunflower oil, benzyl alcohol, deuterium oxide (D_2O), GLOX solution, glucose, cysteamine, glucose oxidase, catalase, bromophenol blue, Ammonium persulfate (APS), Tetramethylethylenediamine (TEMED), Dimethyl sulfoxide (DMSO) and all other chemicals were purchased from Sigma-Aldrich (St. Louis, Missouri, USA). Anhydrous N,N-dimethylformamide (DMF, ≥99.8% anhydrous) was purchased from Scharlab SL (Sentmenat, Spain). T75 flasks, sterile 24-well plates, 12-well plates, and 6-well plates were provided by Sarstedt (Nümbrecht, Germany). EIA/RIA (ELISA) 96-well plate and white 96-well plates were from Corning Costar® (Corning, New York, USA). Stop solution and 3,3´,5,5´-Tetramethylbenzine (TMB) substrate were purchased from Abcam (Cambridge, UK). Luciferase (Luc2) Lentiviral Vector and Turbo Green Fluorescent Protein (tGFP) were provided by Innoprot (Vizcaya, Spain). Bright-Glo™ Luciferase Assay System and Tetrazolium (MTS) were purchased from

Promega (Madison, Wisconsin, USA). Cyanine 3, cyanine 5, and cyanine 5.5 dyes were purchased from Lumiprobe GmbH (Hannover, Germany). Geneticin (G418) and Sodium Dodecyl Sulfate (SDS) were purchased from Fisher (Loughborough, UK). Abiraterone, Abiraterone Acetate, and Dehydroepiandrosterone 3-acetate (DHEA) were provided by Medchem Express (Monmouth Junction, NJ, USA). siGENOME_siRNA (siERG) and scrambled siGENOME_non-targeting_siRNA (SCR) were purchased from Thermo Scientific (Lafayette, Colorado, USA). Mounting medium and fluorescein-labeled Ricinus communis agglutinin I (FITC-Lectin) were purchased from Vector Laboratories (Burlingame, California, USA). Paraformaldehyde (PFA) was provided by Electron Microscopy Sciences (Hatfield, Pennsylvania, USA). Protease inhibitor cocktail (IC 1X) and phosphatase inhibitor cocktail (PhosSTOP 1X) were purchased from Roche (Basel, Switzerland). Black 96-well plates and XenoLight D-luciferin potassium salt were purchased from Perkin Elmer (Waltham, Massachusetts, USA). Acrylamide/Bisacrylamide was provided by VWR Live Science (Radnor, Pennsylvania, USA). Adhesion microscope slides were purchased from Marienfeld-Superior (Lauda-Königshofen, Germany). Mowiol® 4-88 was provided by Carl Roth (Karlsruhe, Germany). 0.22µm filters were purchased from Jet Biofil (Guangzhou, China). Insulin syringes (29G), absorbable sutures 6/0, and isoflurane were purchased form B. Braun VetCare (Barcelona, Spain). Morphine was provided by B. Braun Medical (Barcelona, Spain). Buprenorphine was purchased from RB Pharmaceuticals Ltd (Benckiser, UK). Reusable straight 20 gauge feeding needles were provided by InterFocus (Linton, UK). Ultrapure water with a resistivity of 18 MΩ.cm was used in all aqueous preparations (Milli-Q® ultrapure).

II.1.2. Cell Lines and Culture Conditions

Table 1 describes the prostate cancer (PCa) cell lines, the growth media used, and the main characteristics of each cell line. Cells were maintained at 37ºC in an atmosphere of 5% carbon dioxide and 95% air and underwent passaging weekly in T75 flasks. The complete medium was changed twice a week. All experiments were performed with cells between passage number 10 to 19.

II.1.2.1. Cell Line Growth Medium

Cell line	Origin	Growth Medium	Characteristics
VCaP (ATCC® CRL-2876)	Vertebral metastasis	DMEM (500 ml), 10% FBS (50 ml), 1% Pen/strep (5.5 ml)	AD IGF-1R+ (high levels) PTEN+, ERG+
LnCaP (ATCC® CRL-1740)	Left supraclavicular lymph node	RPMI (500 ml), 10% FBS (50 ml), 1% Pen/strep (5.5 ml)	AD IGF-1R+ PTEN-, ERG-
DU-145 (ATCC® HTB-81)	Brain metastasis	RPMI (500 ml), 10% FBS (50 ml), 1% Pen/strep (5.5 ml)	AI IGF-1R+ PTEN +, ERG-
22Rv1 (ATCC® CRL-2505)	Human prostatic carcinoma xenograft	RPMI (500 ml), 10% FBS (50 ml), 1% Pen/strep (5.5 ml)	AD IGF-1R+ PTEN +, ERG-
PC-3 (ATCC® CRL-1435)	Bone metastasis	RPMI (500 ml), 10% FBS (50 ml), 1% Pen/strep (5.5 ml)	AI IGF-1R+ PTEN -, ERG-
RWPE-1 (ATCC® CRL-11609)	Epithelial cells derived from the peripheral zone of histologically normal adult human prostate	K-SFM (500 ml), Bovine Pituitary Extract (5 ml), Epidermal Growth Factor (1 ml), 10% FBS (50 ml), 1% Pen/strep (5.5 ml)	Normal tissue
VCaP-Luc2 /VCaP-GFP	Lentivirally-transfected VCaP cells (Luciferase/GFP)	DMEM (500 ml), 10% FBS (50 ml), 1% Pen/strep (5.5 ml), 5 ml Geneticin	AD IGF-1R+ (high levels) PTEN +, ERG+

Table 1. Summary of the origin, growth medium, and characteristics of the different PCa Cell Lines. FBS: Heat-inactivated fetal bovine serum. AD: Androgen-Dependent. AI: Androgen-Independent.

II.1.3. Antibodies

Table 2 and **3** describes the antibodies employed in this thesis.

II.1.3.1. Primary Antibodies

Antigen	Host	Dilution	Provider	Antigen Location
IGF-1R-β	rabbit	1:100 (IF) 1:1000 (WB)	Cell Signaling #3027S	IGF-1R-β
EEA1	mouse	1:1000 (IF)	BD Transduction Laboratories #610456	Early endosome marker
LAMP1	rabbit	1:1000 (IF)	Abcam #ab24170	Lysosome marker
Clathrin Heavy Chain (E-11)	mouse	1:50 (IF)	Santa Cruz Biotechnology #sc-271253	Detection of Clathrin HC of mouse, rat, and human origin
Caveolin-1	goat	1:50 (IF)	Abcam #ab192452	antibody-N-terminal in mouse, rat, dog, human, and monkey
Phospho-p44/42 MAPK (Erk1/2) (Thr202/Tyr204)	rabbit	1:500 (WB)	Cell Signaling #4370	p44 and p42 MAP kinase (Erk1 and Erk2) in human, mouse, and rabbit
Phospho-Shc	mouse	1:200 (WB)	Santa Cruz Biotechnology #sc-81519	Tyr 239 and 240 dually phosphorylated Shc of mouse, rat, human and canine
Phospho-IRS-1 (Ser302)	rabbit	1:500 (WB)	Cell Signaling #2384	IRS-1 in mouse and human
Phospho-PI3 Kinase p85 (Tyr458)/p55 (Tyr199)	rabbit	1:300 (WB)	Cell Signaling #4228S	p85 PI3 kinase
Phospho-IGF-1R-β (Tyr1316)	rabbit	1:500 (WB)	Cell Signaling #28897S	Tyr 1316 phosphorylated IGF-1R-β

Androgen Receptor	rabbit	1:1000 (WB)	Cell Signaling #5153	Total androgen receptor human protein
Erg-1/2/3	mouse	1:500 (WB)	Santa Cruz Biotechnology #sc-354	Erg-1/2/3 in mouse, rabbit, and human
α-Tubulin	mouse	1:10000 (WB)	Sigma-Aldrich #T8203	Mouse monoclonal reacts with human, rat, and mouse α–tubulin
α-SMA (Smooth Muscle Actin)	biotin	1:500 (IH)	Progen #BK61501.0.5; K-Nr. D12625	Biotinylated
mCD31	rat	1:100 (IH)	BD Biosciences #553370	Also known as PECAM-1
mVEGFR2	goat	1:20 (IH)	R&D Systems #AF644	VEGFR2 extracellular domain
Ki67	rabbit	1:100 (IH)	Abcam #ab15580	Proliferation marker

Table 2. Summary of primary antibodies employed in this thesis.

II.1.3.2. Secondary Antibodies

Antigen	Dilution	Host	Provider	Antigen Location
Alexa Fluor anti-Rabbit-488	1:500-1:1000 (IF)	donkey	ThermoFisher #A21206	Rabbit IgG (Heavy and Light Chains)
Anti-mouse-Pacific Blue	1:600 (IF)	goat	Invitrogen™ #Z25041	Mouse IgG
Alexa Fluor anti-Mouse-568	1:500 (IF)	goat	ThermoFisher #A21043	Mouse IgM (Heavy Chain)
Anti-Goat-(Cy3)	1:500 (IF)	donkey	Abcam #ab97115	Goat IgG (Heavy and Light Chains)
Anti-Human	1:5000 (IF)	goat	Santa Cruz Biotechnology #sc-2453	Human IgG
Anti-Rabbit	1:5000 (WB)	goat	Sigma-Aldrich #A6154	Rabbit IgG
Anti-Mouse	1:5000 (WB)	rabbit	Sigma-Aldrich #A9044	Mouse IgG
Anti-Rat-Cy3	1:500 (IH)	donkey	Dianova #712-166-153	Rat IgG (Heavy and Light Chains)

Anti-Biotin-AMCA	1:200 (IH)	conjugated streptavidin	Dianova #016-150-084	Biotin
Anti-Rabbit-Cy3	1:500 (IH)	donkey	Dianova #711-166-152	Rabbit IgG (Heavy and Light Chains)
Anti-Goat-Cy3	1:250 (IH)	donkey	Dianova #705-166-147	Goat IgG (Heavy and Light Chains)
Anti-Rat-AMCA	1:50 (IH)	donkey	Dianova #712-155-153	Rat IgG (Heavy and Light Chains)
Alexa Fluor anti-Rabbit-488	1:500 (IH)	donkey	Dianova #711-546-152	Rabbit IgG (Heavy and Light Chains)

Table 3. Summary of secondary antibodies employed in this thesis.

II.1.4. Animals

Male C.B-17/IcrHan®Hsd-*Prkdc*^{scid} mice provided by Envigo Laboratories Inc. (Gannat, France) at 6-8 weeks of age were used for all animal experiments [1-4].

All mice were kept in a specific-pathogen-free facility under constant temperature and humidity using a 12 h light-dark cycle. Food pellets and water were supplied ad-libitum during the whole experiment in all cases. Additionally, to ensure animal well-being, general aspects such as grooming conduct, tumor size, body weight, and behavior were evaluated daily.

II.2. Methods

II.2.1. AVE1642 and PGA-AVE1642 Synthesis

II.2.1.1. Synthesis of Pyridyl Disulfide-modified PGA

200 mg of PGA (1.55 mmol glutamic acid repeat unit, 1 equivalent (equiv.)) was dissolved in 15 ml of DMF (≥99.8% anhydrous) under N_2 flow. Next, 254 mg of 4-(4,6-dimethoxy-1,3,5-triazin-2-yl)-4-methylmorpholinium tetrafluoroborate

(DMTMM.BF_4) (0.77 mmol, 0.5 equiv.) synthesized mainly as described in [5] was dissolved in 4 ml of anhydrous DMF and added. The reaction mixture was stirred for 20 minutes (mins) to activate the carboxyl acid groups of PGA. Then, 72 mg of pyridyl dithiol cysteamine (0.39 mmol, 0.25 equiv.) synthesized according to previously reported methods [6] (dissolved in 1 ml of anhydrous DMF) was added and the pH adjusted to 8 by the addition of N,N-diisopropylethylamine (DIEA). The reaction mixture was then stirred at room temperature (RT) for 48 h, and DMF was evaporated under vacuum. The product was precipitated in cold ether and dried under vacuum. Then, PGA-PD was dissolved in 10 ml of 1 M sodium bicarbonate to obtain the water-soluble sodium salt form of the polymer. After complete dissolution, the buffer was exchanged for Milli-Q water with resistivity of 18 MΩ.cm (Milli-Q® ultrapure) by ultrafiltration using vivaspin tubes with a molecular weight cut-off (MWCO) of 3 kDa (**Figure 1**). The purified product was recovered by freeze-drying — yield: 80%.

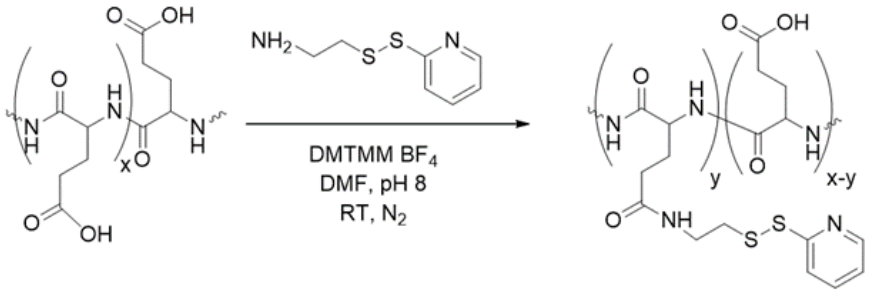

Scheme 1: Modification of PGA with pyridyl dithiol via DMTMM BF_4 activation.

The degree of functionalization was determined by nuclear magnetic resonance (NMR). NMR spectra were recorded at 27ºC (300 K) on a 300 Ultrashield™ (Bruker; Billerica, Massachusetts, USA). Data were processed with the Mestrenova software (Bruker; Billerica, Massachusetts, USA). PGA solutions were typically prepared at 5 mg/ml in deuterium oxide (D_2O).

II.2.1.2. Modification of AVE1642 with N-succinimidyl-S-acetylthiopropionate

AVE1642 was modified with N-succinimidyl-S-acetylthiopropionate (SATP) using a previously described well-established protocol [7]. Briefly, SATP (25 equiv., 2 mg/ml solution in DMSO) was added to 0.55 mg/ml solution of AVE1642 in PBS pH 7.4. The mixture was incubated at RT for 30 mins stirring at 250 revolutions per minute (rpm). Then, the reaction was purified by ultrafiltration with vivaspin centrifugal concentrator tubes with an MWCO of 50 kDa.

II.2.1.3. Conjugation of SATP-modified AVE1642 to PGA-PD

AVE1642-SATP solution in PBS was mixed with a PGA-PD (5 equiv.) solution in PBS and 9.1% v/v deacetylation buffer (0.5 M hydroxylamine-HCl in PBS, 25mM EDTA) to yield thiolated AVE1642. The reaction mixture was incubated overnight at RT stirring at 250 rpm. The purification of the final conjugate was performed by ultrafiltration (vivaspin MWCO 50kDa). The antibody concentration in the PGA-AVE1642 solution was determined using fast protein liquid chromatography (FPLC) and a calibration curve of known concentrations of AVE1642. Briefly, PGA-AVE1642 was treated with 50 mM DTT for 30 mins at RT to detach the polymer from the antibody, and the sample was injected in an AKTA Ettan LC FPLC System (GE Healthcare; Chicago, Illinois, USA) equipped with a Superdex 200 5/150 GL column (GE Healthcare; Chicago, Illinois, USA) working at a flow rate of 0.18 ml/min. Elution was carried out with a buffer of Tris 50 mM, NaCl 150 mM pH 7.5, and absorbance was measured at 280 nm. The calibration curve was generated by injecting AVE1642 standards incubated with DTT in the same conditions and measuring the area under the curve (AUC) of the peak at 1.7 ml (**Figure 2**).

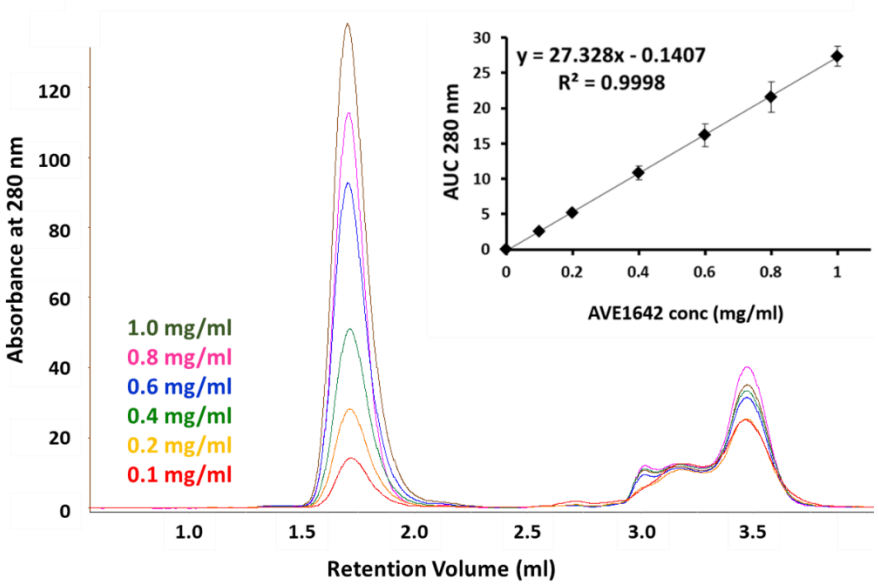

Figure 2: Calibration curve of AVE1642 treated with 50 mM DTT determined using gel filtration with standard concentrations. Absorbance was measured at 280 nm. Each standard was injected four times. The black line in the upper right corner shows the linear fitting of the calibration curve.

II.2.2. Labeling of AVE1642 and PGA-AVE1642 with Cyanine Dyes

100 mg of PGA-PD (18.5% mol PD derivatization, 2.8 x 10^{-3} mmol polymer chain, 1 equiv.) in the sodium salt form was dissolved in 4 ml of PBS pH 7.4. Then, 5.4 mg of EDC and 3.2 mg of NHS (0.028 mmol of each, 10 equiv. with respect to the polymer chain) were dissolved in PBS and added to the solution. The reaction mixture was stirred for 20 mins to activate the carboxyl acid groups of PGA. Then, 9.2 mg of Cy5-amine or 10.6 mg of Cy5.5-amine (0.014 mmol of each, 5 equiv. with respect to the polymer chain) were added, and the reaction was stirred overnight. The excess of unreacted dye was removed by dialysis against Milli-Q water, and the product was lyophilized. Dye content was determined measuring the absorbance at 646 nm for Cy5 and at 684 nm for Cy5.5. The final polymer was used for the conjugation to AVE1642 following the procedure reported in the previous section.

A 2 mg/ml solution of AVE in PBS pH 7.4 was added of 5 equiv. of Cy3-NHS or Cy5.5-NHS, previously dissolved in DMSO, and left to react for 4 h at RT. The excess of unreacted dye was removed by ultracentrifugation. Dye content and antibody concentration were measured by UV-Vis spectroscopy.

II.2.3. Characterization of AVE1642 and PGA-AVE1642

II.2.3.1. Amino-acid Analysis

The molar ratio between the polymer and the antibody in the PGA-AVE1642 conjugate was determined by amino acid analysis (University of Barcelona, Spain) using the following standardized protocol.

Briefly, 100 µl of the solution samples were hydrolyzed in 6 M hydrochloric acid at 110ºC for 24 h. Aliquots of α-aminobutyric acid (AABA) solutions (2.5 mM) were added as an internal standard. The samples were then evaporated, resuspended in high-performance liquid chromatography (HPLC) water (500 µl), and filtered (0.45 µm). The filtered solution of samples was further diluted in HPLC water (200 µl). Subsequently, the samples were derivatized with 6-aminoquinolyl-N-hydroxysuccinimidyl carbamate (AQC) according to the Waters AccQ-Tag^{TM} method [8]. AccQ-Tag derivatized amino acids were analyzed by HPLC with UV detection (λ=254nm) (Waters 600 HPLC gradient system equipped with a Waters 2487 UV detector) and Empower 2 software.

II.2.3.2. Ultraviolet-Visible Spectroscopy

Ultraviolet-visible spectroscopy (UV-VIS) measurements were performed using a JASCO V-630 spectrophotometer at 25ºC with 1.0 cm matched quartz cells and with a spectral bandwidth of 0.5 nm. AVE1642 concentration was determined based on their absorbance at 280 nm considering $A^{0.1\%}_{280}$ = 1.50 mg $mL^{-1}cm^{-1}$.

II.2.3.3. Size-exclusion Chromatography

Analytical size exclusion chromatography (SEC) was performed on an Ettan LC FPLC (GE Healthcare; Chicago, Illinois, USA) system equipped with a Superdex 200 5/150 GL column (GE Healthcare; Chicago, Illinois, USA) working at a flow rate of 0.18 ml/min. Elution was conducted with Tris 50 mM, NaCl 150 mM pH 7.5, and absorbance was measured at 220nm.

II.2.3.4. SDS-PAGE Electrophoresis

Electrophoresis (SDS-PAGE) was performed via the Laemmli-SDS-Page protocol [9]. Samples were mixed (1:2) with loading buffer (50 mM Tris HCl, 2% SDS, 0.1% bromophenol blue, 10% glycerol) and incubated for 5 min at 95ºC to denature the protein. Samples were then loaded into an SDS gel (5% acrylamide, 0.1 cm thickness) and run at 150 V for approximately 1 h 45 mins. Proteins were then visualized by Coomassie blue staining.

II.2.3.5. Dynamic Light Scattering and Zeta Potential Measurements

Dynamic light scattering (DLS) and zeta potential measurements were performed at 25ºC using a Malvern Zetasizer Nano ZS instrument (Worcestershire, UK) equipped with a 532 nm laser at a fixed scattering angle of 173º. AVE1642 and its derivatives were prepared in PBS at 0.2 mg/ml, and the solutions were filtered through a 0.22 µm cellulose membrane filter before analysis. Size distribution was measured (diameter, nm) in triplicate for each sample. Automatic optimization of beam focusing, and attenuation was applied for each sample. Zeta potential measurements were performed using disposable folded capillary cells (Malvern, Worcestershire, UK).

Thermal denaturation was evaluated by DLS by monitoring the hydrodynamic volume and the derived count rate of protein samples from 25ºC to

85ºC. Samples were prepared in PBS at a protein concentration of 0.2 mg/ml. Measurements were performed with an incremental step of 5ºC and an equilibration time of 3 mins.

II.2.3.6. Circular Dichroism Spectroscopy

The secondary structure of AVE1642 and its derivatives were investigated by circular dichroism (CD) using a J-815 CD Spectrometer (Jasco Corporation; Tokyo, Japan). The instrument was connected to a Peltier thermostated cell holder (PTC-423, Jasco Corporation; Tokyo, Japan) with a recirculating cooler (JULABO F250, Jasco Corporation; Tokyo, Japan). Samples were dissolved in PBS pH 7.4 at a protein concentration of 0.1 mg/ml. The spectra were collected between 200 and 250 nm by the average of three continuous scanning at a speed of 20 nm/min. Experiments were conducted in a quartz cuvette with a path length of 0.1 cm. CD data were converted to mean residue ellipticity, expressed in deg cm^2 $dmol^{-1}$, by applying the formula $\Theta_{MWR} = \Theta_{obs}$ (MRW)/10L[C], where Θ_{obs} is the observed ellipticity in degrees, the MRW is the mean residue weight of the protein, [C] is the protein concentration in mg/ml, and L is the optical path length in centimeters. The conjugate was incubated with 50 mM DTT for 30 mins at RT to investigate the secondary structure of the antibody of the PGA-AVE1642 derivative after the removal of the polymer. Then, the sample was purified by ultracentrifugation with a vivaspin MWCO 50 kDa filter to remove PGA. AVE1642 after PGA removal was analyzed by CD to evaluate the secondary structure of the antibody.

CD was also used to evaluate the thermal stability of AVE1642 and its derivatives. During the experiment, the temperature was increased from 25ºC to 90ºC at a rate of 2ºC/min while the molar ellipticity was monitored at 216 nm to investigate any modifications to the β-sheet structure of the antibody. The measurements were conducted using a Jasco J-1500 CD Spectrometer (Jasco Corporation; Tokyo, Japan) equipped with a Peltier thermostatted cell holder

(PTC-517, Jasco Corporation; Tokyo, Japan) and a Jasco CTU-100 circulating bath. Samples were prepared in PBS at 0.1 mg/ml, and the experiments were conducted in a quartz cuvette with a path length of 0.5 cm. The temperature was recorded directly using a temperature probe placed inside the cuvette.

II.2.3.7. ELISA assays

ELISA assays were performed to evaluate the stability and affinity of AVE1642 and PGA-AVE1642. For stability studies, both compounds were incubated separately at 37ºC at 500 rpm for 0, 24, 46, and 72 h. A 5 µg/ml solution of each sample was diluted in 300 µl of FBS. Furthermore, two calibration curves were performed (for AVE1642 and PGA-AVE1642) using the same AVE1642 equiv. concentrations (0, 0.025, 0.1, 0.5, 1, 3 and 5 µg/ml). The different calibration curve points were diluted with 300 µl of FBS serum without previous incubation. In contrast, for affinity studies, different concentrations of AVE1642 and PGA-AVE1642 (from 0.025 to 10 µg/ml) were prepared in PBS without previous incubation (**Figure 3**).

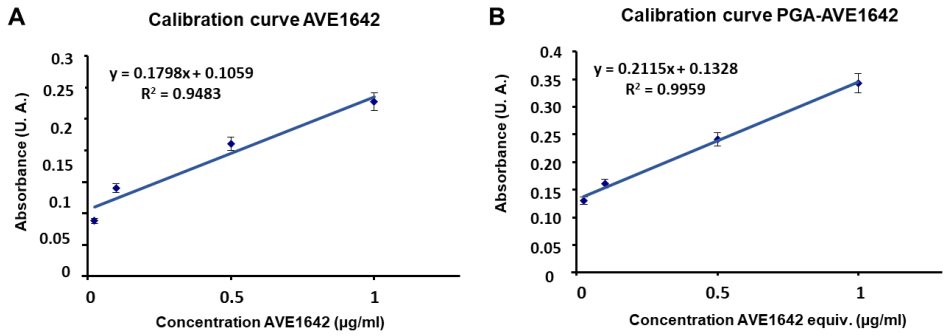

Figure 3: AVE1642 and PGA-AVE1642 calibration curves. A and **B)** Graphs represent Absorbance vs. concentration (µg/ml). The absorbance intensity was evaluated at different AVE1642 and PGA-AVE1642 concentrations (0, 0.025, 0.1, 0.5, 1, 3, and 5 µg/ml AVE1642 equiv.). Data expressed as mean±SEM, n=3.

In an EIA/RIA (ELISA) 96-well plate, 40 µg/ml of VCaP cellular lysate diluted with PBS was added to each well to give 50µl total volume; as a control, wells with PBS without VCaP cellular lysate were also included. The plate was covered with an adhesive sealing sheet and incubated overnight, shaking at 4ºC. Next, the lysates were washed three times with washing buffer (200 µl of PBS and 0.2% (v/v) Tween 20), blocked with 100 µl of 0.2% (v/v) Tween 20 and 5 % (w/v) skimmed milk (blocking buffer), and then incubated for 2 h shaking at RT. After removing the blocking buffer, the lysates were washed twice with washing buffer. Subsequently, 100 µl of each calibration curve and 100 µl of different samples were added to the wells (in duplicate). The plate was covered with an adhesive sealing sheet and incubated overnight, shaking at 4ºC.

The lysates were then washed three times with 200 µl of washing buffer. Next, 100 µl of anti-human (1/5000) primary antibody diluted in blocking buffer and was incubated for 2 h at RT, shaking. The lysates were then washed three times, and 100µl TMB was added to each well and then incubated for 30 mins at RT, shaking in the dark. After this time, 100 µl of stop solution was added, and the absorbance was measured in a spectrophotometer at OD_{450nm}.

II.2.3.8. Hemolysis Assays

Mouse red blood cells (RBCs) were isolated to determine if AVE1642/ PGA-AV1642 promoted hemolysis. Healthy C.B-17/IcrHan®Hsd-*Prkdc*^{scid} male mice were euthanized with CO_2 atmosphere and blood immediately extracted from the heart using a heparinized syringe 0.1% (w/v) and collected in a 15 ml falcon tube. Tubes were then centrifuged for 10 mins at 3000 rpm at 4ºC to isolate erythrocytes from the plasma. The supernatant plasma was carefully removed, and the tubes containing erythrocytes were filled to a total volume of 10 ml with fresh PBS pH 7.4, and then mixed centrifuged for 10 mins at 3000 rpm at 4ºC. The plasma was

removed again, and this procedure was reproduced 4-5 times until clear PBS was obtained.

The supernatant was discarded, and a 2% suspension of fresh erythrocytes (w/v) in PBS was prepared. 2 mg/ml dextran was used as a negative control, 1% Triton X-100 (w/v) as a positive control, and 250 µg/ml AVE1642 and PGA-AVE1642 solutions in PBS were assessed. 100 µl of each sample was added to wells of a U-shaped non-sterile 96-well plate with 100 µl of erythrocytes; the plate was then covered with an adhesive sealing sheet and incubated for 1 h at 37ºC. The plate was then centrifuged for 10 mins at 3000 rpm at RT, and 100 µl of the supernatant of each well (avoiding the pellet) was transferred to a corresponding well in a new non-sterile 96-well plate. Finally, the absorbance was measured in a spectrophotometer at OD_{570nm}.

II.2.4. Lentiviral Infection Protocol

For the *in vivo* PCa model, the VCaP cell line was virally infected separately with the Luciferase (Luc2) Lentiviral Vector (Photinus Pyralis Cumate) to express luciferase and for Turbo Green Fluorescent Protein (tGFP) as a positive transfection control. 1.2 x 10^6 VCaP cells (around 133,000 cells/cm^2) were seeded in a 6-well plate in 2 ml of complete medium per well. The cells were incubated at 37ºC in a 5% CO_2 atmosphere. Once the cells were at 80% confluence, the medium was removed, and the cells were washed with sterile PBS. Luc2 and tGPF stocks contains 1-2 x 10^7 and 0.5-1 x 10^7 particles forming units (pfu)/ml, respectively. Both lentiviral solutions were prepared separately by adding 240 µl of each lentivirus to 960 µl of complete medium. After PBS washing, each lentiviral virus was incubated for 24 h at 37ºC in a 5% CO_2 atmosphere, after which point both solutions were replaced by 2 ml of complete medium.

500 µg/ml of the antibiotic geneticin (G418) was added in the complete medium to select positive cells for lentiviral infection. To detect stable luciferase-expressing cells (VCaP-Luc2), 10,000 cells in 100 µl of complete medium was added to a well in a white 96-well plate. 20µl of Bright-Glo™ Luciferase Assay System was next added, and the fluorescence was immediately evaluated in relative luminescence units (RLU) in the spectrophotometer. In the case of tGFP (VCaP-GFP), 250,000 cells were resuspended in complete medium, and the percentage of selected cells was measured by fluorescence through flow cytometry. Prior to cellular injection *in vivo*, we measured the fluorescence in the VCaP-Luc2 cell line by spectrophotometer to check luciferase stability.

II.2.5. *In vitro* Toxicity Studies

Cells were seeded in a sterile 96-well plate in 50 µl of complete medium. 23,000 VCaP and VCaP-Luc2 cells (around 67,000 cells/cm^2) were incubated for 72h and 10,000 LnCaP, DU-145, 22Rv1, PC-3, and RWPE-1 cells (around 28,000 cells/cm^2) were incubated for 24 h at 37ºC and a 5% CO_2 atmosphere before testing the various treatments. Different incubation times were used to test cells while in exponential growth. 100µl of sterile PBS was added to unused wells in the periphery to avoid medium evaporation.

Four different PGA-AVE1642 conjugates, each one with different PGA chains conjugated to the AVE642 (in a ratio of 2:1; 4:1; 5:1 and 10:1 PGA chain: AVE1642), and free AVE1642 were prepared in a range of concentrations in AVE1642 equiv. (0.006 to 100 µg/ml). Abiraterone was prepared from 0.03 to 10 µg/ml, and both combinations therapies PGA-AVE1642 (2:1) + Abiraterone and AVE1642 + Abiraterone were prepared at 1:10 ratio (PGA-AVE1642/AVE1642:Abiraterone). The VCaP cell line was also treated only with PGA at different concentrations (from 0.0064 to 64.37 µg/ml) of PGA equiv. as a control.

All treatments were incubated for 72 h, and after this time, without removing medium, 20µl of MTS/PMS was added at a 20/1 ratio to each well and incubated for 6 h (in the case of VCaP and VCaP-Luc2 cells) and 3 h (in the case of the other PCa cell types and normal prostate cell type). Different incubation times were selected due to VCaP cell line presenting lower doubling time and mitochondrial breathing compared to the other cell lines. Finally, the samples were measured in the spectrophotometer at $OD_{490\text{-}500nm}$.

GraphPad Prism 8 software was used to fit a dose-response curve to determine IC_{50} values. Once the toxicity results were obtained, any synergistic effect between AVE1642 and PGA-AVE1642 with Abiraterone was evaluated by a Combination Index (CI) measurement employing CompuSyn software [10]. The CI concept was described by *Chou et al.* in 1984 [11]; the CI value quantitatively defines synergism (CI<1), additive effects (CI=1), or antagonism (CI>1).

II.2.6. ERG Gene Silencing by siRNA

Short interfering RNA knockdown of human ERG was performed with siGENOME_siRNA (siERG), as reported in [12] and [13]. Scrambled siGENOME_non targeting_siRNA (SCR) was used as a siRNA control, and non-transfected cells were used as a negative control. 120,000 VCaP cells (around 67,000 cells/cm^2) were seeded in a 24-well plate in a final volume of 500 µl complete growth medium, and cells were incubated for 24 h before the transfection.

siERG and SCR were prepared before the transfection following the next protocol. ERG siRNA (0.025 µM) and 0.625 µl of DharmaFECT® were mixed in 100 µl final volume using medium without FBS or P/S. This solution was incubated at RT for 20 mins in an Eppendorf. Non-targeting siRNA was prepared separately with the same procedure. Then, 400 µl of complete growth medium was added to each Eppendorf, and these solutions were incubated with the cells for 24 h. For

non-transfected cells, the medium was replaced with only complete growth medium.

The media for each condition were then replaced by complete growth medium and 24 h later, VCaP cells from each condition were exposed for 72 h to AVE1642 (0.1 µg/ml), PGA-AVE1642 (0.1 µg/ml AVE1642 equiv.), Abiraterone (1 µg/ml), AVE1642 + Abiraterone (0.1+1 µg/ml), PGA-AVE1642 + Abiraterone (0.1+1 µg/ml), and PGA (0.085 µg/ml).

II.2.7. AVE1642 and PGA-AVE1642 Internalization Studies

II.2.7.1. Flow Cytometry

A calibration curve was constructed to evaluate the fluorescence intensity (FI) to compare the date between AVE1642-Cy5.5 and PGA-AVE1642-Cy5.5 (**See Section II.2.2**) and avoid quenching. Calibration curves used 0.05, 0.1, 0.2, and 0.3 mg/ml of polymer equiv. (PGA) of PGA-AVE1642-Cy5.5 (AVE1642: 1.95 mg/ml, PGA: 1.21 mg/ml and Cy5.5: 0.30% (w/w)) and 0.08, 0.16, 0.32, and 0.49 mg/ml of AVE1642 equiv. for AVE1642-Cy5.5 (AVE1642: 2.33 mg/ml and Cy5.5: 0.36% (w/w)) (**Figure 4**). All concentrations were prepared in PBS, and 100 µl of each was added to a black 96-well plate and the fluorescence measured in a Victor^2 spectrophotometer (PerkinElmer; Waltham, Massachusetts, USA) at an FI for excitation of 640 nm and emission of 700 nm.

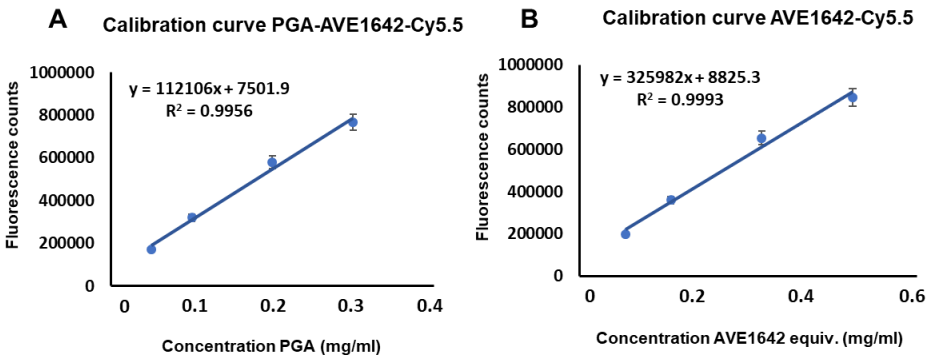

Figure 4: AVE1642-Cy5.5 and PGA-AVE1642-Cy5.5 Fluorescence Calibration Curves. Graphs represent fluorescence vs. concentration (mg/ml). **A)** Fluorescence intensity was assessed for PGA-AVE1642-Cy5.5 concentrations of 0.05, 0.1, 0.2, and 0.3 mg/ml polymer. **B)** AVE1642-Cy5.5 concentrations of 0.08, 0.16, 0.32, and 0.49 mg/ml AVE1642 equiv. Data expressed as mean±SEM, n=3.

240,000 VCaP cells (around 67,000 cells/cm^2) were seeded in a 12-well plate in 1 ml of complete medium. After 72 h, 2 µM of cathepsin B inhibitor CA-074 was incubated for 30 mins to avoid PGA degradation. Next, the plates were divided according to different temperatures tested; plates were kept at 37ºC and 4ºC to study energy-dependent meditated endocytosis.

Then, AVE1642-Cy5.5 and PGA-AVE1642-Cy5.5 were incubated at 0.16 mg/ml AVE1642 equiv. concentration for AVE1642-Cy5.5 and 0.1 mg/ml polymer concentration for PGA-AVE1642-Cy5.5 for up to 3 h at 37ºC and 4ºC. Next, all plates were placed on ice, medium removed, and wells washed three times with 1 ml 0.1% (w/v) PBS-BSA.

Cells were detached by careful pipetting and collected in a final volume of 400 µl of PBS in a 1.5 ml Eppendorf. Data were obtained with the CytoFLEX S flow cytometer (Beckman Coulter; Brea, California, USA).

II.2.7.2. Confocal Microscopy

133,000 VCaP cells (around 67,000 cells/cm^2) were seeded in a 24-well plate in 500 μl of complete medium on a sterile round glass slide (Ø 15mm). After 72 h of incubation, the medium was replaced, and the cells were treated with 0.1 mg/ml polymer concentration for the PGA-AVE1642-Cy5.5 and 0.16 mg/ml AVE1642 equiv. for AVE1642-Cy5.5 (according to the calibration curve performed in the **Section II.2.7.1**) in 150 μl final total volume diluted with complete medium for 30 mins.

The cells were then washed once with 500 μl PBS for 5 mins, PBS removed, and cells fixed with 500 μl 2% (w/v) PFA in PBS for 20 mins at 37ºC. The cells were then washed three times with 500 μl PBS and afterward, cells were blocked in 500μl with 10% (v/v) FBS diluted with PBS for 1 h at 37ºC.

Next, round glass slides were placed in a glass microscope slide, and the cells were incubated overnight at 4ºC in a humidified chamber with 50 μl of the following primary antibodies combinations diluted in 10% (v/v) FBS: (i) anti-rabbit IGF-1R-β (1/100) with anti-mouse EEA1 (1/1000); (ii) anti-rabbit LAMP1 (1/1000); (iii) anti-rabbit IGF-1R-β (1/100) with anti-mouse Clathrin (1/50); (iv) anti-rabbit IGF-1R-β (1/100) with anti-goat Caveolin-1 (1/50).

The following day, round glass slides were washed three times with 100 μl PBS and incubated for 1 h in the dark at RT in 50 μl of the following secondary antibodies combination diluted in 5% (v/v) FBS: (i) Alexa Fluor anti-rabbit-488 (1/1000) with anti-mouse-Pacific blue (1/600); (ii) Alexa Fluor anti-rabbit-488 (1/1000); (iii) Alexa Fluor anti-rabbit-488 (1/1000) with Alexa Fluor anti-mouse-568 (1/500); (iv) Alexa Fluor anti-rabbit-488 (1/1000) with anti-goat-Cy3 (1/500) respectively.

Finally, the secondary antibodies were removed, and the round glass slides were washed three times with 100 µl PBS and covered with a coverslip using VectaShield Mounting Medium for fluorescence with or without DAPI to preserve the fluorescence of the sample.

All confocal images were taken with the confocal laser scanning microscope (Leica TCS SP8; Wetzlar, Germany), and the images were analyzed using the LAS X Life Science software.

II.2.7.3. Stochastic Optical Reconstruction Microscopy

AVE1642 and PGA-AVE1642 were labeled with two different fluorophores, Cyanine 3 (Cy3) and Cyanine 5 (Cy5), respectively (**See Section II.2.2**). To avoid quenching and employ the correct concentration range, we generated a calibration curve for each compound using 0.0005 to 0.005 mg/ml polymer equiv. (PGA) in PBS in the case of PGA-AVE1642-Cy5 (AVE1642: 2.595 mg/ml, PGA-Cy5: 0.018 mg/ml and Cy5: 6.9% (w/w)) and 0.072 to 0.72 mg/ml of AVE1642 equiv. in PBS for AVE1642-Cy3 (AVE1642: 2.22 mg/ml and Cy3: 1.68% (w/w)) (**Figure 5**). 100µl of each concentration was added to the wells of a black 96-well plate in duplicate, and the fluorescence measured in the spectrophotometer at a specific FI (Cy3; 561nm, Cy5; 647nm).

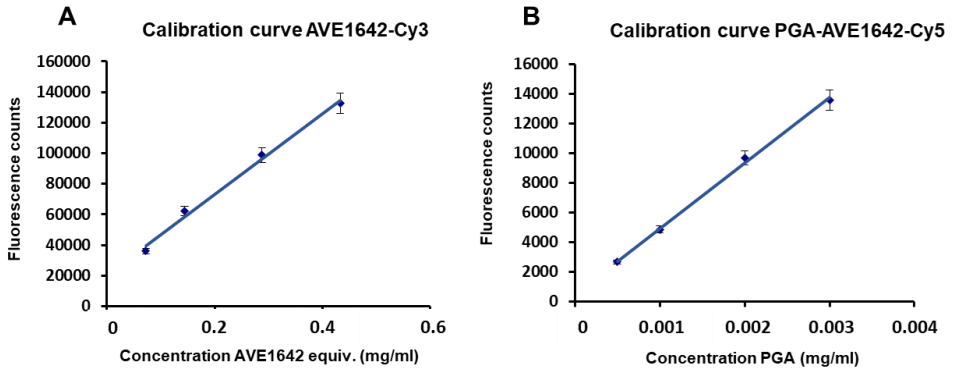

Figure 5: AVE1642-Cy3 and PGA-AVE1642-Cy5 Fluorescence Calibration Curves. The graphs show fluorescence counts vs. concentration (mg/ml). **A)** AVE1642-Cy3 concentrations of 0.072, 0.144, 0.288, and 0.433 mg/ml AVE1642 equiv. **B)** Fluorescence intensity was assessed for PGA-AVE1642-Cy5 concentrations of 0.0005, 0.001, 0.002, and 0.003 mg/ml polymer. Data expressed as mean±SEM, n=3.

VCaP cells were seeded at around 67,000 cells/cm^2 in a final volume of 400µl complete medium on a Nunc™ Lab-Tek™ chamber slide. After 72 h of incubation, the medium was removed, and the cells were incubated at 37ºC with the combination of 0.001 µg/ml polymer concentration for the PGA-AVE1642-Cy5 and 0.03 µg/ml AVE1642 concentration for AVE1642-Cy3 at different times (5, 15, 30, 60 and 180 mins) in 200µl complete medium.

Following treatment, the media was removed, cells were washed with PBS, the cells were fixed with 400µl of 4% PFA for 20 mins at RT, and then cells were washed three times with PBS. Finally, 200µl of Storm Buffer (20 µl glucose (50%), 20 µl cysteamine (MEA 1M), 2 µl GLOX (14 mg glucose oxidase + 50 µl catalase (17 mg/ml)) with PBS were added, and images were taken in Nikon N-STORM 4.0 system configured for total internal reflection fluorescence (TIRF) imaging.

II.2.8. IGF-1R Internalization Analysis

23,000 VCaP cells (around 67,000 cells/cm^2) were seeded in a 96-well plate in a total volume of 100 μl complete medium. Cells were incubated for 72 h and then treated for 15, 30, and 60 mins with 0.1 μg/ml of natural ligand Insulin-like Growth Factor-I (IGF-1) as a positive control, AVE1642, and PGA-AVE1642. A non-treated negative control cell sample was also employed.

After the allotted times, the media was removed, and the cells were washed once using 100 μl of PBS for 5 mins. Cells were then fixed with 100 μl of 2% (w/v) PFA in PBS for 20 mins at 37ºC. Subsequently, the wells were washed three times for 5 mins with 100 μl of PBS and then 100 μl of blocking buffer was added to each well for 1 h at 37ºC to avoid non-specific antibody binding.

Cells were incubated overnight at 4ºC, shaking with 50 μl of anti-rabbit IGF-1R-β primary antibody (1/100) diluted in 10% (v/v) FBS. The primary antibody was then removed, and the cells washed three times for 5 mins with 100 μl PBS. Then, 50 μl of the secondary antibody Alexa Fluor anti-rabbit-488 (1/500) was added in each well diluted in 5% (v/v) FBS. The plate was incubated for 1 h, shaking in the dark at RT. After 1 h, the medium was removed, and the cells were washed three times for 5 mins with 100 μl PBS. 5 μg/ml of DAPI (1/500) diluted in PBS was added to each well in a 100 μl final volume.

Data acquisition was performed in an IN-Cell Analyzer 2200 instrument (GE Healthcare; UK), an inverted epifluorescence microscope equipped with a solid-state illumination source, different objectives, and excitation/emission filters. The images were collected through a 16-bit sCMOS camera. Three pairs of excitation/emission dichroic filters were used to acquire the images: 390/18 excitation and 432.5/48 emission for DAPI, 475/28 excitation and 511.5/23 emission for Alexa Fluor 488. A 20X/0.45 numerical aperture (NA) objective was

used to collect twenty images for each well. After the acquisition, the images were analyzed in the IN-Cell Workstation software (GE Healthcare; UK). Cell segmentation was used to analyze cellular intensity. The cells were segmented, defining a perimeter expressed in μm around the nuclei membrane. The cell intensity of Alexa Fluor 488 was analyzed, and the mean of each well was obtained.

II.2.9. Protein Analysis in Cell and Tumor Samples

II.2.9.1. Cellular Pellet Processing

Detection of endogenous protein levels was analyzed in different exponentially growing PCa and normal prostate cell lines (VCaP, LnCaP, DU-145, 22Rv1, PC-3, RWPE-1, and VCaP-Luc2). All the PCa cell lines were attached in a T75 flask at a cell passage number between 15 and 19. To detach cells, the medium was removed, and all the flasks were washed once with 3 ml of sterile PBS. After removing sterile PBS, 2 ml of trypsin was added, and all the flasks were incubated for 1 min at 37ºC. Once the cells were detached, 8 ml of corresponding complete growth medium was added to inactivate the trypsin, and the cells were collected in a 15 ml falcon.

For mechanisms of action studies, 600,000 VCaP cells (around 67,000 cells/cm^2) were seeded in a 6-well plate in 2 ml of complete medium, and the cells were incubated for 72 h. The medium was then removed, and the cells treated with the positive ligand (IGF-1), AVE1642, and PGA-AVE1642 at 0.1 μg/ml in 2 ml final volume for 15 and 30 mins. Then the cells were detached and collected in a 15 ml falcon as described above.

Then, the cells were centrifuged for 5 mins at 1,600 rpm to obtain the cellular pellet. After discarding the supernatant, the falcons which contained the cellular pellet were introduced immediately into ice before the protein quantification.

II.2.9.2. Tumoral Sample Processing

Tumors treated with AVE1642 and PGA-AVE1642 alone and in combination with Abiraterone Acetate (AA) were frozen in liquid nitrogen and stored at -80ºC after their removal from mice. Tumors were then processed in a mortar in the presence of liquid nitrogen to avoid protein degradation. Once a powder was obtained, the samples were added to a 2 ml Eppendorf and were stored at -80ºC. A small amount of each sample was collected with a spatula and placed in a 1.5 ml Eppendorf to extract tumor proteins.

II.2.9.3. Cellular and Tumoral Extraction and Quantification

To extract the cellular and tumoral proteins and avoid proteolysis and dephosphorylation, 50 μl (for cellular samples) and 100 μl (for tumoral samples) of extraction buffer (IC 1X and a PhosSTOP 1X diluted in Radio-immunoprecipitation [RIPA] buffer [0.15M sodium chloride, 1.0% NP-40, 0.5% sodium deoxycholate, 1% SDS, 50 mM Tris, pH 8.0 with Milli-Q water]) was added, and the samples were incubated for 10 mins on ice and then vortexed for 10 secs for three cycles. Next, the samples were centrifuged 20 mins at 13,200 rpm at 4ºC. The supernatants were collected in a new Eppendorf, and the pellets were discarded.

Protein quantification was determined through by Bradford assay. First, a standard calibration curve was constructed using dilutions of BSA in PBS. Next, all samples were prepared at a 1:10 dilution with PBS. Then, 5 μl of samples for the calibration curve and experimental samples were added in a non-sterile 96-well plate. 200 μl of Bradford reagent was then added to each well, and after 7 mins, the absorbance was measured in a spectrophotometer at OD_{595nm}. The protein quantification in each experimental sample was derived from the calibration curve.

II.2.9.4. Protein Detection

Protein samples were prepared for Western blotting, employing 50 μg of protein for phosphorylated proteins and 20 μg for non-phosphorylated proteins. Both were prepared with 7.5 μl of 4X Loading Buffer (250mM Tris-HCl pH 6.8, 140mM SDS, 30 mM bromophenol blue, 27 mM glycerol, and 0.1 mM DTT) and PBS to obtain a final volume of 30 μl. Then, the samples were denatured at 95ºC for 7 mins to ensure protein denaturation.

Proteins were run on a 1.5 mm-thick gel of 8% polyacrylamide (w/v) concentration following previous specifications [14] for optimal separation of high molecular weight proteins. Polyacrylamide gels were composed of resolving and stacking gels; resolving gels were prepared with 40% (w/v) acrylamide/bisacrylamide stock (29:1) and Milli-Q water with 2.5 μl 1.5 M Tris-HCl pH 8.8, in which 100 μl of 10% (w/v) APS and 10 μl of TEMED were added for gel polymerization; stacking gels were prepared with 500 μl 40% (w/v) acrylamide/bisacrylamide, 1 ml 0.5 M Tris-HCl pH 6.8, 2.42 μl Milli-Q water, 40 μl 10% (w/v) APS, and 4 μl TEMED.

To eliminate bubbles from separating gel before polymerization, 200-300μl of 2-isopropanol were laid over the separating gel and then subsequently removed after acrylamide polymerization with water. The stacking gel mix was placed over the separating gel, and a comb with 10 wells was placed in the gel before gel polymerization. Vertical gel electrophoresis was performed in Mini-Protean Tetra Cell cuvettes (Bio-Rad); gels were placed into the apparatus and 30 μl of samples and 7 μl of protein marker was loaded into the wells. Protein gels were run in Running buffer 1X (25 mM Tris-Base, 192 mM glycine, and 0.1% (w/v) SDS 20% in type II water) at a constant voltage of 95 V during 10 mins and then 120 V until proper protein separation was observed.

After protein separation, the proteins were blotted to a polyvinylidene difluoride (PVDF) transfer membrane. Prior to the transfer, the membrane was activated in methanol for 30 secs and then, in a transfer cassette "sandwich" was constructed (from bottom to top – cathode(-) to anode (+)) of one sponge, two Whatman blotting papers, the polyacrylamide gel, the activated PVDF membrane, another two Whatman blotting papers, and one sponge. This sandwich was placed at 4ºC in a Mini-Protean Tetra Cell cuvettes (Bio-Rad) with an icebox, an agitator, and transfer buffer (4.13 mM Glycine, 5 mM Tris with type II water) and run at 400mA constant amperage for 2 h.

Once transfer assays were finished, PVDF membranes were incubated with Ponceau solution (1% (w/v) Ponceau with 1% (v/v) acetic acid in type II water for 2 mins to verify adequate protein transfer. PVDF membranes were then blocked with PBS pH 7.4 with 0.0005% Tween 20 and 5% (w/v) skimmed milk at RT shaking for 1h.

After removal of the blocking solution, the membrane was incubated with different primary antibodies (anti-rabbit p-IGF-1R-β (Mw:95 kDa), anti-mouse p-Shc (Mw: 63 KDa), anti-rabbit p-MAPK (Mw: 42 KDa), anti-rabbit p-IRS-1 (Mw: 180 KDa), anti-rabbit p-PI3K (Mw: 85 KDa), anti-rabbit IGF-1R-β (Mw: 95 kDa), anti-rabbit Androgen Receptor (AR) (Mw: 110 KDa), anti-mouse ERG (Mw: 55 KDa) and anti-mouse α-tubulin (Mw: 50 KDa) diluted in PBS-Tween 20 with 5% (w/v) skimmed milk) and incubated overnight shaking at 4ºC . The next day, the primary antibodies were removed, and the membrane was washed three times with PBS-Tween 20 buffer for 10 mins. The membrane was then incubated for 1 h shaking at RT with secondary anti-rabbit and anti-mouse antibodies diluted in PBS-Tween 20 with 5% (w/v) skimmed milk. Afterward, the membrane was washed three times with PBS-Tween 20 buffer for 10 mins.

The ECL™ Prime Western Blotting Detection Reagent substrate was used for chemiluminescent detection. The substrates A and B (ratio 1:1), were mixed and poured over the membrane and incubated at RT in the dark for 30 secs. Any excess of the solution was removed, and the membrane was placed in a Hypercassette™, and a Curix 60 film processor was used to visualize the signal in an Amersham Hyperfilm™ MP. Finally, Western blotting images were analyzed by densitometry using ImageJ software, and the proteins levels were normalized to the housekeeping protein α-tubulin.

II.2.10. *In Vivo* Analyses

II.2.10.1. Ethical Considerations

Animal experiments performed were planned following the European Communities Council Directive (86/609/ECC) guidelines and by the Spanish Royal Decree 1201/2005. All experimental procedures were approved by the Institutional 171 Animal Care and Use Committee and carried out by accredited and trained staff, meeting the animal care rules.

II.2.10.2. Development of Orthotopic Prostate Cancer Mouse Model

The orthotopic PCa mice model used C.B-17/IcrHan®Hsd-*Prkdc*^{scid} male strain at 6-8 weeks of age. Thirty mins before surgery, a subcutaneous injection of morphine 2% (5 mg/kg) was administered, and then the mice were anesthetized by isoflurane inhalation with (2-5%) throughout the surgical process. Once the ventral prostate gland was localized, 1 x 10^6 VCaP-Luc2 cells prepared within 1:3 (v/v) of Matrigel and DMEM complete medium in a final volume of 40 µl were orthotopically implanted using an insulin syringe (29G). Next, the muscular area and the skin were sutured separately, employing absorbable 6/0 sutures. Post-surgery, subcutaneous buprenorphine (0.1 mg/kg) was administered every 12 h for 72 h as an anti-inflammatory analgesic.

Tumor growth was measured twice a week via *in vivo* bioluminescence by Xenogen IVIS® Spectrum (Caliper Life Sciences; Hopkinton, Massachusetts, USA) for seven weeks, at which point the tumors reached a maximum size permitted of 1.2 cm^3 [15, 16]. To be able to visualize the tumor luminescence, 150 mg/kg of XenoLight D-luciferin Potassium Salt in sterile PBS was administered subcutaneously as a bioluminescent substrate. Immediately, mice were anesthetized, and 10 mins after injection mice were introduced in the IVIS® Spectrum. Tumor images were acquired using the following parameters: Exposure time: 10 mins, Binning: 8, F/Stop: 1, Emission Filter: Open and Field of View: C. With these parameters, the luminescent tumor signal will be acquired within 20 mins post luciferin injection. In the following animal experiments, we used this schedule. Finally, the luminescence in the tumors was analyzed with the Living Image® (64-bit) program.

II.2.10.3. Enhanced Permeability and Retention Effect Analysis

The orthotopic PCa mice model previously developed was studied to analyze the enhanced permeability and retention (EPR) effect. Evans Blue (EB) dye BSA (8:1 ratio) dissolved in a 0.9% sodium chloride solution was injected intravenously at 10 mg/kg. Each week, a group of six tumor-bearing untreated mice was euthanized 1 h after EB/BSA injection; the tumor growth was weighed and measured by caliper after tumor extraction. Tumors were washed with PBS and incubated at 60ºC for 48 h in 3 ml of formamide to extract the dye from the tumor. The percentage of dye accumulated in the tumor was measured by the spectrophotometer at OD_{620nm} [17-19] and compared against an EB/BSA calibration curve (**Figure 6**).

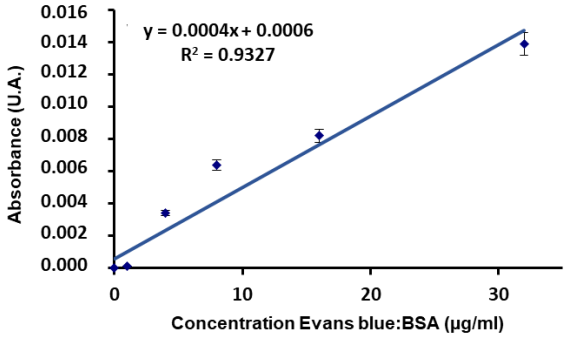

Figure 6: Calibration Curve for Evans blue:BSA Solution. The graphs show the absorbance vs. concentration (µg/ml) at 2, 4, 8, 16, and 32 µg/ml Evans blue:BSA solution. Data expressed as mean±SEM, n=3.

II.2.10.4. Biodistribution Experiment and Fluorescent Quantification

C.B-17/IcrHan®Hsd-*Prkdc*^{scid} mice at maximum EPR effect (0.05 cm^3) were also used for biodistribution studies. Twelve mice were used (n=4). A concentration of 10 mg/kg of AVE1642 equiv. was intravenously (i.v.) injected through the tail vein for labeled PGA-AVE1642-Cy5.5 (AVE1642: 4 mg/ml, PGA-Cy5.5: 0.24% (w/w)) and AVE1642-Cy5.5 (AVE1642: 4 mg/ml, Cy5.5: 0.26% (w/w)). Mice were euthanized at 4 h post-administration, as this represents the maximum tumor accumulation time observed for other PGAs [20-22]. Tumors were carefully removed, weighed, and stored at -80ºC for subsequent homogenization and fluorescent quantification.

For fluorescence quantification, the tumor was resuspended in 1 ml of cold PBS and vigorously mixed. The suspensions were centrifuged at 4000 rpm for 1h at 4ºC, and the supernatants were collected for fluorescent measurement. Tumor supernatants were measured in triplicate (100 µl) in a black 96-well plate using a spectrophotometer (595 nm excitation and 680 nm emission). Furthermore, two calibration curves were performed, one for AVE1642-Cy5.5 and another for PGA-AVE1642-Cy5.5, both at the same AVE1642 equivalent concentrations (0, 0.5,

1, 5, and 10 µg/ml), in order to analyze tumor fluorescence levels (**Figure 7**). Final fluorescent measurements were standardized according to tissue weight.

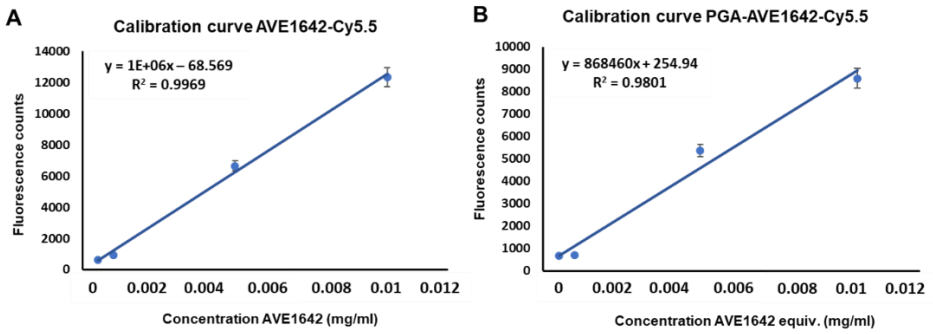

Figure 7: AVE1642-Cy5.5 and PGA-AVE1642-Cy5.5 Fluorescence Calibration Curves. A and **B)** Graphs represent fluorescence vs. concentration (mg/ml) at 0.5, 1, 5, 10 µg/ml AVE1642 equiv. Data expressed as mean±SEM, n=3.

II.2.10.5. Antitumoral Activity Analysis

Compounds were administered once tumors reached a size that allows for the maximum EPR effect (0.05 cm^3, corresponding to week 2) with at least 6 animals used in each group.

AVE1642 and PGA-AVE1642 as a single and combination therapy with AA were i.v. administered starting from the second week at 10 mg/kg once a week for four weeks. AA was administered by oral gavage (20 Gauge, 30 mm length) at 200 mg/kg once a day for 35 days, also starting on week 2, and DHEA as a testosterone/estrogen precursor was subcutaneously administered daily at 0.1 mg as a supplement. AA and DHEA were previously dissolved in 95% sunflower oil/5% benzyl alcohol and 10% DMSO, respectively.

When control animal tumors (animals without treatment) reached a size of 1.2 cm^3 (corresponding the seventh week), all animals were euthanized via carbon dioxide (CO_2) inhalation, and tumors were weighed and measured by caliper after

extraction. Blood was also extracted from the heart employing 21G x 1” needles (Ø 0.80 x 25 mm), and insulin syringes 10 µl 0.1% (w/v) EDTA was added in the insulin syringes to avoid clotting. 100 µl of each sample was centrifuged for 10 mins at 4000 rpm at 4ºC to obtain the plasma used to quantify PSA levels using a Human PSA free (KLK3) ELISA following the manufacturer’s instruction.

II.2.10.6. Tumor Immunohistochemistry

At the experimental endpoint, those mice used for immunohistochemical analyses were injected with 80 µl of FITC-Lectin to aid in the identification of perfused vessels within tumors. The resected tumors were embedded in Tissue-Tek® and frozen in a metal container containing isopropanol located in a box with dry ice. The samples were stored in -80ºC fridge until histological analyses.

Cryosections were made from Tissue-Tek® embedded and frozen tumors with the use of a Cryostat (CM3050 S, Leica; Wetzlar, Germany). Slices with a thickness of 8 µm were taken from distinct levels of the tumor tissue to consider distinct parts of the tumor. Two 8 µm-thick slices were fixed on each adhesion microscope slide that was stored at -80ºC until use in various immunofluorescence experiments.

Analysis of CD31, α-SMA, VGFR2, and Ki67 levels employed a similar experimental procedure. To remove the embedding Tissue-Tek® material, slides were washed in PBS for 2 mins, fixed with 80% methanol for 5 mins at RT, and then with acetone at -20ºC for 2 mins. Slides were then washed three times with PBS for 5 mins. The tumor slices were then surrounded by the hydrophobic marker Pap-Pen® which is used to prevent the aqueous staining solution from spreading out of the sections. To facilitate the diffusion of the Ki67 antibody towards its specific nuclear target, an additional permeabilization step with 0.1% Triton-X 100 in PBS (3 mins at RT) was performed. Tumor slides were then washed for 5 mins with PBS

and incubated at RT in a humid chamber for 1 h with the respective primary antibody diluted in 12% BSA. Tumor slides were then washed three times for 5 mins with PBS and incubated for 45 mins at RT in a humid chamber with the secondary antibody solution in 12% BSA (DAPI was included in this solution to detect nuclei). After washing three times with PBS for 5 mins, the slides were mounted with Mowiol® 4-88 and coverslip (24 x 50mm) to be stored at 4ºC. Mowiol® 4-88 is an embedding medium, and "anti-fade" agent used to reduce light-scattering and light-induced fading (photobleaching) of the fluorophore.

Images at 20X were taken to quantify the area fraction percentage (AF%) (percentage of the fluorescent signal of each protein marker). Moreover, images at 10X were taken to evaluate the vessel functionality and maturity.

The stained tumor sections were analyzed using the fluorescence microscope Axio Imager M2 (Carl Zeiss Oberkochen) with Axio Vision SE64 Rel. 4.9 software. In each tumor section, 3 and 6 representative images at 10X and 20X magnification respectively were acquired from the "core" area (the most central part of the tumor). The images were analyzed using the Microscope Dongle program.

II.3. Statistical Analysis

All values obtained were plotted, displayed as ± SEM from n ≥ 3 assays. Animals experiments were performed using 6-9 animals per group. Statistical significance was evaluated using a paired t-test, two-way ANOVA, test t, or ANOVA test depending on the type of test performed; comparisons with $p<0.0001$ (****), $p<0.001$ (***), $p<0.01$ (**), and $p<0.05$ (*) were considered statistically significant with a 95% confidence interval. GraphPad Prism 8 software was used to performed statistical analyses.

II.4. Bibliography

1. Do, T.-V., et al., *Aurora A kinase regulates non-homologous end-joining and poly(ADP-ribose) polymerase function in ovarian carcinoma cells.* Oncotarget, 2017. **8**(31): p. 50376-50392.
2. Gross, A.C., et al., *IL-6 and CXCL8 mediate osteosarcoma-lung interactions critical to metastasis.* JCI Insight, 2018. **3**(16): p. 99791.
3. Zhang, L., et al., *B-Cell Lymphoma Patient-Derived Xenograft Models Enable Drug Discovery and Are a Platform for Personalized Therapy.* Clinical Cancer Research, 2017. **23**(15): p. 4212-4223.
4. Ryan, M.C., et al., *Therapeutic potential of SGN-CD19B, a PBD-based anti-CD19 drug conjugate, for treatment of B-cell malignancies.* Blood, 2017. **130**(18): p. 2018-2026.
5. Raw, S., *An improved process for the synthesis of DMTMM-based coupling reagents.* Tetrahedron Letters, 2009. **50**: p. 946-948.
6. van der Vlies, A.J., et al., *Synthesis of Pyridyl Disulfide-Functionalized Nanoparticles for Conjugating Thiol-Containing Small Molecules, Peptides, and Proteins.* Bioconjugate Chemistry, 2010. **21**(4): p. 653-662.
7. Talelli, M. and M.J. Vicent, *Reduction Sensitive Poly(l-glutamic acid) (PGA)-Protein Conjugates Designed for Polymer Masked–Unmasked Protein Therapy.* Biomacromolecules, 2014. **15**(11): p. 4168-4177.
8. Ovalles, J.F., M.d.R. Brunetto, and M. Gallignani, *A new method for the analysis of amikacin using 6-aminoquinolyl-N-hydroxysuccinimidyl carbamate (AQC) derivatization and high-performance liquid chromatography with UV-detection.* Journal of Pharmaceutical and Biomedical Analysis, 2005. **39**(1): p. 294-298.
9. Laemmli, U.K., *Cleavage of Structural Proteins during the Assembly of the Head of Bacteriophage T4.* Nature, 1970. **227**(5259): p. 680-685.
10. Chou, T.-C., *Theoretical Basis, Experimental Design, and Computerized Simulation of Synergism and Antagonism in Drug Combination Studies.* Pharmacological Reviews, 2006. **58**(3): p. 621.
11. Chou, T.-C. and P. Talalay, *Quantitative analysis of dose-effect relationships: the combined effects of multiple drugs or enzyme inhibitors.* Advances in Enzyme Regulation, 1984. **22**: p. 27-55.
12. Tomlins, S.A., et al., *Role of the TMPRSS2-ERG gene fusion in prostate cancer.* Neoplasia, 2008. **10**(2): p. 177-188.

13. Magistroni, V., et al., *ERG deregulation induces PIM1 over-expression and aneuploidy in prostate epithelial cells.* PLoS One, 2011. **6**(11): p. 28162-28162.
14. Sambrook, J. and D. Russell, *Preparation of Denaturing Polyacrylamide Gels.* Cold Spring Harbor Protocols, 2006. **2006**(1): p. 3807.
15. Workman, P., et al., *Guidelines for the welfare and use of animals in cancer research.* British Journal of Cancer, 2010. **102**(11): p. 1555-77.
16. Wallace, J., *Humane Endpoints and Cancer Research.* ILAR journal / National Research Council. Institute of Laboratory Animal Resources, 2000. **41**: p. 87-93.
17. Maeda, H., T. Sawa, and T. Konno, *Mechanism of tumor-targeted delivery of macromolecular drugs, including the EPR effect in solid tumor and clinical overview of the prototype polymeric drug SMANCS.* Journal of Controlled Release, 2001. **74**(1): p. 47-61.
18. Maeda, H., *Tumor-Selective Delivery of Macromolecular Drugs via the EPR Effect: Background and Future Prospects.* Bioconjugate Chemistry, 2010. **21**(5): p. 797-802.
19. Arroyo-Crespo, J.J., et al., *Characterization of triple-negative breast cancer preclinical models provides functional evidence of metastatic progression.* International Journal of Cancer, 2019. **145**(8): p. 2267-2281.
20. Duro-Castano, A., et al., *Capturing "Extraordinary" Soft-Assembled Charge-Like Polypeptides as a Strategy for Nanocarrier Design.* Advanced Materials, 2017. **29**(39): p. 1702888.
21. Arroyo-Crespo, J.J., et al., *Anticancer Activity Driven by Drug Linker Modification in a Polyglutamic Acid-Based Combination-Drug Conjugate.* Advanced Functional Materials, 2018. **28**(22): p. 1800931.
22. Duro Castaño, A., et al., *Well-Defined Star-Shaped Polyglutamates with Improved Pharmacokinetic Profiles as Excellent Candidates for Biomedical Applications.* Molecular Pharmaceutics, 2015. **12**(10): p. 3639-49.

Chapter III

PGA Conjugation Alters AVE1642 Bioactivity in Prostate Cancer Models

III.1. Antecedents and Background

As described in the general introduction, several studies have detailed the biological consequences of TMPRSS2:ERG (T2E) fusion gene presence in PCa. Insulin-like growth factors (IGF) also play an important role in PCa development; specifically, IGF-1R promotes normal prostate gland growth and development and can, therefore, contribute to PCa progression.

The presence of the T2E fusion gene has been correlated with increased levels of IGF-1R, while T2E also aids in the classification of PCa patients subtype and the development of specific therapies strategies [1].

Therapeutic approaches for cancer treatment that block IGF-1R activity, including monoclonal antibody (mAb) inhibitors of IGF-1R, IGF-1R tyrosine kinase inhibitors, or IGF-1/IGF-2 neutralizing mAbs, inhibit the activation of intracellular PI3K and MAPK signaling pathways implicated in cell growth and proliferation [2, 3]. Several clinical trials have evaluated IGF-1R inhibiting mAbs in CRPC patients; these include Cixutumumab, Figitumumab, and AMG479 as single agents or in combination with other drugs. However, these therapies failed to display their expected therapeutic potential due to incomplete pathway inhibition or the presence of side toxicities that prompted the clinical trial termination [4].

With a focus on mAb inhibitors of IGF-1R, we sought to evaluate a polymer therapeutics strategy in the hope of improving pathway inhibition, reduce side toxicities, and, therefore, improve therapeutic outcomes in PCa patients [5]. In this chapter, we synthesized and fully characterized a polymer-mAb conjugate as an advanced PCa treatment option. Specifically, we conjugated AVE1642, an anti-IGF-1R mAb, with poly-L-glutamic acid (PGA)-based polymer (generating PGA-AVE1642) following a well-established bioresponsive conjugation strategy in

our lab [6, 7] and then compared anti-tumorigenic activity to the parental mAb through both *in vitro* and *in vivo* analyses.

AVE1642 is a humanized mAb version of the murine mAb EM164 directed against the IGF-1R. Anti-IGF-1R mAb AVE1642 specifically binds and blocks IGF-1R located in the cellular membrane preventing the binding of the natural ligand IGF-1 and the subsequent activation of an intracellular signaling pathway, which result in a decrease in cellular proliferation and the induction of apoptosis. Furthermore, it is reported that AVE1642 induces the regression of human xenografts tumors, inhibits metastasis, and enhances chemosensitivity [8, 9].

Mancarella *et al.* demonstrated that the monoclonal antibody anti-IGF-1R (AVE1642) presented specific cytotoxic effects in T2E-positive PCa cell lines [10].

Previous studies demonstrated the murine mAb EM164 effectiveness in different cellular models such as pancreatic, colon, neuroblastoma, or human myeloma cells. In both neuroblastoma and human myeloma cells, it is reported that EM164 inhibits Akt and MAPK signaling pathways; furthermore, it produces an arrest in the cell cycle in the G1 phase. In addition, xenograft neuroblastoma mice animal studies treated with EM164 intravenously at 40mg/kg twice a week for 4 weeks showed significant antitumor activity, and a synergistic effect in combination with temozolomide (100mg/kg) administered orally for 5 days [11, 12].

Phase I clinical trials of AVE1642 in PCa, pancreatic cancer, and non-small-cell lung cancer (NSCLC), documented tolerability and safety when administered at 6 mg/kg three times per week in combination with other anti-cancer therapies, including docetaxel, gemcitabine, and erlotinib [13]. For instance, phase II clinical trials using anti-IGF-1R mAb inhibitors only experienced a partial response to therapy and a lot of side effects (neutropenia, diarrhea, hyperglycemia, etc.) in CRPC patients [14, 15].

Currently, AVE1642 is being evaluated in clinical trials in different studies such as multiple myeloma, liver carcinoma, and in postmenopausal patients with advanced hormone-dependent breast cancer [53].

III.2. Synthesis of PGA-conjugated AVE1642

As stated in the introduction section, polypeptides offer significant advantages as a polymeric carrier system; therefore, we have selected polyglutamates (PGA) as biodegradable multivalent polymeric carrier following well stablished synthetic methodologies in our lab [7, 16] to design our immunoconjugate. Overall, our conjugation strategy involved the modification of the lysine residues of AVE1642 with a linker that would form cleavable disulfide bonds with a modified PGA polymer [7], thereby generating PGA-AVE1642.

III.2.1. Synthesis of Pyridyl Dithiol-modified PGA

We derivatized PGA (200 glutamic acid units (GAU), polydispersity index (PDI) 1.15) with pyridyl dithiol ethylamine using DMTMM BF_4 (4-(4,6-dimethoxy-1,3,5-triazin-2-yl)-4-methylmorpholinium tetrafluoroborate) as a carboxylic acid activator. We then purified (precipitation in ether) and analyzed the derivatized polymer (PGA-PD) by NMR to quantify the degree of modification (**See Chapter II**, **Section II.2.1.1**) (**Figure 1**).

The ratio of the integrals of the pyridine ring (7.26, 7.79 and 8.36 ppm) to the integral of the main chain proton of PGA (4.35 ppm) was used to calculate the percentage derivatization of PGA with pyridyl dithiol groups, and from this, the molecular weight (Mw) of the modified polymer was also calculated (M_n of the pyridyl dithiol GA unit is 297 and of the GA unit, 151). The degree of functionalization was determined by nuclear magnetic resonance (NMR) at 18-24 mol %.

This analysis established that the subsequent polymer conjugation of AVE1642 employed PGA with a degree of pyridyl dithiol modification between 18.5-23.8%, which corresponds to a modification of ~36 to 48 glutamic acid units (GAU) out of the total 200. From the percentage of modification, we calculated an approximate molecular weight (Mw) of PGA-PD between 35.4 and 37.2 kDa.

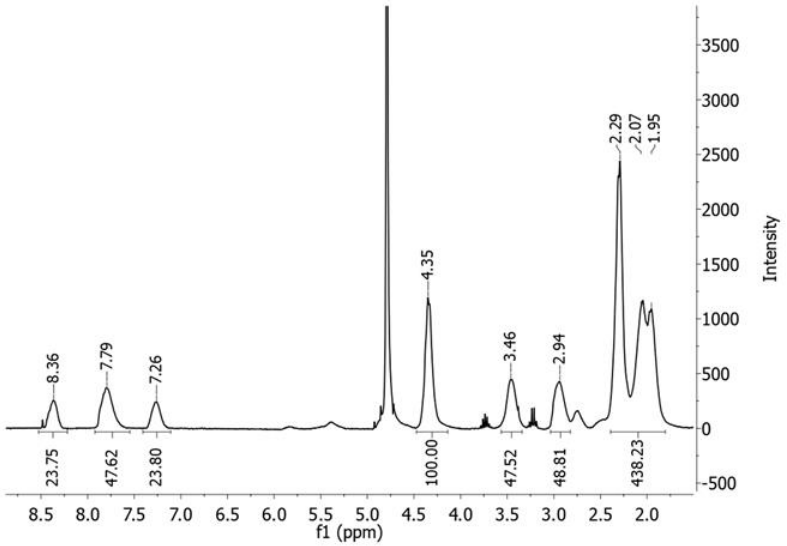

Figure 1: **Representative 1H-NMR spectrum of PGA-PD in D2O.** ^{1}H-NMR (300 MHz, D_2O, ppm): 1.95-2.29 (m, C-C*H*$_2$C*H*$_2$-COONa of PGA side-chain protons), 2.94 and 3.46 (m, C*H*$_2$C*H*$_2$ of ethylamine), 4.35 (m, NH-C*H*-CO of PGA main chain), 7.26 (m, Ar*H*), 7.79 (m, Ar*H*), 8.36 (m, Ar*H*).

III.2.2. Synthesis of N-Succinimidyl-S-acetylthiopropionate-modified AVE1642

We next introduced protected thiol groups into the AVE1642 backbone by partially modifying the accessible lysine residues with an N-Succinimidyl-S-acetylthiopropionate (SATP) linker that can form stable amide bonds with primary amines. Protecting the acetyl group avoids protein dimerization during long-term

storage; furthermore, these protective groups can be easily removed via hydroxylamine hydrochloride treatment to expose free sulfhydryl groups. AVE1642 contains approximately 90 lysine residues, with around 30 accessible for modification [17]. We performed the SATP modification of AVE1642 (to create AVE1642-SATP) with the degree of functionalization 25 equiv. of SATP per antibody, randomly modifying the amine groups of the exposed lysine residues. The yield of the reaction was 85%.

III.2.3. Design and Synthesis of PGA-AVE1642 Conjugates

The conjugation of PGA-PD to AVE1642-SATP exploited the formation of reduction-sensitive disulfide bonds between the PD groups of the modified PGA and the sulfhydryl groups introduced into the structure of AVE1642. While naturally occurring cysteine residues should not be involved in the coupling reaction, as they are present in the disulfide-bonded state, we do note that studies have detected free sulfhydryl groups in IgG samples from serum and recombinant antibodies [18]. We performed the conjugation reaction in the presence of hydroxylamine hydrochloride to deprotect the acetyl group of AVE1642-SATP using different equiv. of PGA (from 5 to 25 equiv.), producing PGA-AVE1642 with different degree of functionalization (from 2 to 10). We removed any excess of the unreacted polymer by ultracentrifugation. The quantification of PGA chains attached to a molecule of AVE1642 was determined by amino acid analysis.

Focusing on the most straightforward approach, with the least PGA chains per mAb, we prepared two batches of PGA-AVE1642 conjugates in which the quantification of PGA chains was 2.2 and 2.8, respectively. The yield of both reactions was 70%. This data confirms the reproducibility of established conjugation protocol.

Figure 2 shows a schematic representation of the general synthetic strategy followed to achieve PGA-AVE1642 conjugates.

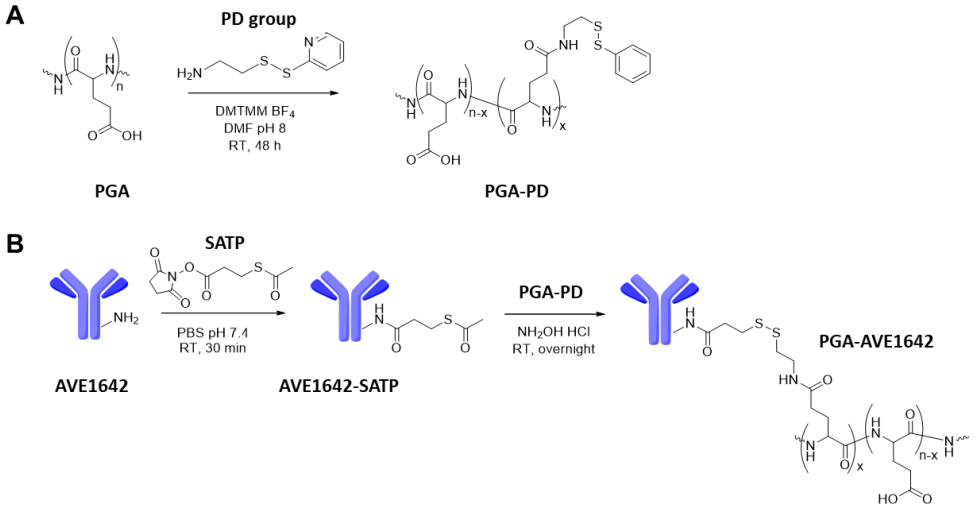

Figure 2: Reaction Scheme of AVE1642 Conjugation to PGA. A) PGA is modified by the PD group to obtain PGA-PD. **B)** AVE1642 is modified by SATP and subsequently conjugated with PGA-PD to obtain the final product PGA-AVE1642.

III.3. Cytotoxicity Analysis Suggests that High Levels of PGA Conjugation do not Negatively Influence AVE1642 Activity in the Adequate Prostate Cancer (PCa) Cell Line.

III.3.1. Selection of Adequate PCa Cell model

AR positively regulates TMPRSS2 gene expression, thereby leading to high levels of the expression of this transmembrane serine protease in prostate tissue. However, upon the formation of the T2E fusion gene, which is overexpressed in certain PCa cell lines [19, 20], the androgen-responsive promoter of the TMPRSS2 genes becomes rearranged within the coding region of the ETS-related gene (ERG), leading to ERG overexpression [21, 22]. High levels of ERG protein then transactivate IGF-1R expression by binding to the promotor. For these reasons, we

analyzed the protein expression levels of IGF-1R-β, AR, and ERG in a panel of PCa cell lines (VCaP, LnCaP, DU-145, 22Rv1, PC-3) and a normal prostate cell line (RWPE-1) by Western blot (**Figures 3.A** and **B**) to confirm the optimal cell line in which to assess PGA-AVE1642 activity.

Overall, we discovered that VCaP cells expressed the highest levels of IGF-1R-β and AR when compared to the other cell lines, while VCaP cells were the only cell line to show detectable levels of ERG protein expression (**Figures 3.A** and **B**).

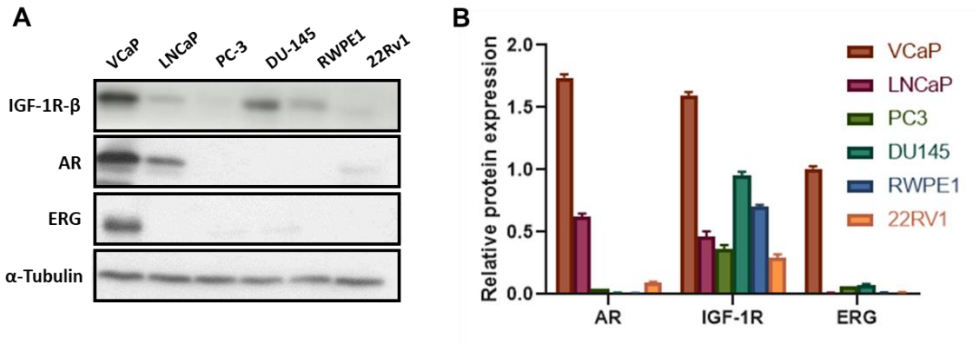

Figure 3: Protein Expression Profiles of Select PCa Cell Lines. A) Western blot analysis of IGF-1R-β, AR, ERG, and α-tubulin in VCaP, LnCaP, DU-145, 22Rv1, and PC-3 PCa cell lines and RWPE-1 as a normal prostate tissue. **B)** Quantified protein expression relative to α-tubulin expression in each PCa cell line. Data expressed as mean±SEM, n=3.

These findings support previous studies reporting that VCaP cells possess the T2E fusion gene and, therefore, overexpress ERG and IGF-1R [23-26]. Furthermore, these findings confirm VCaP cells as the best cell line candidate from those assessed to evaluate the activity of our PGA-AVE1642.

III.3.2. Cytotoxicity of AVE1642 derivatives

Before continuing with an exhaustive characterization with all synthesized conjugates, we analyzed cytotoxicity via MTT assay using a concentration range of 0.003-50 µg/ml AVE1642 equiv. and a 72h incubation in VCaP cells (**Figure 4**). The full characterization of the VCaP cell line can be found in **Section III.4**. Overall, we discovered a trend towards lower cell viability in response to increasing concentrations of PGA-AVE1642 conjugates; however, we failed to observe any significant correlation between PGA chain number and cytotoxicity.

Overall, this suggests that increasing levels of PGA modification do not significantly influence the cytotoxicity/function of AVE1642, high levels of PGA conjugation do not negatively influence AVE1642 activity. However, for chemical economy and simplicity, we moved ahead with the 2:1 PGA-AVE1642 (average 2.8 PGA chains per AVE1642, **Table 1**) conjugate (minimal modification) for all subsequent experiments in this thesis.

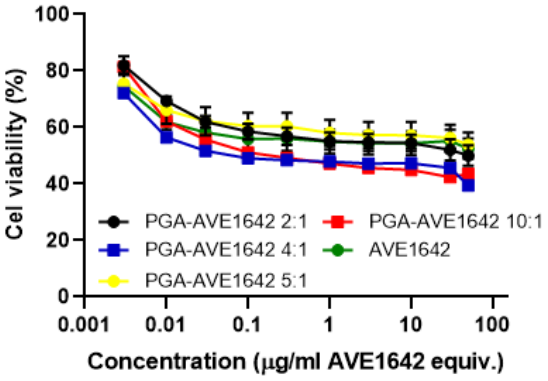

Figure 4: AVE1642 Activity Unaltered after PGA Modification. Graphs represent VCaP cell viability following exposure to PGA-AVE1642 conjugates with increasing numbers of PGA chains per AVE1642 compared to AVE1642 as control versus concentration (µg/ml AVE1642 equiv.). VCaP cells were treated with all the compounds at for 72 h at 37ºC at concentrations between 0.003 and 50 µg/ml AVE1642 equiv. Data expressed as mean±SEM, n>3.

III.4. Characterization of 2:1 PGA-AVE1642 conjugate

We performed full characterization of selected 2:1 PGA-AVE1642 conjugate in order to fully understand how PGA could alter mAb conformation and to assess size, charge, and structure aiming to have the premises for a batch to batch reproducibility process that would facilitate translation if needed.

III.4.1. SDS-PAGE Gel Electrophoresis Analysis

We first characterized the PGA-AVE1642 conjugate by SDS-PAGE (sodium dodecyl sulfate-polyacrylamide gel electrophoresis) to assess hydrodynamic volume. **Figure 5** shows the appearance of unmodified AVE1642 (Mw = 178.5 kDa) as a band at 150-160 kDa, while SATP-modified AVE1642 presented a similar band pattern and, therefore, size. Of note, we did not observe additional species at higher Mw, suggesting the absence of protein dimers or aggregates upon derivatization. The SDS-PAGE analysis of PGA-AVE1642 established a shift to a higher Mw when compared to AVE1642 with a smeared band present between 160 and 220 kDa. PGA alone cannot be detected by SDS PAGE using Coomassie blue staining, although the observed increase in the Mw after polymer conjugation provides evidence of the successful formation of PGA-AVE1642 conjugate.

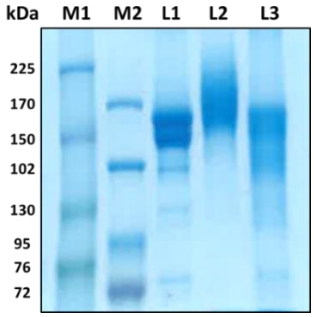

Figure 5: SDS-PAGE (5%) of AVE1642 (≈ 150-160 kDa; L1); PGA-AVE1642 (≈ 160-220 kDa; L2) and AVE1642-SATP (≈150-160 kDa; L3). M1 and M2 are protein markers for different molecular weights. Proteins were stained with Coomassie blue.

III.4.2. Size Analysis by Size Exclusion Chromatography

We next analyzed compound size (hydrodynamic radius) by size exclusion chromatography (SEC), which is based on the separation of compounds by their hydrodynamic volumes: higher molecular weights provide smaller elution volumes and vice-versa. We found an elution volume of unconjugated AVE1642 of 1.7 ml, while the peak of the polymer-antibody conjugate shifted to 1.5 ml, indicating an increase in the hydrodynamic radius.

SATP conjugation to AVE1642 failed to alter the retention volume significantly and, therefore, size, as expected. Peak PGA-PD displayed a retention volume of 2 ml (**Figure 6.A**). In the presence of 50 mM dithiothreitol (DTT), a reducing agent that reduces disulfide bridges, AVE1642 maintained its stability as the elution peak did not change from the retention volume (1.7 ml). However, the incubation of PGA-AVE1642 with DTT led to linker cleavage as the elution peak shifted to a value similar to the retention volume of unconjugated AVE1642 demonstrating its bioresponsiveness (**Figure 6.B**).

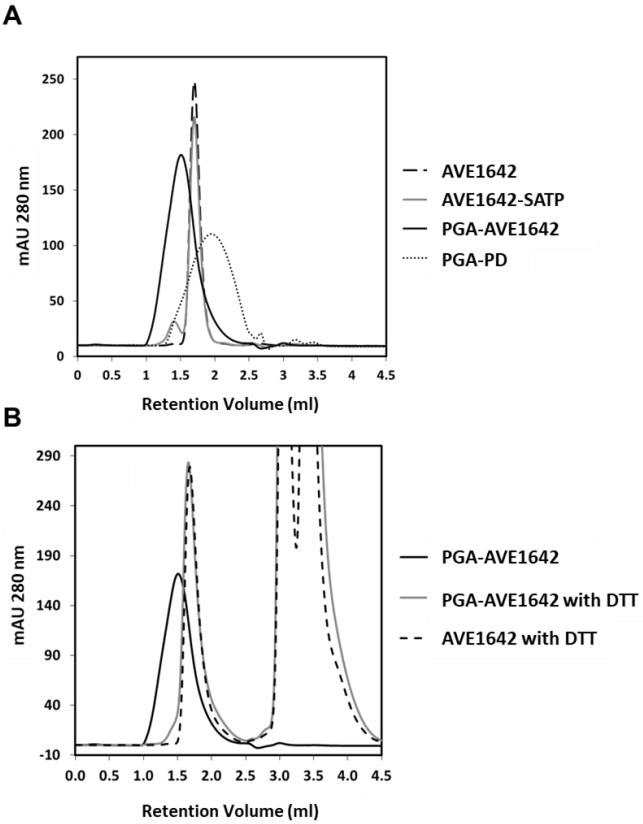

Figure 6: SEC profiles of **A)** AVE1642 (discontinuous black line), AVE1642-SATP (continuous grey line), PGA-AVE1642 (continuous black line), PGA-PD (black dotted line), and **B)** PGA-AVE1642 (continuous black line), PGA-AVE1642 incubated with DTT (continuous grey line), AVE1642 incubated with DTT (discontinuous black line). The y-axis of the chromatogram is a measure of the intensity of absorbance at 280 nm (in units of mAU, or milli-absorbance units).

III.4.3. Size and Charge Analysis by Dynamic Light Scattering and Z-Potential Analyses

Dynamic light scattering (DLS) analysis provides another estimate of size, and we established a hydrodynamic diameter of 13.5 ± 1.7 nm (by intensity) and 7.4 ± 0.6 nm (by number) for unconjugated AVE1642 [27]. Upon conjugation with PGA, we observed an increment in the hydrodynamic size to 17.5 ± 0.6 nm (by

intensity) and 9.4 ± 0.5 nm (by number) due to the contribution of the PGA chains (**Figure 7.A** and **B**).

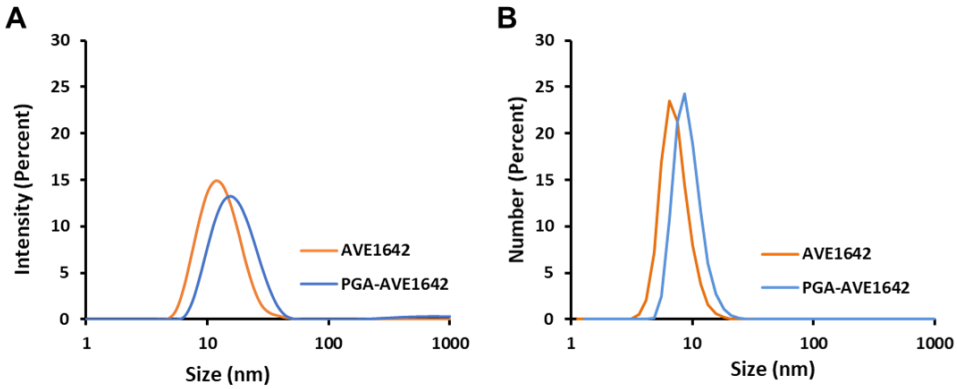

Figure 7: DLS-based evaluation of the average diameter for **A)** AVE1642 and PGA-AVE1642 by intensity. **B)** AVE1642 and PGA-AVE1642 by number.

Zeta potential analysis (provides a measure of charge) of AVE1642 in PBS (pH 7.4) revealed a near-neutral value (-0.5 mV). Once conjugated to PGA, the presence of additional carboxylic groups from the polymer in the conjugate increased the negative charge, and we determined a zeta potential value of -11.7 mV for PGA-AVE1642.

III.4.4. Structural Analysis by Circular Dichroism

We evaluated the secondary structure of AVE1642 and its derivatives by far-UV circular dichroism (FUV-CD) spectroscopy, measuring ellipticity between 200 and 250 nm. We found an AVE1642 spectrum characterized by a single negative peak with a minimum at a wavelength of 216 nm (**Figure 8**), as expected for the β-sheet structure of the immunoglobulin fold [28]. SATP modification of AVE1642 failed to change the secondary structure, as the dichroic signal of AVE1642-SATP remained similar to unmodified AVE1642. At neutral pH, PGA exhibits an extended or disordered random coil due to Coulombic repulsion between ionized glutamate side chains [29]. FUV-CD analysis of PGA-AVE1642 suggested that polymer

conjugation perturbed the β-sheet structure of the antibody given the observed change in the dichroic signal; however, these changes can be attributed to the additional contribution of the PGA spectra rather than a significant alteration to antibody conformation.

We next treated PGA-AVE1642 with DTT to promote the disruption of the antibody-PGA linkers to evaluate whether PGA conjugation irreversibly modifies the AVE1642 structure. FUV-CD analysis following DTT treatment and removal of free PGA by ultracentrifugation established that native AVE1642 and AVE1642 after PGA removal displayed similar CD spectra, suggesting that the conjugation process did not alter the secondary structure of the antibody (**Figure 8**).

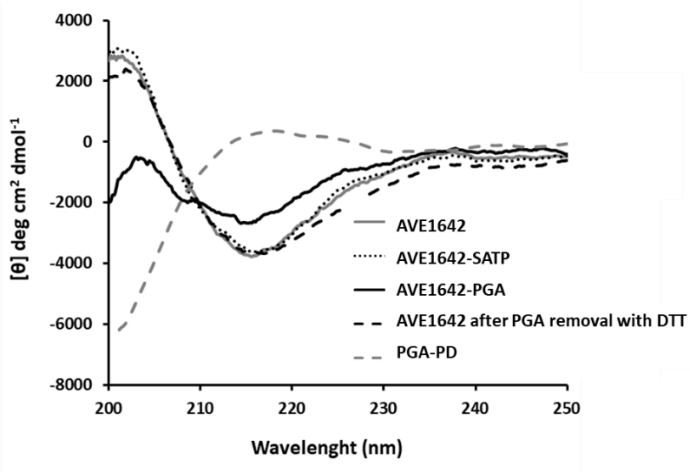

Figure 8: FUV-CD spectra of AVE1642, AVE1642-SATP, PGA-AVE1642, AVE1642 after PGA removal, and PGA-PD.

Finally, we employed CD analysis at 216 nm with a temperature range between 25 to 90ºC to assess thermal stability (**Figures 9.A** and **B**). We failed to observe any change to the dichroic signal for AVE1642 and AVE1642-SATP below 65ºC; however, above this temperature, the antibody began to denature until the signal reached a minimum at approximately 77-79ºC. Denaturation then rapidly increased until protein precipitation.

PGA-AVE1642 exhibited a stable dichroic signal until 55ºC, although heat-induced denaturation failed to promote precipitation of the conjugate, suggesting that PGA-conjugation increased AVE1642 stability at higher temperatures (**Figure 9.A**). We assumed 100% folding of protein structure at 25ºC and 100% unfolded when the ellipticity reached a minimum; from these values, we calculated melting temperatures (T_m) for AVE1642, AVE1642-SATP, and PGA-AVE1642 of 72.5±0.2, 71.7±0.1, and 68±0.1 °C, respectively (**Figure 9.B**).

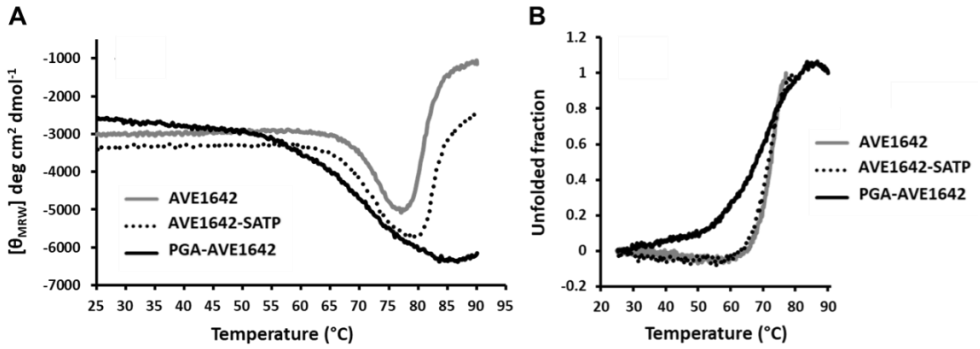

Figure 9. Evaluation of Thermal Denaturation of AVE1642, AVE1642-SATP, and PGA-AVE1642 by CD. **A)** Effect of temperature on molar ellipticity at a wavelength of 216 nm. **B)** fraction of unfolded protein in the range 25-90ºC. The fraction of unfolded protein was calculated by assuming samples were completely folded and completely unfolded at 25ºC and when the ellipticity reached the minimum, respectively.

Overall, the characterization of PGA-AVE1642 demonstrated the successful nature of the conjugation process as the hydrodynamic volume of PGA-AVE1642 conjugate increased due to the presence of the polymer, as shown by SEC, SDS-PAGE, and DLS analysis. Moreover, we provided further evidence for PGA conjugation by the increment in the negative charge of the conjugate, as measured by zeta potential analysis. Finally, CD analysis demonstrated the lack of any significant alterations to the secondary structure of AVE1642.

The following table shows a summary of the different characterization techniques used above (**Table 1**).

	Theoretical Ratio PGA:AVE1642	Exp. Ratio [a]	Size (nm) [b] Intensity Number	PDI [b]	Z-pot (mV) [b]	T melt PBS (ºC) [c]
AVE1642	0:1	0:1	13.5 ± 1.7 7.4 ± 0.6	0.12 ± 0.03	-0.5 ± 0.3	72.5 ± 0.2
PGA-AVE1642	2:1	2.8:1	17.5 ± 0.6 9.4 ± 0.5	0.23 ± 0.03	-11.7 ± 0.9	68 ± 0.1

a. As determined by amino acid analysis b. As determined by DLS c. As determined by CD.

Table 1: Summary of the different characterization techniques.

III.5. PGA-conjugation Enhances Stability, Improves Affinity for IGF-1R and Maintains Hemocompatibility of AVE1642

We next evaluated the stability, function (by assessing affinity for IGF-1R), and hemocompatibility in mouse serum of AVE1642 and PGA-AVE1642 in order to investigate AVE1642 benefits after PGA conjugation and test safety before testing both compounds in further animal studies.

III.5.1. PGA-conjugation Protects AVE1642 from Degradation

We performed stability studies based on an ELISA assay to evaluate the capacity of AVE1642 and PGA-AVE1642 to bind IGF-1R. We incubated 5 µg/ml of AVE1642 and PGA-AVE1642 at 37ºC in standard FBS from 24 to 72 hours to study AVE1642 degradation, and then assessed levels of IGF-1R binding in a VCaP protein lysate that contains high levels of IGF-1R. Any antibody will lead to reduced target binding, as quantified through AVE1642 and PGA-AVE1642 calibration curves (**See Chapter II**, **Section II.2.3.7**). **Figure 10** shows the relative degradation (in percentage) of AVE1642 and PGA-AVE1642 over time (hours). When compared to PGA-AVE1642, which remains relatively stable over time, AVE1642 displays

significantly increased degradation at all time points analyzed, reaching 80% degradation by 72 hours. These results suggest that PGA conjugation improves AVE1642 stability and, therefore, supports enhanced functionality over extended times following administration.

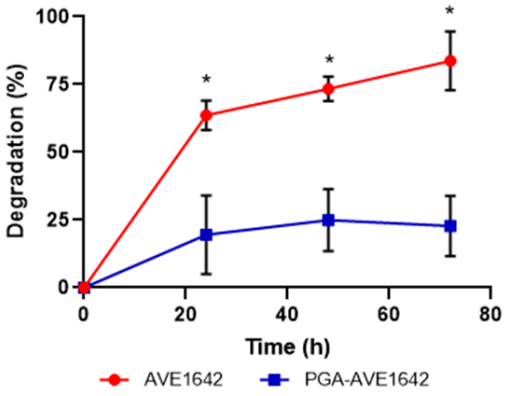

Figure 10: AVE1642 and PGA-AVE1642 Stability Studies. Graphs depict the percentage of degradation vs. time (24, 48, and 72 hours). Data expressed as mean±SEM, n=3. Statistical analysis performed using a paired t-test, *p< 0.05.

III.5.2. PGA Conjugation Enhances the Affinity of AVE1642 for IGF-1R

We employed IGF-1R receptor-binding assays with AVE1642 and PGA-AVE1642 to evaluate their affinity for IGF-1R in VCaP cell lysate using an ELISA assay. We employed varying concentrations of AVE1642 and PGA-AVE1642 (0-10 µg/ml AVE1642 equiv.) diluted in 1X PBS and incubated in the VCaP cell lysate to detect the concentration at which the IGF-1R begins to saturate.

Figure 11 demonstrates the absorbance of both compounds at various concentrations (µg/ml AVE1642 equiv.), showing that PGA-AVE1642 produces an IGF-1R saturation at 2 µg/ml AVE1642 equiv. (observed as a plateau in absorbance). However, we failed to observe IGF-1R saturation with AVE1642 at any of the concentrations tested, suggesting that PGA conjugation increased the affinity of

AVE1642 for IGF-1R. Moreover, PGA-AVE1642 showed significantly higher absorbance over all the concentrations compared with the AVE1642 suggesting higher PGA-AVE1642 binding to IGF-1R compared to AVE1642 treatment.

We also used this data to determine various parameters, including the dissociation constant (K_d) and the maximum binding (B_{max}). For the AVE1642 K_d=3.058 nM and B_{max}=2.675 fmol/mg protein, moreover for the PGA-AVE1642 K_d=0.4524 nM and B_{max}=2.971 fmol/mg protein. The K_d is the concentration of the ligand that occupies half of the receptors at equilibrium, and the B_{max} represents the density of available receptors. While PGA-AVE1642 and AVE1642 displayed similar B_{max} values, we discovered a clear difference between K_d values. PGA-AVE1642 possessed a higher K_d than AVE1642, again suggesting an increase in affinity for IGF-1R. Of note, the similar B_{max} values for both compounds indicate a similar level of IGF-1R expression in the VCaP cell lysate.

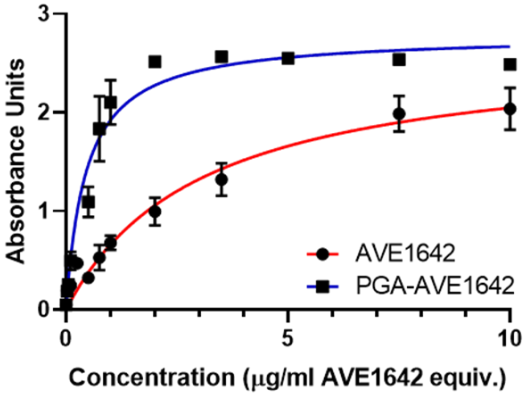

Figure 11: IGF-1R Receptor-binding Assays Comparing PGA-AVE1642 with AVE1642. Graphs depict absorbance vs. concentration (µg/ml). The assay was performed at different AVE1642 and PGA-AVE1642 concentrations in 40 µg of VCaP cell lysate. Data expressed as mean±SEM, n=3. Statistical analysis was performed using a paired t-test, **p< 0.01.

Overall, we demonstrate that PGA-AVE1642 possesses a higher affinity for IGF-1R, thereby a lower concentration of PGA-AVE1642 will saturate the IGF-1R

when compared to the unconjugated mAb. Therefore, we provide evidence that PGA conjugation improves the interaction of AVE1642 with IGF-1R.

III.5.3. PGA Conjugation of AVE1642 does not Promote Hemolysis

We next performed hemolytic studies using isolated male C.B-17/IcrHan®Hsd-*Prkdc*^{scid} red blood cells (RBCs) to study hemocompatibility (and, therefore, safety) of AVE1642 and PGA-AVE1642. We incubated both compounds at 125 µg/ml final concentration (AVE1642 equiv.) in RBCs and compared the log percentage of hemolysis to Triton X-100 (positive control) and dextran (negative control) treatments (**Figure 12**). We failed to encounter any significant levels of hemolysis upon treatment with AVE1642 and PGA-AVE1642 as both gave values similar to the negative control demonstrating hemocompatibility.

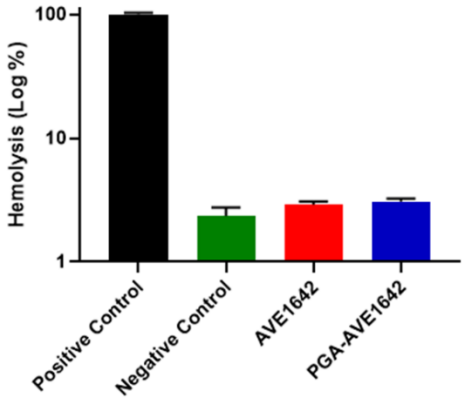

Figure 12: Hemolysis Studies. Hemolytic studies were performed in C.B-17/IcrHan®Hsd-*Prkdc*^{scid} male mice erythrocytes employing 125 µg/ml of AVE1642 and PGA-AVE1642 (AVE1642 equiv.), Triton X-100 as a positive control (stated 100%) and dextran as a negative control. Data expressed as mean±SEM, n=3. Statistical analysis was performed using ANOVA.

III.6. AVE1642 and PGA-AVE1642 Displays Cell Line Specific Cytotoxic Activity

We next investigated the cytotoxic effects of AVE1642, PGA-AVE1642, and PGA alone by assessing cell survival in VCaP cells to determine IC_{50} values of each compound and in additional PCa and normal prostate cell lines to confirm specificity regarding the presence of T2E.

III.6.1. Cytotoxicity of AVE1642 and PGA-AVE1642 in VCaP Cells

We treated VCaP cells with AVE1642 and PGA-AVE1642 at concentrations between 0.003 and 50 μg/ml of AVE1642 equiv. for 72 h. We then calculated the amount of PGA equiv. at each PGA-AVE1642 concentration used to be used as control at concentrations (between 0.0064 and 64.37 μg/ml) to confirm whether any differences in PGA-AVE1642 efficacy relate to PGA conjugation or presence of PGA.

Figures 13.A and **B** demonstrate the alterations to VCaP cell viability following treatment with increasing concentrations of AVE1642, PGA-AVE1642, and PGA by MTS assay. **Figure 13.A** establishes that AVE1642 or PGA-AVE1642 act in a similar manner (increased cytotoxicity/decreased cell viability with an increase in concentration) with an IC_{50} for both compounds established as 0.1 μg/ml AVE1642 equiv. Of note, the plateau in the cell viability curve may indicate the presence of IGF-1R saturation. Meanwhile, **Figure 13.B** establishes a lack of cellular toxicity generated by PGA at any concentration evaluation.

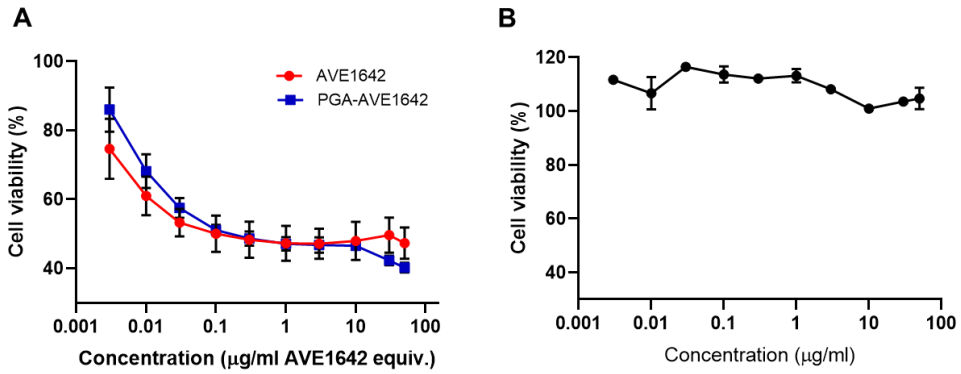

Figure 13: Cytotoxic effects of AVE1642, PGA-AVE1642, and PGA in VCaP Cells Measured by MTS Assay. A) Cell viability following treatment with AVE1642 and PGA-AVE1642. VCaP cells were treated with both compounds for 72 h at 37ºC using concentrations between 0.003 and 50 µg/ml AVE1642 equiv. **B)** VCaP Cell viability following PGA treatment. VCaP cells were treated with PGA at concentrations between 0.0064 and 64.37 µg/ml for 72 h. Data expressed as mean±SEM, n>3.

Overall, these data suggest that AVE1642 induces cytotoxicity, PGA conjugation of AVE1642 does not negatively influence this cytotoxicity, and PGA alone does not promote cytotoxicity in VCaP cells.

III.6.2. Lack of Cytotoxicity of AVE1642 and PGA-AVE1642 in Alternative PCa Cell Lines

We next exposed LnCaP, DU-145, 22Rv1, PC-3 and RWPE-1 cells (and VCaP as control) to AVE1642 (**Figure 14.A**) and PGA-AVE1642 conjugate (**Figure 14.B**) at concentrations between 0.003 and 50 µg/ml AVE1642 equiv. for 72 h and assessed cell viability by MTS assay to confirm the specificity of AVE1642/ PGA-AVE1642 towards T2E presence.

As expected, AVE1642 and PGA-AVE1642 treatments provided similar results in the T2E-bearing VCaP cell line, which displayed a marked sensitivity to treatment (**Figures 14.A** and **B**) [25]. Interestingly, in the other cells tested, only

22Rv1 cells displayed slight sensitivity to the treatments, with an observed 20% decrease in cell viability observed at the higher concentrations (green line, **Figures 14.A** and **B**). This result is most probably related to ERG levels. Although in our experiments using western blot technique (**Figures 3.A** and **B**), we failed to detect ERG levels most probably due to detection limits; it has been reported the existence of ERG levels in 22Rv1 cell line detected by qPCR [30]. Thus, these results suggest that the effectiveness of the treatment depends on the ERG cellular levels. To corroborate this finding, we would need further studies to detect ERG levels using a more sensitive technique such as qPCR.

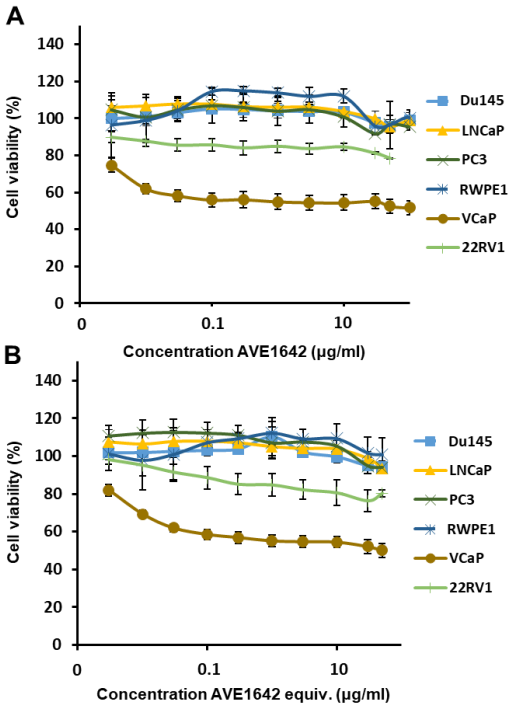

Figure 14: Lack of Cytotoxic Effects of AVE1642 and PGA-AVE1642 in Alternative PCa cell lines. Graphs depict cell viability vs. concentration (µg/ml AVE1642 equiv.) in VCaP, LnCaP, DU-145, 22Rv1, PC-3, and RWPE-1 cell lines. **A)** Cell viability in cells treated with AVE1642. **B)** Cell viability in cells treated with PGA-AVE1642. Both treatments were incubated in cells for 72 h at 37ºC, using concentrations between 0.003 and 50 µg/ml AVE1642 equiv. Data expressed as mean±SEM, n>3.

Overall, only VCaP cells significantly respond to AVE1642 and PGA-AVE1642 exposure, most likely due to the high IGF-1R levels (induced by the overexpression of ERG protein caused by the presence of the T2E fusion gene) and the added overexpression of AR proteins (which also induce the expression of ERG) (**Figures 3.A** and **B**).

III.6.3. AVE1642 and PGA-AVE1642 Mediated Cytotoxicity depends on ERG Expression

To ratify these results, we assessed the requirement of the T2E fusion gene for the activity of AVE1642 and PGA-AVE1642 by silencing ERG expression via small interfering (si)RNA and carrying out Trypan blue dye exclusion cell viability experiments and evaluating ERG protein expression by Western blot assay after treatment with AVE1642 and PGA-AVE1642 (**Figure 15.A**). Following the transfection of VCaP cells with the ERG siRNA or a scrambled siRNA control, we treated cells with AVE1642 and PGA-AVE1642 at 0.1 µg/ml AVE1642 equiv. for 72h. We also treated cells with PGA as control at 0.085 µg/ml (PGA equiv. in the PGA-AVE1642 conjugate at 0.1 µg/ml of AVE1642) and included control cells that were transfected but not treated with AVE1642 and PGA-AVE1642.

Figure 15.B-D depicts the change in cell number (in fold) in response to the various treatments and a representative Western blot that confirms the effective silencing of ERG.

After normalizing the data to the respective controls, we discovered that ERG silencing promotes cell survival during exposure of cells to AVE1642 (**Figure 15.B**) and PGA-AVE1642 (**Figure 15.C**). We observed significant differences observed between untransfected AVE1642-treated cells (NT AVE1642) and ERG siRNA + AVE1642-treated cells (siERG AVE1642) and between the scrambled siRNA control + AVE1642-treated cells (SCR AVE1642) and the ERG siRNA + AVE1642-

treated cells (siERG AVE1642). We also observed significant differences between untransfected PGA-AVE1642 treated cells (NT PGA-AVE1642) and ERG siRNA + PGA-AVE1642 treated cells (siERG PGA-AVE1642) and highly significant changes between scrambled siRNA control + PGA-AVE1642-treated cells (SCR PGA-AVE1642) and ERG siRNA + PGA-AVE1642-treated cells (siERG PGA-AVE1642). We also confirmed the lack of cytotoxicity of PGA (**Figure 15.D**).

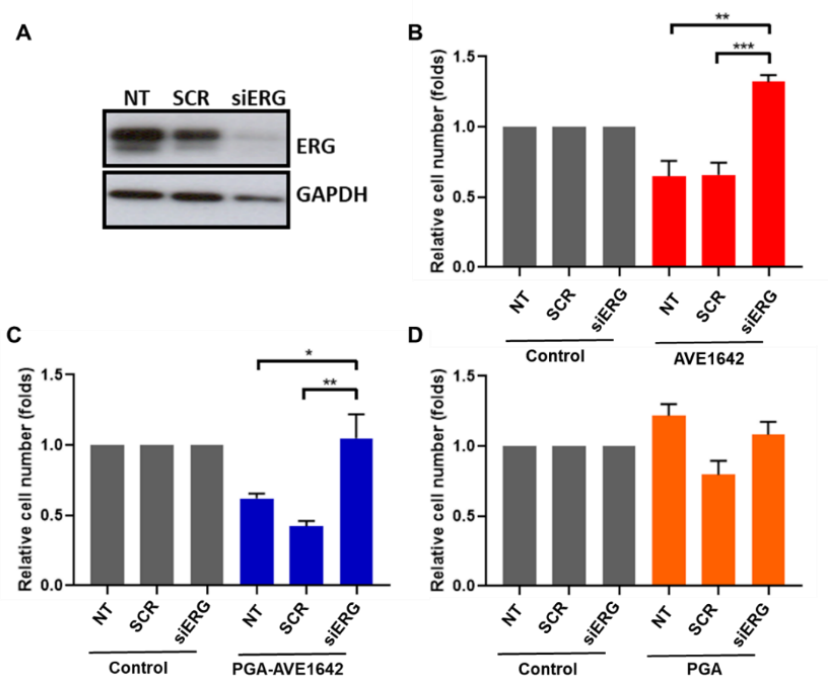

Figure 15: Cell Viability following AVE1642 and PGA-AVE1642 Treatment in the Absence of ERG Expression in VCaP Cells. A) Representative Western blot image shows ERG expression in untransfected VCaP cells (NT) and VCaP cells treated with scrambled siRNA (SCR) and ERG siRNA (siERG). **B-D)** Graph shows cell survival (as measured by Trypan Blue exclusion assay) in untransfected VCaP cells (NT), VCaP cells transfected with scrambled control siRNA (SCR), and VCaP cells transfected with siRNA against ERG (siERG) treated with AVE1642, PGA-AVE1642, or PGA at 0.1 µg/ml AVE1642 equiv. concentration and 0.085 µg/ml PGA equiv. concentration. Data expressed as mean±SEM, n>3. Statistical analysis was performed using ANOVA, *p< 0.05, **p< 0.01.

Overall, these findings establish that the cytotoxic effects of AVE1642 and the PGA-AVE1642 in VCaP cells require the ERG overexpression associated with the presence of the T2E fusion gene. Furthermore, this data provides additional evidence that PGA modification does not alter the function of AVE1642.

III.7. PGA-conjugation Leads to Altered Molecular Responses and Cellular Trafficking *in vitro*

After establishing that AVE1642 and PGA-AVE1642 treatment promotes ERG-dependent cytotoxicity in VCaP cells, we investigated the possibly modified interaction of AVE1642 and PGA-AVE1642 with IGF-1R. To achieve this objective, we evaluated the internalization of IGF-1R, studied AVE1642 and PGA-AVE1642 energy-dependent internalization, and explored cellular trafficking.

III.7.1. PGA-conjugation Prevents IGF-1R Internalization after AVE1642 Binding

We investigated IGF-1R internalization in VCaP cells using the IN-Cell Analyzer 6500HS, a laser-based high-content imaging system featuring IRIS confocal technology to optimize cellular imaging. We treated cells for 15, 30, and 60 minutes in the presence of AVE1642, PGA-AVE1642, and the activating ligand Insulin-like growth factor 1 (IGF-1) as a positive control (0.1 μg/ml) and untreated cells as a negative control and then assessed IGF-1R-β localization by immunofluorescence.

Imaging analysis suggested the presence of IGF-1R primarily at the cell membrane in untreated cells (**Figure 16.A** - w/o treatment) with low levels of intracellular IGF-1R. Both IGF-1 and AVE1642 prompted similar levels of IGF-1R internalization; however, PGA-AVE1642 treatment did not prompt a similar level of internalization and remained primarily at the cell membrane (**Figure 16.A**).

Intracellular IGF-1R quantification (**See Chapter II**, **Section II.2.8**) confirmed the imaging results, demonstrating an increase in IGF-1R intracellular levels after IGF-1 treatment over time (**Figure 16.B**). While AVE1642 treatment provided a similar result, treatment with PGA-AVE1642 led to significantly reduced intracellular levels of IGF-1R at 30 and 60 minutes, 5 and 32 folds, respectively, compared with the AVE1642 treatment (**Figure 16.B**).

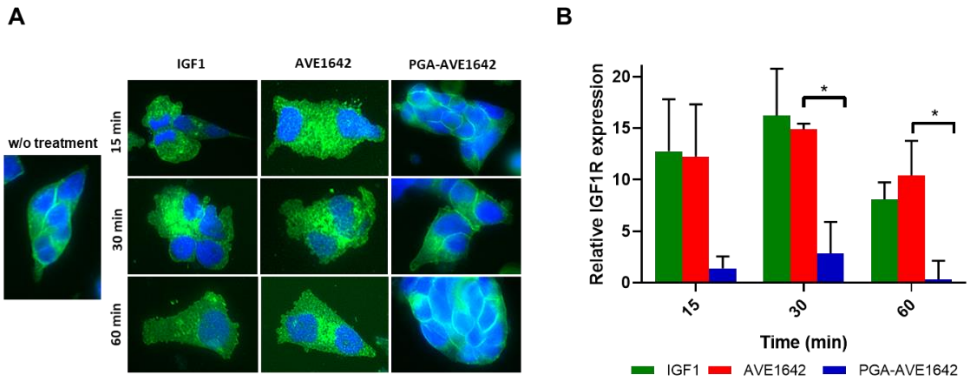

Figure 16: Subcellular Localization and Quantification of IGF-1R by IN Cell analysis. VCaP cells treated for 15, 30, and 60 minutes with 0.1 µg/ml IGF-1, AVE1642, and PGA-AVE1642. **A)** Images show IGF-1R localization following different treatments over time. DAPI (blue) stains the nucleus, while Alexa Fluor anti-rabbit-488 (green) marks the presence of IGF-1R-β. **B)** The relative percentage of IGF-1R levels at different times in the different conditions normalized to basal IGF-1R levels in cells without treatment. Data expressed as mean±SEM, n=3. Statistical analysis performed using two-way ANOVA, *$p < 0.05$.

These results suggest that PGA conjugation of AVE1642 allows for IGF1-R binding at the cell membrane but could delay IGF1-R internalization potentiating; therefore, the inhibitory signal downstream of IGF-1R.

III.7.2. PGA-conjugation of AVE1642 Prevents Energy-dependent Internalization

We next performed endocytic studies to understand how PGA-conjugation affects AVE1642 cellular internalization. For this purpose, we fluorescently labeled AVE1642 and PGA-AVE1642 with the fluorophore Cy5.5 (**See Chapter II**, **Section II.2.2**). To select PGA-AVE1642-Cy5.5 and AVE1642-Cy5.5 concentrations, avoiding quenching effects, we generated fluorescent calibration curves for AVE1642-Cy5.5 and PGA-AVE1642-Cy5.5 (**See Chapter II**, **Section II.2.7.1**). Final chosen concentrations were 0.16 mg/ml of AVE1642 equiv. (or 0.1 mg/ml of polymer). We then incubated VCaP cells for 15, 60, and 180 minutes at 4ºC and 37ºC to evaluate energy-dependent uptake mechanisms, analyzing both the percentage of positive cells (containing PGA-AVE1642-Cy5.5 or AVE1642-Cy5.5) and measuring the fluorescent intensity (FI) from each positive cell. With this data, we quantified the cell internalization efficacy.

The percentage of positive cells (**Figure 17.A**) represents the cells that have internalized AVE1642-Cy5.5 or PGA-AVE1642-Cy5.5 at 4ºC and 37ºC; overall, we obtained the same profile under all conditions tested. We detected an increase in the percentage of positive cells up to 15 minutes, followed by a plateau. Also, a markedly higher uptake at 37ºC than at 4ºC for AVE1642 when compared to PGA-AVE1642 (**Figure 17.A)**, suggesting that AVE1642 is internalized by energy-dependent internalization. In contrast, PGA-AVE1642 showed inhibited energy-dependent internalization, as can be shown by the lack of difference between 37ºC and 4ºC.

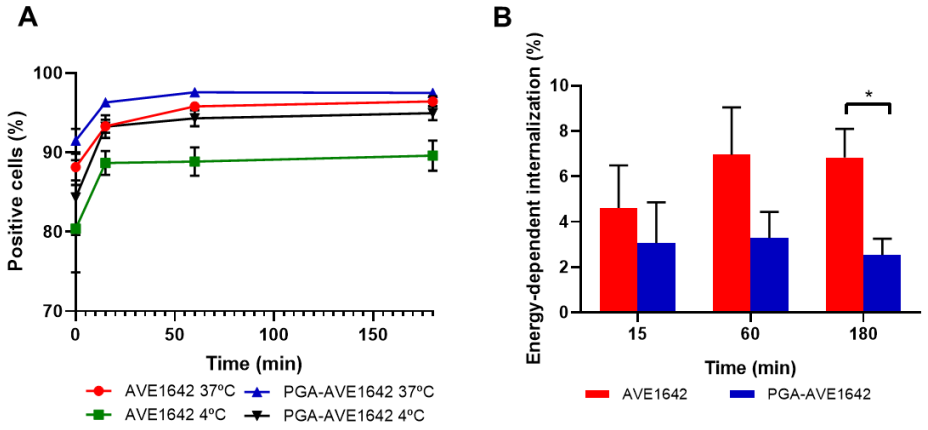

Figure 17: Cell Internalization of AVE1642-Cy5.5 and PGA-AVE1642-Cy5.5 in VCaP cells. A) Percentage of positive cells versus time. **B)** Energy-dependent internalization at 15, 60, and 180 minutes. Autofluorescence was subtracted from each measurement prior to analysis, and a minimum of 10,000 events per sample was analyzed in living single cells. Data expressed as mean±SEM, n=3. Statistical analysis was performed using ANOVA, *$p < 0.05$.

This data illustrated in **Figure 17.B** depicts the amount of compound that internalized in the cell and confirms the different internalization mechanisms between AVE1642 and PGA-AVE1642, with a significant difference, observed at 180 mins. Overall, PGA-AVE1642 displays less or inhibited energy-dependent internalization in VCaP cells when compared to AVE1642.

In summary, we established a lower internalization rate for PGA-AVE1642 when compared to AVE1642, which supports previous imaging-based analysis that indicated an increased colocalization of PGA-AVE1642 at the cell membrane.

III.7.3. PGA-conjugation Modifies AVE1642 Cell Trafficking

Given that the data obtained so far supported differences occurring in the cell internalization mechanisms of PGA-AVE1642-Cy5.5 vs. free AVE1642-Cy5.5, we further analyzed any difference in the final intracellular cell fate in VCaP cells. We

studied colocalization with endocytic vesicle markers clathrin and caveolin-1, as studies have suggested that IGF-1R internalizes via clathrin and caveolin-mediated endocytosis [31]. Furthermore, we studied the colocalization of the labeled compounds with cell organelle markers, including lysosomes (LAMP1) and early endosomes (EEA1), given that many macromolecular systems pass through the lysosomotropic endocytic pathway [32].

We treated VCaP cells for 30 minutes with PGA-AVE1642-Cy5.5 and AVE1642-Cy5.5 at 0.1 mg/ml polymer (PGA-AVE1642) and AVE1642-Cy5.5 at 0.16 mg/ml of AVE1642 equiv. We studied the interactions of PGA-AVE1642-Cy5.5 and AVE1642-Cy5.5 with the endocytic pathway by evaluating colocalization with clathrin and caveolin-1 (**Figure 18**) via confocal microscopy. We discovered that AVE1642-Cy5.5 (red) colocalized with clathrin (blue) (**Figure 18.A** upper panel) and IGF-1R-β (green) to a higher degree than with caveolin-1 (blue) (**Figure 18.A** lower panel) as demonstrated in the merge and merge 3X images. We also established that PGA-AVE1642-Cy5.5 (red) colocalized with IGF-1R-β (green) and caveolin-1 (blue) (**Figure 18.B** lower panel) but not clathrin (blue) (**Figure 18.B** upper panel), as demonstrated in the merge and merge 3X images. Of note, while both compounds colocalize with IGF-1R, the receptor displays retention at the membrane in PGA-AVE1642-Cy5.5 treated cells, while displaying a more cytoplasmic localization in AVE1642-Cy5.5 treated cells.

These findings are supporting by the graphics to the far right of both upper and lower panels of **Figure 18.A** and **B** that illustrates the red, green, and blue channel fluorescent intensity profile across the added white line in the “Merge 3X” image. Colocalization occurs when the intensity profiles overlap in the same area.

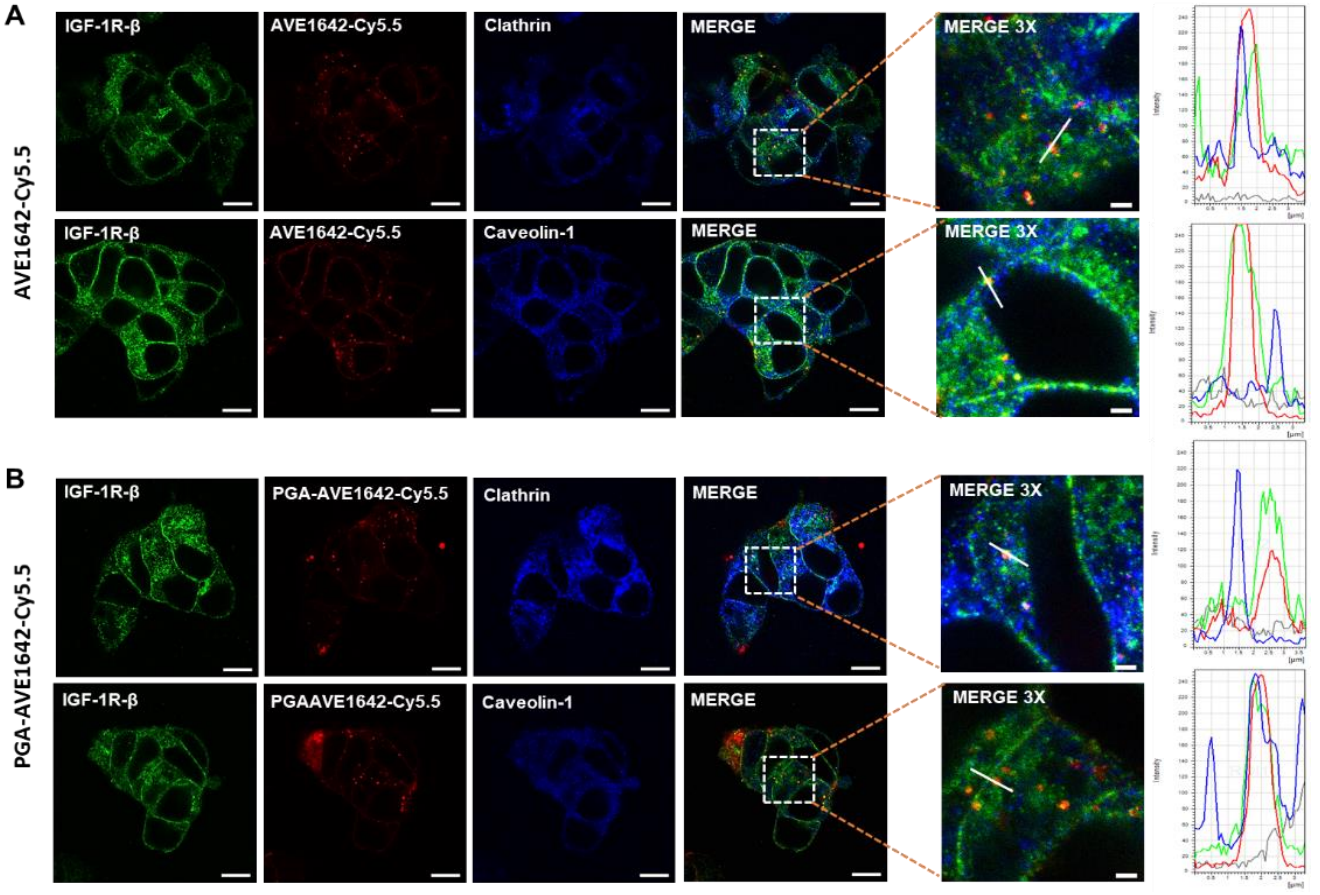

Figure 18: Colocalization of PGA-AVE1642 and AVE1642 with IGF-1R-β, Clathrin, and Caveolin-1. VCaP cells were treated for 30 minutes with PGA-AVE1642-Cy5.5 and AVE1642-Cy5.5 at 0.1 and 0.16 mg/ml, respectively. **A)** Green: (Alexa Fluor anti-rabbit 488) IGF-1R-β, red: AVE1642-Cy5.5, blue: (Alexa Fluor anti-mouse 568) Clathrin (upper panel) and Caveolin-1 (lower panel). **B)** Green: (Alexa Fluor anti-rabbit 488) IGF-1R-β, red: PGA-AVE1642-Cy5.5, blue: (Alexa Fluor anti-mouse 568) Clathrin (upper panel) and Caveolin-1 (lower panel). Merge shows the overlap of three channels, the magnification images were taken at 3X, and the graphics show the different fluorescent profiles (ROI). Scale bars: 10 µm, and 2 µm in Merge 3X. Line graphs on far-right show the fluorescent intensity of red, green and blue channels detected across the vertical/diagonal white lines in Merge 3X image.

It was clear that, while AVE1642 and PGA-AVE1642 mainly enter the cell by IGF-1R mediated endocytosis, PGA conjugation of AVE1642 altered endocytic pathway usage, which may be related to different interactions with IGF-1R.

Colocalization studies were then performed to understand such different interactions further. Fluorescently labeled AVE1642 and PGA-AVE1642 were co-localized with IGF1-R and early endosomes/lysosomes under the same conditions as described in the previous section. **Figure 19.A** (upper panel) shows that AVE1642-Cy5.5 (red) colocalizes with IGF-1R (green) at the cell membrane and both colocalize with the early endosomal marker (EEA1 – in blue) inside the cell; however, PGA-AVE1642-Cy5.5 (red) only colocalizes with IGF-1R (**Figure 19.A** lower panel) at the cell membrane and inside the cell, as demonstrated in the merge images and fluorescent intensity graphs. Meanwhile, **Figure 19.B** shows that both AVE1642-Cy5.5 (red – upper panel) and PGA-AVE1642-Cy5.5 (red – lower panel) colocalized with the lysosomal marker LAMP-1 (green) inside the cell, as demonstrated in the merge images and graphs.

Overall, these studies suggest that AVE1642 and PGA-AVE1642 cellular fate are the lysosomes but follow different endocytic pathways. While AVE1642 is primarily internalized via clathrin-mediated endocytosis and is directed to the lysosomes through endosomes, PGA-AVE1642 is instead internalized by caveolin mediated endocytosis and is directed to the lysosomes with a lack of early endosomal colocalization.

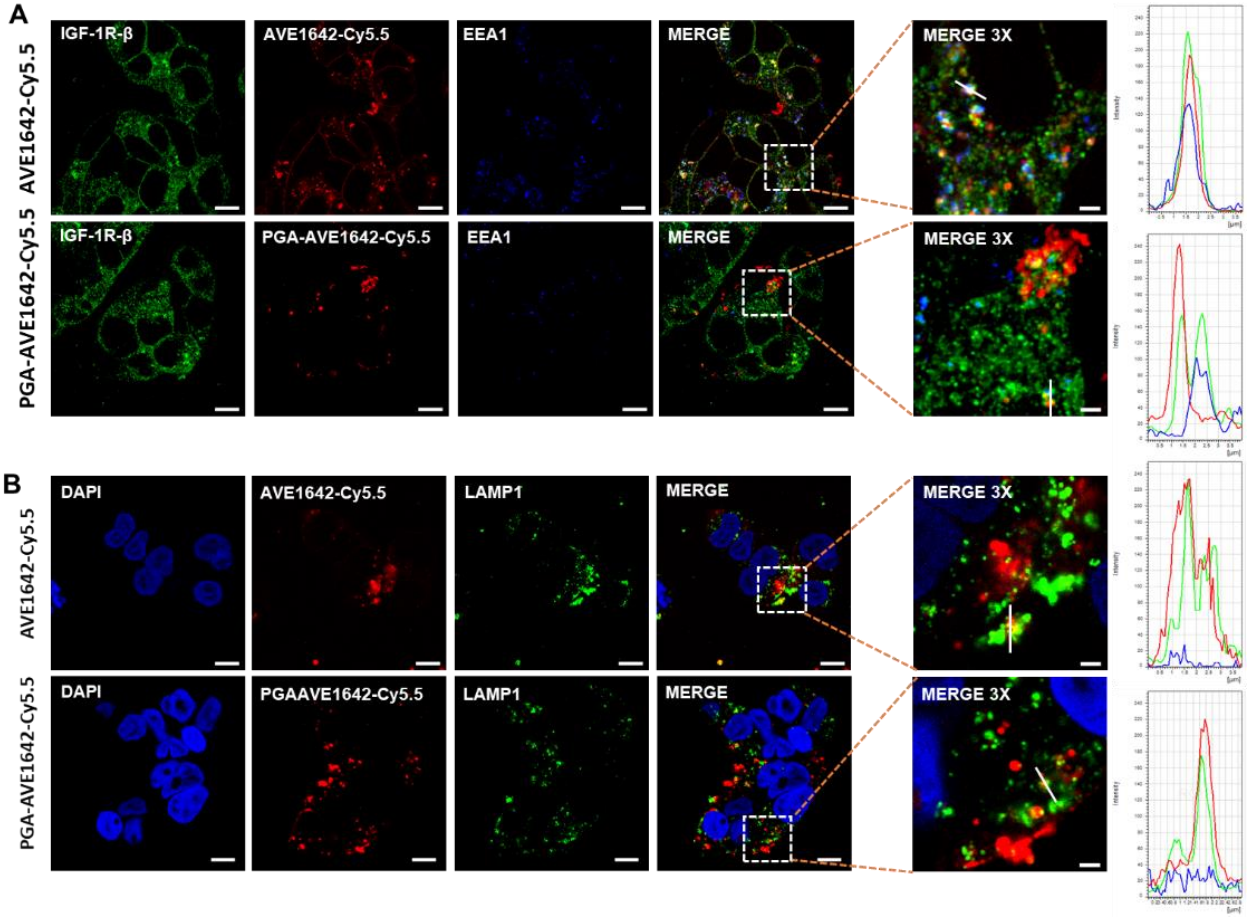

Figure 19: Colocalization of PGA-AVE1642 and AVE1642 with IGF-1R-β and Endosomal and Lysosomal Markers. VCaP cells were treated for 30 minutes with PGA-AVE1642-Cy5.5 and AVE1642-Cy5.5 at 0.1 and 0.16 mg/ml, respectively. **A)** Green: (Alexa Fluor anti-rabbit 488) IGF-1R-β, red: AVE1642-Cy5.5 (upper panel) and PGA-AVE1642-Cy5.5 (lower panel), blue: (Pacific blue anti-mouse 405) early endosome (EEA1) marker. **B)** Blue: DAPI nuclear marker, red: AVE1642-Cy5.5 (upper panel) and PGA-AVE1642-Cy5.5 (lower panel), Green: (Alexa Fluor anti-rabbit 488) lysosome (LAMP1) marker. Merge shows the overlap of three channels, the magnification images were taken at (3X), and the graphics show the different fluorescent profiles (ROI). Scale bars: 10µm, and 2µm in Merge 3X. Line graphs on far-right show the fluorescent intensity of red, green and blue channels detected across the vertical/diagonal white lines in Merge 3X image.

III.7.3.1. Super-resolution Microscopy Confirms that PGA-conjugation Alters AVE1642 Internalization

In order to corroborate our findings, we used stochastic optical reconstruction microscopy (STORM) to study the intracellular localization of AVE1642 and PGA-AVE1642 in the same cell. Super-resolution techniques represent useful tools to determine the detailed spatial distribution of molecules in cells [33]; furthermore, they reveal the ultrastructure of organelles [34].

Fluorescent STORM images are constructed from the high-accuracy localization of individual fluorescent molecules that are switched on and off using light of different wavelengths. The STORM imaging process comprises a series of imaging cycles; in each cycle, only a fraction of the fluorophores in the field of view are switched on, such that each of the activated fluorophores is optically resolvable from the rest, thereby allowing the position of the fluorophore to be determined with high accuracy. Repeating this process for multiple cycles, each causing a stochastically different subset of fluorophores to be turned on, enables the positions of many fluorophores to be determined and the reconstruction of an overall image [35].

For this approach, we labeled AVE1642 and PGA-AVE1642 with Cyanine 3 (Cy3) and Cyanine 5 (Cy5), respectively (**See Chapter II**, **Section II.2.2**). To select a concentration that avoids quenching, we performed fluorescence calibration curves for AVE1642-Cy3 and PGA-AVE1642-Cy5, which suggested a lack of quenching for the concentrations tested (**See Chapter II**, **Section II.2.7.3**). We co-incubated VCaP cells with both compounds at 5, 15, 30, and 60 mins to study any possible colocalization between AVE1642 and PGA-AVE1642; STORM images show PGA-AVE1642-Cy5 in red and AVE1642-Cy3 in green, with merged images showing any overlap (**Figure 20**). Images demonstrated higher intracellular AVE1642-Cy3 levels when compared to PGA-AVE1642-Cy5, which localizes to the

membrane; however, we observed very little colocalization of AVE1642-Cy3 with PGA-AVE1642-Cy5 suggesting that the compounds use differing internalization pathways related with the altered interaction with IGF-1R.

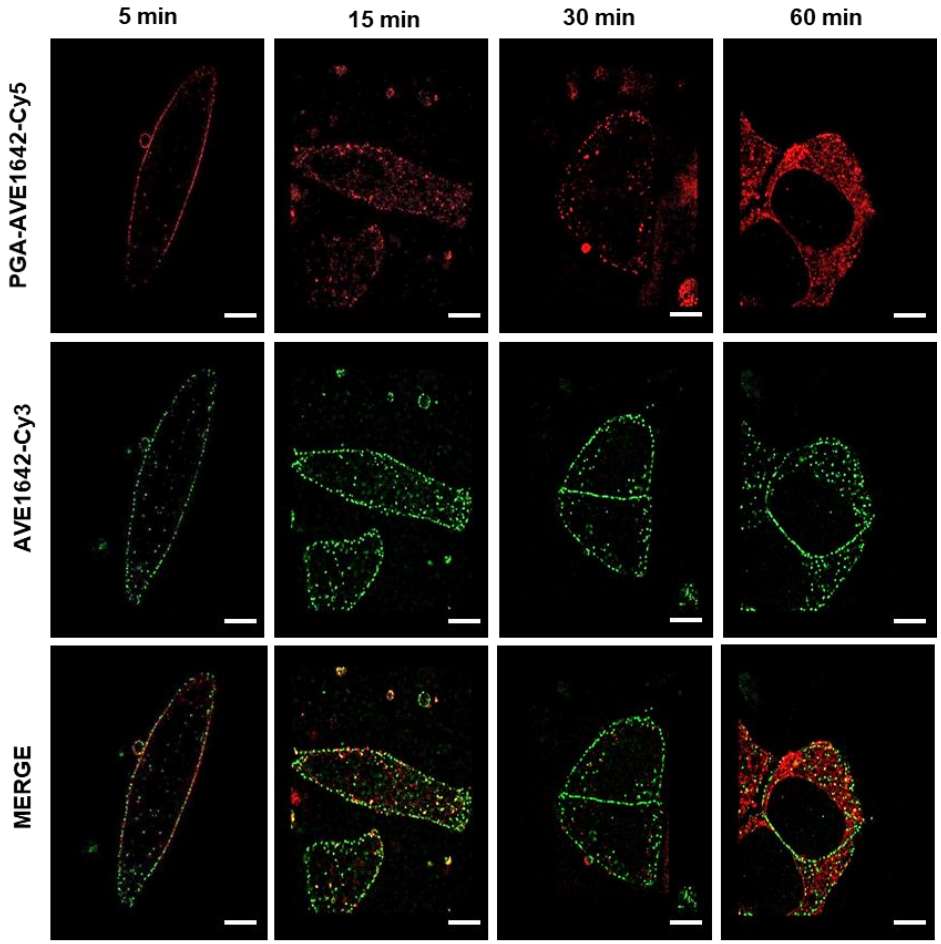

Figure 20: Internalization studies of PGA-AVE1642-Cy5 and AVE1642-Cy3 by STORM microscopy. VCaP cells were co-incubated for 5, 15, 30, and 60 minutes at with PGA-AVE1642-Cy5 (red) and AVE1642-Cy3 (green). The merged images show the overlap of two channels. Scale bar: 5 µm.

Previous experiments (**See Sections III.7.1**, and **III.7.2**) demonstrated that PGA-AVE1642 is retained at the cell membrane for an extended period when compared to AVE1642; for this reason and to further explore colocalization, we first incubated VCaP cells with PGA-AVE1642-Cy5 for 60 mins to allow a higher level of internalization and then co-incubated with the AVE1642-Cy3 for 15 and 30 minutes (**Figure 21**). However, even given a higher level of PGA-AVE1642-Cy5 internalization, we failed to observe remarkable levels of colocalization, providing further evidence that AVE1642-Cy3 with PGA-AVE1642-Cy5 employ differing internalization routes.

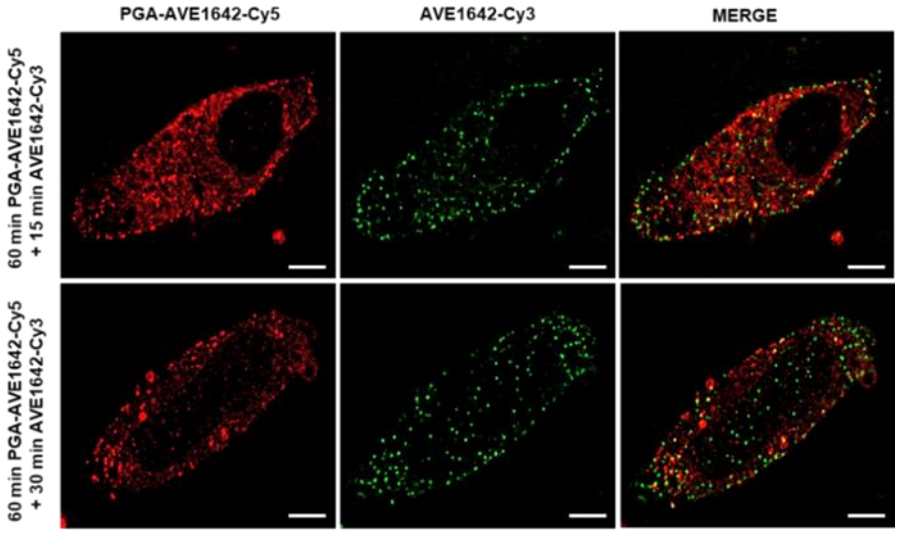

Figure 21: Intracellular localization studies of PGA-AVE1642-Cy5 and AVE1642-Cy3 by STORM microscopy. VCaP cells first treated with PGA-AVE1642-Cy5 (red) for 60 minutes, followed by AVE1642-Cy3 (green) co-incubated for 15 and 30 minutes. Merge shows any overlap between the two channels. Scale bar: 5 µm.

III.7.3.2. PGA-conjugation Prevents the Activation of PI3K and MAPK Pathways by AVE1642

Signaling through the IGF-1R controls cell growth and differentiation in normal and malignant cells. Ligands such as IGF-1 induce IGF-1R phosphorylation and activation and the induction of downstream signaling pathways. Following the activation of the Insulin receptor substrate 1 (IRS-1) and SHC-transforming protein 1 (Shc) adaptor proteins by activated IGF-1R, IRS-1 binds the regulatory subunit of phosphoinositide 3-kinase (PI3K) stimulating its phosphorylation and activation, which then activates Protein kinase B (AKT) signaling via phosphorylation to regulate the mammalian target of rapamycin (mTOR) activity. Meanwhile, Shc phosphorylation and activation stimulates mitogen-activated protein kinase (MAPK) activation through phosphorylation. The activation of said pathways blocks apoptosis and promotes tumorigenesis [36-38], and so blocking the activation of these signaling pathways may help to inhibit tumor formation [2, 39].

To determine the mechanism of action of the AVE1642 and PGA-AVE1642 conjugate, we evaluated the phosphorylation and activation status of various proteins involved in downstream signaling from the IGF-1R pathway by Western blotting. We treated VCaP cells with IGF-1, AVE1642, and PGA-AVE1642 at 0.1 μg/ml AVE1642 equiv. for 15 and 30 minutes and then probed cell lysates for levels of individual members of these signaling pathways - phospho-Shc and phospho-IRS-1 (adaptor proteins phosphorylated after IGF-1R activation), phospho-MAPK (phosphorylated after Shc activation to promote downstream signaling), phospho-PI3K (phosphorylated and activated by IRS-1), and α-tubulin (housekeeping protein used for normalization).

Figure 22.A shows a representative Western blotting image, while **Figures 22.B-E** depicts the densitometry analysis with ImageJ software after normalization to α-tubulin expression. As expected, IGF-1 treatment (positive control) induced a

significant increase in the phosphorylation of all proteins under study at 15 and 30 mins. Interestingly, AVE1642 treatment induced a significant increase in the phosphorylation levels of Shc and MAPK (**Figures 22.B** and **C**) and a decrease in the phosphorylation levels of p-IRS-1 (**Figure 22.D**) at both time points times; furthermore, we detected similar phosphorylation levels of PI3K compared to the control (**Figure 22.E**).

However, treatment with PGA-AVE1642 failed to induce phosphorylation of the proteins under study, and indeed, phosphorylation levels tended to fall to below those found in the untreated control. This inhibition displayed significance for p-Shc at 15 mins compared to AVE1642 treatment and at 30 minutes compared to IGF-1 and AVE1642 treatment (**Figure 22.B**). We also found a significant decrease at 15 mins for p-MAPK compared to IGF-1 and AVE1642 treatment, a highly significant decrease at 30 minutes for p-MAPK compared to both IGF-1 and AVE1642 treatment (**Figure 22.C**), and a significant decrease at 30 mins for p-IRS-1 when compared to IGF-1 (**Figure 22.D**). However, p-PI3K displays a non-significant trend towards inhibition without reaching significance (**Figure 22.E**).

Overall, these results suggest that PGA-AVE1642 treatment may improve IGF-1R inhibition by the inhibition of MAPK and PI3K downstream signaling pathways due to the inhibition of both Shc and IRS-1 adaptor proteins.

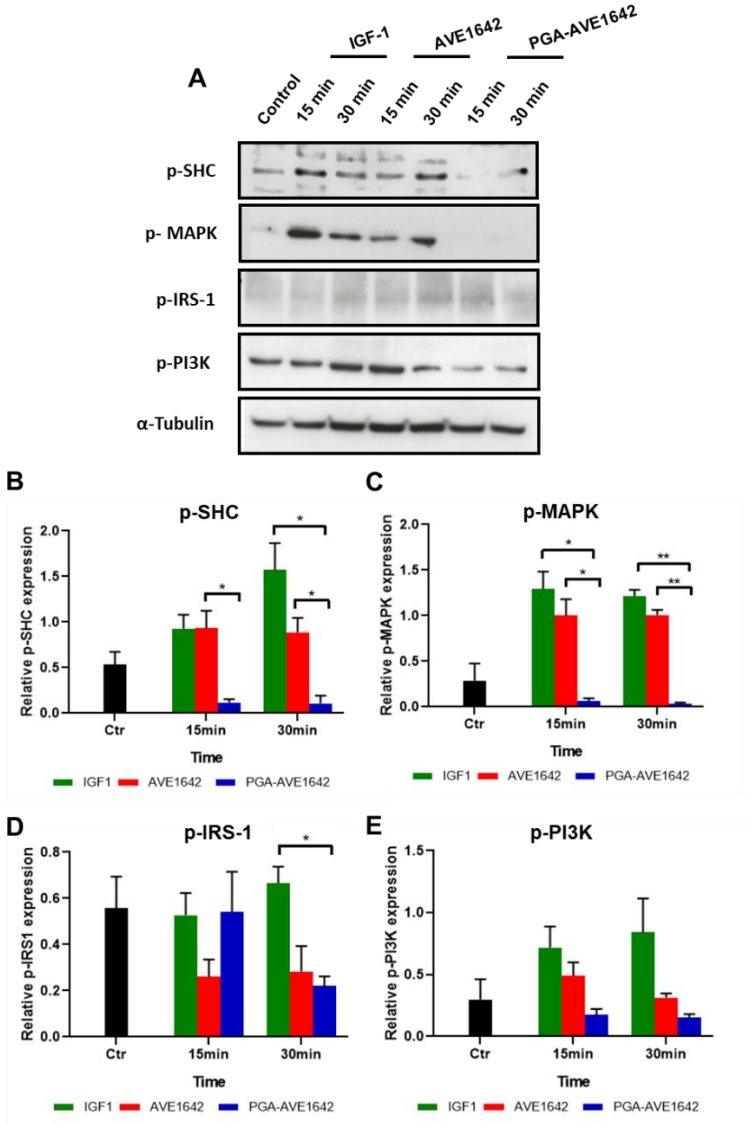

Figure 22: Phosphorylation Status of IGF-1R Downstream Proteins Following AVE1642 and PGA-AVE1642 Treatment. **A)** Western blot analysis of p-Shc, p-MAPK, p-IRS-1, p-PI3K, and α-tubulin expression in VCaP cells treated with IGF-1, AVE1642, and PGA-AVE1642 at 0.1µg/ml AVE1642 equiv. at 15 and 30 minutes. **B-E)** Quantification of protein expression analysis normalized to α-tubulin expression with ImageJ software. Data expressed as mean±SEM, n>3. Statistical analysis was performed using two-way ANOVA, *p< 0.05, **p< 0.01.

III.8. Development of an Orthotopic PCa Mouse model

As our *in vitro* studies suggested the improved function of AVE1642 following PGA-conjugation, related to an increase in stability, affinity, and IGF-1R inhibition, we next aimed to evaluate AVE1642 and PGA-AVE1642 *in vivo* in a newly developed preclinical orthotopic mouse model using modified T2E-expressing VCaP cells that would allow optical imaging monitoring.

III.8.1. Development of Stable Luciferase Expressing VCaP Cells

We employed T2E-positive VCaP cells in the development of the orthotopic PCa mice model. To allow *in vivo* tumor growth monitoring using minimally invasive procedures (such as IVIS® Spectrum technology), we transfected VCaP cells with lentiviral particles containing a plasmid coding for luciferase (Luc) and an antibiotic resistance cassette (G418) to positively select transfected cells (**Figure 23.A**). We also transfected VCaP cells with a green fluorescent protein (GFP) plasmid as a positive transfection control (**Figure 23.B**).

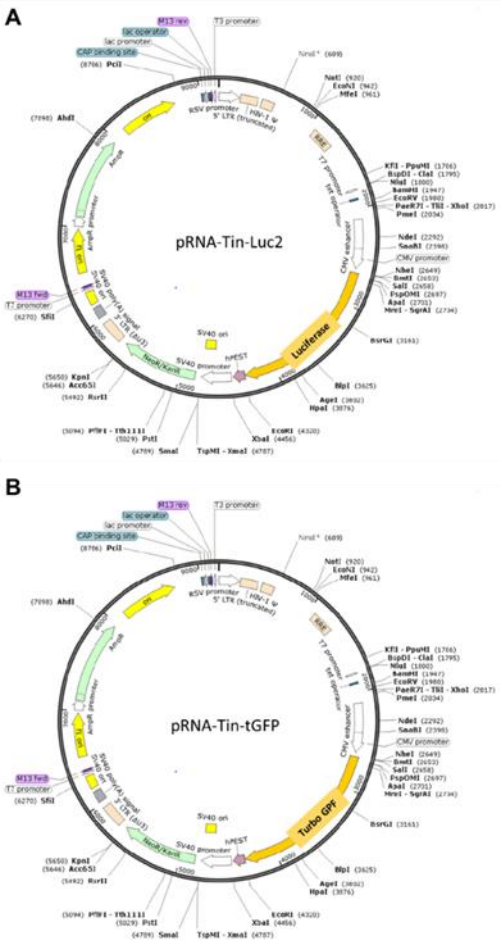

Figure 23: Plasmid Map of pRNA-Tin-Luc2 and pRNA-Tin-tGFP. **A)** Luciferase and **B)** GFP transgenes are regulated under the same T3 promoter. The respective pRNA-Tin-Luc2 and pRNA-Tin-tGFP plasmids also contain a G418 (geneticin) antibiotic resistance cassette.

After lentiviral transduction with the pRNA-Tin-Luc2 plasmid and antibiotic selection, we observed high and stable levels of luciferase expression (**Figure 24.A**). After the transduction of the pRNA-Tin-tGFP plasmid, we determined the GFP transfection rate by flow cytometry (**Figure 24.B**), discovering that 80% of cells expressed GFP after antibiotic selection (regions B and C).

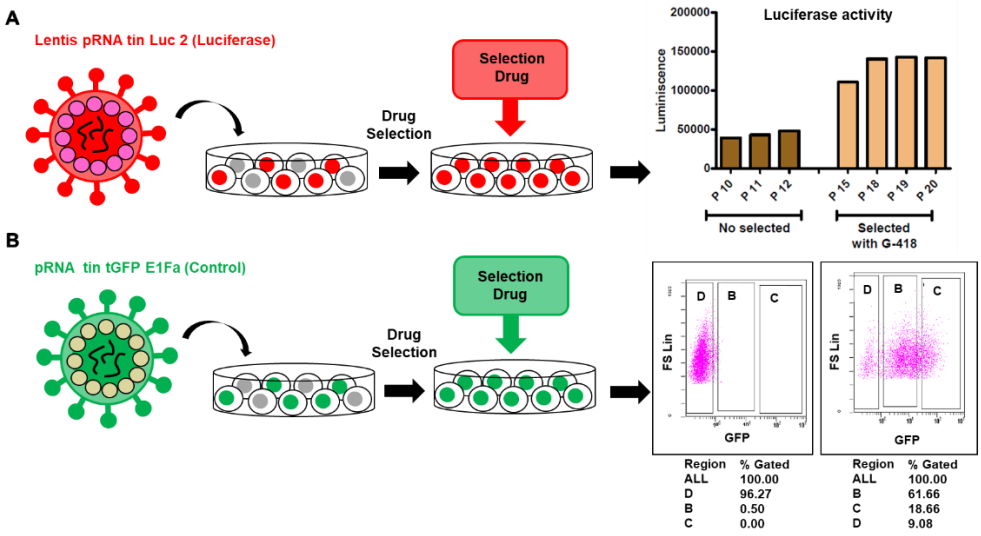

Figure 24: Schematic Representation of Lentiviral infection of VCaP Cells. VCaP cells were infected with lentiviral particles containing plasmids encoding **(A)** luciferase and **(B)** GFP. After infection, luciferase and GFP positive cells were selected with G418. Luminescence analysis for luciferase **(A)** and flow cytometry analysis for GFP **(B)** demonstrates efficient and stable transfection.

We next sought to confirm that lentiviral infection of the VCaP cell line (designated VCaP-Luc2) did not affect essential cell characteristics. Western blotting analysis confirmed the maintenance of IGF-1R-β, AR, and ERG expression levels after VCaP cell line transfection (**Figure 25.A**), while responses to AVE1642 and PGA-AVE1642 remained the same in VCaP cells (**Figure 13.A**) and VCaP-Luc2 cells (**Figure 25.B**); both cell lines demonstrated similar levels of cytotoxicity with increasing concentrations of both AVE1642 and PGA-AVE1642.

These findings suggest the suitability of VCaP-Luc2 cells for the development of the orthotopic PCa mouse model.

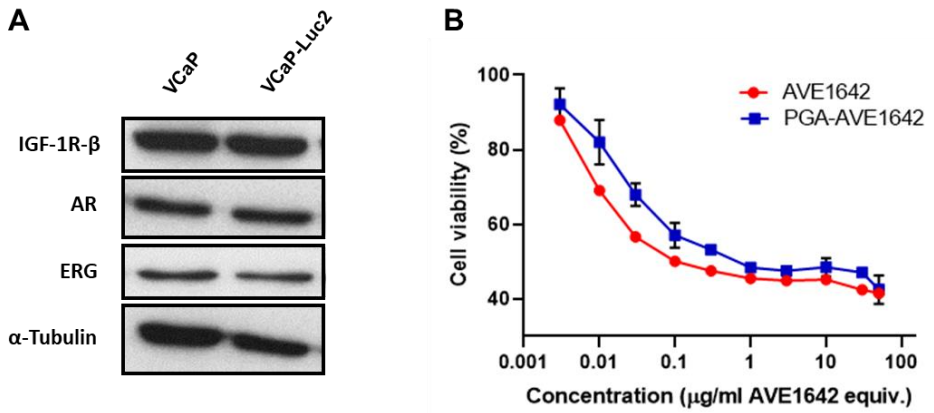

Figure 25: Protein Expression and AVE1642 and PGA-AVE1642 Response in VCaP-Luc2 Cells. A) Western blot analysis of IGF-1R-β, AR, and ERG (α-tubulin as a housekeeping gene) in VCaP-Luc2 cells, demonstrating no significant changes after transfection. **B)** The response of VCaP-Luc2 cells to AVE1642 and PGA-AVE1642 treatment remains similar to that of parental cells (**See Figure 13.A**).

III.8.2. Optimization of the Orthotopic PCa Mouse Model

As a first step towards the optimization of the orthotopic PCa mouse model, we determined the required time for the tumor to reach the maximum allowed size of approximately 1.2 cm^2 (**See Chapter II**, **Section II.2.12**). We injected 1 x 10^6 million VCaP-Luc2 cells into the prostate glands of 28 male C.B-17/IcrHan®Hsd-*Prkdc*^{scid} mice between 6-8 weeks of age and evaluated tumor growth weekly through the IVIS® Spectrum after subcutaneous luciferin administration (150 mg/kg). We weighed animals each week and euthanized four animals per week after IVIS-based analyses to measure the extracted tumor using a caliper and to collect blood samples.

We observed homogeneous and exponential tumor growth localized to the ventral prostate gland (**Figure 26.A** IVIS® Spectrum images and **B** expressed in photons per second for each week). Tumor volumes measured by caliper (**Figure 26.C**) confirmed the IVIS® Spectrum data.

Furthermore, we analyzed prostate-specific antigen (PSA) levels in the blood as PSA testing represents a standard tool for PCa diagnosis [40]. Our analysis established an increase in PSA blood levels over time when compared with the healthy animals, with a clear correlation between PSA levels (**Figure 26.D**) and tumor size (**Figure 26.C**).

Finally, from a safety point of view, daily monitoring of the general aspect of mice did not reveal any deterioration in animal welfare, while we failed to observe any weight loss in mice during the experimental timeframe (**Figure 26.E**).

In summary, these analyses demonstrated that tumors reached a maximal size by seven weeks, thereby delimiting the experimental timeframe.

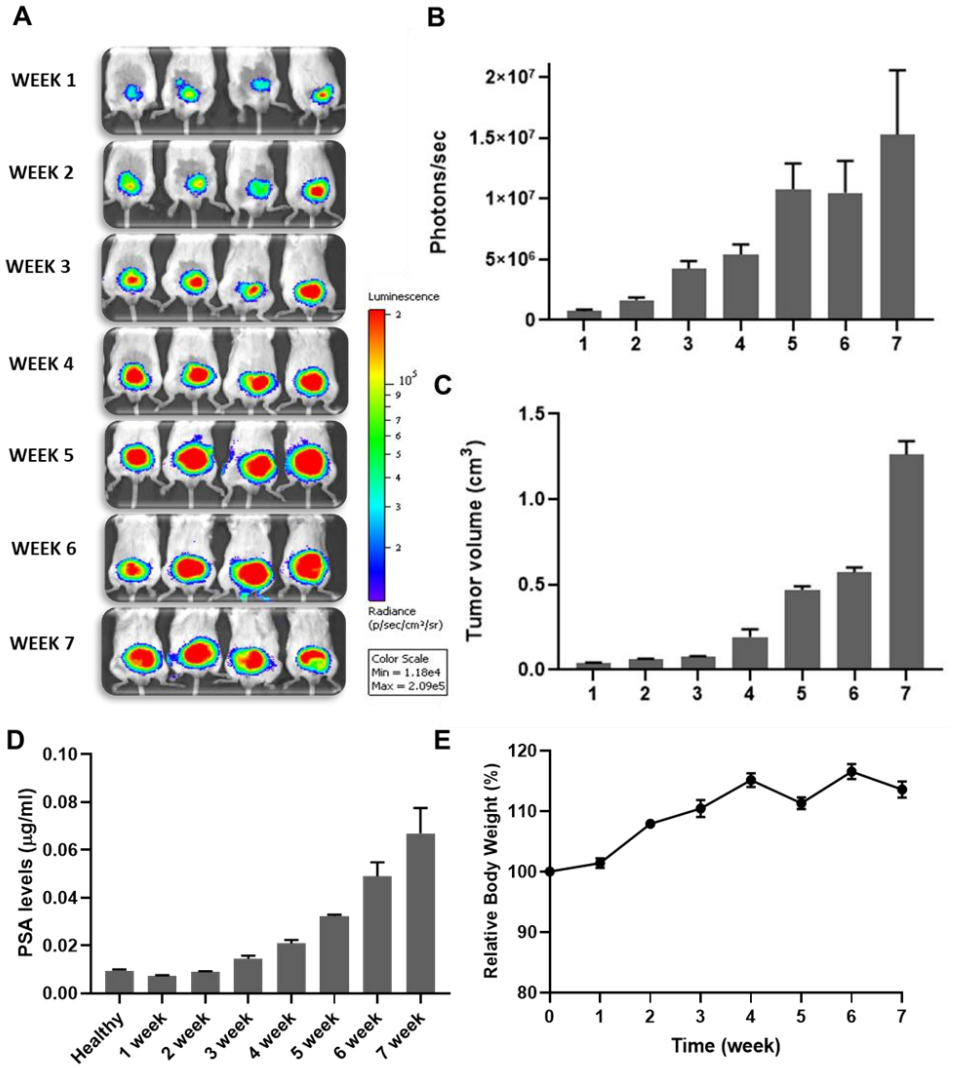

Figure 26: Optimization of the Orthotopic PCa Mouse Model. C.B-17/IcrHan®Hsd-*Prkdc*^{scid} mice were injected in the ventral prostate gland with 1 x 10^6 million VCaP-Luc2 cells. **A)** Topographic tumor growth images displaying growth, as evaluated using IVIS® Spectrum. **B)** Tumor growth over time evaluated as photons per second, data derived from IVIS® Spectrum analysis. **C)** Tumor volume expressed in cm^3 over time, measured with a caliper. **D)** Relative body weight (as a percentage) over time suggests maintained mouse body weight. **E)** PSA levels in mouse blood serum analyzed by ELISA assay. Data expressed as mean±SEM, n>3.

III.8.3. Analysis of Luciferase Stability *in vivo*

The next optimization step involved the optimization of the timeframe required to obtain a representative luminescent signal in the tumor and the "working window" in which the luminescent signal is maintained. This step ensures similar exposure times and reproducibility and comparability across experiments.

We used three male C.B-17/IcrHan®Hsd-*Prkdc*^{scid} mice between 6-8 weeks of age and injected 1 x 10^6 VCaP-Luc2 cells into the ventral prostate gland. After one week, we subcutaneously administered 150 mg/Kg of luciferin and introduced animals into the IVIS® Spectrum immediately following anesthesia.

We then acquired luminescence data every five minutes (photons/second) for 50 mins. **Figure 27** demonstrates a plateau of the luminescent signal between 20 and 40 mins, suggesting this as the working window to detect the luciferase signal from the tumor.

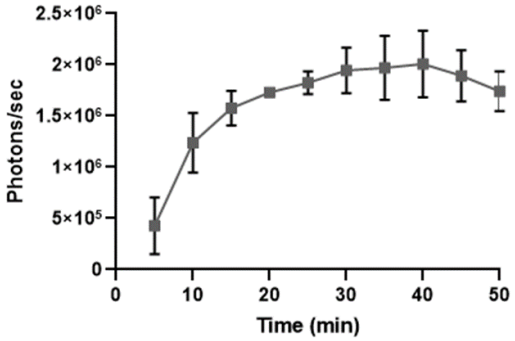

Figure 27: Luciferase Detection over Time in an Orthotopic PCa Mouse Model. Graph depicts luciferase detected signal expressed in photons per second versus time (minutes). 150 mg/kg of luciferin was injected subcutaneously into three male C.B-17/IcrHan®Hsd-*Prkdc*^{scid} mice, and tumor luminescence acquired every 5 minutes for 50 minutes. Data expressed as mean±SEM, n=3.

Given the results of this experiment, we measured luminescence 20 minutes post luciferin injection.

III.8.4. Analysis of the Enhanced Permeability and Retention Effect

We analyzed the EPR effect in relation to tumor size to determine the optimal timeframe for treatment administration (AVE1642 and PGA-AVE1642) [41, 42] by assessing tumor vascular permeability; this can alter during tumor development, thereby affecting passive tumor accumulation of nanomedicines.

We injected VCaP-Luc2 cells into the ventral prostate gland in male C.B-17/IcrHan®Hsd-*Prkdc*^{scid} mice model at 6-8 weeks of age and evaluated tumor growth using the IVIS® Spectrum and animal weight for seven weeks. At various stages during tumor development, we intravenously injected four mice with a solution of Evans Blue/BSA and then euthanized the mice and extracted, measured, and weighed tumors one hour later. We next incubated tumors in formamide for 48 h at 60ºC to extract any accumulated dye and quantified dye levels by measuring absorbance at 620 nm in a spectrophotometer and comparing against an Evans Blue/BSA calibration curve (**See Chapter II**, **Section II.2.13**). Higher dye levels generally correlate to higher levels of passive accumulation through the EPR effect.

Figure 28 depicts changes to tumor weight volume in cm^3 (red) and relative dye accumulation (green), showing a clear inverse correlation between these two parameters. Week 2 represents the maximal timepoint for dye accumulation, and hence the EPR effect, and we chose this time point to administer treatments. At this stage, the average tumor size is approximately 0.05 cm^3.

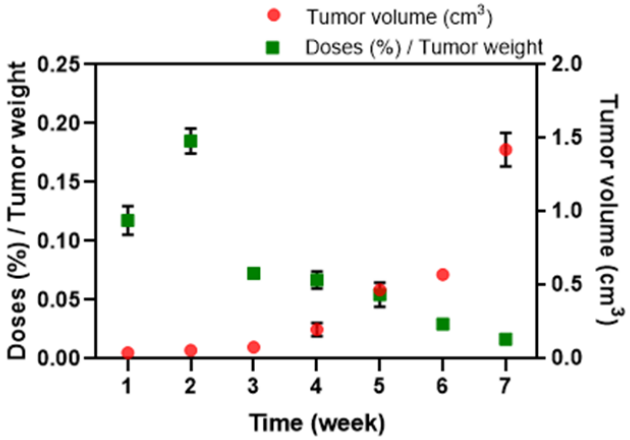

Figure 28: Tumor Permeability as a Function of Tumor Weight. Graphic shows the percentage of injected EB dye dose per gram of tumor (dose (%)/tumor weight) (green) and tumor volume (cm^3) (red) both versus time (weeks). Data expressed as mean ±SEM, n>3.

IV.8.5. PGA-conjugation Maintains AVE1642 Tumor Accumulation

To investigate tumor accumulation of AVE1642 and PGA-AVE1642, we intravenously injected PBS (control), AVE1642-Cy5.5, and PGA-AVE1642-Cy5.5 at 10mg/kg AVE1642 equiv. into PCa model mice (n=4) at two weeks after tumor imitation to coincide with the maximum EPR effect (0.05 cm^3). After four hours, we removed tumors, lysate, and detected fluorescence of Cy5.5 by spectrophotometer against a calibration curve (**See Chapter II**, **Section II.2.14**).

Figure 29 shows the percentage of injected dose per gram of tissue in tumor samples treated with AVE1642-Cy5.5 and PGA-AVE1642-Cy5.5; overall, we did not detect significant differences between the two treatments suggesting similar tumor accumulation kinetics.

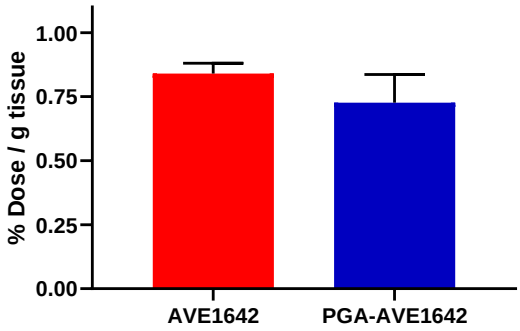

Figure 29: Cy5.5 Tumor Accumulation following AVE1642 and PGA-AVE1642 Administration to PCa Model Mice. Graph shows the percentage of dose per gram of tissue (Doses (%)/g Tissue) for AVE1642-Cy5.5 and PGA-AVE1642-Cy5.5 after 4 hours. Data expressed as mean±SEM, n>3.

The lack of increased AVE1642 accumulation after PGA conjugation may be due to non-significant changes observed in the size of the PGA-AVE1642, as it has also been described that mAb active targeting prevalence is greater than passive targeting by EPR to enable specific binding receptors which are overexpressed in the tumor and not in the healthy tissue. In the case of a poor vasculature and low EPR effect, there are two primary strategies to increase the drug accumulation bypassing the EPR effect, such as targeting tumor blood vessels or release the drug within tumor vasculature [43].

III.9. *In vivo* Antitumoral Activity of AVE1642 and PGA-AVE1642

After characterizing and optimizing the orthotopic PCa mice model, we investigate the antitumoral potential and safety of the AVE1642 and PGA-AVE1642. Furthermore, we explored the mechanisms of action in the tumor samples to identify the therapeutic input.

III.9.1. PGA-conjugation Improves AVE1642 Antitumor Activity

We next compared the antitumor activity of AVE1642 and PGA-AVE1642 conjugate *in vivo* using our optimized PCa mouse model previously described (**See Section III.8.2**). We monitored tumor growth by IVIS® Spectrum and weighed animals weekly. At week 2, when tumors reach a size of 0.05 $cm^{3,}$ and the EPR effect is maximal, we randomly divided mice into three groups (n=9), and we euthanized mice two weeks after the final treatment (**Figure 30.A**).

i. Control group with PBS (i.v.)

ii. AVE1642 (i.v.) once a week for four weeks at 10 mg/kg

iii. PGA-AVE1642 (i.v.) once a week for four weeks at 10mg/kg (AVE1642 equiv.)

Figure 30.B depicts representative IVIS® Spectrum luminescence pictures, which a comparable increase in tumor size for control-treated mice over seven weeks; furthermore, AVE1642 and PGA-AVE1642 treated mice displayed inhibited tumor growth as evidenced by lower luminescence compared with the control group. Moreover, PGA-AVE1642 treated mice showed lower luminescence signals in comparison with the AVE1642 group. However, the quantification of IVIS® Spectrum data, as shown in **Figure 30.C**, provides evidence of similar luminescence values in tumors following AVE1642 and PGA-AVE1642 treatment. This was probably due to the luminescence signal variation or differences in tumor density. Therefore, *ex vivo* quantification post-experiment it was required.

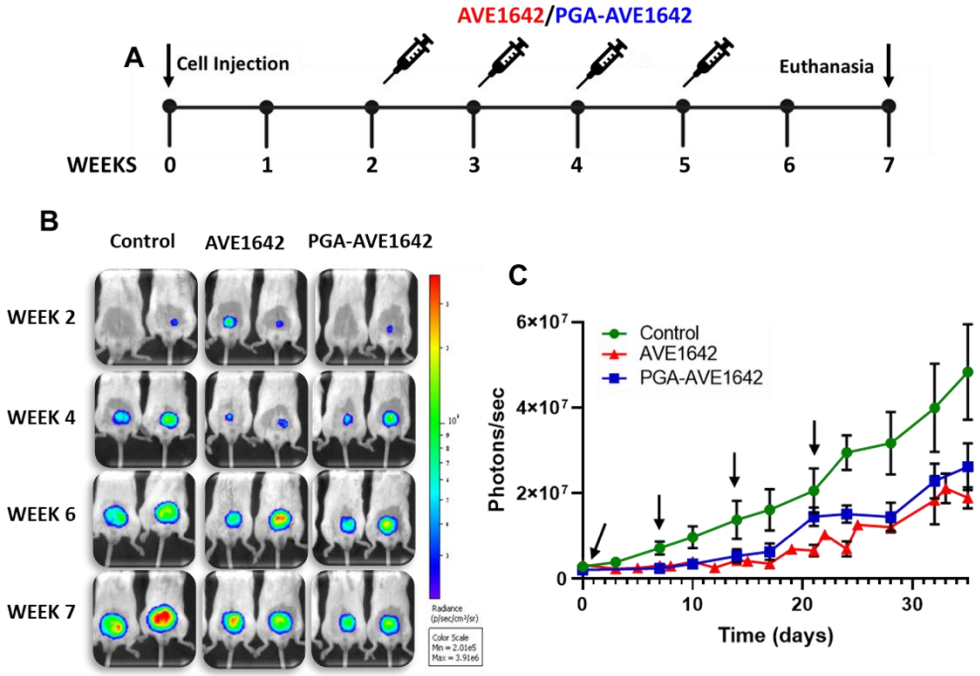

Figure 30: Tumor Progression by Bioluminescence Detection Following AVE1642 and PGA-AVE1642 Treatment in an Orthotopic PCa Mouse Model. Mice were treated with AVE1642 and PGA-AVE1642 at 10 mg/kg (AVE1642 equiv.) or PBS vehicle control. **A)** Schematic representation for *in vivo* animal experiment timeline following AVE1642 and PGA-AVE1642 treatments. **B)** Topographic tumor growth images evaluated in IVIS® Spectrum over time in three different groups. **C)** Tumor growth over time evaluated in each group as photons/second (Data derives from IVIS® Spectrum experiments, black arrows indicate the timings of the treatments). Data expressed as mean±SEM, n>3. Statistical analysis was performed using ANOVA.

Caliper measurements of tumor size, as shown in **Figure 31.A**, provide evidence of a highly significant reduction in tumor size following AVE1642 and PGA-AVE1642 treatment when compared to PBS control-treated mice, and a significant reduction in tumor size for PGA-AVE1642 when compared to AVE1642. **Figure 31.B** shows representative pictures of tumors at week 7 for the three different treatment modalities.

We also analyzed serum levels of PSA (**Figure 31.C**); AVE1642 and PGA-AVE1642 treatment led to a significant reduction in PSA levels compared to control; furthermore, PGA-AVE1642 treatment showed a highly significant reduction in PSA levels compared to AVE1642 treated mice.

We also analyzed tumor density following resection at the experimental endpoint. **Figure 31.D** demonstrates an inverse correlation between tumor density and tumor size (**Figure 31.A**) following treatments; mice treated with PGA-AVE1642 possessed tumors with a significantly higher density than control or AVE1642 treated mice, while we discovered no significant differences between control and AVE1642 treated mice. This could support different cell death pathways triggered by the different compounds. Maybe for this reason, we observed a slightly increased luminescence in the tumors treated with PGA-AVE1642 compared with AVE1642 treatment (**Figure 30.C**).

We also confirmed treatment safety, as we failed to observe significant losses in mouse body weight over time in response to any treatment modality (**Figure 31.E**).

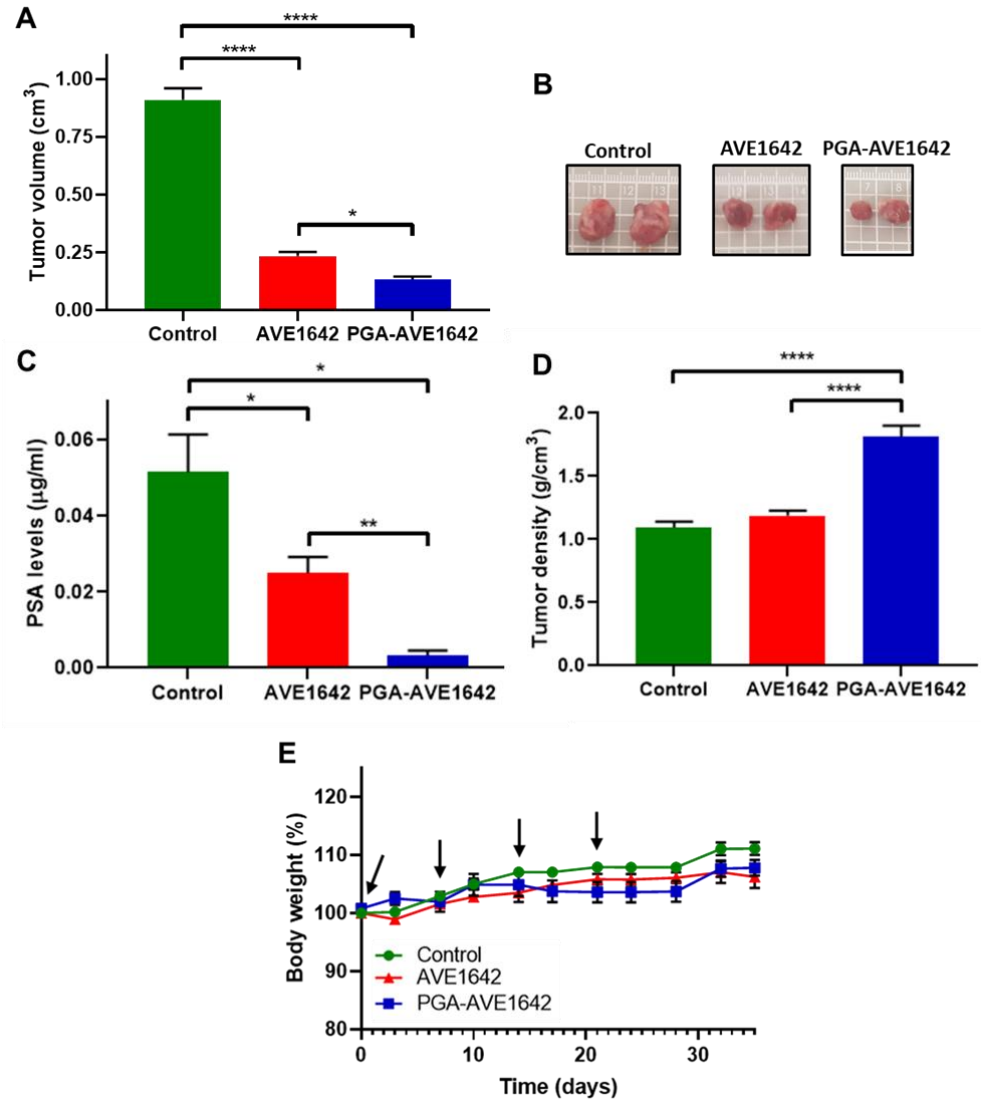

Figure 31: Antitumor Activity of AVE1642 and PGA-AVE1642 in an Orthotopic PCa Mouse Model. A) Tumor volume expressed in cm^3 at the experimental endpoint. **B)** Representative pictures of tumors at the experimental endpoint. **C)** PSA levels in the control animals and both treatments expressed in µg/ml. **D)** Tumor density measured in g/cm^3. **E)** Relative body weight percentage after the first administration (black arrows indicate the timings of the treatments). Data expressed as mean±SEM, n>3. Statistical analysis performed using ANOVA, *$p < 0.05$, **$p < 0.01$, ****$p < 0.0001$.

As a control, we also tested the effects of PGA treatment to determine the safety and any potential intrinsic antitumor activity using 8.45 mg/kg PGA per animal to provide an administration of PGA similar to mice treated with PGA-AVE1642.

We failed to observe any differences between PBS vehicle control and PGA treated mice in IVIS® Spectrum analysis of tumor development (**Figure 32.A**), the quantification of tumor evolution in photons per second (derived from the IVIS® Spectrum analysis) (**Figure 32.B**), tumor size measured by caliper at experimental endpoint (**Figures 32.C** and **D**) , PSA levels (**Figure 32.E**), tumor density (**Figure 32.F**), or alteration to body weight (**Figure 32.G**). Overall, this suggests a lack of intrinsic antitumor activity for PGA.

In summary, we provide evidence of the increased antitumor effect of PGA-AVE1642 in comparison to AVE1642, and to explore the mechanisms behind this improvement, we next investigated the mechanism of action in tumor samples and studied the tumor microenvironment for potential alterations.

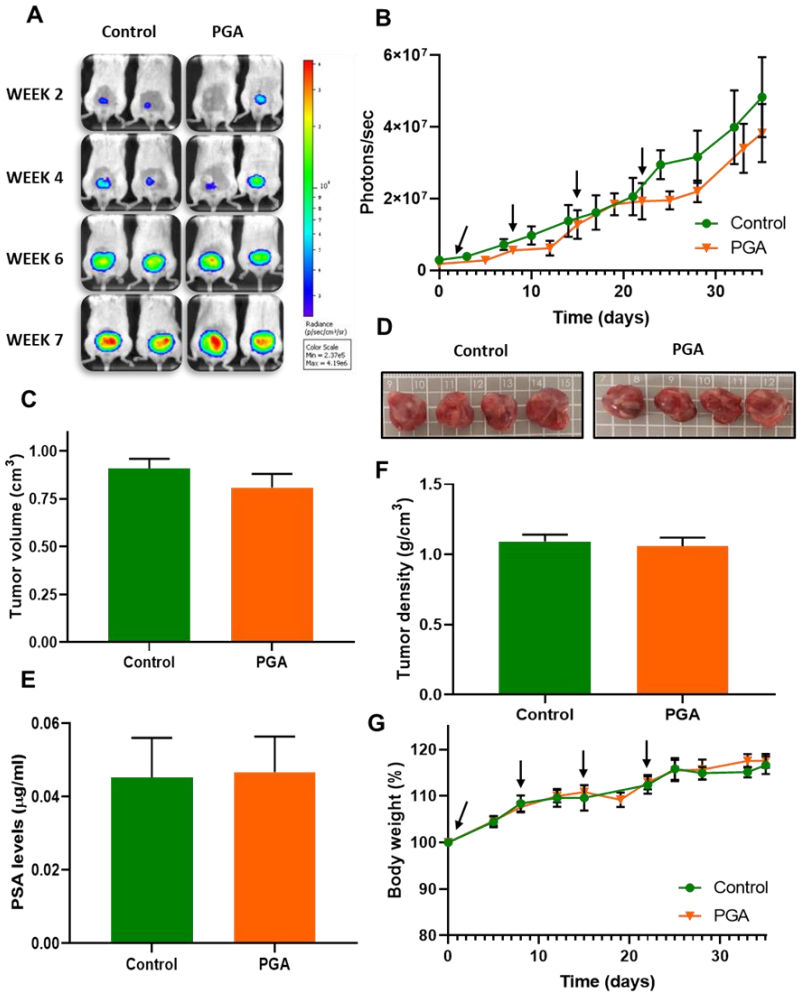

Figure 32: Antitumor Activity of PGA in Orthotopic PCa Mouse Model. Mice were treated with PGA at 8.45 mg/kg (PGA equiv. in PGA-AVE1642 conjugate), and the same parameters in **Figures 30** and **31** were determined. **A)** Topographic tumor growth images evaluated in IVIS® Spectrum over time. **B)** Tumor growth over time measured in photons/second (black arrows indicate the timings of the treatments). **C)** Tumor volume expressed in cm^3 at the experimental endpoint. **D)** Representative pictures of tumors at the experimental endpoint. **E)** PSA levels measured in µg/ml at the experimental endpoint. **F)** Tumor density measured in g/cm^3 at the experimental endpoint. **G)** Relative body weight percentage over time (black arrows indicate the timings of the treatments). Data expressed as mean±SEM, n>3. Any statistical analysis performed by t-test.

III.9.2. PGA Conjugation of AVE1642 Improves IGF-1R Inhibition

Tumors of CRPC patients generally present with the overexpression of IGF-1R and AR [44, 45]; IGF-1R promotes PI3K and MAPK pathway activity and tumor progression, while AR enhances ERG gene expression in the T2E positive patients, with ERG then mediating the transcriptional upregulation of IGF-1R transcription. For these reasons, mirroring our previous *in vitro* analysis, we analyzed levels of proteins downstream of IGF-1R signaling present in tumor samples at experimental endpoint (phosphorylated p-Shc, p-MAPK, and p-PI3K proteins) (**See Section III.7.3.2**) to determine the activation status. We also evaluated total IGF-1R-β (t-IGF-1R-β), AR, and ERG protein levels, which are related to the presence of the T2E fusion gene, to study their modulation after exposure of tumor-bearing mice to the various treatment modalities (**Figure 33**).

Overall, we observed a lack of significant changes for p-MAPK, AR, and ERG expression in response to any treatment (**Figures 33.C**, **F,** and **G**); however, we discovered a significant reduction in p-PI3K and t-IGF-1R expression in tumors from PGA-AVE1642 treated mice when compared to control (**Figures 33.D** and **E**). We also observed a significant reduction in protein levels between PGA-AVE1642 and AVE1642 treated mice for p-Shc, p-PI3K, t-IGF-1R levels (**Figures 33.B**, **D,** and **E**). Compared to the findings from the *in vitro* studies, after AVE1642 treated tumors did not display a similar phosphorylation pattern, although PGA-AVE1642 treated tumors did display a similar p-Shc and p-PI3K profile (**See Section III.7.3.2**).

These results suggest that PGA conjugation enhances IGF-1R inhibition by AVE1642 due to the robust simultaneous inhibition of both the Shc adaptor protein and PI3K signaling pathways.

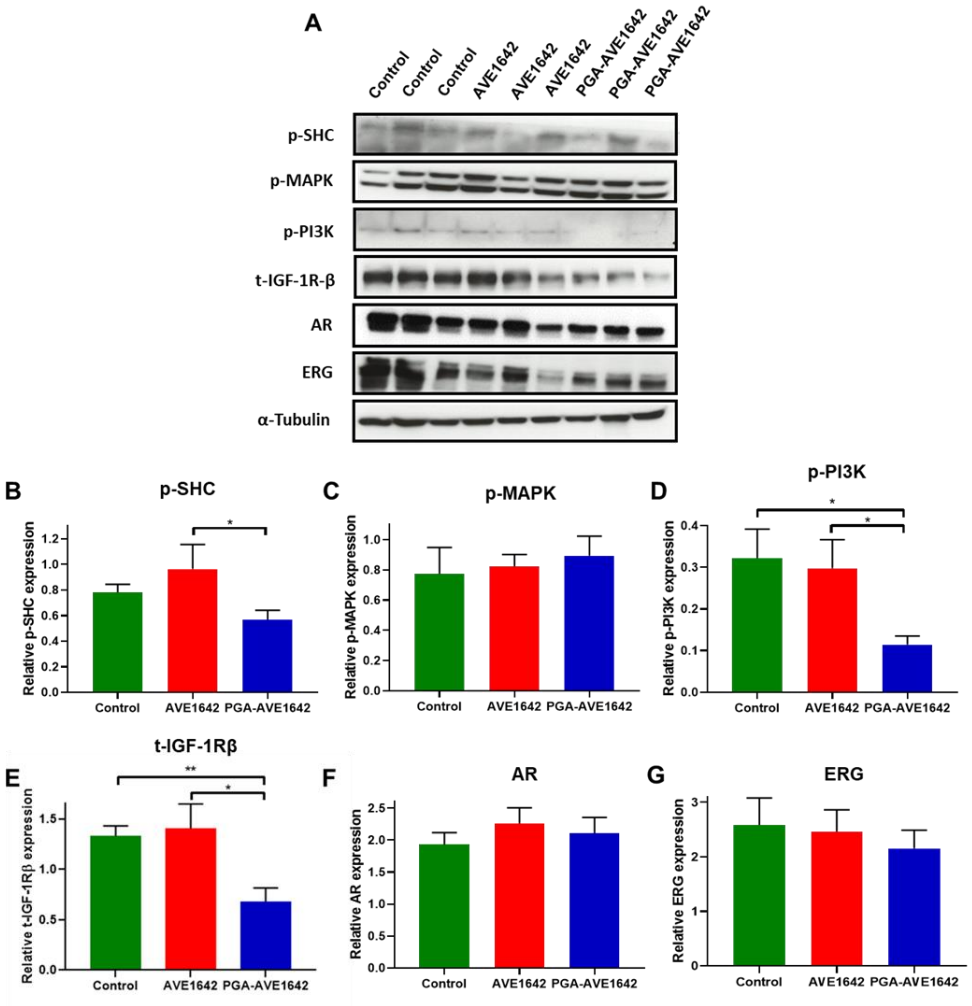

Figure 33: Analysis of IGF-1R Downstream Protein Expression After AVE1642 and PGA-AVE1642 Treatment in the Orthotopic PCa Mouse Model. Protein expression in tumor lysates following treatment as analyzed by Western blot assay. **A)** Representative Western blot image. **B-G)** Graph represents the protein expression relative to α-tubulin expression, as quantified with ImageJ software. Data expressed as mean±SEM, n>3. Statistical analysis was performed using ANOVA, *p< 0.05, **p< 0.01.

III.10. Modulation of the Tumor Microenvironment by AVE1642 and PGA-AVE1642

The tumor microenvironment (TME) is the collective term for those components surrounding the tumor/tumor cells, comprising non-cancerous stromal components, such as the extracellular matrix (ECM), blood vessels, infiltrating inflammatory cells, and a variety of associated tissue-specific cells. This unique environment emerges during tumor progression via complex interactions between the host and tumor tissues and has been proposed as a target for anti-tumor therapies [46, 47].

For these reasons, we studied PCa TME architecture and responses to AVE1642 and PGA-AVE1642 exposure in collaboration with Prof. Twan Lammers Laboratory at the Center for Biohybrid Medical Systems (CBMS), Aachen, Germany, during a short research visit.

III.10.1. Evaluation of Tumor Vasculature in the Orthotopic PCa Mouse Model

To evaluate the tumor-associated vasculature upon AVE1642 and PGA-AVE1642 therapies, we investigate important tumor vasculature parameters, such as vessel functionality and maturity, via immunofluorescence analysis of CD31, α-SMA, and Lectin distribution.

CD31 (also known as platelet endothelial cell adhesion molecule-1 [PECAM-1]) is a 140kDa type I integral membrane glycoprotein that is highly expressed on endothelial cells; therefore, it provides information about intratumoral micro-vessels density. Lectin, a carbohydrate-binding protein, permits the visualization of perfused (functional) vessels to provide information on vessel functionality and maturation. Meanwhile, α-SMA (smooth muscle actin) is the prominent actin

isoform expressed by vascular smooth muscle cells, pericyte, and myofibroblasts and provides information regarding vessel maturity [48, 49].

First, we analyzed the area fraction % (AF%) covered by CD31, α-SMA, and Lectin by acquiring representative images of tumor-bearing prostate tissue from C.B-17/IcrHan®Hsd-*Prkdc*^{scid} male mice treated with PBS (Control), AVE1642, or PGA-AVE1642 using a fluorescence microscope at 20X magnification and quantified the fluorescent signal using AxioVision software (**Figures 34.A** and **B**).

At the morphological level (**Figure 34.A**), blood vessels appeared elongated with a large lumen in the control group. In AVE1642 and PGA-AVE1642 treated mice, blood vessel number decreased, and morphology altered: AVE1642 treatment promoted shorter and thinner vessels compared to control, while PGA-AVE1642 treatment prompted vessel fragmentation, as suggested by the appearance of "spot-like" vessel staining.

The quantification of the fluorescence for each marker protein (**Figures 34.B**, **C** and **D**) suggested a lack of significant alteration of CD31 expression, although we do note a trend for reduced expression upon AVE1642 and PGA-AVE1642 treatment, which agrees with the reduction in vessel number observed at the morphological level. We discovered significantly lower Lectin levels in PGA-AVE1642 treated mice when compared to both control and AVE1642 treated mice, suggesting that PGA-AVE1642 treatment promotes a decrease in the perfusion of vessels. However, α-SMA levels displayed a significant reduction in the AVE1642 treated mice (in comparison to both control and PGA-AVE1642 treated groups) only, suggesting a higher impact of AVE1642 on vessel maturity than for PGA-AVE1642.

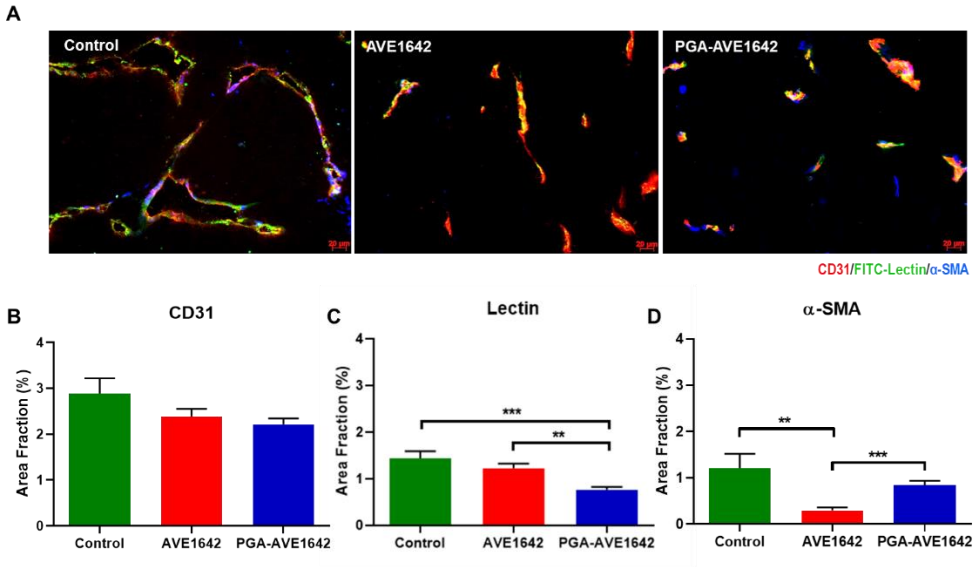

Figure 34: Study of CD31, α-SMA, and Lectin as Markers of Tumor-Associated Vessels following Treatment with AVE1642 and PGA-AVE1642. A) Representative images of vessel morphology in response to each treatment at 20X magnification. CD31 (red) marks endothelial cells, Lectin (green) indicates perfused vessels, and α-SMA (blue) indicates mature vessels. Scale bar 20µm. **B-D)** The graph represents the area fraction % of CD31, Lectin, and α-SMA obtained with AxioVision software. Data expressed as mean±SEM, n>3. Statistical analysis was performed using ANOVA, **p< 0.01, ***p< 0.001.

To further understand tumor vasculature, we evaluated vessel functionality and maturity in more detail (**Figure 35**). To this end, we counted CD31+ vessels (indicates total number of vessels), CD31+ and Lectin+ vessels (indicates functional vessels) and CD31+, Lectin+, and α-SMA+ (indicates mature functional vessels). In order to normalize the values with the total number of vessels, the functionality was calculated by dividing the total number of double-positive vessels with the CD31 positive vessels, and maturity by dividing the total number of triple-positive vessels with the CD31 positive vessels.

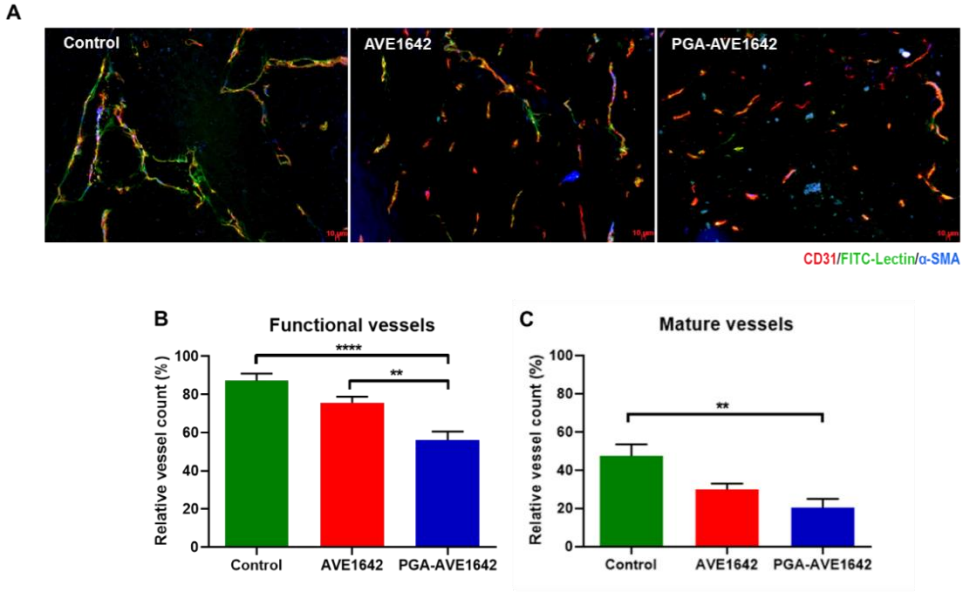

Figure 35: Determination of the Functionality and Maturity of Tumor-Associated Vessels following Treatment with AVE1642 and PGA-AVE1642. A) Representative images of vessel morphology in response to treatments at 10X magnification. CD31 (red) marks endothelial cells, Lectin (green) indicates perfused vessels, and α-SMA (blue) indicates vessel maturity. Scale bar 10µm. **B-C)** Graphs represent the relative vessel count % percentage of functional vessels (CD31+ and lectin+/CD31+) and mature vessels (CD31+ lectin+ and α-SMA+/ CD31+). Data expressed as mean±SEM, n>3. Statistical analysis performed using ANOVA, **p< 0.01, ****p< 0.0001.

Overall, our findings confirmed that AVE1642 and PGA-AVE1642 treatment promote changes in vessel functionality and maturity (**Figures 35.B** and **C**). PGA-AVE1642 treatment significantly reduced the number of functional vessels compared to both control and AVE1642 treatment. AVE1642 failed to promote significant differences when compared to control, although there does exist a downward trend. PGA-AVE1642 treatment also significantly reduced vessel maturity in comparison with control. Furthermore, there exist non-significant downward trends for AVE1642 when compared to control and PGA-AVE1642 when compared to AVE1642.

As a summary, these analyses suggest that PGA conjugation promotes an AVE1642-mediated decrease in vessel functionality and maturity.

III.10.2. Cell Proliferation and Angiogenic Studies in the Orthotopic PCa Mice Tumors

We also undertook a histological analysis of tumor samples in following AVE1642 and PGA-AVE1642 exposure to evaluate alterations to tumor cell proliferation and angiogenesis.

III.10.2.1. PGA-conjugation Significantly Improves Inhibition of Prostate Tumor Proliferation by AVE1642

We investigated prostate tumor proliferation after treatment through the detection of the Ki67 proliferation marker in tumor tissues [50].

We captured representative images of Ki67 stained tumor sections from each treatment group (**Figure 36.A**). Quantification of Ki67 staining (**Figure 36.B**) established that while AVE1642 treatment significantly reduced cell proliferation when compared to an untreated control, treatment with PGA-AVE1642 provided a significantly greater decrease in cell proliferation when compared to control and AVE1642 suggesting a stronger antiproliferative effect following PGA-AVE1642 treatment.

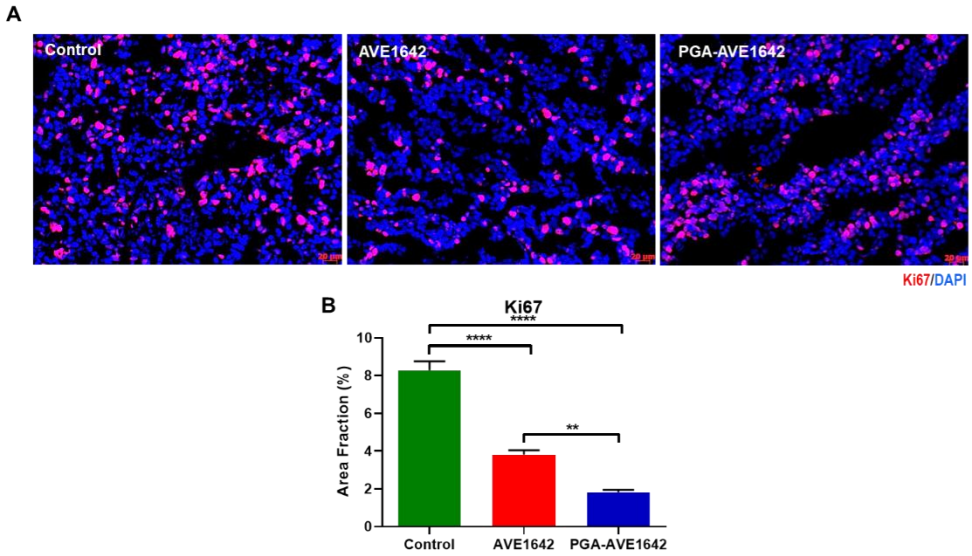

Figure 36: Histological analysis of Ki67 staining in Prostate Tumor Tissue Samples. A) Representative images of tumor samples in each treatment group at 20X magnification. Ki67 (red) marks proliferative cells, and DAPI (blue) marks nuclei. Scale bar 20µm. **B)** Graph represents the area fraction % of the Ki67 fluorescence signal for the three treatment groups analyzed with the AxioVision software. Data expressed as mean±SEM, n>3. Statistical analysis performed using ANOVA, **p< 0.01, ****p< 0.0001.

III.10.2.2. PGA-conjugation Significantly Improves Inhibition of Tumor Angiogenesis by AVE1642

VEGFR2, the receptor for the angiogenic growth factor VEGF, is expressed by several cell types, including hematopoietic cells, but it is primarily observed in vasculature endothelial cells [51]. Abnormal tumor vasculature leads to severe alterations to the tumor microenvironment, such as decreased pH and hypoxia. These modifications result in the upregulation of VEGF and VEGFR2 through a paracrine positive feedback mechanism [52].

As in the previous experiments, we captured representative images for VEGFR2 staining in each treatment group **Figure 37.A**. Quantification of staining

(**Figure 37.B**) confirmed a significant reduction in VEGFR2 levels in AVE1642 treated mice and a highly significant reduction in VEGFR2 levels in PGA-AVE1642 treated mice when compared to control. Furthermore, PGA-AVE1642 treatment prompted a significant reduction in VEGFR2 levels when compared to AVE1642 treated mice. Overall, these results suggest PGA conjugation results in improved antiangiogenic effectiveness of AVE1642.

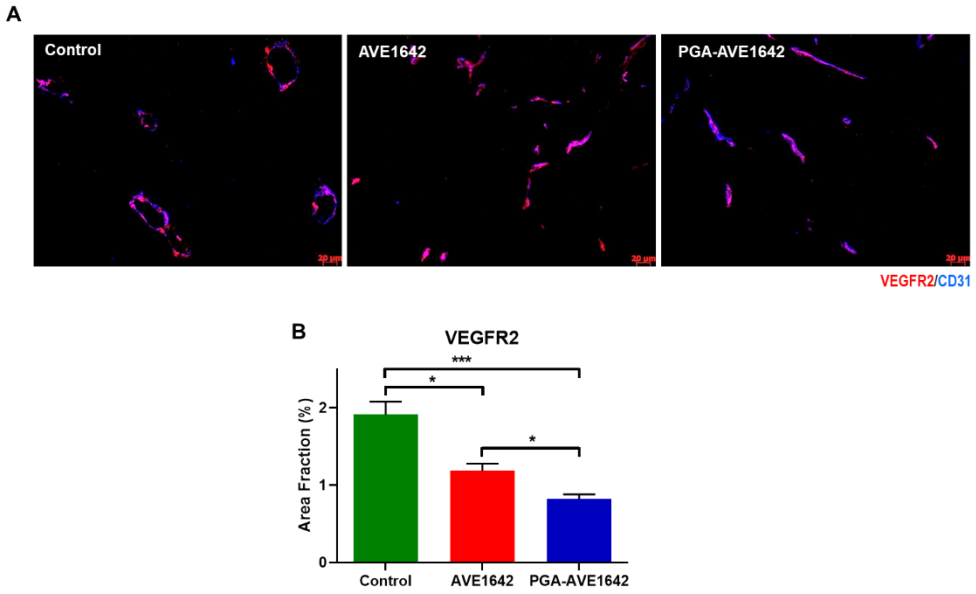

Figure 37: Histological Analysis of VEGFR2 Staining in Prostate Tumor Samples. A) Representative images for each treatment group at 20X magnification. VEGFR2 (red) marks angiogenesis, and DAPI (blue) marks nuclei. Scale bar 20µm. **B)** Graph represents the quantification of the VEGFR2 signal expressed as the area fraction % in all the treatment groups analyzed with AxioVision software. Data expressed as mean±SEM, n>3. Statistical analysis was performed using ANOVA, **p< 0.01, ****p< 0.0001.

III.11. Conclusions

As a conclusion from this chapter, chemical characterization promoted evidence to the presence of polymer conjugation to AVE1642 due to an increase in different parameters such as the Mw, the hydrodynamic volume, the diameter, and a more negative zeta potential value. Furthermore, PGA conjugation did not change the secondary AVE1642 structure, suggesting the same AVE1642 functionality, which shows us that PGA-AVE1642 maintained the antibody variable region and its specificity for binding. In addition, PGA conjugation may enhance AVE1642 stability because precipitation is avoided. Moreover, we provide evidence that PGA conjugation improves the activity of AVE1642 *in vitro* and *in vivo*. We demonstrate that PGA conjugation can enhance AVE1642 binding affinity to IGF-1R, protect AVE1642 from degradation in serum, and alter AVE1642 cellular trafficking. The subsequent robust inhibition of IGF-1R by PGA-AVE1642 prevents the activation of both MAPK and PI3K signaling pathways leading to enhanced antitumoral activity *in vitro* and in an orthotopic PCa mouse model. Finally, we analyzed crucial tumor-associated vasculature parameters, including vessel functionality and maturity. We discovered that PGA-AVE1642 treatment significantly decreases vessel functionality and maturity and tumor angiogenesis when compared to unconjugated AVE1642, which is associated with decreased tumor cell proliferation.

These encouraging results suggest that PGA-AVE1642 could be then identified as an excellent alternative therapeutic strategy to AVE1642 in PCa patients.

III.12. Bibliography

1. Mancarella, C., et al., *Insulin-like growth factor 1 receptor affects the survival of primary prostate cancer patients depending on TMPRSS2-ERG status.* BMC Cancer, 2017. **17**(1): p. 367-367.
2. Chen, H.X. and E. Sharon, *IGF-1R as an anti-cancer target--trials and tribulations.* Chinese Journal of Cancer, 2013. **32**(5): p. 242-252.
3. Simpson, A., et al., *Insulin-Like Growth Factor (IGF) Pathway Targeting in Cancer: Role of the IGF Axis and Opportunities for Future Combination Studies.* Targeted Oncology, 2017. **12**(5): p. 571-597.
4. Aggarwal, R.R., C.J. Ryan, and J.M. Chan, *Insulin-like growth factor pathway: A link between androgen deprivation therapy (ADT), insulin resistance, and disease progression in patients with prostate cancer?* Urologic Oncology: Seminars and Original Investigations, 2013. **31**(5): p. 522-530.
5. Duncan, R., *Polymer therapeutics as nanomedicines: New perspectives.* Current Opinion in Biotechnology, 2011. **22**: p. 492-501.
6. Roncador, A., et al., *Use of polymer conjugates for the intraperoxisomal delivery of engineered human alanine:glyoxylate aminotransferase as a protein therapy for primary hyperoxaluria type I.* Nanomedicine: Nanotechnology, Biology and Medicine, 2017. **13**(3): p. 897-907.
7. Talelli, M. and M.J. Vicent, *Reduction Sensitive Poly(l-glutamic acid) (PGA)-Protein Conjugates Designed for Polymer Masked–Unmasked Protein Therapy.* Biomacromolecules, 2014. **15**(11): p. 4168-4177.
8. Maloney, E., et al., *An anti-insulin-like growth factor I receptor antibody that is a potent inhibitor of cancer cell proliferation.* Cancer research, 2003. **63**: p. 5073-83.
9. Sachdev, D., et al., *The type I insulin-like growth factor receptor regulates cancer metastasis independently of primary tumor growth by promoting invasion and survival.* Oncogene, 2009. **29**: p. 251-62.
10. Mancarella, C., et al., *ERG deregulation induces IGF-1R expression in prostate cancer cells and affects sensitivity to anti-IGF-1R agents.* Oncotarget, 2015. **6**(18): p. 16611-16622.
11. Geoerger, B., et al., *Anti-insulin-like growth factor 1 receptor antibody EM164 (murine AVE1642) exhibits anti-tumour activity alone and in combination with temozolomide against neuroblastoma.* European Journal of Cancer, 2010. **46**(18): p. 3251-3262.

12. Descamps, G., et al., *CD45neg but Not CD45pos Human Myeloma Cells Are Sensitive to the Inhibition of IGF-1 Signaling by a Murine Anti-IGF-1R Monoclonal Antibody, mAVE1642.* The Journal of Immunology, 2006. **177**(6): p. 4218.
13. Macaulay, V.M., et al., *Phase I study of humanized monoclonal antibody AVE1642 directed against the type 1 insulin-like growth factor receptor (IGF-1R), administered in combination with anticancer therapies to patients with advanced solid tumors.* Annals of Oncology, 2013. **24**(3): p. 784-791.
14. Chi, K.N., et al., *A Phase II Pharmacodynamic Study of Preoperative Figitumumab in Patients with Localized Prostate Cancer.* Clinical Cancer Research, 2012. **18**(12): p. 3407.
15. Dean, J.P., et al., *Response of the insulin-like growth factor (IGF) system to IGF-IR inhibition and androgen deprivation in a neoadjuvant prostate cancer trial: effects of obesity and androgen deprivation.* The Journal of Clinical Endocrinology and Metabolism, 2013. **98**(5): p. 820-828.
16. Zagorodko, O., et al., *Polypeptide-Based Conjugates as Therapeutics: Opportunities and Challenges.* Macromolecular Bioscience, 2017. **17**(1): p. 1600316.
17. Jain, N., et al., *Current ADC Linker Chemistry.* Pharmaceutical Research, 2015. **32**(11): p. 3526-3540.
18. Liu, H. and K. May, *Disulfide bond structures of IgG molecules: structural variations, chemical modifications and possible impacts to stability and biological function.* MAbs, 2012. **4**(1): p. 17-23.
19. Lucas, J.M., et al., *The androgen-regulated protease TMPRSS2 activates a proteolytic cascade involving components of the tumor microenvironment and promotes prostate cancer metastasis.* Cancer Discovery, 2014. **4**(11): p. 1310-1325.
20. Wang, Z., et al., *Significance of the TMPRSS2:ERG gene fusion in prostate cancer.* Molecular Medicine Reports, 2017. **16**(4): p. 5450-5458.
21. Linn, D.E., et al., *Deletion of Interstitial Genes between TMPRSS2 and ERG Promotes Prostate Cancer Progression.* Cancer Research, 2016. **76**(7): p. 1869-1881.
22. Murphy, S.J., et al., *Retention of Interstitial Genes between TMPRSS2 and ERG Is Associated with Low-Risk Prostate Cancer.* Cancer Research, 2017. **77**(22): p. 6157.

23. Paulo, P., et al., *Molecular Subtyping of Primary Prostate Cancer Reveals Specific and Shared Target Genes of Different ETS Rearrangements.* Neoplasia, 2012. **14**: p. 600.
24. Tomlins, S., et al., *Role of the TMPRSS2–ERG gene fusion in prostate cancer.* Neoplasia, 2008. **10**: p. 177-188.
25. Mancarella, C., et al., *ERG deregulation induces IGF-1R expression in prostate cancer cells and affects sensitivity to anti-IGF-1R agents.* Oncotarget, 2015. **6**(18): p. 16611-22.
26. Rahim, S., et al., *YK-4-279 inhibits ERG and ETV1 mediated prostate cancer cell invasion.* PLoS One, 2011. **6**: p. 19343.
27. Gagnon, P., et al., *Transient conformational modification of immunoglobulin G during purification by protein A affinity chromatography.* Journal of Chromatography A, 2015. **1395**: p. 136-142.
28. Ito, T. and K. Tsumoto, *Effects of subclass change on the structural stability of chimeric, humanized, and human antibodies under thermal stress.* Protein Science, 2013. **22**(11): p. 1542-1551.
29. Gooding, E.A., et al., *pH-dependent helix folding dynamics of poly-glutamic acid.* Chemical Physics, 2013. **422**: p. 115-123.
30. Wyce, A., et al., *Inhibition of BET bromodomain proteins as a therapeutic approach in prostate cancer.* Oncotarget, 2013. **4**(12): p. 2419-29.
31. Martins, A., et al., *IGF1R Signaling in Ewing Sarcoma Is Shaped by Clathrin-/Caveolin-Dependent Endocytosis.* PLoS One, 2011. **6**: p. 19846.
32. Duncan, R., *Designing polymer conjugates as lysosomotropic nanomedicines.* Biochemical Society Transactions, 2007. **35**(1): p. 56.
33. da Silva, R.M.P., et al., *Super-resolution microscopy reveals structural diversity in molecular exchange among peptide amphiphile nanofibres.* Nature Communications, 2016. **7**: p. 11561-11561.
34. Shim, S.-H., et al., *Super-resolution fluorescence imaging of organelles in live cells with photoswitchable membrane probes.* PNAS, 2012. **109**(35): p. 13978-13983.
35. Bates, M., S.A. Jones, and X. Zhuang, *Stochastic Optical Reconstruction Microscopy (STORM): A Method for Superresolution Fluorescence Imaging.* Cold Spring Harbor Protocols, 2013. **2013**(6): p. 498-520.
36. Zha, J. and M.R. Lackner, *Targeting the Insulin-like Growth Factor Receptor-1R Pathway for Cancer Therapy.* Clinical Cancer Research, 2010. **16**(9): p. 2512.

37. Griffeth, R., V. Bianda, and S. Nef, *The emerging role of insulin-like growth factors in testis development and function.* Basic and Clinical Andrology, 2014. **24**: p. 12.
38. Fumihiko, H. and T. Shin-Ichiro, *40 YEARS OF IGF1: IGF1 receptor signaling pathways.* Journal of Molecular Endocrinology, 2018. **61**(1): p. 69-86.
39. Subbiah, V., L.S. Angelo, and R. Kurzrock, *Insulin-like growth factor 1 receptor (IGF-1R) inhibitor: another arrow in the quiver – Will it hit the moving target?.* Expert Opinion on Investigational Drugs, 2011. **20**(11): p. 1471-1477.
40. Jyoti, S., et al., *Prostate cancer screening by prostate-specific antigen (PSA); a relevant approach for the small population of the Cayman Islands.* Cancer Causes & Control, 2017. **29**(1): p. 87-92.
41. Vicent, M. and R. Duncan, *Polymer conjugates: Nanosized medicines for treating cancer.* Trends in Biotechnology, 2006. **24**: p. 39-47.
42. Duncan, R. and M.J. Vicent, *Polymer therapeutics-prospects for 21st century: The end of the beginning.* Advanced Drug Delivery Reviews, 2013. **65**(1): p. 60-70.
43. Golombek, S.K., et al., *Tumor targeting via EPR: Strategies to enhance patient responses.* Advanced Drug Delivery Reviews, 2018. **130**: p. 17-38.
44. Recouvreux, M.V., et al., *Androgen Receptor Regulation of Local Growth Hormone in Prostate Cancer Cells.* Endocrinology, 2017. **158**(7): p. 2255-2268.
45. Wu, J. and E. Yu, *Insulin-like growth factor receptor-1 (IGF-IR) as a target for prostate cancer therapy.* Cancer Metastasis Reviews, 2014. **33**(2-3): p. 607-617.
46. Wang, M., et al., *Role of tumor microenvironment in tumorigenesis.* Journal of Cancer, 2017. **8**(5): p. 761-773.
47. Shi, J., et al., *Tumor microenvironment promotes prostate cancer cell dissemination via the Akt/mTOR pathway.* Oncotarget, 2018. **9**(10): p. 9206-9218.
48. Skalli, O., et al., *Alpha-smooth muscle actin, a differentiation marker of smooth muscle cells, is present in microfilamentous bundles of pericytes.* Journal of Histochemistry & Cytochemistry, 1989. **37**(3): p. 315-321.
49. Ehling, J., et al., *Micro-CT imaging of tumor angiogenesis: quantitative measures describing micromorphology and vascularization.* The American Journal of Pathology, 2014. **184**(2): p. 431-441.

50. Scholzen, T. and J. Gerdes, *The Ki-67 protein: From the known and the unknown.* Journal of Cellular Physiology, 2000. **182**(3): p. 311-322.
51. Veikkola, T., et al., *Regulation of Angiogenesis via Vascular Endothelial Growth Factor Receptors.* Cancer Research, 2000. **60**(2): p. 203.
52. Goel, H.L. and A.M. Mercurio, *VEGF targets the tumour cell.* Nature Reviews Cancer, 2013. **13**(12): p. 871-882.
53. https://clinicaltrials.gov/

Chapter IV

Evaluation of a Novel Combination Therapy for Castration-Resistant Prostate Cancer

IV.1. Antecedents and Background

Despite the promising initial responses of CRPC patients to strategies that block androgen signaling (e.g., abiraterone and enzalutamide [1]) or the PI3K/Akt pathway (e.g., PI3K/mTOR inhibitors, TKR inhibitors [1]), long term results have not proven as successful as anticipated, often due to the increased activity of reciprocal signaling pathways.

For example, the PI3K/Akt pathway suffers from reciprocal feedback with the AR signaling pathway in PCa, and the cross-regulation of these oncogenic pathways promotes tumor growth [2, 3]. Therefore, the dual inhibition of these pathways may effectively inhibit prostate tumor growth; as an example, preclinical research has provided evidence for potent anti-tumor synergism between PI3K/Akt inhibition and androgen deprivation therapy (ADT) [4].

At the clinical level, multiple trials have assessed the outcomes of combination approaches involving immunotherapy, hormone therapy, chemotherapy, radiotherapy, and surgery to improve clinical outcomes, with many of them combining antibody-based approaches with conventional treatments. Focusing on the use of mAbs, for example, Phase II trials are underway to investigate combination immunotherapies for PCa; these include the combination of Sipuleucel-T, a personalized immunostimulant and the first immunotherapy for CRPC approved in 2010 by the FDA [5], with a PD-1 immune response inhibitor (anti-PD-1 mAb, CT-011 - NCT01420965) or an inhibitor of T-cell proliferation and activation (anti-CTLA4 mAb, ipilimumab - NCT01804465). Several clinical trials are also evaluating combinations of ADTs with immunotherapies, including enzalutamide with anti-PD-1 mAbs (pembrolizumab - NCT03753243, and atezolizumab - NCT03016312). Furthermore, clinical trials of conventional chemotherapeutics with immunotherapies have also been undertaken, including

Ipatasertib (a small molecule inhibitor of AKT) with atezolizumab (NCT03673787), evofosfamide and ipilimumab (NCT03098160), and cabozantinib (small-molecule inhibitor of the tyrosine kinases) with atezolizumab (NCT03170960). Additionally, various modes of radiation therapy have been assessed in combination with Sipuleucel-T (NCT02463799, NCT01807065) and different anti-PD-1 mAbs (pembrolizumab - NCT03093428 and nivolumab - NCT03543189) [6].

Of particular interest to our laboratory, polymer therapeutic-based approaches to single and combination therapies offer numerous advantages. The modification of active agents, such as those described above, with polymers, can allow for the enhanced passive targeting to adequately vascularized tumors [7-9], the crossing of critical biological barriers [10], elevated blood plasma stability, targeted release, altered trafficking, increased solubility and the chemical stability, modified pharmacokinetics, and reduced toxicity and adverse effects [11, 12]. In the realm of combination therapy, polymer-based approaches can promote tumor targeting of multiple active agents at the correct ratio for synergistic anti-tumor effects [13]. As an example of the potential of this approach, a recent study established that treatment with a polyacetal-based combination therapy combining curcumin as an antitumoral agent associated with Wnt/β-catenin pathway modulation and diethylstilbestrol as an ADT (PA-Curc-DES) induced S-phase cell cycle arrest in human PCa cell lines through the specific release of both drugs in the tumor cell or in the tumor microenvironment [14].

Irrespective of the therapeutic approach employed, enhanced treatment strategies must be provided to only those patients who will respond. Importantly to the work carried out in this chapter, inhibiting the IGF-1R and androgen pathways lead to increased cytotoxicity in only those PCa cells expressing the TMPRSS2-ERG (T2E) transgene [15]. Therefore, the construction of a polymer-based combination therapy that would permit the potent inhibition of both these

pathways in the same cell may further improve PCa treatment outcomes in T2E-positive patients.

In the previous chapter, we highlighted the robust anti-tumor activity of PGA-AVE1642 in T2E-expressing cells. In this chapter, we evaluated the antitumoral synergy of PGA-AVE1642 with abiraterone, a drug that inhibits the generation of androgens, and hence acts to inhibit AR signaling.

Abiraterone is a selective inhibitor of the CYP17 enzyme - a 17,20-lyase, and 17α-hydroxylase from the cytochrome P450 family that aids the synthesis of androgens and cortisol in the testicles, adrenal glands, and within tumors using cholesterol as an initial precursor. Therefore, the administration of abiraterone will inhibit androgen production and, in theory, inhibit the growth of androgen-dependent PCa cells and tumors (**Figure 1**) [16, 17]. Following oral administration to CRPC patients, abiraterone acetate becomes rapidly hydrolyzed to abiraterone in the bloodstream [18].

Therefore, in this chapter, we sought to describe the possible synergism between AVE1642/PGA-AVE1642 and abiraterone *in vitro* and evaluate anti-tumor activity *in vivo*.

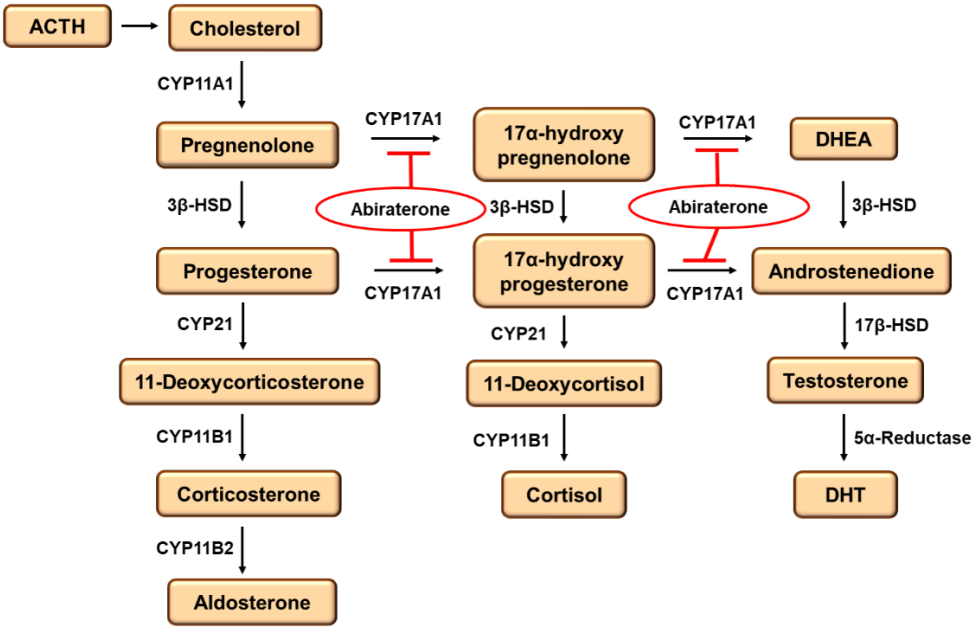

Figure 1: Overview of the Mechanisms of Action of Abiraterone. Abiraterone as an anti-androgen drug blocks 17α-hydroxylase and 17,20-lyase enzymatic activity to avoid both the conversion of pregnenolone to 17-hydroxy-pregnenolone and dehydroepiandrosterone (DHEA) and the conversion of progesterone to 17-hydroxy-progesterone and androstenedione.

IV.2. PGA-AVE1642 Synergizes with Abiraterone in VCaP cells

In the previous chapter, we demonstrated that the T2E fusion gene-expressing VCaP cell line, which expresses high levels of IGF-1R and AR, displayed sensitivity to AVE1642 and PGA-AVE1642. *In vitro* analyses demonstrated that PGA conjugation improved the stability and affinity and altered the cell trafficking of AVE1642, and *in vivo* experiments provided evidence for improved antitumorigenic activity. We next sought to evaluate the consequences of inhibiting both the PI3K/Akt and AR pathways in PCa cells/tumors by anti-IGF-1R inhibition using AVE1642 or PGA-AVE1642 and androgen synthesis inhibition using abiraterone.

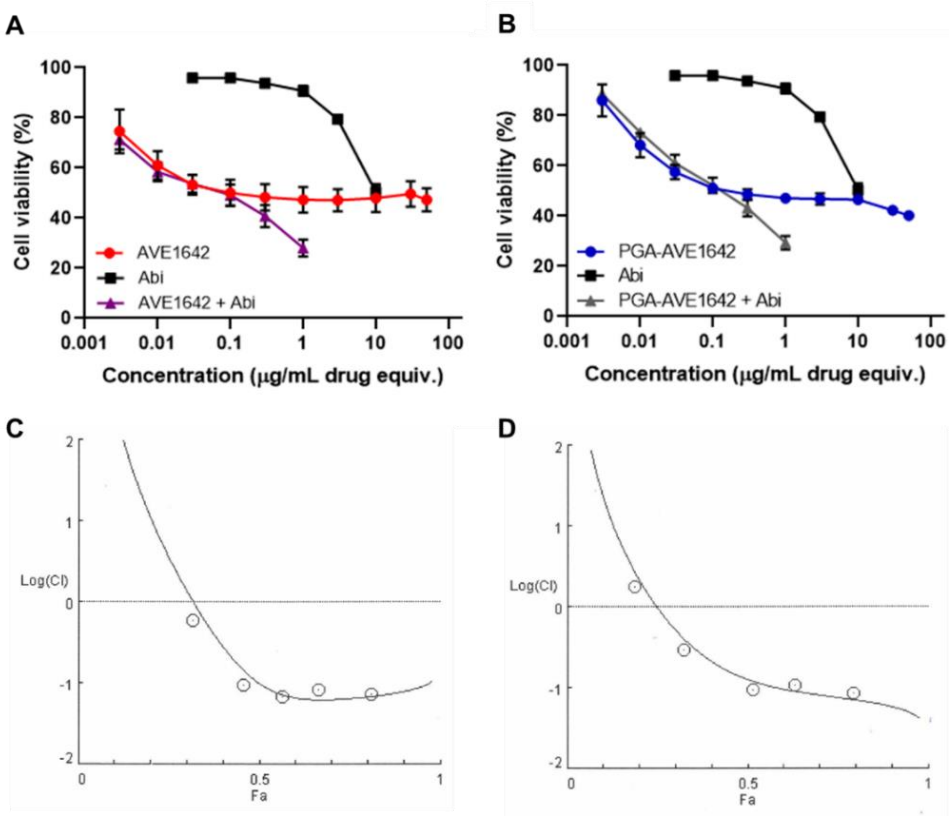

Figure 2: Synergism of AVE1642/PGA-AVE1642 and Abiraterone in VCaP cells. A) Graph depicts cell viability versus drug equiv. (µg/ml) for abiraterone and AVE1642 alone and in combination. Combination therapies are represented in AVE1642 µg/ml equiv. **B)** Graph depicts cell viability versus drug equiv. (µg/ml) for abiraterone and PGA-AVE1642 alone and in combination. Combination therapies are represented in AVE1642 µg/ml equiv. **C)** Plot of the log(CI) index vs. the effect (Fa) of AVE1642 in association with abiraterone at a 1:10 ratio using CompuSyn software. The plot of the CI indicates synergy between two treatments at 0.01, 0.03, 0.1, 0.3, and 1 µg/ml AVE1642 in combination with abiraterone at 0.1, 0.3, 1, 3, and 10 µg/ml. **D)** Plot of the log(CI) index vs. the effect (Fa) of PGA-AVE1642 in association with abiraterone at a 1:10 ratio using CompuSyn software. The plot of the CI indicates synergy between two treatments at 0.03, 0.1, 0.3, and 1 µg/ml PGA-AVE1642 in combination with abiraterone at 0.3, 1, 3, and 10 µg/ml. Data expressed as mean±SEM, n>3.

We treated VCaP cells for 72 hours with AVE1642, PGA-AVE1642 (from 50 to 0.003 µg/ml AVE1642 equiv.), or abiraterone (from 10 to 0.03 µg/ml), and combinations of AVE1642 or PGA-AVE1642 with abiraterone at a 1:10 ratio respectively (1 unit of AVE1642 equiv. and 10 units of abiraterone). **Figures 2.A** and **B** demonstrate that abiraterone treatment alone reduced cell viability at concentrations above 1 µg/ml drug equiv., while AVE1642 and PGA-AVE1642 treatment produced the expected reduction in cell viability. The combination therapy of AVE1642 or PGA-AVE1642 with abiraterone provided a synergistic effect in both cases, with a more significant cytotoxic effect observed at reduced concentrations when compared to abiraterone or AVE1642/PGA-AVE1642 treatments alone. Both combination therapies exhibited similar cytotoxicity profiles with the same IC_{50} concentration (~0.1 µg/ml drug equiv.).

As synergistic interactions between drugs represent a crucial issue in pharmacology, we determined the combination index (CI) and the fraction affected (Fa) to study synergism using the CompuSyn software. The CI value is calculated from drug cytotoxicity, and indicates a synergistic (CI<1), additive (CI=1), or antagonist (CI>1) effect, while Fa values represent the cytotoxicity of the combination therapies [19]. **Figures 2.C** and **D** depict the plot of the log(CI) index versus the effect (Fa) of AVE1642/PGA-AVE1642 in combination with abiraterone to detect any synergy. Values above zero indicate antagonism, while a value below negative indicate synergy. Specifically, **Figure 2.C** demonstrates synergy (CI<1) for AVE1642 at 0.01, 0.03, 0.1, 0.3 and 1 µg/ml AVE1642 equiv. in combination with abiraterone at 0.1, 0.3, 1, 3, and 10 µg/ml. Moreover, **Figure 2.D** demonstrate synergy (CI<1) for PGA-AVE1642 at 0.03, 0.1, 0.3 and 1 µg/ml AVE1642 equiv. in combination with abiraterone at 0.3, 1, 3, and 10 µg/ml.

The results confirm the results obtained in **Figures 2.A** and **B** for both combination therapies.

Overall, AVE1642 or PGA-AVE1642 treatment, in combination with abiraterone, provided synergistic cytotoxic effects in VCaP cells when employed at a 1:10 ratio. For subsequent *in vitro* experiments, we used the IC_{50} values for both combination therapies (0.1 μg/ml AVE1642 equiv. with 1 μg/ml abiraterone) at which we found a synergistic effect. CI value analysis indicated the presence of a synergistic effect (CI<1) for abiraterone treatment in combination with either AVE1642 (CI=0.06) and PGA-AVE1642 (CI=0.07) in VCaP cells at IC_{50} μg/ml drug equiv. concentrations.

IV.3. Combination Therapy Exhibits T2E-dependent Synergistic Effects in Prostate Cancer Cells

We next determined the synergistic effect of AVE1642/PGA-AVE1642 and abiraterone in additional PCa cell lines (22Rv1, DU-145, LNCaP, and PC-3) and a normal prostate epithelial cell line (RWPE-1) and compared these findings to VCaP cells to study the requirement for the T2E fusion gene. Each PCa cell line also exhibits different androgen-responsiveness - 22Rv1, LNCaP, and VCaP cells are androgen-dependent, while the DU-145 and PC-3 cell lines are androgen-independent.

Treatment of cells with abiraterone alone for 72 hours demonstrated a trend towards increasing cytotoxicity with increasing abiraterone concentrations; treatment with 10 μg/ml abiraterone prompted a ~50% reduction in cell viability in 22Rv1, VCaP, and RWPE-1 cells, and a ~25% reduction in PC-3, DU-145 and LNCaP cells (**Figure 3**). These results suggest 22Rv1 and VCaP androgen-dependent PCa cell lines display higher sensitivity to abiraterone, which may be due to higher AR levels when compared to androgen-independent PC-3 and DU-145 PCa cell lines (**See Chapter III**, **Figure 3**).

Of note, although we detected an anti-androgenic effect in androgen-independent PCa cell lines at higher abiraterone concentrations, we did not detect AR expression. Furthermore, we failed to detect a stronger abiraterone efficacy in LNCaP androgen-dependent cell lines despite showing higher AR levels. Additionally, normal prostate tissue showed an androgenic effect at higher concentrations despite not expressing AR (**See Chapter III**, **Figure 3**).

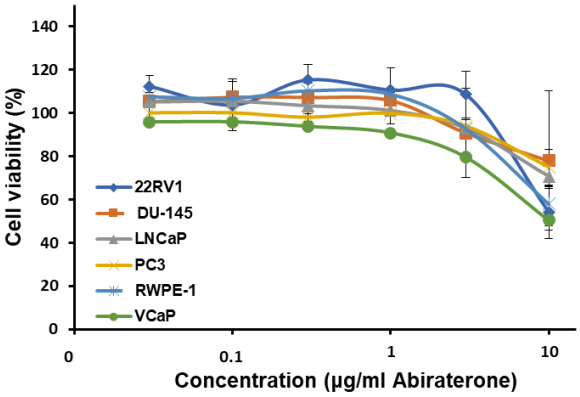

Figure 3: Cytotoxic Effects of Abiraterone in Normal Prostate Epithelium and PCa Cell Lines. PCa cells (22Rv1, DU-145, LNCaP, PC-3, and VCaP) and RWPE-1 as a control normal prostate epithelium cell line were treated for 72 hours with increasing concentrations of abiraterone. Graph shows the cell viability (%) versus concentration of abiraterone (µg/ml). Data expressed as mean±SEM, n=3.

Overall, the VCaP androgen-dependent cells generally displayed higher sensitivity to abiraterone at all the concentrations evaluated compared with the other cell lines.

We next studied our combination therapies in these cell lines to determine the specificity of the synergistic effect; we treated cells with AVE1642 (**Figure 4.A**) or PGA-AVE1642 (**Figure 4.B**) combined with abiraterone at 1:10 ratio for 72 hours. **Tables 1.A** and **B** depict the observed reductions in cell viability (as a percentage) after the indicated treatments in the different cell lines. Overall, the T2E-positive

VCaP cell line displayed the highest sensitivity with both combination therapies providing for a similar decrease in cell viability at the IC_{50} values for the combination therapy (0.1 µg/ml AVE1642 equiv. and 1 µg/ml abiraterone) (**Figures 4.A** and **B** green line and **Table 1.A**). However, LNCaP, 22Rv1, and RWPE-1 also displayed a heightened response to AVE1642/PGA-AVE1642 and abiraterone at higher concentrations (ten times IC_{50} values) (**Table 1.B**). Moreover, DU-145 and PC-3 have a remarkably low response after both combination therapies compared with the other cell lines at higher concentrations (**Table 1.B**).

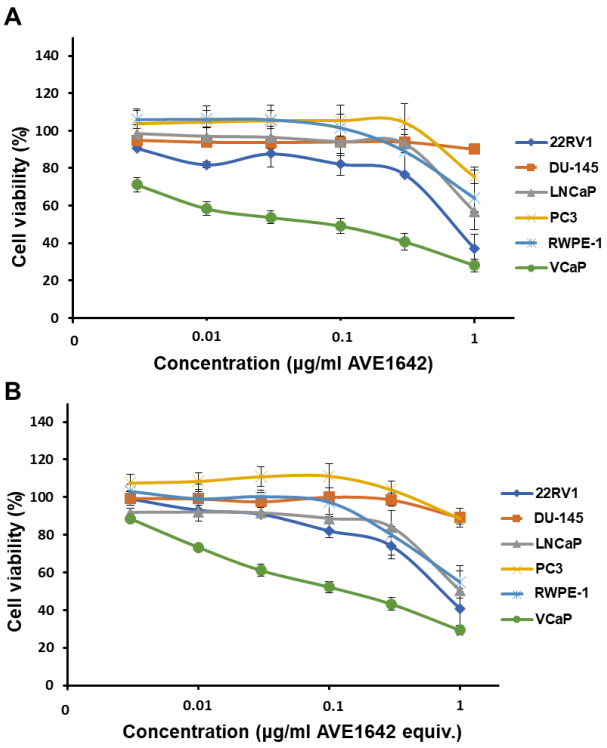

Figure 4: VCaP Cells Display Higher Sensitivity to Combination Therapy. Graphs represent the cell viability percentage versus the concentration (µg/ml AVE1642 equiv.) in different PCa cell lines (VCaP, LnCaP, DU-145, 22Rv1, and PC-3) and RWPE-1 as normal tissue. **A)** AVE1642 in combination with abiraterone treatment. **B)** PGA-AVE1642 in combination with abiraterone treatment. Data expressed as mean±SEM, n=3.

Importantly, the responses of LNCaP and RWPE-1 cells to both combination therapies at higher concentrations derives solely from the effect of abiraterone, as these cell lines did not respond to AVE1642 or PGA-AVE1642 treatment (**See Chapter III**, **Figure 13**) (**Table 1.B**). In contrast, the response of the 22Rv1 cell line to the combination therapies at the higher concentrations provided further evidence for synergy between AVE1642/PGA-AVE1642 and abiraterone (**Table 1.B**).

We next enumerated the synergistic effect of the combination therapies in each of the relevant cell lines. By the calculation of the CI value using the CompuSyn program, we detected a synergistic effect (CI<1) for abiraterone in combination with AVE1642 (CI=0.015) and PGA-AVE1642 (CI=0.017) in the 22Rv1 cell line with both combination therapies at the higher concentration tested.

A

0.1µg/ml AVE1642 and PGA-AVE1642 1µg/ml Abiraterone	AVE1642 (% cell death)	PGA-AVE1642 (% cell death)	Abiraterone (% cell death)	AVE1642 + Abiraterone (% cell death)	PGA-AVE1642 + Abiraterone (% cell death)	AVE1642 + Abiraterone (CI Value)	PGA-AVE1642 + Abiraterone (CI Value)
VCaP	44.12	41.46	9.21	50.81	47.77	**<1**	**<1**
LNCaP	0	0	0	5.97	11.43	>1	>1
22Rv1	21.51	16.84	0	17.83	17.99	>1	>1
DU-145	0	0	0	6.05	0	>1	>1
PC3	0	0	0.19	0	0	>1	>1
RWPE-1	0	0	0	0	2.60	>1	>1

B

1µg/ml AVE1642 and PGA-AVE1642 10µg/ml Abiraterone	AVE1642 (% cell death)	PGA-AVE1642 (% cell death)	Abiraterone (% cell death)	AVE1642 + Abiraterone (% cell death)	PGA-AVE1642 + Abiraterone (% cell death)	AVE1642 + Abiraterone (CI Value)	PGA-AVE1642 + Abiraterone (CI Value)
VCaP	45.07	44.86	49.60	71.95	70.60	**<1**	**<1**
LNCaP	0	0	29.25	43.28	49.52	>1	>1
22Rv1	21.36	27.70	45.00	63.08	59.23	**<1**	**<1**
DU-145	0	0	22.03	9.77	10.88	>1	>1
PC3	0	0	25.03	24.70	11.17	>1	>1
RWPE-1	0	0	42.14	36.12	26.35	>1	>1

Table 1: Percent cell viability reduction in normal prostate and PCa cell lines in response to various treatment approaches. A) Values in % cell death for IC_{50} combination therapies concentrations (0.1 µg/ml AVE1642 equiv. and 1 µg/ml abiraterone). **B)** Values in % cell death for 10x IC_{50} combination therapies concentrations (1 µg/ml AVE1642 equiv. and 10 µg/ml abiraterone). CI<1 synergistic, CI=1 additive, or CI>1 antagonist effect.

Overall, while we observed a range of sensitivities in various cell lines to the combination therapies under evaluation, only the VCaP cell line provided evidence for an appreciable synergistic effect over a range of concentrations, we found synergism for our combination therapies in the 22Rv1 cell line only at concentrations of ten times the IC_{50} values.

IV.4. The Synergistic Effect of the Combination Therapy Requires T2E Expression

We next studied the specificity of the combination therapy in the presence of the T2E fusion gene in VCaP cells by assessing cell viability after ERG gene silencing via small interfering (si)RNA expression. We investigated ERG silencing in 1) control VCaP cells, and VCaP cells treated with 2) AVE1642 and abiraterone (0.1 μg/ml and 1 μg/ml respectively), and 3) PGA-AVE1642 and abiraterone (0.1 μg/ml AVE1642 equiv. and 1 μg/ml respectively).

Figure 5 shows the relative change in cell number (in fold) in response to each treatment and a representative Western blot image that confirms ERG silencing (**Figure 5.A**). We calculated the effectiveness of the various treatments after normalization to their respective untreated control groups. We discovered that ERG gene silencing (siERG) negates the effect of AVE1642 /abiraterone (**Figure 5.B**) and PGA-AVE1642 /abiraterone treatments (**Figure 5.C**) on cell survival, with significant differences between the untreated (NT) and ERG siRNA (siERG) in the cells treated with AVE1642/abiraterone and highly significant changes between scramble siRNA control (SCR) and ERG siRNA (siERG) in the cells treated with AVE1642/abiraterone. Furthermore, we also observed significant differences between the NT and ERG siRNA (siERG) in the cells treated with PGA-AVE1642/abiraterone and between scramble siRNA control (SCR) and ERG siRNA (siERG) in the cells treated with PGA-AVE1642/abiraterone.

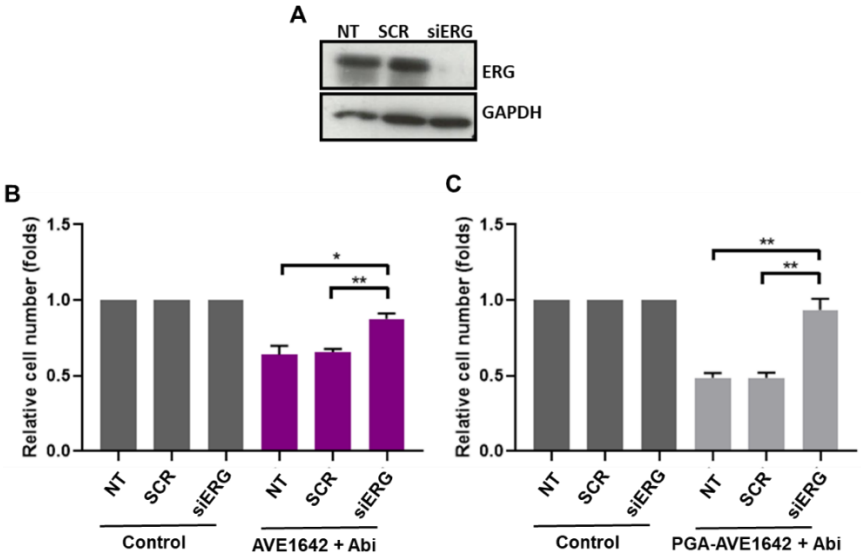

Figure 5: Influence of ERG Expression on the Cytotoxic Effect of Single and Combination Therapies in VCaP Cells. A) Representative Western blot image shows ERG expression in VCaP cell line under untransfected (NT), scrambled siRNA (SCR), and ERG siRNA treated (siERG) conditions. **B-C)** Graph shows cell viability (as measured by Trypan Blue exclusion assay) in untransfected VCaP cells (NT), VCaP transfected with scrambled control siRNA (SCR), and VCaP transfected with siRNA against ERG (siERG) treated with AVE1642 at 0.1 µg/ml in combination with abiraterone at 1 µg/ml, and PGA-AVE1642 at 0.1 µg/ml AVE1642 equiv. in combination with abiraterone at 1 µg/ml along 72 hours. Data expressed as mean±SEM, n>3. Statistical analysis was performed using ANOVA, *p< 0.05, **p< 0.01.

These results suggest that the effectiveness of the AVE1642/PGA-AVE1642 and abiraterone combination therapy requires ERG overexpression, which is caused by the presence of the T2E fusion gene.

IV.5. Antitumoral Activity of Prostate Cancer Combination Therapy *In vivo*

Our next steps focused on the study of our combinatorial therapeutic approach in the preclinical PCa mouse model described in the previous chapter (**See Section III.8.2**) by comparing single and combination therapies and analyzing the mechanism of action in tumor samples to determine alterations to intracellular signaling pathways.

IV.5.1. Optimization of the Orthotopic Mouse PCa Model to Evaluate Responses to Combination Therapy

Abiraterone blocks CYP17A1 enzyme activity, thereby blocking dehydroepiandrosterone (DHEA) production. The loss of DHEA then impacts dihydrotestosterone (DHT) production and inhibits androgen synthesis in humans [20]. However, CYP17A1 expression differs between human and rodents. In humans, the CYP17A1 gene is expressed in the adrenal glands and in the gonads but not in the placenta; in the rodent, CYP17A1 is expressed in the gonads and the placenta but not in the adrenal glands [21]. In particular, the Cyp17a1 gene in rodents suffers from epigenetic silencing and the complete lack of adrenal androgens such as DHEA [21, 22]. Of note, androgen-dependent PCa cell lines present the CYP17A1 enzyme; in contrast, androgen-independent PCa cell lines fail to express CYP17A1 levels [23]. However, abiraterone also inhibits 3β-hydroxysteroid dehydrogenase/isomerase (3βHSD), an enzyme that can synthesize DHT in CRPC from the DHEA precursor in the adrenal glands [24]. Therefore, to mimic human adrenal physiology conditions, we supplemented the mice with DHEA to study the effect of abiraterone in our mouse model (**See Figure 1**).

As human CRPC is treated with abiraterone acetate (shortened to AA in figures below) orally, we also treated mice in this manner by oral gavage, with abiraterone acetate converted into abiraterone in the bloodstream.

We first evaluated the effect of abiraterone acetate treatment without DHEA supplementation using our VCaP-Luc2 PCa mouse model (**See Chapter III**, **Section III.8.2**). At week two, we randomly divided mice into two groups (n=5), and we monitored tumor growth by IVIS® Spectrum and weighed animals weekly (**Figure 6.A**).

i. Vehicle control group with 95% sunflower oil and 5% benzyl alcohol (abiraterone acetate vehicle) by oral gavage daily from the second to the seventh week

ii. Abiraterone acetate treated group at 200 mg/kg by oral gavage daily from the second to the seventh week

We failed to observe any differences between vehicle control and abiraterone acetate treatment in the IVIS® Spectrum analysis of tumor development (**Figure 6.B**), the quantification of tumor evolution expressed in photons per second (derived from the IVIS® Spectrum analysis) (**Figure 6.C**), tumor volume measured by caliper at the experimental endpoint (**Figure 6.D**), or in representative images of the tumors at the week seven (**Figure 6.E**). Furthermore, we failed to observe any significant loss in body weight during the experiment (**Figure 6.F**).

Surprisingly, despite the expression of CYP17A1 and 3βHSD enzymes in the gonads, and the expression of 3βHSD enzyme in the adrenal glands, we failed to detect any antitumorigenic activity of abiraterone *in vivo*. These results provide evidence for lack of anti-tumoral activity for abiraterone in the absence of DHEA.

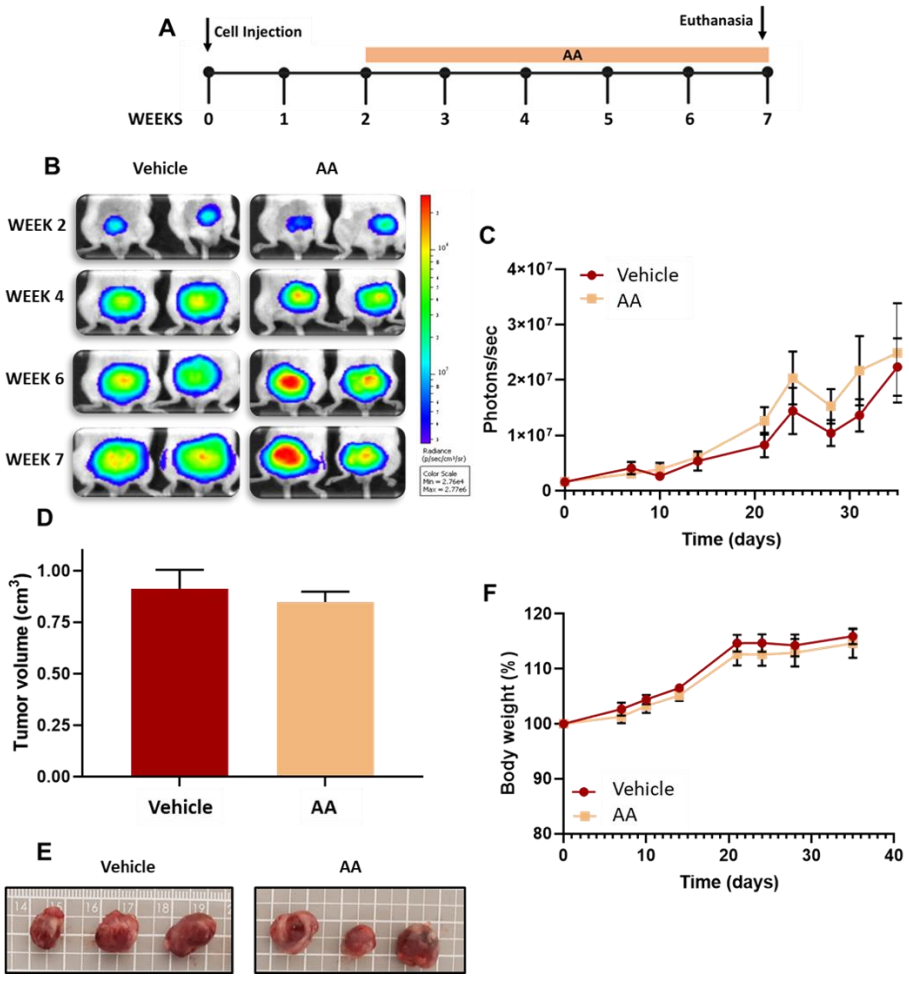

Figure 6: Antitumor Activity of Abiraterone Acetate in the Absence of DHEA in a VCaP-Luc2 Orthotopic PCa Mouse Model. Mice were treated with vehicle (95% sunflower oil with 5% benzyl alcohol) as control and abiraterone acetate (AA) at 200 mg/kg, both administered by oral gavage daily from the second week until the seventh week after the surgery. **A)** Schematic representation of abiraterone acetate treatment without DHEA supplement. **B)** Topographic tumor growth images evaluated in IVIS® Spectrum over time. **C)** Tumor growth over time assessed in each group as photons/second. **D)** Tumor volume expressed in cm^3 at the experimental endpoint measured by caliper. **E)** Representative tumor images after resection at the experimental point. **F)** Relative body weight percentage over time. Data expressed as mean±SEM, n>3. Statistical analysis performed by t-test.

We next investigated abiraterone acetate activity in our PCa mouse model in the presence of DHEA. DHEA supplementation promotes the synthesis of DHT through 3βHSD activity in the adrenal glands, and in the gonads. As in previous *in vivo* studies, following induction of tumors, we arbitrarily divided animals into three groups (n=5), and we evaluated tumor growth by IVIS® Spectrum twice a week and continuously monitored animal weight (**Figure 7.A**).

i. Vehicle control group with s.c. injections of 10% DMSO (DHEA vehicle) each day until the end of the experiment (seventh week) and, from week 2, with 95% sunflower oil and 5% benzyl alcohol daily by oral gavage (abiraterone acetate vehicle)

ii. DHEA treated group with s.c. injections of 0.1 mg DHEA each day from the surgery until the end of the experiment.

iii. DHEA and abiraterone acetate treated group with s.c. injections of 0.1 mg DHEA each day until the end of the experiment (seventh week) and, when tumors reached a size representative of the maximum EPR effect (0.05 cm^3) (week 2), we administered abiraterone acetate by oral gavage daily at 200 mg/kg each day until the end of the experiment

Figure 7.B depicts representative IVIS® Spectrum luminescence images, which highlights a comparable increase in tumor size for vehicle control and DHEA-only treated mice over seven weeks. We expected this result, as studies have shown that a lack of tumor response at the concentrations of DHEA employed (0.1 mg/day) [25]. However, the exposure of DHEA-treated mice to abiraterone acetate led to a significant reduction in tumor size compared to DHEA-only and vehicle control-treated mice. Quantification of IVIS® Spectrum data for five mice in each group, as shown in **Figure 7.C**, established a general increase in tumor size over time for vehicle-treated and DHEA supplemented mice, while DHEA supplemented

abiraterone acetate treated mice displayed lower tumor growth, although we did not find significant differences at the experimental endpoint due to the considerable variation in luminescent signal. Caliper measurements of tumor size, as shown in **Figure 7.D**, confirmed the reduction in tumor volume following abiraterone acetate treatment of DHEA-treated mice compared to vehicle and DHEA groups. In contrast, we failed to observe significant differences between vehicle and DHEA-supplemented only groups with regards to tumor size measurements made by caliper. Moreover, representative images of tumors from the three different groups of treated mice at week seven demonstrate similar tumor size between vehicle and DHEA treated groups; in contrast, the exposure of DHEA-treated mice to abiraterone acetate led to an evident reduction in tumor size (**Figure 7.E**). We also confirmed that treatment did not induce mouse body weight loss during the experiment, suggesting overall safety (**Figure 7.F**).

In summary, these data indicate that abiraterone acetate treatment requires DHEA supplementation to exhibit an anti-tumor therapeutic effect, which causes 3βHSD inhibition and the blockade of DHT synthesis in both the adrenal glands and gonads. Tumors can also foster intratumoral steroidogenesis from adrenal androgens such as DHEA and androstenedione or by de novo synthesis in tumor tissue from cholesterol to promote continued tumor growth [20, 21]. Despite the possibility of using multiple pathways for intratumoral androgen synthesis, the conversion of DHT through the “backdoor pathway” seems to be the major route for producing DHT. The backdoor pathway is based on the synthesis of DHT through pregnenolone (primary backdoor) and DHEA (secondary backdoor) bypassing testosterone synthesis, in which both alternative pathways require 3βHSD enzyme (**Figure 8**). For these reasons, our results confirm previous findings in which abiraterone inhibits the enzyme 3βHSD in the adrenal glands and the gonads, while also suggesting that abiraterone may also inhibit intratumoral androgens synthesis [20, 26].

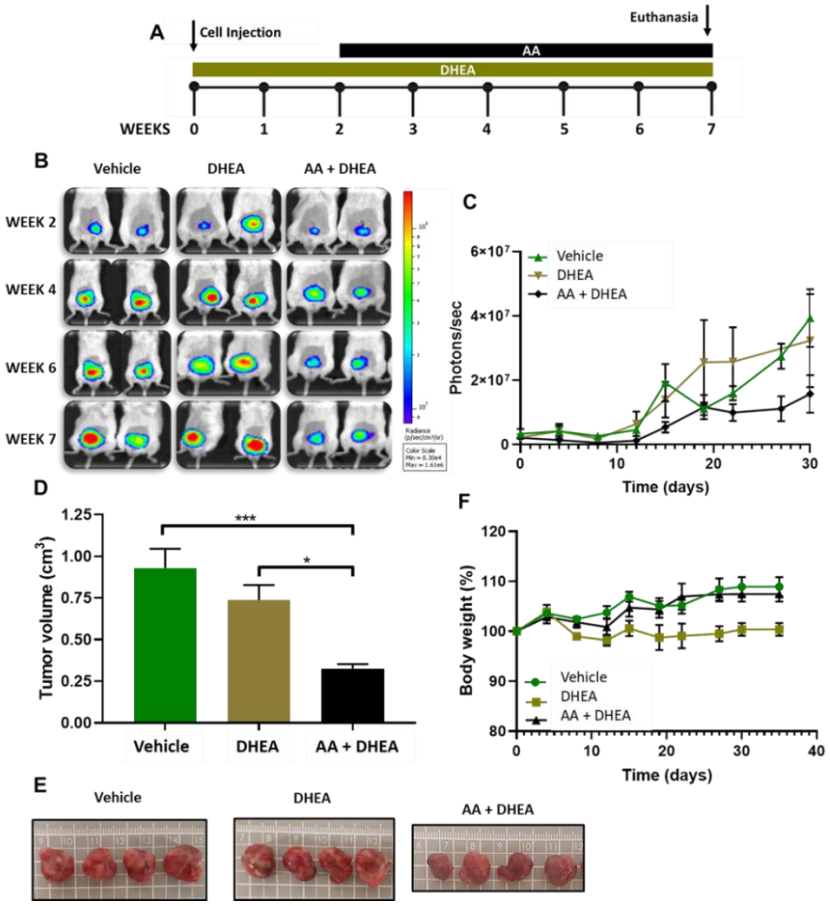

Figure 7: Antitumor Activity of Abiraterone Acetate in an Orthotopic PCa Mouse Model Supplemented with DHEA. Mice were treated in three groups i) vehicle control (subcutaneous injection of 10% DMSO and with 95% sunflower oil with 5% benzyl by oral gavage), ii) DHEA supplementation at 0.1 mg/day, and iii) DHEA supplementation and abiraterone acetate (AA) treatment (200 mg/kg). The same parameters, as in **Figure 6,** were studied. **A)** Schematic representation of experimental setup. **B)** Topographic tumor growth images evaluated in IVIS® Spectrum over time. **C)** Tumor growth over time evaluated as photons/second from IVIS® Spectrum experiments. **D)** Tumor volume measured by calipers at the experimental endpoint (expressed in cm^3). **E)** Representative images of tumors at the experimental endpoint. **F)** Changes to relative body weight percentage after the first administration. Data expressed as mean±SEM, n>3. Statistical analysis performed by ANOVA, *$p < 0.05$, ***$p < 0.001$.

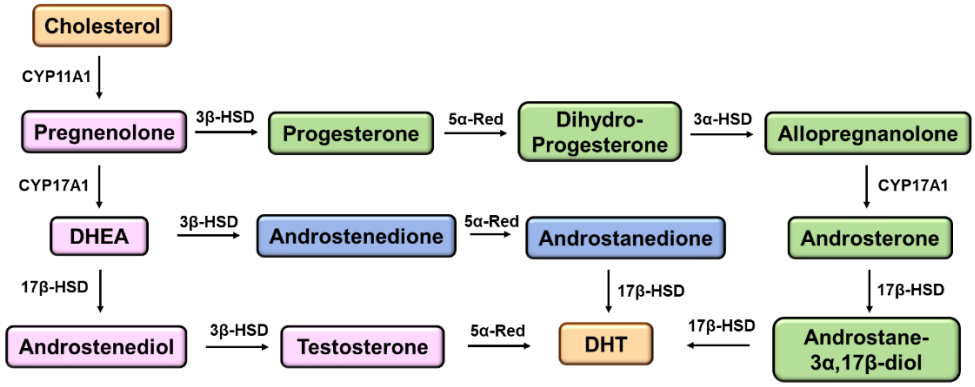

Figure 8: "Backdoor Pathway" of DHT Synthesis. Frontdoor pathway is represented in pink, which is used to synthesize DHT through testosterone. Primary and secondary backdoor pathways are represented in green and blue, respectively. Both pathways synthesize DHT bypassing intratumoral testosterone production. *Adapted from* [27]**.**

IV.5.2. DHEA Supplementation Does Not Interfere with the Anti-tumoral Activity of AVE1642 and PGA-AVE1642

We next assessed the effect of DHEA supplementation on the anti-tumoral activity of AVE1642 and PGA-AVE1642 *in vivo*. After tumor induction in PCa mice model, we randomly divided the mice into five groups (n=6) in the second week coinciding with the maximum EPR effect (0.05 cm^3) (**Figure 9.A**);

i. Vehicle control injected with PBS (i.v.) and 10% DMSO (s.c.)

ii. AVE1642 (i.v.) once a week for four weeks (10 mg/kg)

iii. PGA-AVE1642 (i.v.) once a week for four weeks (10 mg/kg AVE1642 equiv.)

iv. AVE1642 (i.v.) with DHEA supplementation (s.c. at 0.1 mg/day for the duration of the experiment)

v. PGA-AVE1642 (i.v.) with DHEA supplementation (s.c. injection at 0.1 mg/day for the duration of the experiment)

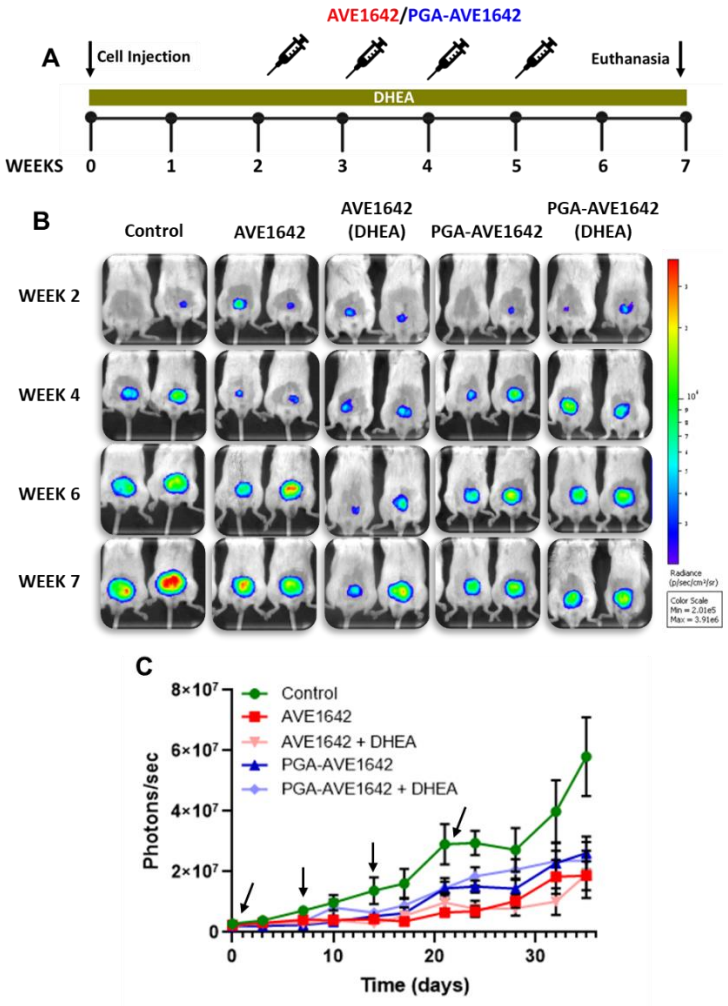

Figure 9: Tumor Growth Monitoring by Bioluminescence Detection Following AVE1642 and PGA-AVE1642 Treatment with and without DHEA in an Orthotopic PCa Mouse Model. Mice were treated with AVE1642 and PGA-AVE1642 at 10mg/kg (AVE1642 equiv.) with and without 0.1 mg/day of DHEA supplement and PBS/DMSO vehicle as a control. **A)** Schematic representation of experimental setup. **B)** Topographic tumor growth images evaluated in IVIS® Spectrum. **C)** Tumor growth expressed as photons/second (black arrows indicate the administering point of AVE1642 and PGA-AVE1642 treatments). Data expressed as mean±SEM, n>3.

Figures 9.B and **C**, which depict the IVIS® Spectrum analysis of tumor development and detection of photons/sec as a measure of tumor growth derived from IVIS® Spectrum analysis respectively, demonstrate higher tumor growth in the control group in comparison with the other four groups. In addition, we detected a similar lower tumor growth and tumor luminescence in mice treated with AVE1642/PGA-AVE1642 with and without DHEA supplement, confirming that the DHEA does not interfere with AVE1642/PGA-AVE1642 function.

Figure 10.A shows tumor volume measured by caliper at the experimental endpoint; tumors from mice treated with AVE1642/PGA-AVE1642 with and without DHEA displayed a highly significant decrease in tumor volume in comparison with control mice. Moreover, we failed to obtain significant differences for AVE1642 and PGA-AVE1642 treatment groups when comparing those treated with DHEA and those untreated. **Figure 10.B** illustrates representative tumor pictures in the seventh week for the five different conditions, demonstrating a lack of difference in tumor size between DHEA treated and untreated mice.

To further corroborate our results, we quantified serum PSA levels after the different treatment modalities. Both AVE1642 and PGA-AVE1642 with and without DHEA showed significant lower PSA levels compared with the vehicle-treated group, although again, we failed to find significant differences between DHEA treated and untreated mice (**Figure 10.C**). Finally, the treatments failed to induce significant losses o mouse body weight during the experimental timeframe (**Figure 10.D**).

Overall, these findings establish that DHEA supplementation does not interfere with the therapeutic activity of AVE1642 and PGA-AVE1642.

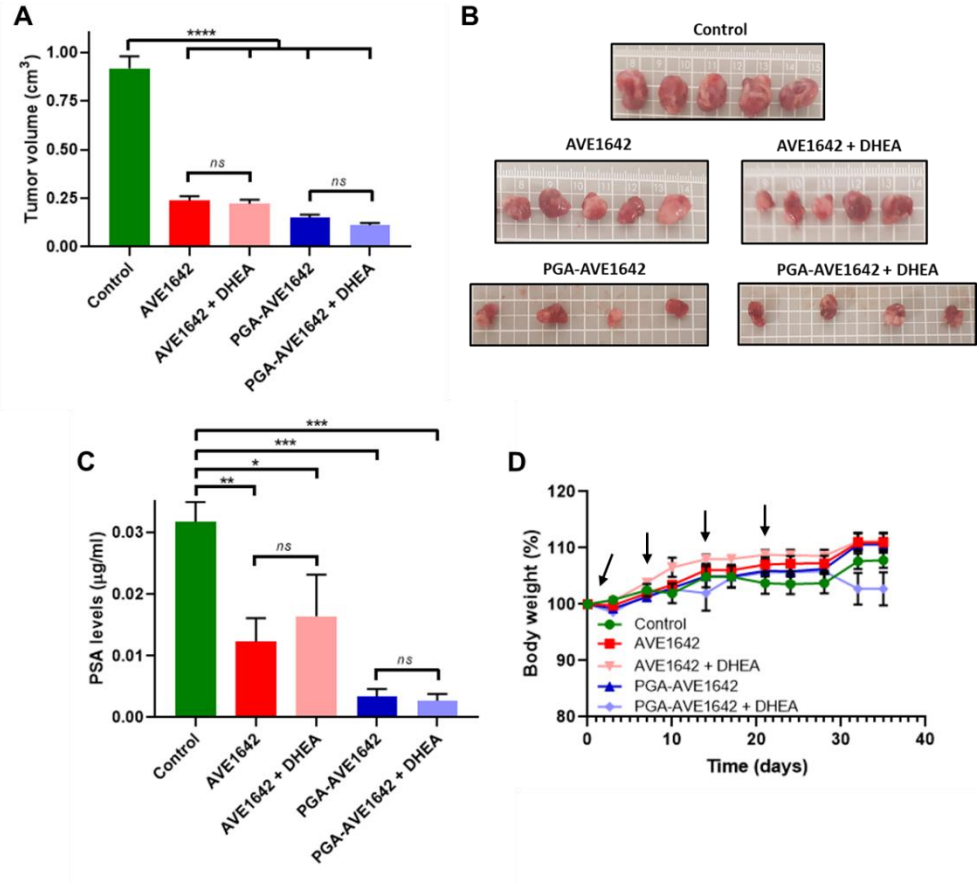

Figure 10: Antitumor Activity of AVE1642 and PGA-AVE1642 Treatment with and without DHEA Supplement in an Orthotopic PCa Mouse Model. A) Tumor volume expressed in cm^3 at the experimental endpoint. **B)** Representative tumor images at the experimental point. **C)** Serum PSA levels expressed in µg/ml. **D)** Alterations to body weight percentage after the first treatment administration (black arrows indicate the administering point of the AVE1642 and PGA-AVE1642 treatments). Data expressed as mean±SEM, n>3. Statistical analysis was performed using ANOVA, *p < 0.05, **p < 0.01, ***p < 0.001, *ns*=no significant.

IV.5.3. Evaluation of Combination Therapy in an Orthotopic Prostate Cancer Mouse Model

We next evaluated the combination of AVE1642 or PGA-AVE1642 with abiraterone acetate in an orthotopic PCa mouse model to investigate potential synergism *in vivo*.

As in previous *in vivo* animal experiments, we induced tumors in mice and monitored tumor evolution by IVIS® Spectrum and animal weight. During the second week, we randomly divided mice into six separate groups (n=6) (**Figure 11.A**).

i. Vehicle control group treated with PBS (i.v. - AVE1642/PGA-AVE1642 vehicle), 95% sunflower oil and 5% benzyl alcohol (oral gavage - (abiraterone acetate vehicle), and 10% DMSO (s.c. - DHEA vehicle)

ii. AVE1642 (i.v.) once a week for four weeks at 10 mg/kg

iii. PGA-AVE1642 (i.v.) once a week for four weeks at 10mg/kg (AVE1642 equiv.)

iv. Abiraterone acetate daily at 200 mg/kg from week 2 to week 7 (oral gavage) and DHEA at 0.1 mg per day (s.c.) for the entire experiment

v. AVE1642 in combination with abiraterone acetate and DHEA

vi. PGA-AVE1642 in combination with abiraterone acetate and DHEA

Figure 11.B, which depicts the IVIS® Spectrum analysis of tumor development, demonstrates higher tumor growth in the vehicle control group (i) in comparison with the other five groups. In addition, the quantification of IVIS® Spectrum corroborated the reduction in tumor size for treatment modalities (ii)-(vi) when compared to the vehicle control (i) (**Figure 11.C**).

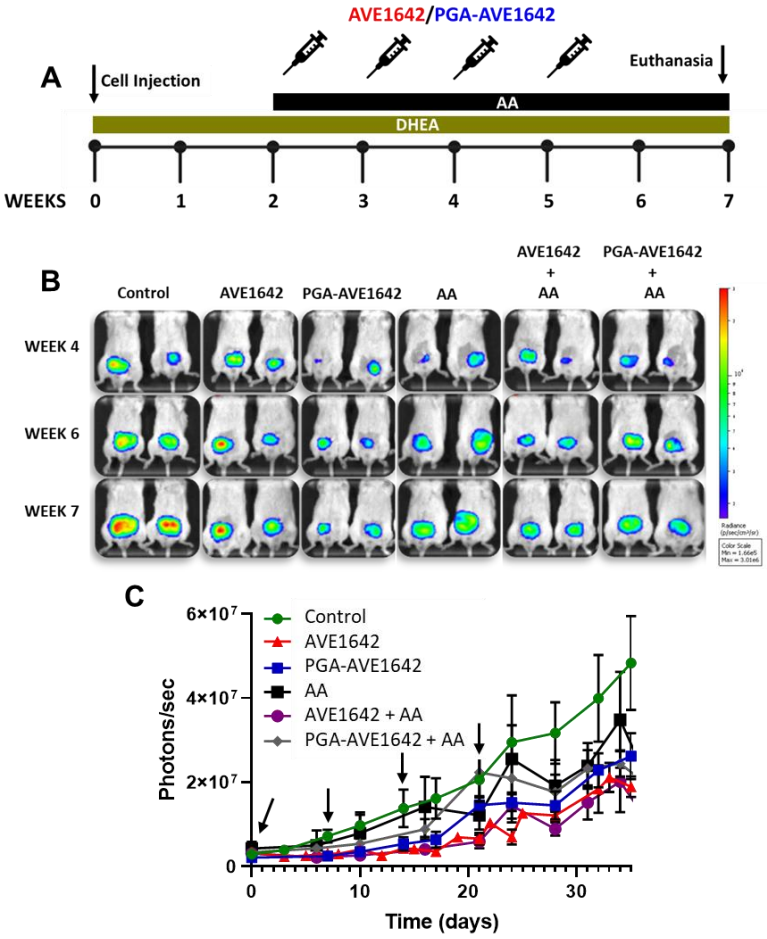

Figure 11: Tumor Progression Following Treatment with Combination Therapies in an Orthotopic PCa Mouse Model. Mice were treated with AVE1642 and PGA-AVE1642 at 10 mg/kg (AVE1642 equiv.) alone and in combination with 200 mg/kg abiraterone acetate and DHEA at 0.1mg/day. In addition, i.v. abiraterone acetate was administered alone with DHEA at 0.1mg/day. **A)** Schematic representation for abiraterone acetate treatment with DHEA in combination with AVE1642 and PGA-AVE1642. **B)** Representative topographic tumor growth images evaluated in IVIS® Spectrum over different time points for the six treatment modalities. **C)** Tumor growth over time evaluated in each group as photons/second (black arrows indicate the timings of the AVE1642 and PGA-AVE1642 treatments). Data expressed as mean±SEM, n>3.

Figure 12.A (tumor volume measured by caliper at experimental endpoint) demonstrates a significant decrease in tumor size following treatment modalities (ii)-(vi) when compared to control. As single treatments, AVE1642 (ii), PGA-AVE1642 (iii), and abiraterone acetate in the presence of DHEA (iv) led to reduced tumor size. AVE1642 and abiraterone acetate (v) in the presence of DHEA led to a synergistic antitumoral effect with a significant decrease in tumor size observed when compared to AVE1642 treatment alone; however, we failed to see a similar synergistic antitumor effect for PGA-AVE1642 and abiraterone acetate (vi) in the presence of DHEA. **Figure 12.B** shows representative tumor images at the experimental timepoint for the five different treatment conditions.

We also quantified serum PSA levels (**Figure 12.C**), and while abiraterone acetate alone failed to reduce PSA levels significantly in the presence of DHEA, AVE1642, PGA-AVE1642, and both combination therapies significantly downregulated PSA levels in the presence of DHEA. Interestingly, while abiraterone acetate treatment synergized with AVE1642 to produce a significant reduction in PSA levels compared to AVE1642 alone, we failed to observe a similar relationship for PGA-AVE1642.

We also analyzed tumor density at the experimental endpoint (**Figure 12.D**), finding a significant increase in tumor density following treatment with PGA-AVE1642, abiraterone acetate in the presence of DHEA, and PGA-AVE1642 in combination with abiraterone acetate in the presence of DHEA when compared to control. However, AVE1642 or AVE1642 and abiraterone acetate in the presence of DHEA failed to have a significant effect when compared to vehicle control. We also confirmed that the treatment modalities under evaluation did not significantly affect mouse body weight during the experiment (**Figure 12.E**).

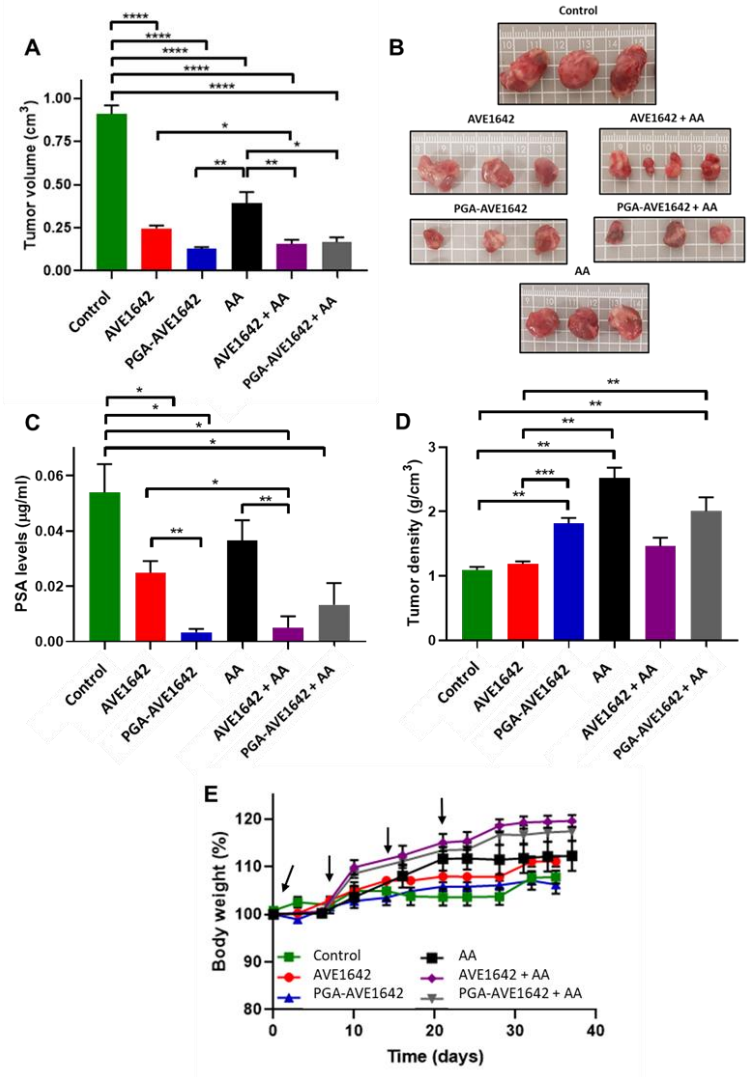

Figure 12: Antitumor Activity of Combination Therapies in the Presence of DHEA in an Orthotopic PCa Mouse Model. A) Tumor volume expressed in cm^3 in the seventh week (measured by caliper). **B)** Representative tumor images at the experimental point. **C)** Serum PSA levels expressed in µg/ml measured at the experimental endpoint. **D)** Tumor density measured in g/cm^3 at the experimental endpoint. **E)** Changes to body weight percentage following first treatment administration (black arrows indicate the timings of the AVE1642 and PGA-AVE1642 treatments). Data expressed as mean±SEM, n>3. Statistical analysis was performed using ANOVA, *p < 0.05, **p < 0.01, ***p<0.001.

Overall, both combination therapies led to a significant reduction in tumor size. AVE1642 and abiraterone acetate treatment in the presence of DHEA has a synergistic effect, as we observed a significant reduction in tumor size and a reduction in PSA levels when compared to AVE1642. In contrast, we failed to find significant differences in tumor size and PSA levels for PGA-AVE1642 and abiraterone acetate treatment in the presence of DHEA when compared to PGA-AVE1642 treatment alone, suggesting a low level or a lack of any synergistic effect.

IV.6. Combination Therapy Improves IGF-1R Inhibition

To further investigate the potential synergetic effects of our combination therapies, understanding the differential outcome observed in the *in vivo* experiments, we evaluated tumor lysates derived from mice from the previous experiment for levels of phosphorylated proteins downstream of the IGF-1R signaling pathways (p-Shc, p-MAPK, p-PI3K, and p-IGF-1R-β) to determine the activation/inhibition of different signaling pathways. Furthermore, we also studied total IGF-1R-β, AR, and ERG protein levels (**Figures 13.A** and **B**).

Figure 14 depicts the Western blotting analysis evaluated by band densitometry, and **Table 1** provides a summary of the results. We observed similar profiles for total and phosphorylated IGF-1R-β (**Figures 14.A** and **E**), a lack of any effect following abiraterone acetate treatment, but a significant decrease in response to both combination therapies, with no significant differences observed between AVE1642/abiraterone acetate and PGA-AVE1642/abiraterone acetate.

We observed an interesting phospho-Shc profile (**Figure 14.B**); while abiraterone acetate treatment significantly reduced p-Shc levels, AVE1642/abiraterone acetate failed to stimulate a similar response and displayed no significant differences when compared to the control. However,

PGA-AVE1642/abiraterone acetate treatment did reduce p-Shc levels, although not to the level observed in the abiraterone acetate-only treated tumors.

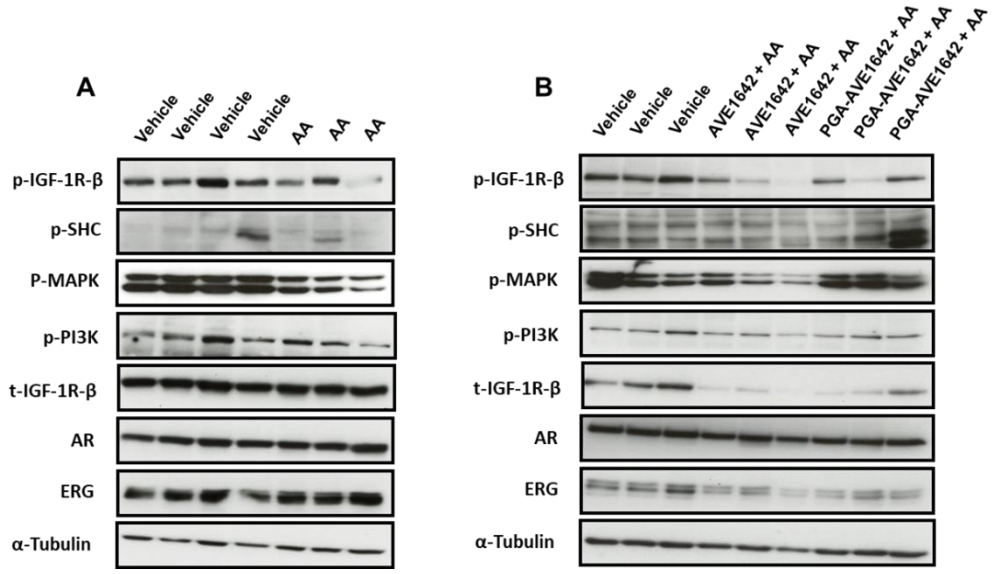

Figure 13: Protein expression in tumor lysates following treatment analyzed by Western blot for control and abiraterone acetate (AA) treatments **(A)** and control and combination therapy treatments **(B)** in the presence of DHEA.

We observed a lack of significant differences for p-MAPK, p-PI3K, and AR expression in response to any treatment (**Figures 14.C**, **D,** and **F**), while we also observed a decrease in p-PI3K protein levels in response to both combination therapies, although this did not reach significance (**Figure 14.D**). We also detected a non-significant decrease in p-MAPK protein levels after AVE1642/abiraterone acetate treatment compared with the other treatments (**Figure 14.C**). Finally, AVE1642/abiraterone acetate treatment reduced levels of total ERG (**Figure 14.G**) compared to both control and abiraterone acetate-only treatment, although the reduction observed after PGA-AVE1642/abiraterone acetate treatment only displayed significance when compared to abiraterone acetate treatment and not the vehicle control.

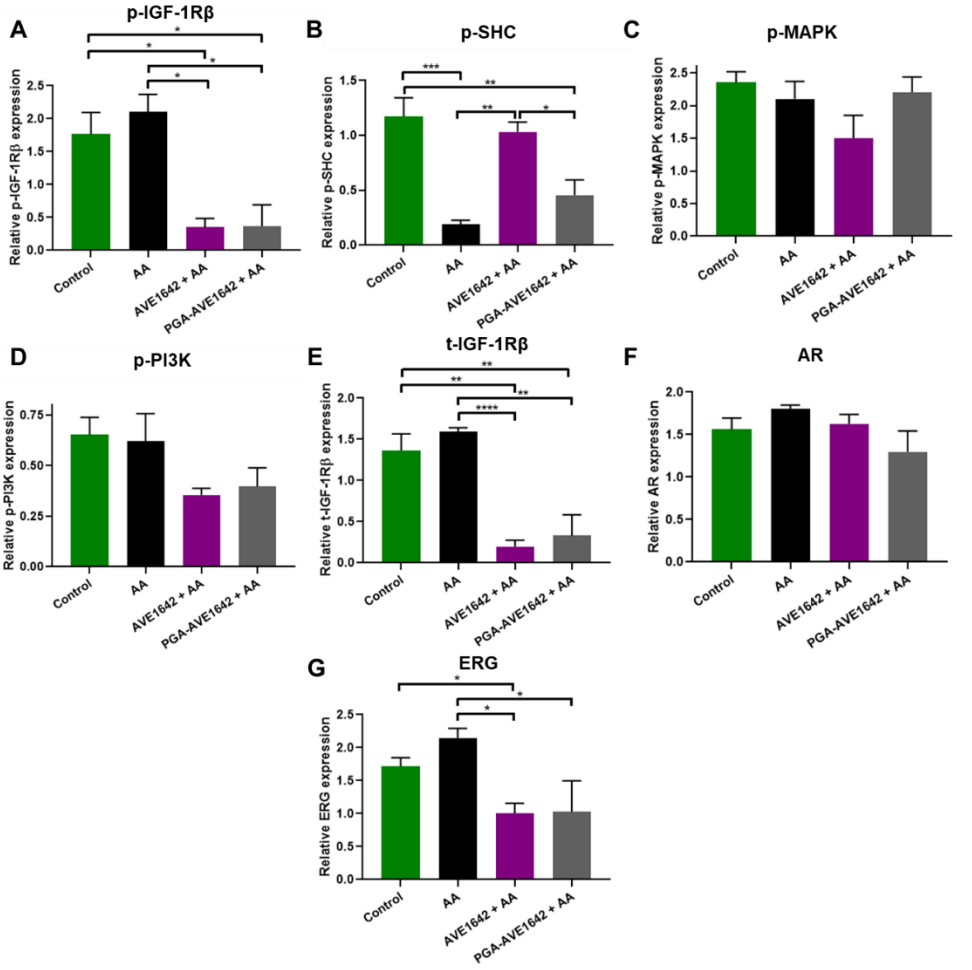

Figure 14: Investigation of IGF-1R and AR Signaling Pathways Following Combination Therapy Treatment in an Orthotopic PCa Mouse Model in the Presence of DHEA. Protein quantification in tumor lysates. **A-G)** Graph represents protein expression relative to α-tubulin by quantification with the ImageJ software. Data expressed as mean±SEM, n>3. Statistical analysis was performed using ANOVA, *p < 0.05, **p < 0.01, ***p<0.001, ****p < 0.0001.

In addition, and related to AVE1642 and PGA-AVE1642 data from the previous chapter (**See Chapter III**, **Section III.9.2.**), we detected a greater decrease in p-Shc protein levels with respect to the vehicle control after the combination therapy PGA-AVE1642/abiraterone acetate compared with PGA-AVE1642 treatment alone, while, in contrast, we obtained similar results after AVE1642/abiraterone acetate combination therapy compared with AVE1642 treatment alone (Data on all treatment modalities combined and presented in **Table 1**).

We also detected a decrease in the p-MAPK levels with respect to the vehicle control after treatment with combination therapy AVE1642/abiraterone acetate compared with the free AVE1642 treatment, which showed similar phosphoprotein levels in comparison with control; in contrast, we obtained similar results after PGA-AVE1642/abiraterone acetate combination therapy compared with PGA-AVE1642 treatment (**Table 1**).

Furthermore, we observed a decrease in p-PI3K protein levels with respect to the control after the combination therapy AVE1642/abiraterone acetate compared with the free AVE1642 treatment, which did not show differences in comparison with the control; in addition, p-PI3K levels remained lower than control after PGA-AVE1642 treatment with and without abiraterone acetate (**Table 1**).

We detected a greater decrease in total IGF-1R protein levels with respect to the control after AVE1642/abiraterone acetate combination therapy compared with the free AVE1642 treatment, which did not show differences compared with the control; additionally, we detected a more significant decrease in t-IGF-1R after the combination therapy PGA-AVE1642/abiraterone acetate compared with PGA-AVE1642 (**Table 1**).

Interestedly, we failed to detect any variations in AR levels after AVE1642 and PGA-AVE1642 treatments with and without combination therapy with abiraterone acetate. Finally, we discovered a more robust decrease in ERG protein levels respect to the control after both combination therapies compared with the free AVE1642 and PGA-AVE1642 treatments, which did not show differences in comparison with the control (**Table 1**).

Treatment	AVE1642 (folds)	PGA-AVE1642 (folds)	AA (folds)	AVE1642 + AA (folds)	PGA-AVE1642 + AA (folds)
p-IGF-1R-β	*nd*	*nd*	~	5.1	4.8
p-SHC	~	1.4	6.2	~	2.5
p-MAPK	~	~	~	1.6	~
p-PI3K	~	2.1	~	1.8	1.6
t-IGF-1R-β	~	1.9	~	6.8	5.2
AR	~	~	~	~	~
ERG	~	~	~	1.7	1.7

Table 1: Summary table. Changes to total protein levels and protein phosphorylation in response to various treatment modalities expressed as a decrease in fold compared to the control (Data synthesized from this Chapter and **Chapter III**, **Figure 33** and **Chapter IV**, **Figure 14**). *nd*: not detected, ~: no changes compared with the control.

As a summary, both combination therapies inhibited IGF-1R signaling, as evidenced by the significant reduction of p-IGF-1R-β, t-IGF-1R-β, and ERG levels. Furthermore, responses to both combination therapies displayed broad similarities - the inhibition of both Shc or MAPK and PI3K signaling pathways. PGA-AVE1642/abiraterone acetate combination therapy provided a stronger inhibition of p-Shc levels when compared to AVE1642/abiraterone acetate treatment and also inhibited PI3K phosphorylation. In contrast, AVE1642/abiraterone acetate treatment inhibited MAPK phosphorylation more

robustly when compared to PGA-AVE1642/abiraterone acetate treatment and also inhibited PI3K phosphorylation.

We also discovered that the AVE1642/abiraterone acetate combination therapy produced stronger inhibition of p-MAPK, p-PI3K, t-IGF-1R, and ERG levels when compared AVE1642 treatment alone. Furthermore, PGA-AVE1642/abiraterone combination therapy provided for stronger inhibition of p-Shc, t-IGF-1R, and ERG protein levels when compared to PGA-AVE1642 treatment alone (**Table 1**).

These results represent a synergistic effect after AVE1642/abiraterone acetate combination therapy; furthermore, the results from the PGA-AVE1642/abiraterone acetate combination therapy also suggests at least some level of synergism. Therefore, abiraterone acetate might not be necessary as co-administration with PGA-AVE1642 but could help to enhance the long-term anticancer activity in the clinics as a maintenance treatment after a possible PGA-AVE1642 regime due to our observations in the reinforcement of the effective anticancer molecular pathways.

IV.7. Conclusions

As a summary, our *in vitro* analyses suggested a synergistic effect of both combination therapies, while our *in vivo* results indicated synergism for the AVE1642/abiraterone acetate combination therapy compared to lower synergism for PGA-AVE1642/abiraterone acetate due to the already enhanced activity of AVE1642 upon PGA conjugation. Although our results provide evidence that abiraterone acetate avoids AR transcription genes, our findings also suggest a correlation between abiraterone acetate treatment and p-Shc levels. We obtained similar tumor growth inhibition in response to both combination therapies due to the inhibition of both IGF-1R downstream signaling pathways. Abiraterone acetate treatment explains the *in vivo* synergy observed in AVE1642/abiraterone acetate combination therapy because we detect inhibition of MAPK pathway probably due to the inhibition of Shc phosphorylation through androgen crosstalk downregulation. For this reason, we detected lower tumor growth and PSA levels compared with free AVE1642 treatment. In contrast, we detected similar tumor growth, PSA levels, and inhibition of both Shc and PI3K signaling pathways after PGA-AVE1642 treatment with and without abiraterone acetate. The lack of a potent synergistic effect in this case perhaps derives from the already efficient inhibition of Shc phosphorylation by PGA-AVE1642 monotherapy; however, we detected a more significant inhibition of Shc phosphorylation after PGA-AVE1642/abiraterone acetate treatment compared with PGA-AVE1642 treatment alone. This could suggest that in any case, abiraterone could reinforce as an adjuvant or maintenance treatment those antitumor effects provided by PGA-AVE1642 in CRPC patients.

IV.8. Bibliography

1. Nevedomskaya, E., S. Baumgart, and B. Haendler, *Recent Advances in Prostate Cancer Treatment and Drug Discovery.* International Journal of Molecular Sciences, 2018. **19**: p. 1359.
2. Carver, B., et al., *Reciprocal Feedback Regulation of PI3K and Androgen Receptor Signaling in PTEN-Deficient Prostate Cancer.* Cancer Cell, 2011. **19**: p. 575-86.
3. Qi, W., et al., *Reciprocal feedback inhibition of the androgen receptor and PI3K as a novel therapy for castrate-sensitive and -resistant prostate cancer.* Oncotarget, 2015. **6**(39): p. 41976-41987.
4. Marques, R.B., et al., *High Efficacy of Combination Therapy Using PI3K/AKT Inhibitors with Androgen Deprivation in Prostate Cancer Preclinical Models.* European Urology, 2015. **67**(6): p. 1177-1185.
5. Handy, C.E. and E.S. Antonarakis, *Sipuleucel-T for the treatment of prostate cancer: novel insights and future directions.* Future Oncology, 2018. **14**(10): p. 907-917.
6. Boettcher, A.N., et al., *Past, Current, and Future of Immunotherapies for Prostate Cancer.* Frontiers in Oncology, 2019. **9: p.** 884.
7. Maeda, H., *Tumor-Selective Delivery of Macromolecular Drugs via the EPR Effect: Background and Future Prospects.* Bioconjugate Chemistry, 2010. **21**(5): p. 797-802.
8. Maeda, H., K. Tsukigawa, and J. Fang, *A Retrospective 30 Years After Discovery of the EPR Effect of Solid Tumors: Next-Generation Chemotherapeutics and Photodynamic-therapy—Problems, Solutions, Prospects.* Microcirculation, 2015. **23**(3): p. 173-82.
9. Ojha, T., et al., *Pharmacological and Physical Vessel Modulation Strategies to Improve EPR-mediated Drug Targeting to Tumors.* Advanced Drug Delivery Reviews, 2017. **119**: p. 44-60.
10. Niño-Pariente, A., V. Nebot, and M. Vicent, *Relevant Physicochemical Descriptors of "Soft Nanomedicines" to Bypass Biological Barriers.* Current Pharmaceutical Design, 2015. **22**(9): p. 1274-91.
11. Wicki, A., et al., *Nanomedicine in cancer therapy: Challenges, opportunities, and clinical applications.* Journal of Controlled Release, 2015. **200**: p. 138-157.

12. Duncan, R. and R. Gaspar, *Nanomedicine(s) under the Microscope.* Molecular Pharmaceutics, 2011. **8**(6): p. 2101-2141.
13. Greco, F. and M. Vicent, *Combination therapy: Opportunities and challenges for polymer–drug conjugates as anticancer nanomedicines.* Advanced Drug Delivery Reviews, 2009. **61**: p. 1203-1213.
14. Plyduang, T., et al., *Polyacetal-Based Combination Therapy for the Treatment of Prostate Cancer.* Macromolecular Rapid Communications, 2018. **39**(19): p. 1800265.
15. Mancarella, C., et al., *ERG deregulation induces IGF-1R expression in prostate cancer cells and affects sensitivity to anti-IGF-1R agents.* Oncotarget, 2015. **6**(18): p. 16611-16622.
16. Taneja Samir, S., *Re: Abiraterone plus Prednisone in Metastatic, Castration-Sensitive Prostate Cancer.* Journal of Urology, 2018. **199**(1): p. 26-28.
17. Purshouse, K. and A.S. Protheroe, *Abiraterone acetate in combination with prednisone in the treatment of metastatic hormone-sensitive prostate cancer: clinical evidence and experience.* Therapeutic Advances in Urology, 2019. **11**: p. 1756287218820804.
18. Han, C., R. Patel, and I. Kim, *Pharmacokinetics, pharmacodynamics and clinical efficacy of abiraterone acetate for treating metastatic castration-resistant prostate cancer.* Expert Opinion on Drug Metabolism & Toxicology, 2015. **11**: p. 1-9.
19. Chou, T.-C., *Theoretical Basis, Experimental Design, and Computerized Simulation of Synergism and Antagonism in Drug Combination Studies.* Pharmacological Reviews, 2006. **58**: p. 621-81.
20. Li, R., et al., *Abiraterone Inhibits 3 -Hydroxysteroid Dehydrogenase: A Rationale for Increasing Drug Exposure in Castration-Resistant Prostate Cancer.* Clinical Cancer Research, 2012. **18**: p. 3571-9.
21. Missaghian, E., et al., *Role of DNA methylation in the tissue-specific expression of the CYP17A1 gene for steroidogenesis in rodents.* The Journal of Endocrinology, 2009. **202**: p. 99-109.
22. Kosir, R., et al., *Circadian expression of steroidogenic cytochromes P450 in the mouse adrenal gland - Involvement of cAMP-responsive element modulator in epigenetic regulation of Cyp17a1.* The FEBS Journal, 2011. **279**: p. 1584-93.

23. Giatromanolaki, A., et al., *CYP17A1 and Androgen-Receptor Expression in Prostate Carcinoma Tissues and Cancer Cell Lines.* Current Urology, 2019. **13**(3): p. 157-165.
24. Hara, T., et al., *Enhanced androgen receptor signaling correlates with the androgen-refractory growth in a newly established MDA PCa 2b-hr human prostate cancer cell subline.* Cancer Research, 2003. **63**: p. 5622-8.
25. Hara, T., et al., *Enhanced Androgen Receptor Signaling Correlates with the Androgen-refractory Growth in a Newly Established MDA PCa 2b-hr Human Prostate Cancer Cell Subline.* Cancer Research, 2003. **63**(17): p. 5622.
26. Ando, T., et al., *Dihydrotestosterone synthesis pathways from inactive androgen 5α-androstane-3β,17β-diol in prostate cancer cells: Inhibition of intratumoural 3β-hydroxysteroid dehydrogenase activities by abiraterone.* Scientific Reports, 2016. **6**: p. 32198.
27. Frasinyuk, M., et al., *Application of Mannich Bases to the Synthesis of Hydroxymethylated Isoflavonoids As Potential Antineoplastic Agents.* Organic & Biomolecular Chemistry, 2015. **13**(46): p. 11292-301.

General Discussion

General Discussion

PCa is the second most frequent cancer in men and the fifth major cause of cancer death around the world [1, 2]. Fortunately, an early diagnosis can provide a relatively good prognosis; however, the metastatic form of PCa (mainly castration-resistant prostate cancer (mCRPC)), it is still an unmet clinical need and requires not only better diagnostic tools due to tumor heterogeneity (identification of biomarkers) but also for better therapeutic approaches adequate to the patient needs [3]. For these reasons, in this Ph.D. thesis, we aimed to design advanced therapeutics; in particular, we generated a polymer-based nanoconjugate, as part of a single and combination therapy [4], which specifically targeted mCRPC patients with poor prognosis (T2E-positive PCa subtype) [5].

Mancarella *et al.* demonstrated that the AVE1642 anti-IGF-1R monoclonal antibody presented specific cytotoxic effects in T2E-positive PCa cell lines [6] and the combination of AVE1642 with abiraterone led to synergistic effects in this same cell type [6]. Unfortunately, AVE1642 was discontinued during phase II clinical trials in CRPC patients, due to a partial response to therapy and multiple side effects (neutropenia, diarrhea, hyperglycemia, etc.) [157, 158].

Therefore, as a first step in this thesis, we investigated how conjugation of the PGA polypeptide altered the biological properties of a human mAb (AVE1642) in the hope of increased anti-tumoral activity of AVE1642 in aggressive PCa and reduced side effects.

Many strategies exist to improve the stability of antibodies that are quickly eliminating by the renal system and reduce intrinsic immunogenicity which can promote an immune response [7]. PEGylation is the most widely explored strategy, providing increased stability to an antibody, with some examples in routine clinical use (e.g., Cimzia®) [8]. However, PEG also suffers from non-biodegradability which

limits its use in chronic administrations. Polypeptides represent a promising alternative [9]. PGA is fully biodegradable, multivalent, mimics natural proteins in the body, and displays biocompatibility and low immunogenicity [10]. Side-chain carboxylic groups make PGA a versatile multivalent platform for the conjugation of multiple differing moieties (allowing the development of combination therapies) and have already proved to be an effective drug delivery system [11].

To this end, we covalently conjugated AVE1642 to PGA through a reducible disulfide bridge and fully characterized the resultant polymer conjugate (PGA-AVE1642) by SDS-PAGE, size exclusion chromatography, amino acid analysis, and DLS analysis. These techniques demonstrated an increase in AVE1642 Mw, size, and the negative zeta potential after PGA conjugation, thereby demonstrating polymer conjugate formation (**See Chapter III**, **Figures 5-7**). CD analysis established a β-sheet structure for AVE1642, and a random-coiled structure for PGA polymer. Upon the PGA conjugation, the resulting spectra showed an additive contribution of both AVE1642 and PGA polymer. To confirm that conjugation does not negatively impact AVE1642 structure, we cleaved PGA from AVE1642 and found a similar CD spectra, thereby suggesting that PGA does not alter the structure of the antibody and has the same β-sheet structure as a parental AVE1642 (**See Chapter III**, **Figure 8**). Furthermore, we employed CD to analyze thermal stability, finding evidence that PGA conjugation may improve the stability of AVE1642 (**See Chapter III**, **Figure 9**).

As we focused on a specific patient subtype, the selected preclinical models are crucial for the adequate development of our therapeutics. For this reason , we studied protein expression levels in different PCa cell lines (VCaP, LnCaP, DU-145, 22Rv1, and PC-3) and in a non-cancerous prostate cell line (RWPE-1) to select those lines with the desired characteristic (overexpression of ERG protein due to the presence of the T2E fusion gene). We selected the VCaP cell line as our *in vitro*

model due to the expression of the T2E fusion gene and high expression levels of IGF-1R-β and AR due to ERG protein overexpression (**See Chapter III**, **Figure 3**). This result also demonstrates a direct association between IGF-1R and T2E expression, in good agreement with the findings of Mancarella *et al*. [6], who described this relationship in patient-derived PCa samples [5].

The presence of the T2E fusion gene and high IGF-1R levels indicate the appearance of a malignant cellular phenotype that promotes CRPC progression [5, 12]. The classification of PCa according to a specific molecular marker could allow for the identification of different aggressive PCa subtypes and the choice or design of specific therapeutic approaches. While many IGF-1R inhibitors have been developed as PCa therapies, none are targeted to a specific PCa patient subtype. Furthermore, clinical trials of IGF-1R inhibitors have not achieved the expected success due to partial responses [13-18] and side toxicities [12, 13, 19], and for this reason, most IGF-1R inhibitors have been discontinued. In the present study, we confirmed previously reported data [6] and demonstrated that only the T2E-positive expressing PCa cell (VCaP) displayed selected sensitivity in response to treatment with AVE1642 compared to T2E-negative PCa cell lines (DU-145, PC-3, 22Rv1, LNCaP, and RWPE-1), mainly due elevated levels of ERG expression (**See Chapter III**, **Figure 14-15**). Overall, this highlights the potential utility of AVE1642 treatment in patients with the T2E fusion gene. Of note, the modification of AVE1642 with increasing levels of PGA did not negatively impact the cytotoxic activity of the antibody (**See Chapter III**, **Figure 4**), as compared to the results described by Chapman *et al*., which demonstrated the loss of antigen-binding following modification with increasing levels of PEG [8].

We next focused on understanding the consequence of the inhibition of IGF-1R of AVE1642 after PGA conjugation. IGF-1R, a vital receptor tyrosine kinase located in the cell plasma membrane, is involved in cell proliferation and survival in

normal and malignant cells [20]. Simpson *et al*. and Singh *et al*. demonstrated that the IGF-1 ligand binds to IGF-1R and promotes receptor autophosphorylation, internalization, and the activation of PI3K/Akt/mTOR and Ras/Raf/MAPK intracellular signaling pathways [21, 22]. Our results corroborate these findings, after IGF-1 positive ligand incubation, the IGF-1R internalizes (**See Chapter III**, **Figure 16**), triggering the phosphorylation of both MAPK and PI3K signaling pathways (**See Chapter III**, **Figure 22**). As King *et al*. previously reported [23], inhibition of IGF-1R activity by an anti-IGF-1R mAb or TKI treatment prevents IGF-1R autophosphorylation, inhibits activation of intracellular signaling pathways, and slows cell growth and proliferation. Fascinatingly, we discovered that inhibition of IGF1-R with PGA-AVE1642 inhibited downstream signaling pathways in a different manner to AVE1642. Treatment with AVE1642 did not inhibit IGF-1R internalization after binding, and IGF-1R became internalized in a similar manner to IGF-1 positive ligand stimulation (**See Chapter III**, **Figure 16**). These findings correlate well with our data regarding the mechanism of action evaluated by Western blot assays showing that AVE1642 inhibits only the PI3K signaling pathway and not the MAPK signaling pathway, which is involved in the receptor internalization (**See Chapter III**, **Figure 22**). These results differ from previous studies of AVE1642 by Geoerger *et al*. and Descamps *et al*., which established the inhibition of both MAPK and PI3K signaling pathways after AVE1642 incubation in neuroblastoma cells [24] and human myeloma cells [25]. The differential findings likely derive from the cell lines employed and the concentrations of AVE1642 used. However, a study by Crudden *et al*. established that some IGF-1R targeted antagonists actually functioned as agonists and promoted the activation of IGF-1R signaling [26]; this could also partly occur for AVE1642 in VCaP cells. In the case of the PGA-AVE1642 treatment, we observed an increase in the levels of IGF-1R at the cell membrane, with internalization inhibited (**See Chapter III**, **Figure 16**) and both MAPK and PI3K signaling pathways inhibited (**See Chapter III**, **Figure 22**). Our

findings suggest, for the first time, that polymer conjugation of AVE1642 leads to enhanced activity related to its interaction with IGF-1R at the cell membrane.

Macromolecular systems such as antibodies [27, 28] are uptaken by cells by energy-dependent mechanisms employing endocytosis [29, 30]. Our results suggest that AVE1642 employs energy-dependent internalization mechanisms; however, we found more PGA-AVE1642 binding in the cell membrane (**See Chapter III**, **Figure 17**). These results are directly correlated with the previous IGF-1R internalization data (**See Chapter III**, **Figure 16**) in which we detected lower IGF-1R internalization following PGA-AVE1642 treatment. The lower IGF-1R internalization could be triggered by the higher PGA-AVE1642 cellular membrane binding, which results in different cell internalization pathways. Our results indicated that the AVE1642 mainly colocalized with clathrin, while PGA-AVE1642 mostly colocalized with caveolin-1 (**See Chapter III**, **Figure 18**). However, both AVE1642 and PGA-AVE1642 finally localized to the lysosomes. Osher *et al*. and Martins *et al*. demonstrated that IGF-1R internalization could be mediated by both clathrin and caveolin mediated endocytosis [31, 32]. We demonstrated that only AVE1642 and not PGA-AVE1642 colocalizes with early endosomes (**See Chapter III**, **Figure 19**), suggesting that PGA conjugation changes the cellular internalization pathway employed. We corroborated this data through studies of AVE1642-Cy3 and PGA-AVE1642-Cy5 at the same time in the same cell by STORM microscopy showing a very low colocalization between both compounds (**See Chapter III**, **Figures 20** and **21**). With all these results in mind, we propose that AVE1642 promotes IGF-1R internalization via clathrin-mediated endocytosis and provides for only PI3K signaling pathway inhibition before being shuttled into early endosomes and degraded in the lysosome. Previous findings from Martins *et al*. demonstrated the MAPK pathway is mainly regulated by clathrin [32]; this result correlates with our AVE1642-Cy5.5 findings. In contrast, PGA-AVE1642 promotes lower IGF-1R internalization after binding, and this is associated with the inhibition of both MAPK

and PI3K signaling pathways. The inhibition of IGF-1R activity may lead to inhibited internalization and migration to the endosomes and the subsequent avoidance of receptor recycling and IGF-1R transcriptional inhibition by inhibiting IGF-1R nuclear translocation [33, 34]. However, we do also observe evidence for the eventual internalization of PGA-AVE1642 via caveolae-dependent endocytosis and direct passage to the lysosome [35].

To validate our results in a preclinically relevant *in vivo* PCa model for the T2E subtype, we optimized an orthotopic PCa mouse model [36] employing luciferase-expressing VCaP cells to study the antitumoral activity of AVE1642 and PGA-AVE1642 therapies *in vivo* (**See Chapter III**, **Figure 26** and **Figure 28**). We discovered similar safety profiles and tumor accumulation for AVE1642 and PGA-AVE1642 treatment (**See Chapter III**, **Figure 29**), which could be explained due to the relatively similar sizes, even given PGA conjugation (**See Chapter III**, **Figure 7**). Even given this similarity in tumor accumulation, we observed enhanced antitumoral activity for PGA-AVE1642 when compared to AVE1642 (**See Chapter III**, **Figures 30** and **31**). Furthermore, we detected a direct correlation between tumor size and PSA levels and an inverse correlation between tumor size and tumor density (**See Chapter III**, **Figure 31**). PSA levels are known to correlate with cancer progression [37], while higher density can indicate the presence of necrotic areas. Previous findings in PCa mouse tumors confirmed that the faster development of necrosis and an increase in tumor density associated with higher antitumor activity [38].

Studies aiming to investigate mechanisms of action in tumor samples provided evidence for a lack of MAPK and PI3K pathway inhibition in response to AVE1642 treatment (**See Chapter III**, **Figure 33**). Even though IGF-1R activity is linked to tumor growth [39], we still observed an antitumorigenic effect (**See Chapter III**, **Figures 30** and **31**). This result could be explained as the

experiment was performed two weeks after the last dose administration. We speculate that more rapid AVE1642 degradation and lower IGF-1R affinity in comparison with the PGA-AVE1642 conjugate might be the reason why AVE1642 treatment promotes the activation of the pathways after this time.

In contrast, PGA-AVE1642 treatment robustly inhibited the Shc adaptor protein and PI3K pathways in tumor samples demonstrating that the PGA-AVE1642 therapy provides a complete IGF-1R inhibition that is correlated with the lower IGF-1R protein expression (**See Chapter III**, **Figure 33.B**, **D** and **E**). We believe that higher PGA-AVE1642 stability and the increased affinity of PGA-AVE1642 for IGF-1R leads to increased PGA-AVE1642-IGF-1R binding at the cell membrane, the more robust inhibition of downstream signaling, and the subsequent reduction in tumor growth. Furthermore, despite Shc adaptor protein inhibition following PGA-AVE1642 treatment, we fail to observe a decrease in the phosphorylation p-MAPK protein levels (**See Chapter III**, **Figure 33.C**), indicating that this protein can be activated by receptors other than IGF-1R, such as epidermal growth factor receptor (EGFR), platelet-derived growth factor receptor (PDGFR), VEGFR, fibroblast growth factor receptor (FGFR), IL-1R or tumor necrosis factor receptor (TNF-R) [40]. Furthermore, higher AR levels detected after PGA-AVE1642 treatment (**See Chapter III**, **Figure 33.F**) relate to the negative crosstalk between both PI3K and AR pathway [41]; the high AR may explain high ERG protein levels (**See Chapter III**, **Figure 33.G**), as AR acts as an ERG promotor [6].

Of note, we also demonstrated the safety but also the lack of anti-tumorigenic effect of PGA alone, suggesting that the enhanced antitumorigenic activity of PGA-AVE1642 treatment is not related to the inherent activity of PGA (**See Chapter III**, **Figure 32**).

To achieve a better understanding of the differential therapeutic outputs upon PGA conjugation, we also studied the influence of AVE1642 and PGA-AVE1642

on the TME by investigating blood vessel maturity, functionality, cellular proliferation, and angiogenesis via immunohistochemistry. Both therapeutic approaches promoted a decrease in vessel functionality; however, those tumors treated with PGA-AVE1642 displayed significantly lower vessel functionality (**See Chapter III**, **Figure 35.B**), which was associated with lower vessel maturity compared to the AVE1642 treatment and control groups (**See Chapter III**, **Figure 35.C**). The stronger decrease in vessel maturity in response to PGA-AVE1642 treatment may be related to the function of pericytes, cells that bind to vascular endothelial cells [42] and play an essential role in structural regulation endothelial cells through angiogenesis [43]. The angiogenic process is considered finished when pericytes surround the endothelial cells; this activity is associated with vessel growth, maturation, and termination [44]. Since pericyte function relates to blood vessel maturation in the last step of angiogenesis, our hypothesis states that PGA-AVE1642 treatment inhibits the maturation of the vessels and prevents pericyte binding to endothelial cells. In order to confirm this hypothesis, our next step is to perform cellular migration studies in human VCaP cell line cocultivated with murine fibroblast cells following both AVE1642 and PGA-AVE1642 treatments. Through the histological characterization of tumor-associated microenvironment employing VEGFR2 as an angiogenic marker, we also found that both treatment approaches display an anti-angiogenic effect being significantly greater for PGA-AVE1642 (**See Chapter III**, **Figure 37**) perhaps due to a decrease in vessel maturity by the pericyte-mediated mechanism explained above. Histological analysis (Ki67) also provided evidence for a reduction in tumor cell proliferation in response to both treatment approaches; again, we observed a greater effect for PGA-AVE1642 when compared to AVE1642 (**See Chapter III**, **Figure 36**).

Angiogenesis plays a critical role in the progression of CRPC, and the inhibition of angiogenic pathways provide an effective strategy to prevent tumor growth. Furthermore, vessel density shows a clear correlation with Gleason score

and predict disease progression in PCa [45] and previous findings demonstrated a connection between the PI3K pathway and angiogenesis via increased VEGF secretion by hypoxia-inducible factor 1 (HIF-1) dependent and independent mechanisms [46]. We hypothesized that the observed decrease in angiogenesis might directly relate to the decrease in tumor cell proliferation and tumor growth through the inhibition of the PI3K signaling pathway. Furthermore, the possible role of AVE1642 and PGA-AVE1642 treatment approaches in the tumor microenvironment may prevent pericyte migration; for this reason, vessels remain immature, thereby preventing angiogenesis.

In summary, **while PGA protects AVE1642, offering a greater plasma stability, conjugation also modulates cell trafficking pathways and TME-targeted effects. This triggers an enhanced therapeutic output that allows enhanced tumor reduction at lower doses, which should provide for lower systemic side effects.**

To further improve PCa treatment with PGA-AVE1642, we next evaluated a combination therapy-based approach. Polymer-based combination therapeutics represent a fascinating approach to PCa treatment, with numerous advantages over single-drug treatments [47]. As both Carver *et al.* and Crumbaker *et al.* described a reciprocal feedback loop regulation between both PI3K/Akt and AR pathways in PCa; AR inhibition therapy can lead to the activation of PI3K/Akt signaling to drive PCa progression [48, 49]. Therefore, our second step in this thesis focused on the implementation of an anti-androgen drug (abiraterone) in combination with the AVE1642 and PGA-AVE1642 IGF-1R inhibitors *in vitro* and *in vivo* to study possible synergistic therapeutic effects towards improved advanced therapeutics.

Several mechanisms are involved in CRPC progression, including AR gene amplification, protein overexpression, mutations, and splice variants, and the adrenal and intertumoral synthesis of androgens [50, 51]. Various therapeutics can

inhibit AR ligand-binding and androgen synthesis to block androgen-dependent AR signaling and thus prevent the CRPC progression. Abiraterone, irreversibly inhibits CYP17A1 and 3βHSD enzymes, prevents the nuclear translocation of AR and the subsequent increase in AR and TMPRSS2 levels and, additionally, blocks PSA synthesis [52-54].

Our *in vitro* results demonstrate that high concentrations of abiraterone promoted a cytotoxicity effect in all tested cell lines. The androgen-dependent VCaP cell line displayed the highest sensitivity to abiraterone; however, VCaP, 22Rv1, and RWPE-1 cell lines all displayed a ~50% reduction in cell viability at higher drug concentrations (10 μg/ml). Furthermore, the androgen-independent cell lines (DU-145 and PC-3) displayed lower sensitivity to the treatment, with only a ~25% decrease in cell viability, similar to the LNCaP androgen-dependent cell line (**See Chapter IV**, **Figure 3**). We next studied the expression of AR levels by Western blot assay (**See Chapter III**, **Section III.3.1**), finding that PC-3 and DU-145 PCa cells fail to express AR levels, corroborating previous findings [55]. The effectiveness of abiraterone at high concentrations in the androgen-independent PC-3 and DU-145 cell lines may be explained due to levels of AR below the detection level of the Western blot assay. Indeed, other studies have demonstrated that the PC-3 and DU-145 PCa cell lines express low but detectable AR by quantitative PCR [56, 57] and we hope evaluate AR mRNA levels in the near future. Furthermore, studies performed by Grossebrummel *et al*. reported that abiraterone influenced the cell cycle and apoptosis in androgen-independent PC-3 cells, which also could explain the responsiveness of the PC-3 cell line to abiraterone treatment [58] (**See Chapter IV**, **Figure 3**). We also found that abiraterone treatment did not affect the androgen-dependent LNCaP PCa cell line despite the presence of high levels of AR, although previous findings by Bedussi *et al.* and Fragni *et al.* demonstrated androgen-sensitivity in those PCa cell lines [50, 59]. For this reason, we believe that LNCaP cells may be insensitive to the drug concentrations employed in this study

(**See Chapter IV**, **Figure 3**). Previous studies demonstrated that T2E-positive PCa tumors display better responses to abiraterone when compare to T2E-negative PCa tumors [6]. We confirmed a higher sensitivity of the VCaP cell line to abiraterone treatment, thereby suggesting that treatment effectiveness requires the presence of T2E (**See Chapter IV**, **Figure 3**).

To investigate the functional effect of our combination therapies in different PCa cell lines, we studied the synergy between AVE1642 or PGA-AVE1642 with abiraterone using cell viability data processed by CompuSyn software. We observe a synergistic effect in VCaP cells with AVE1642/abiraterone and PGA-AVE1642/abiraterone, demonstrating that polymer conjugation of the antibody does not detract from AVE1642 activity as part of a combination therapy (**See Chapter IV**, **Figure 4**). Moreover, we also discovered a synergistic effect in 22Rv1 cells at the highest tested concentrations (for both AVE1642 and PGA-AVE1642), obtaining an ~60% loss in cell viability (**See Chapter IV**, **Figure 4**, **Table 1.B**). The results illustrate that the combination therapy promotes higher sensitivity in VCaP cells compared to 22Rv1 cells, most likely due to the presence of the T2E fusion gene (**See Chapter IV**, **Figure 4**). This suggests that by choosing T2E-positive patients, we could potentially improve outcomes with a reduced dose, thereby inhibiting any side-effects.

To validate the importance of the T2E fusion gene in combination therapies, we performed similar cytotoxicity studies with ERG gene silencing in the VCaP cell line. We demonstrated that the sensitivity of VCaP cells to both AVE1642/abiraterone and PGA-AVE1642/abiraterone significantly decreases upon ERG gene silencing; however, PGA conjugation to AVE1642 does not alter the T2E dependence (**See Chapter IV**, **Figures 5.B** and **C**).

Next, we determined the suitability and effectivity of both combination therapies in our preclinical orthotopic PCa mice model. First, we studied

abiraterone acetate as a single therapy to confirm an effect before moving to the combination therapy. Due to the lack of CYP17A1 expression in mice adrenal glands, we administered the DHEA precursor supplement to mimic human adrenal physiology conditions [60, 61]. The second essential target for abiraterone treatment, as established by Riu *et al.,* is 3β-hydroxysteroid dehydrogenase/isomerase (3βHSD), an enzyme that can synthesize DHT from DHEA in the adrenal glands [62]. 3βHSD also plays a vital role in intratumoral androgen synthesis by the "backdoor pathway" [63] involving the prevention of DHEA conversion to AD and blockage of AR nuclear translocation and the expression of AR target genes. Riu *et al.* demonstrated tumor growth inhibition after abiraterone acetate administration in those mice supplemented with DHEA [62]. Our model also required DHEA supplementation to achieve significant tumor reduction (**See Chapter IV**, **Figure 7**), most probably due to the extremely low levels of CYP17A1 enzyme (**See Chapter IV**, **Figure 6**). The mechanism of action is related to 3βHSD inhibition and the blockade of DHT synthesis, as confirmed by the measurement of PSA levels. A significant decrease in PSA levels after abiraterone acetate treatment with DHEA supplementation (**See Chapter IV**, **Figure 12.C**) suggests inhibition of the 3βHSD enzyme due to DHT downregulation thus prevention of both AR activation as reported by Riu *et al.* [62] and subsequent AR nuclear translocation leading to inhibition of the AR-mediated PSA gene transcription [64]. These and previous results provide evidence for the fundamental nature of DHEA in the mouse model for the efficacy of abiraterone acetate efficacy at different levels (adrenal glands, gonads, and intratumorally). DHEA supplementation normally promotes tumor growth due to its status as an androgen precursor and an AR pathway activator; however, in our experiments, the animals treated with DHEA showed similar tumor growth to control, which agrees with a previous study that fails to report elevated tumor growth at the employed concentration (**See Chapter IV**, **Figure 7**) [65].

After confirming the efficacy of abiraterone acetate monotherapy, we moved to study the combination therapy. First, we corroborated that DHEA supplementation did not interfere with the therapeutic potential of AVE1642 and PGA-AVE1642 (**See Chapter IV**, **Figures 9** and **10**). Next, we identified a notable synergistic effect in tumors treated with AVE1642/abiraterone acetate; we observed a more significant inhibition of tumor growth and lower PSA levels when compared with AVE1642 alone or abiraterone acetate alone. However, PGA-AVE1642/abiraterone acetate treatment did not improve the anti-tumoral effect when compared to PGA-AVE1642 treatment alone, and we obtained similar alterations to tumor growth and PSA levels (**See Chapter IV**, **Figure 12**).

To further understand the cellular mechanism at play *in vivo*, we studied alterations to the MAPK and PI3K signaling pathways in tumors extracted from mice from the previous experiment. While AVE1642 single treatment promoted only PI3K pathway inhibition (**See Chapter IV**, **Table 1**), the AVE1642/abiraterone acetate displayed obvious synergy (**See Chapter IV**, **Figures 14.C** and **D**) to allow for the inhibition of both PI3K and MAPK pathway inhibition. While AVE1642/abiraterone acetate treatment prompted reduced levels of p-MAPK and p-PI3K, AVE1642 monotherapy did not affect the phosphorylation levels of these proteins (**See Chapter IV**, **Table 1**). For AVE1642/abiraterone acetate treatment, we also detected a decrease in total IGF-1R protein levels (**See Chapter IV**, **Figure 14.E**), an effect possibly related to lower ERG protein expression as a consequence of the mechanism of action of abiraterone acetate, which inhibits androgen synthesis and avoids AR activation and binding to the ERG promotor [66, 67]. In addition, our findings for the AVE1642/abiraterone acetate combination therapy suggest that the MAPK inhibition pathway could impede IGF-1R internalization, thereby preventing IGF-1R transcription resulting in lower IGF-1R levels [68-70].

We also studied the PGA-AVE1642 conjugate in combination with abiraterone acetate in a similar manner. Studies regarding the mechanism of action in tumor samples after PGA-AVE1642 treatment, both in the presence and absence of abiraterone acetate, demonstrated a similar inhibition of tumor growth and the attenuation of both MAPK (through Shc) and PI3K signaling pathways (**See Chapter IV**, **Figures 14.B** and **D**). However, the attenuation of p-Shc is much stronger in the case of the PGA-AVE1642/abiraterone acetate combination treatment, (**See Chapter IV**, **Table 1**). The inhibition of both MAPK and PI3K pathways suggests that PGA-AVE1642 therapy provides a complete inhibition of IGF-1R with and without abiraterone acetate. However, we obtained stronger total IGF-1R inhibition and a more significant decrease in ERG protein levels in PGA-AVE1642/abiraterone acetate combination therapy compared with the PGA-AVE1642 treatment alone (**See Chapter IV**, **Figure 13.G**, **Table 1**). As for the data regarding AVE1642/abiraterone acetate treatment, we obtained similar levels of ERG and total IGF-1R inhibition after PGA-AVE1642/abiraterone acetate combination (**See Chapter IV**, **Table 1**). Additionally, we detected lower p-IGF-1R protein levels in comparison with the control group after both AVE1642/abiraterone acetate and PGA-AVE1642/abiraterone acetate treatments, indicating that both anti-IGF-1R inhibitors (AVE1642 and PGA-AVE1642) bind and block their therapeutic target (**See Chapter IV**, **Figure 14.A**).

Unexpectedly, both combination therapies and abiraterone acetate treatment alone failed to decrease AR levels compared to the control group, even though our studies clearly demonstrate that abiraterone acetate promotes an anti-tumoral effect (**See Chapter IV**, **Figure 14.F**). Of note, our Western blot analysis detected total AR levels – further analysis of mRNA expression and AR phosphorylation status in the future may help to explain this unexpected finding.

After abiraterone acetate treatment alone, we found that p-MAPK and p-PI3K protein levels did not significantly change in comparison with the control group, a finding perhaps related to the crosstalk between AR and PI3K pathways, with the abiraterone acetate treatment promoting PI3K pathway activation [71]. Additionally, total IGF-1R-β maintained high expression levels due to ERG protein expression that acts on the IGF-1R promotor to stimulate higher levels of transcription levels (**See Chapter IV**, **Figure 14.E**) [6]. The unexpectedly high ERG protein levels after abiraterone acetate treatment suggest AR activation by an androgen-independent pathway; in this way, AR could be activated without androgen ligand promoting ERG transcription. Furthermore, p-IGF-1R-β protein expression studies did not reveal any significant alterations in response to abiraterone acetate treatment when compared with the control groups, indicating that IGF-1R is not affected by abiraterone acetate treatment alone (**See Chapter IV**, **Figure 14.A**).

Interestingly, after abiraterone acetate treatment, we detected a significant reduction in p-Shc levels with respect to the control (**See Chapter IV**, **Figure 14.B**). The Shc adaptor protein plays a vital role in cancer progression and metastasis by transmitting activated TKR phosphorylation signaling downstream. Recent studies have established that androgens can increase p-Shc phosphorylation in hormone-sensitive human prostate or breast cancer cells promoting higher tumoral cell growth [72, 73], thereby helping to corroborate our findings.

Furthermore, we hypothesize that AVE1642 requires abiraterone acetate treatment to promote a synergistic effect to inhibit both MAPK and PI3K signaling pathways and decreased tumor growth. In contrast, PGA-AVE1642 with and without abiraterone acetate treatment promote the same antitumor characteristics; for this reason, we conclude abiraterone acetate might not be

necessary after PGA-AVE1642 administration but could help to enhance the long-term anticancer activity as a maintenance treatment after a possible PGA-AVE1642 regime.

As the main conclusions from our studies, we propose the following mechanism of action schemes for AVE1642 and PGA-AVE1642 with and without abiraterone acetate (**Figures 1**, **2**, and **3**).

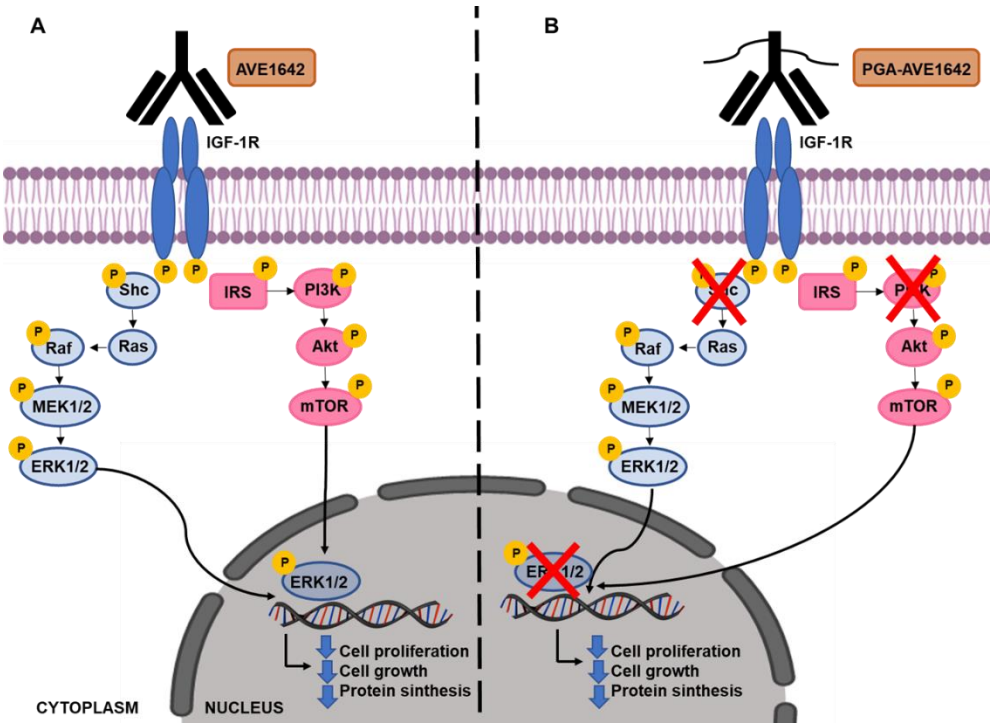

Figure 1: Proposed Differential Mechanisms of Action for AVE1642 vs. PGA-AVE1642 Treatment. A) After AVE1642 treatment, p-Shc, p-MAPK, and p-PI3K levels remain similar and associated with significantly decreased tumor growth and PSA levels. **B)** After PGA-AVE1642 treatment, p-Shc, and p-PI3K levels decrease, suggesting inhibition of both MAPK and PI3K signaling pathways, and this associated with enhanced tumor growth inhibition and PSA level decrease when compared with AVE1642 treatment.

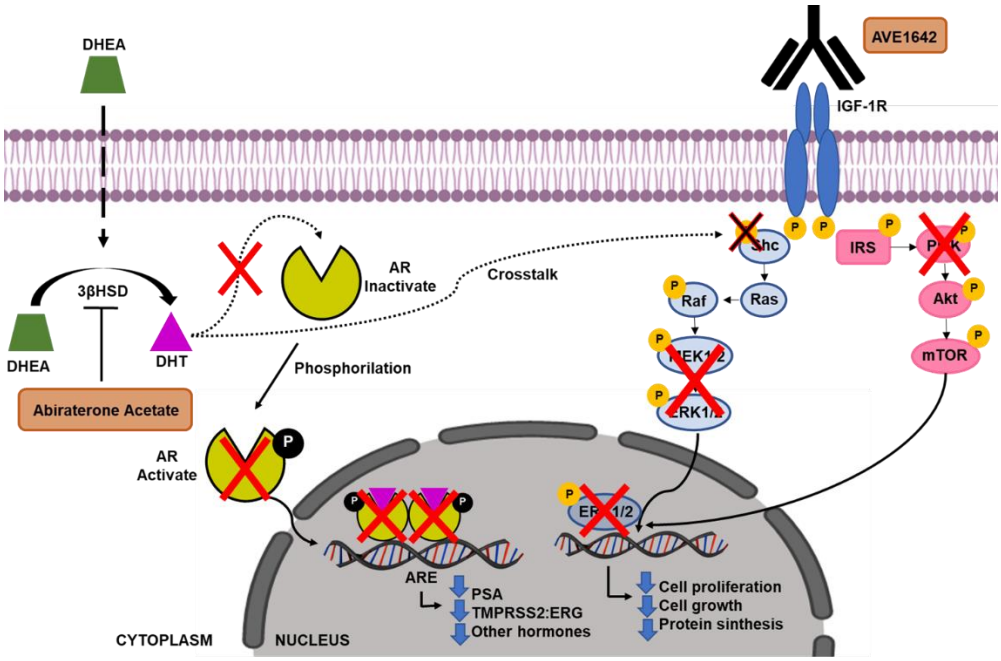

Figure 2: Proposed Mechanism of Action for AVE1642/Abiraterone Acetate Combination Therapy. After AVE1642/abiraterone acetate combination therapy, inhibition of both MAPK and PI3K signaling pathways leads to decreased tumor growth. Reduced p-MAPK levels associate with crosstalk between androgen signaling and Shc. Abiraterone acetate treatment promotes a decrease in androgen levels and the subsequent inhibition of Shc phosphorylation, thereby avoiding the activation of the downstream signaling pathways. Abiraterone acetate treatment also prevents AR nuclear translocation, thereby decreasing PSA and ERG levels.

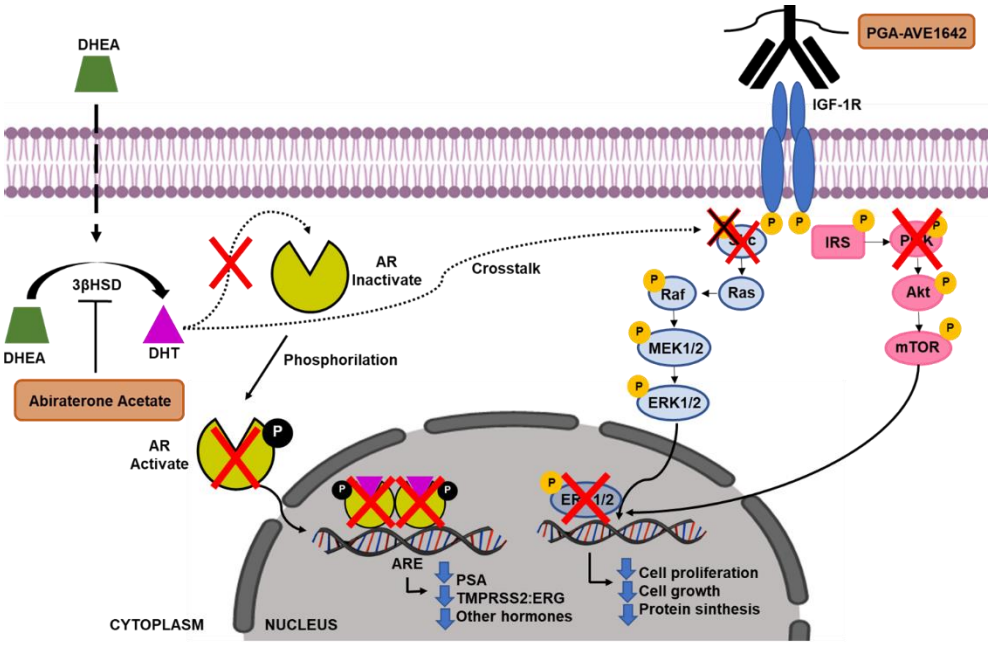

Figure 3: Downstream Signaling Pathways *In Vivo* After PGA-AVE1642/Abiraterone Acetate Combination Therapy. After PGA-AVE1642/abiraterone acetate combination therapy, the lower p-Shc and p-PI3K protein levels observed suggest inhibition of both MAPK (through the p-Shc inhibition) and PI3K signaling pathways, leading to tumor growth inhibition. Higher p-Shc inhibition is promoted by both IGF-1R inhibition by PGA-AVE1642 treatment and the crosstalk between androgen synthesis and Shc phosphorylation. Furthermore, abiraterone acetate treatment also avoids AR nuclear translocation, thereby decreasing PSA and ERG levels.

Bibliography

1. Siegel, R.L., K.D. Miller, and A. Jemal, *Cancer statistics, 2018.* CA: A Cancer Journal for Clinicians, 2018. **68**(1): p. 7-30.
2. Bray, F., et al., *Global cancer statistics 2018: GLOBOCAN estimates of incidence and mortality worldwide for 36 cancers in 185 countries.* CA: A Cancer Journal for Clinicians, 2018. **68**(6): p. 394-424.
3. Asmane, I., et al., *New Strategies for Medical Management of Castration-Resistant Prostate Cancer.* Oncology, 2011. **80**(1-2): p. 1-11.
4. Duncan, R., *Polymer therapeutics as nanomedicines: New perspectives.* Current Opinion in Biotechnology, 2011. **22**: p. 492-501.
5. Mancarella, C., et al., *Insulin-like growth factor 1 receptor affects the survival of primary prostate cancer patients depending on TMPRSS2-ERG status.* BMC Cancer, 2017. **17**(1): p. 367.
6. Mancarella, C., et al., *ERG deregulation induces IGF-1R expression in prostate cancer cells and affects sensitivity to anti-IGF-1R agents.* Oncotarget, 2015. **6**(18): p. 16611-16622.
7. Maso, K., et al., *Chapter One - Molecular platforms for targeted drug delivery*, in *International Review of Cell and Molecular Biology*, L. Galluzzi, Editor. 2019, Academic Press. p. 1-50.
8. Chapman, A.P., *PEGylated antibodies and antibody fragments for improved therapy: a review.* Advanced Drug Delivery Reviews, 2002. **54**(4): p. 531-545.
9. Duncan, R., *Polymer therapeutics: Top 10 selling pharmaceuticals — What next?*. Journal of Controlled Release, 2014. **190**: p. 371-380.
10. Zagorodko, O., et al., *Polypeptide-Based Conjugates as Therapeutics: Opportunities and Challenges.* Macromolecular Bioscience, 2017. **17**(1): p. 1600316.
11. Arroyo-Crespo, J.J., et al., *Tumor microenvironment-targeted poly-L-glutamic acid-based combination conjugate for enhanced triple negative breast cancer treatment.* Biomaterials, 2018. **186**: p. 8-21.
12. Aggarwal, R.R., C.J. Ryan, and J.M. Chan, *Insulin-like growth factor pathway: A link between androgen deprivation therapy (ADT), insulin resistance, and disease progression in patients with prostate cancer?* Urologic Oncology: Seminars and Original Investigations, 2013. **31**(5): p. 522-530.

13. Dean, J.P., et al., *Response of the insulin-like growth factor (IGF) system to IGF-IR inhibition and androgen deprivation in a neoadjuvant prostate cancer trial: effects of obesity and androgen deprivation.* The Journal of Clinical Endocrinology and Metabolism, 2013. **98**(5): p. 820-828.
14. Scotlandi, K., et al., *Antitumor Activity of the Insulin-Like Growth Factor-I Receptor Kinase Inhibitor NVP-AEW541 in Musculoskeletal Tumors.* Cancer Research, 2005. **65**(9): p. 3868.
15. Garofalo, C., et al., *Efficacy of and resistance to anti-IGF-1R therapies in Ewing's sarcoma is dependent on insulin receptor signaling.* Oncogene, 2011. **30**(24): p. 2730-2740.
16. Garofalo, C., et al., *Identification of common and distinctive mechanisms of resistance to different anti-IGF-IR agents in Ewing's sarcoma.* Molecular Endocrinology, 2012. **26**(9): p. 1603-1616.
17. Molife, L.R., et al., *The insulin-like growth factor-I receptor inhibitor figitumumab (CP-751,871) in combination with docetaxel in patients with advanced solid tumours: results of a phase Ib dose-escalation, open-label study.* British Journal of Cancer, 2010. **103**(3): p. 332-339.
18. Langer, C.J., et al., *Randomized, phase III trial of first-line figitumumab in combination with paclitaxel and carboplatin versus paclitaxel and carboplatin alone in patients with advanced non-small-cell lung cancer.* Journal of Clinical Oncology, 2014. **32**(19): p. 2059-2066.
19. de Bono, J.S., et al., *Phase II Randomized Study of Figitumumab plus Docetaxel and Docetaxel Alone with Crossover for Metastatic Castration-Resistant Prostate Cancer.* Clinical Cancer Research, 2014. **20**(7): p. 1925.
20. Du, Z. and C.M. Lovly, *Mechanisms of receptor tyrosine kinase activation in cancer.* Molecular Cancer, 2018. **17**(1): p. 58.
21. Singh, P., J. Alex, and F. Bast, *Insulin receptor (IR) and insulin-like growth factor receptor 1 (IGF-1R) signaling systems: Novel treatment strategies for cancer.* Medical Oncology, 2014. **31**: p. 805.
22. Simpson, A., et al., *Insulin-Like Growth Factor (IGF) Pathway Targeting in Cancer: Role of the IGF Axis and Opportunities for Future Combination Studies.* Targeted Oncology, 2017. **12**(5): p. 571-597.
23. King, H., et al., *Can we unlock the potential of IGF-1R inhibition in cancer therapy?.* Cancer Treatment Reviews, 2014. **40**(9): p. 1096-1105.

24. Geoerger, B., et al., *Anti-insulin-like growth factor 1 receptor antibody EM164 (murine AVE1642) exhibits anti-tumour activity alone and in combination with temozolomide against neuroblastoma.* European Journal of Cancer, 2010. **46**(18): p. 3251-3262.
25. Descamps, G., et al., *CD45neg but Not CD45pos Human Myeloma Cells Are Sensitive to the Inhibition of IGF-1 Signaling by a Murine Anti-IGF-1R Monoclonal Antibody, mAVE1642.* The Journal of Immunology, 2006. **177**(6): p. 4218.
26. Crudden, C., A. Girnita, and L. Girnita, *Targeting the IGF-1R: The Tale of the Tortoise and the Hare.* Frontiers in Endocrinology, 2015. **6**: p. 64.
27. Duncan, R. and S.C.W. Richardson, *Endocytosis and Intracellular Trafficking as Gateways for Nanomedicine Delivery: Opportunities and Challenges.* Molecular Pharmaceutics, 2012. **9**(9): p. 2380-2402.
28. Cantón, I. and G. Battaglia, *Endocytosis at the Nanoscale.* Chemical Society Reviews, 2012. **41**: p. 2718-39.
29. Duro-Castano, A., et al., *Capturing "Extraordinary" Soft-Assembled Charge-Like Polypeptides as a Strategy for Nanocarrier Design.* Advanced Materials, 2017. **29**(39): p. 1702888.
30. Arroyo-Crespo, J.J., et al., *Anticancer Activity Driven by Drug Linker Modification in a Polyglutamic Acid-Based Combination-Drug Conjugate.* Advanced Functional Materials, 2018. **28**(22): p. 1800931.
31. Osher, E. and V.M. Macaulay, *Therapeutic Targeting of the IGF Axis.* Cells, 2019. **8**(8): p. 895.
32. Martins, A.S., et al., *IGF1R signaling in Ewing sarcoma is shaped by clathrin-/caveolin-dependent endocytosis.* PloS One, 2011. **6**(5): p. e19846-e19846.
33. Sarfstein, R., *Minireview: Nuclear Insulin and Insulin-like Growth Factor-1 Receptors: A Novel Paradigm in Signal Transduction.* Endocrinology, 2013. **154**: p. 1672-1679.
34. Aleksic, T., et al., *Nuclear IGF1R Interacts with Regulatory Regions of Chromatin to Promote RNA Polymerase II Recruitment and Gene Expression Associated with Advanced Tumor Stage.* Cancer Research, 2018. **78**(13): p. 3497.
35. Mundy, D.I., et al., *Caveolin targeting to late endosome/lysosomal membranes is induced by perturbations of lysosomal pH and cholesterol content.* Molecular Biology of the Cell, 2012. **23**(5): p. 864-880.

36. Park, S.I., et al., *Pre-clinical mouse models of human prostate cancer and their utility in drug discovery.* Current Protocols in Pharmacology, 2010. **Chapter 14**: p. 14.15.
37. Jyoti, S., et al., *Prostate cancer screening by prostate-specific antigen (PSA); a relevant approach for the small population of the Cayman Islands.* Cancer Causes & Control, 2017. **29**(1): p. 87-92.
38. Shen, Y.-H., et al., *Arg-Gly-Asp (RGD)-Modified E1A/E1B Double Mutant Adenovirus Enhances Antitumor Activity in Prostate Cancer Cells In Vitro and in Mice.* PLoS One, 2016. **11**: p. 0147173.
39. Sun, Y., X. Sun, and B. Shen, *Molecular Imaging of IGF-1R in Cancer.* Molecular imaging, 2017. **16**: p. 1536012117736648.
40. Cargnello, M. and P.P. Roux, *Activation and function of the MAPKs and their substrates, the MAPK-activated protein kinases.* Microbiology and Molecular Biology Reviews, 2011. **75**(1): p. 50-83.
41. Wang, Y., J. Kreisberg, and P. Ghosh, *Cross-talk between the androgen receptor and the phosphatidylinositol 3-kinase/Akt pathway in prostate cancer.* Current Cancer Drug Targets, 2007. **7**: p. 591-604.
42. Armulik, A., A. Abramsson, and C. Betsholtz, *Endothelial/Pericyte Interactions.* Circulation Research, 2005. **97**(6): p. 512-523.
43. Rajabi, M. and S.A. Mousa, *The Role of Angiogenesis in Cancer Treatment.* Biomedicines, 2017. **5**(2): p. 34.
44. Hellström, M., et al., *Lack of pericytes leads to endothelial hyperplasia and abnormal vascular morphogenesis.* The Journal of Cell Biology, 2001. **153**(3): p. 543-553.
45. Mukherji, D., et al., *Angiogenesis and anti-angiogenic therapy in prostate cancer.* Critical Reviews in Oncology/Hematology, 2013. **87**(2): p. 122-131.
46. Karar, J. and A. Maity, *Pi3k/akt/mTOR pathway in angiogenesis.* Frontiers in Molecular Neuroscience, 2011. **4**: p. 51.
47. Greco, F. and M. Vicent, *Combination therapy: Opportunities and challenges for polymer–drug conjugates as anticancer nanomedicines.* Advanced Drug Delivery Reviews, 2009. **61**: p. 1203-1213.
48. Carver, B.S., et al., *Reciprocal feedback regulation of PI3K and androgen receptor signaling in PTEN-deficient prostate cancer.* Cancer Cell, 2011. **19**(5): p. 575-586.
49. Crumbaker, M., L. Khoja, and A.M. Joshua, *AR Signaling and the PI3K Pathway in Prostate Cancer.* Cancers, 2017. **9**(4): p. 34.

50. Fragni, M., et al., *Abiraterone acetate exerts a cytotoxic effect in human prostate cancer cell lines.* Naunyn-Schmiedeberg's Archives of Pharmacology, 2019. **392**(6): p. 729-742.
51. Huang, Y., et al., *Molecular and cellular mechanisms of castration resistant prostate cancer.* Oncology Letters, 2018. **15**(5): p. 6063-6076.
52. Fizazi, K., et al., *Abiraterone plus Prednisone in Metastatic, Castration-Sensitive Prostate Cancer.* New England Journal of Medicine, 2017. **377**(4): p. 352-360.
53. Duarte, C., A. Jimeno, and E.R. Kessler, *Abiraterone acetate to treat metastatic castration-resistant prostate cancer in combination with prednisone.* Drugs of Today, 2019. **55**: p. 5.
54. Rehman, Y. and J.E. Rosenberg, *Abiraterone acetate: oral androgen biosynthesis inhibitor for treatment of castration-resistant prostate cancer.* Drug Design, Development and Therapy, 2012. **6**: p. 13-18.
55. van Bokhoven, A., et al., *Molecular characterization of human prostate carcinoma cell lines.* The Prostate, 2003. **57**(3): p. 205-225.
56. Alimirah, F., et al., *DU-145 and PC-3 human prostate cancer cell lines express androgen receptor: Implications for the androgen receptor functions and regulation.* FEBS Letters, 2006. **580**(9): p. 2294-2300.
57. Buchanan, G., et al., *PC-3 cells with enhanced androgen receptor signaling: A model for clonal selection in prostate cancer.* The Prostate, 2004. **60**(4): p. 352-366.
58. Grossebrummel, H., et al., *Cytochrome P450 17A1 inhibitor abiraterone attenuates cellular growth of prostate cancer cells independently from androgen receptor signaling by modulation of oncogenic and apoptotic pathways.* International Journal of Oncology, 2015. **48**(2): p. 793-800.
59. Bedussi, F., et al., *Amiloride Is Effective in the Management of Abiraterone-Induced Mineralocorticoid Excess Syndrome without Interfering with Its Antineoplastic Activity.* Pharmacology, 2017. **100**: p. 261-268.
60. Kosir, R., et al., *Circadian expression of steroidogenic cytochromes P450 in the mouse adrenal gland - Involvement of cAMP-responsive element modulator in epigenetic regulation of Cyp17a1.* The FEBS Journal, 2011. **279**: p. 1584-93.
61. Missaghian, E., et al., *Role of DNA methylation in the tissue-specific expression of the CYP17A1 gene for steroidogenesis in rodents.* The Journal of Endocrinology, 2009. **202**: p. 99-109.

62. Li, R., et al., *Abiraterone Inhibits 3 -Hydroxysteroid Dehydrogenase: A Rationale for Increasing Drug Exposure in Castration-Resistant Prostate Cancer.* Clinical Cancer Research, 2012. **18**: p. 3571-9.
63. Ando, T., et al., *Dihydrotestosterone synthesis pathways from inactive androgen 5α-androstane-3β,17β-diol in prostate cancer cells: Inhibition of intratumoural 3β-hydroxysteroid dehydrogenase activities by abiraterone.* Scientific Reports, 2016. **6**: p. 32198.
64. Kim, J. and G. Coetzee, *Prostate specific antigen gene regulation by androgen receptor.* Journal of Cellular Biochemistry, 2004. **93**: p. 233-41.
65. Hara, T., et al., *Enhanced Androgen Receptor Signaling Correlates with the Androgen-refractory Growth in a Newly Established MDA PCa 2b-hr Human Prostate Cancer Cell Subline.* Cancer Research, 2003. **63**(17): p. 5622.
66. Ayala, G., et al., *Expression of ERG protein in prostate cancer: variability and biological correlates.* Endocrine-Related Cancer, 2015. **22**(3): p. 277-287.
67. Navaei, A.H., et al., *Correlation between ERG Fusion Protein and Androgen Receptor Expression by Immunohistochemistry in Prostate, Possible Role in Diagnosis and Therapy.* Journal of Cancer, 2017. **8**(13): p. 2604-2613.
68. Meisel Sharon, S., et al., *TMPRSS2-ERG fusion protein regulates insulin-like growth factor-1 receptor (IGF1R) gene expression in prostate cancer: involvement of transcription factor Sp1.* Oncotarget, 2016. **7**(32): p. 51375-51392.
69. Hellawell, G.O., et al., *Expression of the Type 1 Insulin-like Growth Factor Receptor Is Up-Regulated in Primary Prostate Cancer and Commonly Persists in Metastatic Disease.* Cancer Research, 2002. **62**(10): p. 2942.
70. Liao, Y., et al., *Up-regulation of insulin-like growth factor axis components in human primary prostate cancer correlates with tumor grade.* Human Pathology, 2005. **36**(11): p. 1186-1196.
71. Yadav, S.S., et al., *Combination effect of therapies targeting the PI3K- and AR-signaling pathways in prostate cancer.* Oncotarget, 2016. **7**(46): p. 76181-76196.
72. Lee, M.-S., et al., *p66Shc protein is upregulated by steroid hormones in hormone-sensitive cancer cells and in primary prostate carcinomas.* International Journal of Cancer, 2004. **108**(5): p. 672-678.
73. Kumar, S., et al., *Steroids up-regulate p66Shc longevity protein in growth regulation by inhibiting its ubiquitination.* PLoS One, 2011. **6**(1): p. 15942.

Final Conclusions

Final Conclusions

Our work focused on a polymer therapeutics approach to PCa therapy, where we investigated how PGA conjugation altered the biological properties of a human monoclonal antibody (AVE1642) in the hope of increased anti-tumoral activity of AVE1642 in aggressive PCa. We demonstrated enhanced monoclonal antibody bioactivity after PGA conjugation and explored the potential of combination therapy as an advanced treatment option for a subtype of PCa patients, T2E positive patients.

The main conclusions of this thesis can be summarized as follows:

1. We developed a new polymer-antibody conjugate at an optimal ratio of 2:1 (two PGA chains per one AVE1642).

2. PGA conjugation increases the hydrodynamic volume and negative charge of AVE1642 although the secondary structure of AVE1642 is maintained.

3. PGA conjugation does not promote hemolysis in mice serum, providing proof of safety, protects AVE1642 from degradation in serum improving AVE1642 stability, improves thermal stability of AVE1642, but does not improve AVE1642 tumor accumulation.

4. PGA conjugation does not alter AVE1642 function and maintains the selectivity of AVE1642 to ERG overexpression associated with the presence of T2E fusion gene in PCa cells.

5. PGA conjugation modifies cellular trafficking *in vitro*. AVE1642 and PGA-AVE1642 become targeted to the lysosomes by different endocytic pathways. While AVE1642 primarily internalizes via clathrin-mediated endocytosis and is directed to the lysosomes through endosomes, PGA-AVE1642 instead internalizes via caveolin mediated endocytosis and is

directed to the lysosomes, with a lack of early endosomal colocalization probably due to differential interactions with the receptor.

6. We optimized a novel preclinical orthotopic mice model of advanced PCa using the VCaP cell line transfected with luciferase.

7. PGA conjugation of AVE1642 leads to an altered molecular response *in vitro* and *in vivo,* improving the antitumoral activity preventing the activation of both PI3K and MAPK signaling pathways, thus improving AVE1642 effectiveness. However, while we obtain an inhibition of PI3K signaling pathway *in vitro* following AVE1642 treatment, we fail to detect pathway inhibition *in vivo*.

8. PGA-AVE1642 improves IGF-1R inhibition by preventing energy-dependent internalization of IGF-1R, thereby inhibiting both the PI3K and MAPK pathways. AVE1642 allows IGF-1R internalization and prevents downstream PI3K signaling pathway activation.

9. PGA-AVE1642 treatment promotes more robust alterations to the TME when compared to AVE1642, including a decrease in both the functionality and maturity of blood vessels. Furthermore, PGA-AVE1642 significantly improves the inhibition of prostate tumor proliferation and angiogenesis compared with AVE1642 treatment.

10. *In vitro* studies demonstrated a T2E-dependent synergistic effect for PGA-AVE1642 and AVE1642 treatments in combination with abiraterone. However, while we obtained a synergistic anti-tumor effect for AVE1642 treatment in combination with abiraterone *in vivo*, we failed to find an additive effect for PGA-AVE1642 and abiraterone treatment due to the differential molecular mechanism of action upon PGA conjugation as both combination therapies promoted a dual inhibition pathway via PI3K and MAPK.

Memoria de la Tesis

1. Introducción

1.1. Cáncer de Próstata: Definición y Progresión

La incidencia del cáncer ha aumentado recientemente debido a varios factores, entre ellos, el aumento de la esperanza de vida, las mejoras en el diagnóstico y el aumento de la exposición a diferentes factores de riesgo. El cáncer de próstata (CaP) representa el segundo cáncer más común y la quinta causa principal de muerte en hombres, con 1,3 millones de casos nuevos y 359.000 muertes asociadas en el año 2018 [1].

Generalmente, la mayoría de los casos diagnosticados de CaP son adenocarcinomas, un tumor maligno formado por estructuras glandulares en el tejido epitelial [2]. Los CaP primarios o localizados presentan una amplia gama de opciones de tratamiento que varían según la edad del paciente, el estadio clínico del tumor, los niveles de biomarcadores (incluido el antígeno prostático específico (PSA)) o la puntuación de Gleason (un sistema de clasificación que mide la agresividad del tumor en función de su aspecto microscópico) [3]. La prostatectomía radical y la radioterapia representan tratamientos estándar para el CaP localizado. Independientemente de los resultados iniciales positivos obtenidos empleando estas terapias, la recurrencia de la enfermedad ocurre en un tercio de los pacientes.

En esta etapa recurrente, la terapia de privación de andrógenos (ADT) representa el tratamiento indicado. El CaP se considera un tumor hormonodependiente en el que se necesita la activación del receptor de andrógenos (AR) para su supervivencia. El CaP resistente a la castración (CRPC) se desarrolla como consecuencia de la resistencia a la ADT, lo que conduce a una alta mortalidad debido a un mal pronóstico y a la falta de terapias específicas [4].

Existen varios mecanismos involucrados en la progresión del CRPC como son alteraciones en las vías involucradas en la reparación del DNA [5], la desregulación de los genes implicados en la señalización de la ruta PI3K-Akt mTOR [6] y las más frecuentes relacionadas con alteraciones del AR [7].

A pesar de los recientes avances en la detección temprana y tratamiento del CaP localizado, el número de muertes es elevado. Este hecho se debe a la ausencia de biomarcadores con utilidad clínica y la subclasificación molecular del CaP, además de la falta de terapias personalizadas [8]. Para resolver estos problemas, necesitamos una comprensión más profunda del desarrollo de la enfermedad y de los mecanismos biológicos que controlan la identidad del tumor.

1.2. Biomarcadores en el Cáncer de Próstata

Actualmente, la detección del PSA, el examen rectal digital y la biopsia de tejido prostático representan las herramientas clínicas empleadas generalmente para diagnosticar el CaP. Cabe destacar que los niveles de PSA además de aumentar por el CaP, también pueden variar por enfermedades benignas de la próstata como la prostatitis o la hiperplasia prostática benigna [9]. Por lo tanto, el diagnóstico basado en los niveles de PSA no permite una gran precisión en la estrategia de tratamiento, lo que puede llevar a un tratamiento inadecuado de los pacientes.

La integración de datos genómicos, transcriptómicos, epigenéticos y metabolómicos ha llevado al descubrimiento de diversos biomarcadores de CaP de nueva generación. Estos avances aumentan la precisión en la decisión de un tratamiento efectivo.

Entre estos biomarcadores destacan: el gen *PCA3*, el cual está sobreexpresado en más del 95% de los casos primarios de CaP [10], el gen *SCHLAP1* el cual también está sobreexpresado en el CaP agresivo [11], la detección de la variante AR 7 (AR-V7) en células tumorales circulantes [12] y las alteraciones

genómicas en *PTEN*, las cuales representan un paso clave en el desarrollo de CaP agresivo [13]. Además, el reordenamiento cromosómico y las deleciones intracromosómicas son aberraciones comunes en el CaP que llevan a la formación de genes de fusión.

Principalmente, la fusión del gen *TMPRSS2-ERG* (T2E) es el reordenamiento cromosómico más frecuente en CaP. El gen *TMPRSS2* codifica una proteasa serina transmembrana regulada por AR, por lo tanto, está altamente expresada en el tejido prostático. Diversos estudios han demostrado que el promotor 5' del gen *TMPRSS2* se puede fusionar con la región codificante del gen *ERG* produciendo un aumento de su expresión. *ERG* codifica una proteína oncogénica que desempeña un papel importante en la progresión de la enfermedad [14]. El gen de fusión *T2E* se ha visto que puede tener un papel crítico en la subclasificación de pacientes con CaP y en el desarrollo de estrategias terapéuticas específicas [14].

1.3. Terapias para el Cáncer de Próstata

Las terapias tradicionales empleadas para tratar el CRPC incluyen la quimioterapia y las terapias hormonales. Docetaxel y cabazitaxel son los agentes quimioterapéuticos más utilizados para el CRPC, pero, a pesar de mostrar resultados prometedores, presentan una supervivencia media de 18 meses [15].

Se han desarrollado nuevas terapias hormonales basadas en el importante papel que el AR desempeña en el CaP. La evolución del CaP a CRPC depende de la capacidad que adquieren las células cancerosas para crecer con niveles bajos de andrógenos debido a las aberraciones en el AR que mantienen la actividad transcripcional en ausencia del ligando. La abiraterona es un inhibidor irreversible y altamente selectivo de la enzima CYP17A1 que, por lo tanto, bloquea la producción de andrógenos tanto en la próstata como en las glándulas adrenales. La enzalutamida es otro fármaco antiandrogénico que inhibe directamente la

translocación nuclear del AR y su unión al ADN. Otros fármacos antiandrogénicos incluyen apalutamida y darolutamida [16]. También se ha demostrado que las terapias hormonales pueden presentar ciertas sinergias con los agentes clásicos quimioterapéuticos.

Las nuevas terapias incluyen inhibidores de PARP como olaparib o niraparib [17], la aplicación de Radium-223, un radioisótopo que induce roturas de doble cadena de ADN [18], y Sipuleucel-T, la primera inmunoterapia para CRPC [16].

1.4. Nanomedicina y Polímeros Terapéuticos

Lamentablemente, a pesar de la gran cantidad de fármacos empleados para tratar el CaP avanzado, la falta de eficiencia ha provocado que no se mejoren las tasas de supervivencia ni se reduzcan los efectos secundarios, por lo que es necesario el desarrollo de nuevos tratamientos para el CRPC.

En este contexto, la nanomedicina, definida como la aplicación de la nanotecnología en el campo médico, representa un medio prometedor para la creación de estrategias de tratamiento eficaces. Este enfoque ha permitido el desarrollo de nanofármacos y métodos para el transporte selectivo de medicamentos.

Los polímeros terapéuticos (PT) se consideran la primera generación de nanomedicamentos poliméricos más exitosa representando una de las disciplinas nanomédicas más innovadoras en cuanto al tratamiento del cáncer. Las terapias con polímeros abarcan una amplia familia de sistemas que incluyen conjugados de fármaco-polímero, proteína-polímero, micelas poliméricas, liposomas o cualquier agente terapéutico unido a una estructura polimérica [19].

Las características intrínsecas de los PT ofrecen las siguientes ventajas: una mayor capacidad para cruzar barreras biológicas, un mejor control de la

farmacocinética, una mayor acumulación pasiva en el tumor a través del efecto de permeabilidad y retención (EPR), un aumento en el tiempo de circulación sanguínea, aumentan la solubilidad, reducen la toxicidad e incluyen la capacidad de llevar más de un agente activo, permitiendo así la terapia combinada [20].

1.5. Terapia Personalizada en el Cáncer de Próstata

Las nuevas estrategias de tratamiento contra el CRPC han tenido en cuenta los conocimientos sobre la biología del CaP y gracias a esto se han empezado a desarrollar enfoques terapéuticos utilizando polímeros.

Estudios previos demostraron una sobreexpresión de IGF-1R en un subtipo de pacientes de CaP caracterizado por la presencia de T2E. IGF-1R está relacionado con la invasión tumoral y metástasis a través de la activación de las rutas de señalización intracelular PI3K y MAPK [21].

AVE1642 es un anticuerpo monoclonal humanizado (mAb) dirigido contra IGF-1R. Los ensayos clínicos en fase II que utilizan inhibidores de IGF-1R no han logrado demostrar la eficacia de este tratamiento en pacientes con CRPC, tal vez debido a una inhibición incompleta de la vía y a la falta de un subtipo adecuado de pacientes. Sin embargo, se demostró que el AVE1642 presenta efectos citotóxicos significativos en las líneas celulares T2E+ en comparación con las células T2E-. De esta manera, se demuestra que el AVE1642 tiene un efecto terapéutico específico en un subtipo específico de pacientes que presentan el gen de fusión T2E [21].

Es importante remarcar que la inhibición de la ruta PI3K ocasionada por el bloqueo del receptor IGF-1R utilizando AVE1642 produciría un aumento en los niveles de andrógenos ocasionando el crecimiento tumoral por la existencia de un entrecruzamiento entre las rutas PI3K y AR [22], por lo que, en esta tesis doctoral, proponemos el diseño de una terapia de combinación empleando el polímero

PGA-AVE1642 para bloquear la ruta PI3K y la abiraterona para bloquear la síntesis de andrógenos en un subtipo específico de pacientes T2E+.

2. Objetivos

El objetivo a largo plazo de esta tesis doctoral es el desarrollo de terapias avanzadas para el tratamiento del CaP en un estadio avanzado de forma personalizada, siendo aún una necesidad clínica. En particular, nos centramos en el diseño y el desarrollo de un conjugado biocompatible y biodegradable formado por polímero unido a un anticuerpo (PGA-AVE1642) para bloquear IGF-1R con el fin de mejorar los resultados terapéuticos en el subtipo de cáncer de próstata positivos para T2E. Además, debido a la retroalimentación recíproca negativa entre el receptor de andrógenos (AR) y las vías de señalización PI3K/Akt, nuestro paso siguiente es estudiar la terapia de combinación utilizando AVE1642 o PGA-AVE1642 con abiraterona para promover una mayor inhibición de ambas vías – una estrategia que podría representar un método prometedor para tratar el PCa avanzado.

Estos aspectos principales se lograrán a través de los siguientes objetivos específicos:

1. Desarrollo, síntesis y caracterización química de un nuevo conjugado utilizando un portador polimérico biodegradable y multivalente (ácido polilutámico L-glutámico o PGA) conjugado con un anticuerpo humano monoclonal anti-IGF-1R (AVE1642) para el tratamiento del cáncer de próstata resistente a la castración metastásica (mCRPC). La caracterización completa del PGA-AVE1642 se realizará mediante una serie de técnicas (por ejemplo, SEC, DLS y FUV-CD) para determinar parámetros como el tamaño, la carga y la estructura.

2. Estudio del efecto que ejerce la conjugación del PGA en la estabilidad del AVE1642, mediante la evaluación de su afinidad al IGF-1R, y estudiar su seguridad a través de ensayos de hemocompatibilidad.

3. Análisis de la citotoxicidad de AVE1642/PGA-AVE1642 y estudio de su dependencia con la sobreexpresión de ERG asociada con la presencia del gen de fusión T2E en varias líneas celulares de cáncer de próstata y células normales de próstata.

4. Estudio de la influencia del PGA en el tráfico y el destino celular de AVE1642 *in vitro* por microscopía confocal/STORM en la línea celular VCaP mediante el etiquetado de AVE1642 y PGA-AVE1642 con diferentes fluoróforos.

5. Investigación de la respuesta molecular de AVE1642 y PGA-AVE1642 *in vitro* en la línea celular VCaP por análisis de proteínas.

6. Diseño y optimización *in vivo* de un modelo de ratón ortotópico de cáncer de próstata avanzado utilizando la línea celular VCaP transfectada con luciferasa, que se utilizará para testar la actividad antitumoral de AVE1642 y PGA-AVE1642 a través de la monitorización de la progresión tumoral por imagen óptica (IVIS Spectrum®). También se estudiarán los tumores a nivel proteico para explorar las diferentes respuestas moleculares a ambos tratamientos, AVE1642 y PGA-AVE1642.

7. Evaluación de las alteraciones del microambiente tumoral, como la funcionalidad, la madurez de los vasos sanguíneos, la proliferación tumoral y la angiogénesis, después del tratamiento AVE1642 y PGA-AVE1642 mediante inmunohistoquímica.

8. Estudio *in vitro* e *in vivo* de la sinergia entre AVE1642/PGA-AVE1642 en combinación con abiraterona evaluando la dependencia de ambas terapias combinadas en la presencia de T2E.

3. Material y Métodos

3.1. Cromatografía de Exclusión Molecular

La cromatografía de exclusión molecular se realizó en un sistema FPLC equipado con una columna Superdex. La elución de la muestra se realizó con Tris 50 mM, NaCl 150 mM pH 7.5, y la absorbancia se determinó a 220 nm.

3.2. Electroforesis SDS-PAGE

Las muestras se mezclaron (1:2) con tampón de carga y se incubaron durante 5 minutos a 95ºC para desnaturalizar la proteína. A continuación, las muestras se cargaron en un gel SDS y migraron durante 1 h 45 min a 150 V. Las proteínas fueron visualizadas tras tinción con azul de Coomassie.

3.3. Dispersión Dinámica de la Luz (DLS) y Medidas del Potencial Z

Ambos parámetros se determinaron a 25ºC utilizando el detector Malvern Zetasizer Nano ZS equipado con un láser de 532 nm con un ángulo de dispersión fijo de 173º. Previamente, las muestras fueron preparadas en PBS a 0,2 mg/ml y filtradas a través de un filtro de membrana de celulosa de 0,22 µm. Las medidas de DLS mostraron el tamaño de la muestra y las medidas del potencial Z determinaron la carga superficial.

3.4. Análisis de Aminoácidos

La relación molar entre el PGA y el AVE1642 en el conjugado PGA-AVE1642 se determinó mediante análisis de aminoácidos en la Universidad de Barcelona. Se hidrolizaron 100 µl de las muestras en ácido clorhídrico 6 M a 110ºC durante 24 horas. A continuación, las muestras se evaporaron, se resuspendieron en 500 µl de agua Milli-Q y se filtraron utilizando una membrana de celulosa de 0,45 µm. La solución filtrada se diluyó en 200 µl de agua Milli-Q y posteriormente las muestras

se derivatizaron con AQC según el método AccQ-Tag™. Los aminoácidos fueron analizados por HPLC mediante detección UV a 254 nm.

3.5. Estudios ELISA

Se realizaron ensayos ELISA para evaluar la estabilidad y afinidad del AVE1642 y PGA-AVE1642. En una placa ELISA se añadieron 40 µg/ml de lisado celular de VCaP diluido en PBS y la placa se incubó en agitación durante toda la noche a 4ºC. Al día siguiente, después de tres lavados con PBS-Tween, los lisados fueron bloqueados con tampón de bloqueo (0.2% (v/v) Tween 20 y 5 % leche) durante 2 horas a temperatura ambiente. El tampón de bloqueo fue eliminado tras tres lavados con PBS-Tween y se añadieron 100 µl de sus correspondientes curvas de calibración y 100 µl de las diferentes muestras. La placa se incubó en agitación durante toda la noche a 4ºC y, tras tres nuevos lavados con PBS-Tween, se incubaron durante 2 horas 100 µl del anticuerpo primario anti-humano. Finalmente, se retiró el anticuerpo y los lisados se incubaron con 100 µl de TMB durante 30 minutos en oscuridad. Después de este tiempo, se añadieron 100 µl de solución de parada. La absorbancia se midió en un espectrofotómetro a 450 nm.

3.6. Estudios MTS

Las células fueron sembradas en una placa estéril de 96 pocillos en un volumen de 50 µl de medio e incubadas durante 24 o 72 horas en función del crecimiento exponencial. Transcurrido este tiempo, los diferentes tratamientos fueron preparados en medio y filtrados utilizando una membrana de celulosa de 0,22 µm. Tras una incubación de 72 horas a 37ºC, se añadieron 20 µl de MTS/PMS (proporción 20:1) y permaneció a 37ºC durante 3 o 6 horas dependiendo de la línea celular y respiración mitocondrial. Finalmente, las muestras se midieron en el espectrofotómetro a 490-500 nm.

3.7. Estudios IN Cell

Las células fueron incubadas en una placa de 96 pocillos en un volumen de 100 µl de medio durante 72 horas. Posteriormente, las células se trataron durante 15, 30 y 60 minutos con 0,1 µg/ml de IGF-1, AVE1642 y PGA-AVE1642. Después de lavar con PBS, las células se fijaron con 100 µl de PFA durante 20 minutos a 37ºC y fueron bloqueadas durante una hora a la misma temperatura. Luego, se incubaron 50 µl de anticuerpo primario IGF-1R-β durante toda la noche a 4ºC en agitación. A continuación, después de tres lavados con PBS, se añadieron 50 µl del anticuerpo secundario anti-conejo Alexa-488 y la placa fue incubada durante una hora en oscuridad. Después de lavar con PBS, la señal de IGF-1R fue adquirida y analizada en IN-Cell Analyzer.

3.8. Citometría de Flujo

Las células se sembraron en una placa de 12 pocillos y fueron incubadas durante 72 horas. Después, se incubaron 2 nM del inhibidor de la catepsina B (CA-074) durante 30 minutos para evitar la degradación de la PGA. A continuación, unas placas se mantuvieron a 37ºC para estudiar la endocitosis dependiente de energía mientras que otras se incubaron a 4ºC para inhibir este mecanismo. Luego, los compuestos AVE1642-Cy5.5 (0,16 mg/ml) y PGA-AVE1642-Cy5.5 (0,1 mg/ml) fueron añadidos directamente al medio celular y se incubaron durante 3 horas, 1 hora, 15 minutos y 0 minutos a 37ºC y 4ºC. Finalmente, las células fueron lavadas con PBS-BSA y se recogieron en un volumen final de 400 µl. Los datos se obtuvieron empleando el citómetro de flujo CytoFLEX S.

3.9. Microscopía Confocal

Las células fueron sembradas en una placa de 24 pocillos sobre un portaobjetos de vidrio redondo. Tras 72 horas de incubación, las células fueron tratadas durante 30 minutos con PGA-AVE1642-Cy5.5 (0,1 mg/ml) y AVE1642-Cy5.5

(0,16 mg/ml). A continuación, el medio fue retirado y las células se fijaron con PFA durante 20 minutos a 37ºC para después bloquear con tampón de bloqueo (10% (v/v) FBS diluido con PBS) durante 1 hora a 37ºC. Posteriormente, las células se incubaron toda la noche a 4ºC con 50 µl de las siguientes combinaciones de anticuerpos primarios: (i) anti-conejo IGF-1R-β con anti-ratón EEA1; (ii) anti-conejo LAMP1; (iii) anti-conejo IGF-1R-β con anti-ratón Clathrin (1/50); (iv) anti-conejo IGF-1R-β con anti-cabra Caveolin-1. Al día siguiente, se descartaron los anticuerpos primarios y las células se incubaron durante una hora en oscuridad con 50 µl de la siguiente combinación de anticuerpos secundarios: i) anti-conejo Alexa-488 con anti-ratón Pacific blue; ii) anti-conejo Alexa-488; iii) anti-conejo Alexa-488 con anti-ratón Alexa-568; iv) anti-conejo Alexa-488 con anti-cabra-Cy3 respectivamente. Finalmente, las células fueron lavadas con PBS y diferentes imágenes se adquirieron con el microscopio Leica TCS SP8 para su análisis utilizando el software LAS X Life Science.

3.10. Western Blot

Las muestras celulares y tumorales fueron procesadas de forma diferente. Las células fueron sembradas en una placa de 6 pocillos y se incubaron durante 72 horas antes de ser tratadas con IGF-1, AVE1642 y PGA-AVE1642 a 0,1 µg/ml durante 15 y 30 minutos. A continuación, se retiró el medio y, tras lavar con PBS, las células se incubaron con tripsina-EDTA durante 1 minuto a 37 ºC para posteriormente inactivarla añadiendo 1,5 ml de medio. Finalmente, las células se centrifugaron durante 5 minutos a 400 rcf y el sedimento celular se introdujo en hielo para su posterior extracción proteica. En cambio, los tumores fueron extraídos e introducidos en nitrógeno líquido. Una vez congelados, fueron machacados y el polvo obtenido fue introducido en un tubo para su posterior extracción proteica.

Para extraer las proteínas celulares y tumorales, 100 µl de tampón de extracción fueron añadidos en las diferentes muestras, las cuales se introdujeron

10 minutos en hielo y se agitaron en vórtex 10 segundos durante tres sucesivos ciclos. A continuación, las muestras se centrifugaron 20 minutos, a 13.200 rpm a 4ºC y en el sobrenadante, mediante absorbancia a 595 nm, se cuantificó la cantidad de proteína utilizando el reactivo Bradford.

50 µg de las muestras de proteína obtenidas fueron diluidas en tampón de carga y posteriormente se desnaturalizaron a 95ºC durante 7 minutos. Las muestras se separaron electroforéticamente en geles de poliacrilamida del 8% en tampón Running 1X. Después, las muestras se transfirieron a una membrana PVDF con tampón de transferencia a 400 mA durante dos horas a 4ºC. Una vez transferidas las proteínas, las membranas se bloquearon durante una hora a temperatura ambiente y diferentes anticuerpos primarios fueron diluidos en tampón de bloqueo e incubados en agitación durante toda la noche a 4ºC (anti-conejo p-MAPK, anti-ratón p-Shc, anti-conejo p-PI3K, anti-conejo IGF-1R-β, anti-conejo AR, anti-ratón ERG y anti-ratón α-tubulina). Al día siguiente, los anticuerpos primarios fueron retirados tras tres lavados con PBS-Tween y las membranas se incubaron durante una hora en agitación a temperatura ambiente con los anticuerpos secundarios anti-conejo y anti-ratón. A continuación, la señal quimioluminiscente se detectó empleando el sustrato ECL y la imagen fue adquirida en Amercham Hyperfilm. Finalmente, las imágenes fueron analizadas por densitometría utilizando el programa ImageJ.

3.11. Infección Lentiviral

Para monitorizar el crecimiento tumoral *in vivo*, la línea celular VCaP fue infectada por separado con el vector lentiviral luciferasa y con el vector lentiviral GFP como control de transfección positivo. Las células fueron sembradas en una placa de 6 pocillos y se incubaron a 37ºC hasta la obtención de un 80% de confluencia. A continuación, se prepararon ambas soluciones lentivirales por separado, las cuales se añadieron a las células y fueron incubadas durante 24 horas.

Transcurrido este tiempo, el medio fue reemplazado por medio completo y se procedió a la selección de aquellas células positivas para la infección empleando 500 µg/ml del antibiótico geneticina.

3.12. Efecto de Permeabilidad y Retención (EPR)

Para determinar el EPR en el modelo animal, el colorante Evans blue:BSA (proporción 8:1) fue disuelto en una solución de cloruro de sodio al 0,9%. Cada semana, un grupo de seis ratones portadores de tumores sin tratar fueron sacrificados una hora después de la inyección por vía intravenosa de 10 mg/kg de colorante. Los tumores fueron pesados e incubados a 60ºC durante 48 horas en 3 ml de formamida para extraer el colorante del tumor. El porcentaje de este colorante fue determinado mediante absorbancia a 620 nm.

3.13. Efectividad Antitumoral en el Modelo Animal

Para desarrollar el modelo ortotópico animal de CaP se empleó la cepa C.B-17/IcrHan®Hsd-*Prkdc*^{scid}. Los ratones fueron inyectados subcutáneamente con morfina (5 mg/kg) treinta minutos antes de la cirugía, y fueron anestesiados por inhalación con isoflurano (2-5%) durante todo el proceso quirúrgico. Una vez localizada la glándula prostática, se inyectaron un millón de células VCaP-Luc2 ortotópicamente en un volumen final de 40 µl empleando una aguja de insulina (29G). A continuación, el área muscular y la piel se suturaron por separado y, después de la cirugía, se administró buprenorfina subcutánea (0,1 mg/kg) cada 12 horas durante 72 horas como analgésico antiinflamatorio. El crecimiento tumoral fue monitorizado dos veces por semana a través de la señal luminiscente tumoral mediante la tecnología IVIS Spectrum. Para poder visualizar la luminiscencia del tumor, se administraron por vía subcutánea 150 mg/kg del sustrato luciferina.

Los compuestos se administraron una vez los tumores alcanzaron un tamaño que permitía el máximo efecto de EPR (0,05 cm^3, correspondiente a la

segunda semana) con 6 animales utilizados en cada grupo. AVE1642 y PGA-AVE1642 como terapia única y combinada con acetato de Abi se administraron por vía intravenosa tras dos semanas a 10 mg/kg una vez a la semana durante cuatro semanas. El acetato de abiraterona se administró por vía oral a 200 mg/kg una vez al día durante 35 días consecutivos también a partir de la segunda semana, y el DHEA se administró como suplemento diario por vía subcutánea a 0,1 mg. Cuando los tumores de los animales control (animales sin tratamiento) alcanzaron un tamaño de 1,2 cm^3 (correspondiente a la séptima semana), todos los animales fueron sacrificados por inhalación de dióxido de carbono (CO_2), y los tumores fueron pesados y medidos con calibre después de la extracción. También se extrajo sangre del corazón, la cual se centrifugó durante 10 minutos a 4000 rpm a 4ºC para obtener el plasma utilizado y cuantificar los niveles de PSA.

3.14. Inmunohistoquímica Tumoral

Para los análisis inmunohistoquímicos tumorales, los ratones tratados con los diferentes compuestos fueron inyectados con 80 µl de FITC-lectina para identificar los vasos perfundidos en el tumor. Después, los tumores fueron extraídos, incluidos en OCT y congelados, conservándolos a -80ºC hasta su análisis histológico. Se hicieron secciones tumorales de 8 µm de grosor con el criostato y se fijaron en un portaobjetos.

Para el análisis de los marcadores VEGFR2 y Ki67 se empleó un procedimiento experimental similar. Para eliminar el OCT, las muestras se lavaron en PBS y posteriormente se fijaron inicialmente con metanol al 80% durante cinco minutos y luego con acetona a -20ºC durante dos minutos a temperatura ambiente. A continuación, las muestras se lavaron tres veces con PBS durante cinco minutos. Para facilitar la difusión del anticuerpo Ki67 hacia el núcleo, se realizó un paso adicional de permeabilización con 0,1% de Triton-X 100 en PBS durante tres minutos a temperatura ambiente. Las muestras tumorales se lavaron durante cinco

minutos con PBS y se incubaron en una cámara húmeda durante una hora con los respectivos anticuerpos primarios diluidos en 12% BSA (anti-cabra VEGFR2 y anti-conejo Ki67). Posteriormente, las muestras se lavaron tres veces durante cinco minutos con PBS y se incubaron durante 45 minutos en una cámara húmeda con los respectivos anticuerpos secundarios diluidos en 12% BSA (anti-cabra-Cy3 y anti-conejo-Cy3). Después de lavar tres veces con PBS durante cinco minutos, las secciones tumorales se analizaron con el microscopio de fluorescencia Axio Imager M2 y las imágenes fueron cuantificadas utilizando el programa Dongle.

4. Resultados

4.1. La Conjugación del PGA Altera la Bioactividad de AVE1642 en Modelos de Cáncer de Próstata

4.1.1. Síntesis y Caracterización Química de PGA-AVE1642

La unión del PGA al AVE-1642 se realizó mediante dos pasos. En el primer paso, los grupos amida del AVE1642 fueron modificados con SATP y la concentración del AVE1642 se determinó midiendo la absorbancia a 280 nm. El segundo paso consistió en la conjugación del PGA al AVE1642-SATP, en la que fue necesaria una modificación previa del PGA con PD para obtener PGA-PD.

Una vez obtenido el PGA-AVE1642, se caracterizó siguiendo diferentes técnicas para determinar el tamaño, la carga superficial y el número de cadenas de PGA. Mediante cromatografía de exclusión molecular y análisis SDS-PAGE encontramos un incremento en el volumen hidrodinámico del PGA-AVE1642 respecto al AVE1642. Además, la técnica de DLS corroboró estos resultados mostrando un tamaño de 13,5 ± 1,7 nm para AVE1642, mientras que el tamaño para el conjugado PGA-AVE1642 fue de 17,5 ± 0,6 nm. Además, el potencial Z mostró una carga superficial para el PGA-AVE1642 más negativa con un valor de -11,7 mV debido a la presencia del PGA aniónico. Finalmente, el análisis de

aminoácidos determinó la conjugación de un promedio de 2,8 cadenas de PGA por cada molécula de AVE1642.

4.1.2. La Conjugación del PGA Aumenta la Estabilidad y la Afinidad de AVE1642

La estabilidad y la afinidad de AVE1642 y PGA-AVE1642 se evaluaron mediante ensayos ELISA. Para determinar la estabilidad, ambos compuestos se diluyeron en suero y se incubaron a 37ºC durante 72 horas. Durante este periodo se recogieron alícuotas a diferentes tiempos (0, 24, 48 y 72 horas) y se incubaron con lisados proteicos de la línea celular VCaP que sobreexpresaba IGF-1R. Mientras el PGA-AVE1642 se mantiene estable a lo largo del tiempo, el AVE1642 muestra una mayor degradación. Estos resultados sugieren que la conjugación del AVE1642 al PGA puede ayudar a mantener la estabilidad del AVE1642 y, por lo tanto, funcionar durante largos periodos de tiempo después de la administración. Para estudiar la afinidad, diferentes concentraciones de AVE1642 y PGA-AVE1642 fueron testadas tras diluirlas en PBS y posteriormente incubadas en este lisado para detectar la concentración a la que el IGF-1R empieza a saturarse. Se demostró que PGA-AVE1642 produce una saturación del IGF-1R a 2 µg/ml de AVE1642 equivalentes. Sin embargo, no pudimos apreciar la saturación de IGF-1R con AVE1642 en ninguna de las concentraciones probadas. Esto indica que el PGA-AVE1642 mejora la interacción con el IGF-1R en comparación con el AVE1642.

4.1.3. Citotoxicidad de AVE1642 y PGA-AVE1642 en la Línea Celular VCaP

Tratamos las células VCaP con AVE1642 y PGA-AVE1642 durante 72 horas a 37ºC entre 50 y 0,003 µg/ml en equivalentes de AVE1642. Adicionalmente, se comprobó la citotoxicidad de portador PGA entre 64,37 y 0,0064 µg/ml. La viabilidad celular fue evaluada mediante ensayos MTS. Ambos tratamientos mostraron la misma toxicidad celular, la cual se debe al efecto del AVE1642 ya que

el portador PGA no mostró efectos citotóxicos. Estos resultados nos muestran que la unión del PGA al AVE1642 no afecta a la estructura de este ni a su funcionalidad, por lo que el AVE1642 sigue manteniendo su actividad. Además, se realizaron estudios *in vitro* en diferentes líneas celulares de CaP (VCaP, LNCaP, PC-3, DU145 y 22Rv1) y en la línea celular control (RWPE-1) para determinar mediante ensayos MTS la actividad toxicológica del AVE1642 y PGA-AVE1642. En general, sólo las células VCaP portadoras del gen de fusión T2E respondieron a los tratamientos AVE1642 y PGA-AVE1642.

4.1.4. La Conjugación Previene la Internalización de IGF-1R

Investigamos la internalización de IGF-1R en las células VCaP usando "IN Cell Analyzer". Se trataron las células durante 15, 30 y 60 minutos en presencia de AVE1642, PGA-AVE1642 y el factor de crecimiento insulínico activador 1 (IGF-1) como control positivo a 0,1 µg/ml y se cuantificó los niveles de IGF-1R por inmunofluorescencia. Tanto el IGF1 como el AVE1642 provocaron la internalización citoplasmática del IGF-1R, mientras que el tratamiento con PGA-AVE1642 evitó la internalización de IGF-1R. Estos resultados sugieren que la conjugación de PGA podría modificar la interacción con IGF-1R evitando su internalización celular.

4.1.5. La Conjugación Mejora la inhibición de IGF-1R

Para llevar a cabo este experimento, previamente ambos compuestos fueron marcados con el fluoróforo Ciane 5.5 para poder visualizarlos y cuantificarlos mediante citometría de flujo. Una vez marcados, cada uno de los compuestos se incubó durante 0, 15, 60 y 180 minutos tanto a 37ºC como a 4ºC. La incubación a 4ºC permite inhibir los mecanismos de internalización dependientes de energía, de este modo podemos determinar si la internalización es dependiente o independiente de energía comparando con los resultados obtenidos a 37ºC. Los resultados mostraron una mayor unión en membrana del conjugado polimérico

PGA-AVE1642 en comparación con AVE1642. En resumen, PGA-AVE1642 mejora la unión celular a IGF-1R mejorando su inhibición y posterior internalización.

4.1.6. La Conjugación Altera el Tráfico Celular

Para realizar este experimento, ambos compuestos fueron marcados con el fluoróforo Ciane 5.5 para poder visualizarlos mediante microscopía confocal. Cada uno de ellos se incubó durante 30 minutos en las células VCaP para permitir su internalización. Posteriormente, mediante inmunofluorescencia, se estudió la interacción de ambos compuestos con su receptor IGF-1R, mostrando una colocalización tanto con el PGA-AVE1642 como con el AVE1642. Seguidamente, empleando la misma técnica, se estudió la interacción de ambos compuestos con la clatrina, la caveolina-1, los endosomas y los lisosomas para estudiar las diferentes vías de endocitosis. El PGA-AVE1642 principalmente colocalizó con caveolina-1 y los lisosomas, en cambio el AVE1642 colocalizó en su mayoría con la clatrina, los endosomas y los lisosomas. Este resultado nos sugiere la posibilidad que ambos compuestos internalicen por rutas endocíticas diferentes, relacionado con los cambios en su bioactividad y tal vez con la diferente interacción con el IGF-1R.

4.1.7. PGA-AVE1642 Evita la Activación de las Rutas PI3K y MAPK

Para determinar el mecanismo de acción de ambos compuestos, las proteínas involucradas en la ruta endocítica del receptor IGF-1R fueron detectadas mediante ensayos de Western blot. Las células fueron tratadas con el ligando positivo (IGF-1) y ambos inhibidores (PGA-AVE1642 y AVE1642) durante 15 y 30 minutos. Una vez transcurrido este tiempo se realizó una extracción proteica y se estudió la expresión de diferentes proteínas fosforiladas mediante western blot para detectar la activación y/o inhibición de las distintas rutas dependiendo del tratamiento administrado. Las proteínas detectadas fueron las siguientes: p-Shc, p-MAPK y p-PI3K. Las células tratadas con el ligando positivo (IGF-1) mostraron una

activación de ambas rutas (Shc/MAPK y PI3K) debido a la fosforilación de las proteínas Shc, MAPK y PI3K. En el caso de las células tratadas con AVE1642, pudimos observar una inhibición de la ruta PI3K debido a los bajos niveles de expresión de la proteína p-PI3K, pero observamos una activación de la ruta Shc/MAPK indicada por una fosforilación de las proteínas p-Shc y p-MAPK. En cambio, cuando las células fueron tratadas con PGA-AVE1642 se detectó la inhibición de ambas rutas (Shc/MAPK y PI3K) debido a los bajos niveles de expresión de las proteínas p-Shc, p-MAPK y p-PI3K. Estos resultados sugieren un mecanismo de acción diferente para ambos inhibidores: por un lado, el AVE1642 inhibe la ruta PI3K y mantiene activa la ruta de Shc/MAPK, la cual está involucrada en la internalización de IGF-1R, mientras que el tratamiento con PGA-AVE1642 inhibe ambas rutas, Shc/MAPK y PI3K, lo cual explica que en experimentos previos no observáramos una internalización de IGF-1R. En general, estos resultados sugieren que el tratamiento con PGA-AVE1642 mejora la inhibición de IGF-1R mostrada por la inactivación de las rutas de señalización intracelulares.

4.1.8. La Conjugación Mejora la Actividad Antitumoral de AVE1642

Para validar los resultados obtenidos en los ensayos *in vitro*, se optimizó un modelo ortotópico de CaP. Para poder evaluar el crecimiento tumoral en el modelo ortotópico es necesario que las células de interés expresen luciferasa. Una vez transfectada la línea celular VCaP con luciferasa (VCaP-Luc2), se confirmó mediante Western Blot y ensayos de viabilidad celular que dicha transfección no afectaba a los diferentes niveles de expresión de las proteínas involucradas en la diana terapéutica del tratamiento (IGF-1R-β, AR y ERG) y que mantenía la viabilidad celular comparándola con la línea celular sin transfectar.

Seguidamente, la optimización del modelo se llevó a cabo utilizando ratones C.B-17/IcrHan®Hsd-*Prkdc*^{scid} e inyectando un millón de células VCaP-Luc2 en la zona ventral prostática. El crecimiento del tumor fue monitorizado

semanalmente utilizando la tecnología IVIS® Spectrum. Se pudo observar un crecimiento tumoral homogéneo y una localización intraprostática obteniendo el máximo volumen tumoral permitido a las siete semanas. Para determinar el punto máximo de acumulación tumoral y de este modo empezar a administrar el tratamiento en dicho punto, se realizaron estudios de EPR. Los resultados mostraron una mayor acumulación en la segunda semana de crecimiento tumoral.

Una vez establecido y optimizado el modelo animal, se administró el tratamiento a partir de la segunda semana tras la inyección celular a una concentración de 10 mg/kg tanto del AVE1642 como del PGA-AVE1642 una vez por semana durante cuatro semanas y se evaluó el crecimiento del tumor mediante IVIS hasta la séptima semana. Ambos compuestos mostraron una reducción significativa del crecimiento del tumor comparado con el tumor no tratado, pero aquellos tumores tratados con PGA-AVE1642 tuvieron significativamente una mayor actividad antitumoral en comparación con los tumores tratados con AVE1642. Posteriormente, se midieron los niveles de PSA y se determinó la densidad de los tumores. Los niveles de PSA se correlacionaron directamente con el volumen tumoral, en cambio, se pudo observar una correlación inversa entre el volumen tumoral y la densidad. Aquellos tumores con un menor volumen presentaron una mayor densidad posiblemente ocasionado por la presencia de zonas necróticas y calcificaciones. Adicionalmente, como control, los animales fueron tratados con el portador PGA a 8,45 mg/kg empleando la misma pauta de administración anteriormente descrita. El tamaño tumoral, los niveles de PSA y la densidad no mostraron diferencias en comparación con el control, confirmando de este modo la seguridad del PGA.

4.1.9. PGA-AVE1642 Mejora la Inhibición de IGF-1R In Vivo

Para explicar la mayor efectividad antitumoral con el tratamiento PGA-AVE1642, nuestro siguiente paso se centró en el estudio de las diferentes rutas de señalización en el tumor comparando ambos tratamientos con el grupo control. Se estudió la expresión de diferentes proteínas fosforiladas mediante western blot para detectar la activación y/o inhibición de las distintas rutas dependiendo del tratamiento administrado. Las proteínas detectadas fueron las siguientes: p-Shc, p-MAPK, p-PI3K, IGF-1R total, AR y ERG. En general, no se observaron cambios significativos en la expresión de p-MAPK, AR y ERG, sin embargo, cuando se comparó con el control, se descubrió una reducción significativa en la expresión de IGF-1R-β y p-PI3K en los tumores tratados con PGA-AVE1642. Además, también observamos una reducción significativa en los niveles de proteínas p-Shc, p-PI3K e IGF-1R-β entre los tumores tratados con PGA-AVE1642 y AVE1642. Estos resultados sugieren que el PGA-AVE1642 mejora la inhibición del IGF-1R debido a la inactivación de las vías de señalización p-Shc y p-PI3K.

4.1.10. PGA-AVE1642 Mejora la Inhibición de la Proliferación Celular y la Angiogénesis

Se investigó la proliferación celular en las muestras tumorales mediante la detección del marcador de proliferación Ki67. La cuantificación de este marcador reveló una reducción significativa de la proliferación celular en los tumores tratados con AVE1642 en comparación con el grupo control. En cambio, el tratamiento con PGA-AVE1642 proporcionó una disminución significativamente más robusta en la proliferación celular en comparación con el grupo control y AVE1642.

Adicionalmente, se estudió el marcador angiogénico VEGFR2 después de los diferentes tratamientos. La cuantificación de este marcador confirmó una reducción significativa de los niveles de VEGFR2 en los tumores tratados con

AVE1642 y una reducción significativa más marcada en los tumores tratados con PGA-AVE1642. Además, el tratamiento PGA-AVE1642 provocó una reducción significativa de los niveles de VEGFR2 en comparación con los tumores tratados con AVE1642. Estos resultados sugieren que la conjugación de PGA mejora la eficacia antiangiogénica de AVE1642.

4.2. Evaluación de una Nueva Terapia de Combinación para el Cáncer de Próstata Resistente a Castración

4.2.1. La Terapia de Combinación Mantiene la Inhibición de IGF-1R In Vivo

Para estudiar la terapia de combinación en el modelo animal, el acetato de abiraterona fue administrado solo y en combinación con los tratamientos AVE1642 y PGA-AVE1642. Ambas terapias de combinación mostraron una reducción significativa del crecimiento tumoral en comparación con el grupo control, pero hay que remarcar que los tumores tratados con AVE1642 en combinación con acetato de abiraterona tuvieron significativamente una mayor actividad antitumoral en comparación con los tumores tratados con cada tratamiento por separado, mostrando de este modo un efecto sinérgico *in vivo*. En cambio, los tumores tratados con PGA-AVE1642 en combinación con acetato de abiraterona no mostraron un efecto sinérgico *in vivo* ya que el crecimiento tumoral no reveló diferencias significativas en comparación con los tumores tratados con PGA-AVE1642. Posteriormente, se determinaron los niveles de PSA y la densidad tumoral. Los niveles de PSA se correlacionaron con el volumen tumoral, en cambio, solo los tumores tratados con acetato de abiraterona mostraron un aumento de la densidad en comparación con el resto de los tratamientos.

Para explicar el efecto antitumoral obtenido, se estudiaron diferentes proteínas fosforiladas y no fosforiladas para detectar el estado de activación y/o inhibición de las rutas de señalización. Las proteínas detectadas fueron las

siguientes: p-Shc, p-MAPK, p-PI3K, p-IGF-1R-β, IGF-1R-β AR y ERG. En general, no se observaron cambios significativos en la expresión de p-MAPK y AR. Sin embargo, cuando se comparó con el control, se descubrió una reducción significativa de p-IGF-1R-β, p-Shc, p-PI3K, IGF-1R-β y ERG en ambas terapias de combinación y una reducción significativa en p-Shc en los tumores tratados con acetato de abiraterona. Estos resultados sugieren que ambas terapias de combinación inhiben completamente el IGF-1R debido a la inactivación de las vías de señalización p-Shc y p-PI3K.

5. Conclusiones

Nuestro trabajo se centró en el uso de polímeros terapéuticos como enfoque terapéutico para la terapia de CaP, donde investigamos cómo la conjugación del PGA alteraba las propiedades biológicas de un anticuerpo monoclonal humano (AVE1642) con la esperanza de aumentar la actividad antitumoral de AVE1642 en el CaP agresivo. Demostramos una mayor bioactividad del anticuerpo monoclonal después de la conjugación con PGA y exploramos el potencial de la terapia de combinación como una opción de tratamiento avanzada para un subtipo de pacientes con CaP.

Las principales conclusiones de esta tesis son las siguientes:

1. Hemos optimizado el desarrollo de un nuevo conjugado formado por la unión del polímero a un anticuerpo, siendo la mejor relación 2:1 (dos cadenas de poliglutamato (PGA) por cada AVE1642).

2. La conjugación del PGA aumenta el volumen hidrodinámico y la carga negativa de AVE1642, aunque se mantiene la estructura secundaria del AVE1642.

3. La conjugación del PGA no promueve la hemólisis en suero de ratón, lo que demuestra su seguridad, protege al AVE1642 de la degradación en suero

mejorando la estabilidad del AVE1642, mejora la estabilidad térmica del AVE1642, sin embargo, no mejora la acumulación de AVE1642 en los tumores.

4. La conjugación del PGA no altera la funcionalidad de AVE1642 y mantiene la selectividad de AVE1642 para la sobreexpresión de ERG asociada con la presencia del gen de fusión T2E en las células de CaP.

5. La conjugación del PGA modifica el tráfico celular *in vitro*. AVE1642 y PGA-AVE1642 se dirigen a los lisosomas por diferentes vías endocíticas. Mientras que el AVE1642 se internaliza principalmente por endocitosis mediada por clatrina y se dirige a los lisosomas a través de endosomas, el PGA-AVE1642 se internaliza principalmente por endocitosis mediada por caveolina y se dirige a los lisosomas con una ausencia de colocalización endosómica probablemente debido a interacciones diferenciales con el receptor.

6. Optimizamos un nuevo modelo de ratón ortotópico para el CaP avanzado utilizando la línea celular VCaP transfectada con luciferasa.

7. La conjugación del PGA permite una alteración de la respuesta molecular *in vitro* e *in vivo* mejorando la actividad antitumoral evitando la activación de ambas vías de señalización PI3K y MAPK, mejorando así la efectividad del AVE1642. Sin embargo, mientras obtenemos una inhibición de la activación de la vía de señalización PI3K después del tratamiento con AVE1642 *in vitro*, no detectamos ninguna inhibición de las vías *in vivo*.

8. PGA-AVE1642 mejora la inhibición de IGF-1R al prevenir la internalización dependiente de energía de IGF-1R, inhibiendo tanto la vía del PI3K como la del MAPK. AVE1642 permite la internalización de IGF-1R y evita la activación de la vía de señalización PI3K.

9. El tratamiento PGA-AVE1642 promueve alteraciones más robustas en el microambiente tumoral en comparación con el AVE1642, como una disminución tanto en la funcionalidad como de la madurez de los vasos sanguíneos. Además, el PGA-AVE1642 mejora significativamente la inhibición de la proliferación del tumor de próstata y la angiogénesis en comparación con AVE1642.

10. Los estudios *in vitro* mostraron un efecto sinérgico dependiente de la presencia del gen de fusión T2E para los tratamientos con PGA-AVE1642 y AVE1642 en combinación con abiraterona. Sin embargo, mientras se obtuvo un efecto antitumoral sinérgico para el tratamiento con AVE1642 en combinación con abiraterona *in vivo*, no se encontró un efecto aditivo para el tratamiento con PGA-AVE1642 y abiraterona debido al mecanismo de acción molecular diferencial tras la conjugación del PGA ya que ambas terapias de combinación promovieron una doble vía de inhibición a través de PI3K y MAPK.

6. Bibliografía

1. Bray, F., et al., *Global Cancer Statistics 2018: GLOBOCAN Estimates of Incidence and Mortality Worldwide for 36 Cancers in 185 Countries: Global Cancer Statistics 2018.* CA: A Cancer Journal for Clinicians, 2018. **68**(6): p. 394-424.
2. Antonarakis, E., et al., *The natural history of metastatic progression in men with prostate-specific antigen recurrence after radical prostatectomy: Long-term follow-up.* BJU International, 2011. **109**: p. 32-9.
3. Gleason, D., *Gleason DF. Classification of prostatic carcinomas. Cancer Chemother Rep 50: 125-128.* Cancer Chemotherapy Reports. Part 1, 1966. **50**: p. 125-8.
4. Ryan, C. and Tindall, D. *Androgen Receptor Rediscovered: The New Biology and Targeting the Androgen Receptor Therapeutically.* Journal of Clinical Oncology, 2011. **29**: p. 3651-8.
5. Beggs, R. and E. Yang, *Targeting DNA repair in precision medicine*. Advances in Protein Chemistry and Structural Biology, 2019. **115**: p. 135-155.

6. Crumbaker, M., L. Khoja, and A.M. Joshua, *AR Signaling and the PI3K Pathway in Prostate Cancer.* Cancers, 2017. **9**(4): p. 34.
7. Beltran, H., et al., *Targeted Next-generation Sequencing of Advanced Prostate Cancer Identifies Potential Therapeutic Targets and Disease Heterogeneity.* European Urology, 2012. **63**(5): p. 920-6.
8. Miyahira, A., et al., *Tumor cell heterogeneity and resistance; report from the 2018 Coffey-Holden Prostate Cancer Academy Meeting.* The Prostate, 2018. **79**(3): p. 244-258.
9. Tabayoyong, W. and R. Abouassaly, *Prostate Cancer Screening and the Associated Controversy.* Surgical Clinics of North America, 2015. **95**(5): p. 1023-39.
10. Koo, K., et al., *Merging new-age biomarkers and nanodiagnostics for precision prostate cancer management.* Nature Reviews Urology, 2019. **16**(5): p. 302-317.
11. Yin, C., et al., *Molecular Profiling of Pooled Circulating Tumor Cells from Prostate Cancer Patients Using a Dual-Antibody-Functionalized Microfluidic Device.* Analytical Chemistry, 2018. **90**(6): p. 3744-3751.
12. Bryce, A. and E. Antonarakis, *Androgen receptor splice variant 7 in castration-resistant prostate cancer: Clinical considerations.* International Journal of Urology, 2016. **23**(8): p. 653.
13. Jamaspishvili, T., et al., *Clinical implications of PTEN loss in prostate cancer.* Nature Reviews Urology, 2018. **15**(4): p. 222-234.
14. Eryilmaz, I.E., et al., *T2E (TMPRSS2-ERG) fusion transcripts are associated with higher levels of AMACR mRNA and a subsequent prostate cancer diagnosis in patients with atypical small acinar proliferation.* Gene, 2018. **645**: p. 69-75.
15. Sumanasuriya, S. and J. de Bono, *Treatment of Advanced Prostate Cancer—A Review of Current Therapies and Future Promise.* Cold Spring Harbor Perspectives in Medicine, 2017. **8**: p. 030635.
16. Nevedomskaya, E., S. Baumgart, and B. Haendler, *Recent Advances in Prostate Cancer Treatment and Drug Discovery.* International Journal of Molecular Sciences, 2018. **19**: p. 1359.
17. Adashek, J.J., R.K. Jain, and J. Zhang, *Clinical Development of PARP Inhibitors in Treating Metastatic Castration-Resistant Prostate Cancer.* Cells, 2019. **8**(8): p. 860.

18. Sartor, O., et al., *Effect of radium-223 dichloride on symptomatic skeletal events in patients with castration-resistant prostate cancer and bone metastases: Results from a phase 3, double-blind, randomised trial.* The Lancet Oncology, 2014. **15**(7): p. 738-46.
19. Duncan, R. and M. Vicent, *Polymer Therapeutics-Prospects for 21st Century: The End of the Beginning.* Advanced Drug Delivery Reviews, 2012. **65**(1): p. 60-70.
20. Duncan, R., et al., *Polymer-drug conjugates: Towards a novel approach for the treatment of endrocine-related cancer.* Endocrine-Related Cancer, 2005. **12 Suppl 1**: p. 189-99.
21. Mancarella, C., et al., *ERG deregulation induces IGF-1R expression in prostate cancer cells and affects sensitivity to anti-IGF-1R agents.* Oncotarget, 2015. **6**(18): p. 16611-16622.
22. Lee, S., et al., *Crosstalking between Androgen and PI3K/AKT Signaling Pathways in Prostate Cancer Cells.* The Journal of Biological Chemistry, 2014. **290**(5): p. 2759-68.